Acoustical Physics, Vol. 48, No. 1, 2002, pp. 1–7. Translated from Akusticheskiĭ Zhurnal, Vol. 48, No. 1, 2002, pp. 5–11.

Acoustic Tomography of Dynamic Processes in a Sea Shelf Zone with the Use of Complex Signals

V. A. Akulichev, V. V. Bezotvetnykh, S. I. Kamenev, E. V. Kuz'min, Yu. N. Morgunov, and A. V. Nuzhdenko

Pacific Oceanological Institute, Far-East Division, Russian Academy of Sciences, Baltiĭskaya ul. 43, Vladivostok, 690041 Russia

e-mail: akulich@marine.febras.ru

Received April 4, 2001

Abstract—Experimental data are presented on the use of single receiving and transmitting systems in acoustic tomography of dynamic processes in a shallow sea. The experiments are based on the use of the transmission tomography and opposite-direction sounding with complex phase-manipulated signals. The original data are those obtained by the authors in 1990–2000 on the shelf of the Sea of Japan near the Gamov Peninsula, in the vicinity of the acoustical-hydrophysical experimental site of the Pacific Oceanological Institute. A possibility of using combined transmitting–receiving systems (transceivers) for monitoring the temperature and fields of currents in the ocean is demonstrated. © *2002 MAIK "Nauka/Interperiodica".*

Acoustic tomography is widely known as a promising method for monitoring the currents and temperature fields in the ocean. However, its implementation in coastal regions faces great difficulties. In this paper, we consider the experiments performed at the shelf of the Sea of Japan with the aim to show possible ways of settling the problem of acoustic tomography of the sea medium in shallow-water regions.

The Sea of Japan is an important object for studying the laws of climate formation, ventilation of the near-bottom water layers, migration of sea animals, spread and accumulation of pollutants, and many other processes of natural and antropogenic characters, which influence the environment in the Asian Pacific Region. In such studies, the changes in the temperature regimes and in the dynamics of the water bulk are the key points. The cold Maritime and warm Tsushima currents, which travel in opposite directions, give rise to a frontal zone and a great number of vortex systems. The situation becomes still more intricate because of the dynamic processes in the coastal regions of the ocean, which are associated with the bottom topography and tidal flows. With such an environment, the efficiency of contact methods that are traditional for oceanology depends on the possibility to arrange the measuring devices at distances that do not exceed the spatial correlation lengths of the processes to be studied, and to perform long-term observations. The technical and economical considerations led to new measuring technologies in the oceanographic practice, which are based on the acoustic tomography technique. The implementation of this technique often requires complicated and expensive devices. For instance, in [1, 2], for monitoring the current and temperature fields, vertical arrays are proposed that consist of acoustic transceivers (i.e., combined sources and receivers of sound) and hydrophones. Such systems are practically inapplicable in shallow-water regions with intense ship traffic and high current speeds. On the other hand, according to many publications [2–4], the use of single bottom-moored systems for the transmission and reception of probing signals can lead to errors caused by the insufficient time resolution of the ray arrivals and, hence, to the impossibility of their identification. However, the advantages of the aforementioned systems are so evident and promising that, in our opinion, further and deeper studies are needed to develop simple and highly efficient devices for acoustical methods of monitoring the sea medium. Here, we present the data of the experiments on the acoustic tomography using single bottom-moored systems and probing signals of high complexity.

To test the technique and the instrumental implementation of the tomographic system, an acoustical-hydrophysical site was arranged at the coastal testing ground of the Pacific Oceanological Institute, near the Gamov Peninsula. The experimental site included fixed self-contained transmitting and receiving systems that can be installed at an arbitrary point and are cable-connected with the coastal laboratory equipped with controlling, data-collecting, and processing devices [5].

1063-7710/02/4801-0001$22.00 © 2002 MAIK "Nauka/Interperiodica"

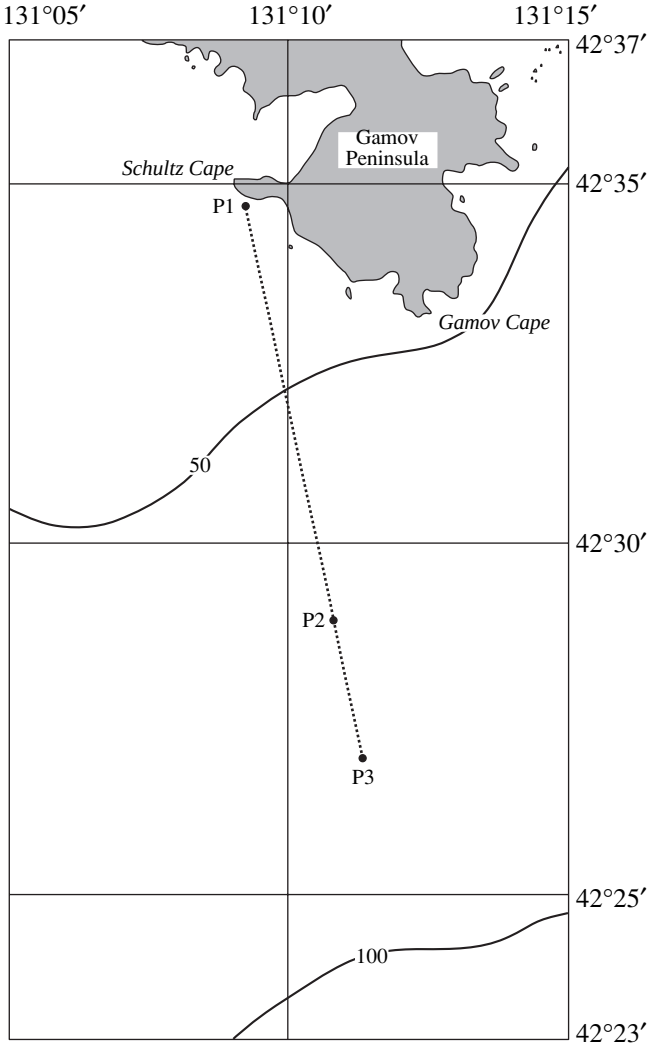

Fig. 1. Acoustic paths and locations of the transmitting and receiving systems: P1, transceiver 1; P2, transceiver 2; and P3, single hydrophone (radio-hydroacoustical buoy).

As probing signals, phase-manipulated ones, namely, M-sequences, were used, with 511 symbols in each sequence, the characteristic polynomial $X^9 + X^4 + 1$, and the symbol lengths that were equal to 4 or 8 periods of the carrier frequency. The phase shift φ was specified to be zero for the symbol "1" and φ = 174.934° for the symbol "0." Such values of the shift ensured a smoothing of the envelope of the signal amplitude spectrum and a partial suppression of the side peaks of the correlation function. For the signal reception, radio-acoustic buoys with hydrophones were used; the buoys were positioned at different points of the site, 1 m above the bottom. The received signal was subjected to the cross-correlation processing with the transmitted one. The correlation maximums determine the arrival times of the ray groups or modes that propagate over different paths. In these studies, we did not intend to solve the inverse problem of reconstructing the hydrophysical parameters of the sea medium by means of a theoretical inversion method. Instead, we approximately calculated the average sound speed and flow velocity to estimate the accuracy of the method.

In the opposite-direction sounding, the arrival times t_n^- and t_n^+ were measured for the nth ray group (the nth mode) that corresponded to the signal propagation against and along the flow, respectively. Then, the sum $S_n = t_n^+ + t_n^-$ and the difference $\Delta t_n = t_n^- - t_n^+$ of the arrival times were found. Finally, the component $V_n = \Delta t_n c_n^2 / 2r$ of the flow velocity was determined along the path of the length r for the nth ray group (mode), and the propagation velocity $c_n = 2r/S_n$ of this group was calculated. In this procedure, we assumed that the field of velocities V_n and c_n was horizontally uniform and that $V_n \ll c_n$. The relations used in the calculations were based on the generalized reciprocity principle [6].

In the course of the experiments carried out from October 1999 to November 2000, we used different depths of the transceivers, receivers, and transmitters, as well as different distances between them. We also studied the parameters of the tidal internal waves, the currents, and the water temperature on the shelf to test and adapt different techniques of measuring the temperature and current fields to the specific conditions of the Sea of Japan. As a result, a representative body of experimental data was obtained (about 400 h of continuous records).

Here, we present the data of two experiments on studying the possibility to use single bottom-moored systems for acoustically monitoring the temperature and the fields of currents in a shallow-water sea. Figures 1 and 2 show the map and the diagram of these experiments.

To begin, we consider the experiment on measuring the flow velocity by opposite-direction sounding. This experiment was performed in October 2000.

The transmitter of an acoustic transceiver 1 that was 150 m offshore and 1 m above the bottom (sea depth 27 m, point P1) was electrically supplied and controlled through a cable from the coastal station. Transceiver 2 that was located 12 km away from the coastline and also 1 m above the bottom (sea depth 60 m, point P2) was self-contained in its energy supply. In both transceivers, electromagnetic-type transducers were used as the sound sources with a central frequency of 250 Hz and a bandwidth of 60 Hz. The signals received by the hydrophones of transceivers 1 and 2, both mounted 20 cm apart from the centers of the emitting transducers, were radio-transmitted to the coastal laboratory for the data acquisition and analysis.

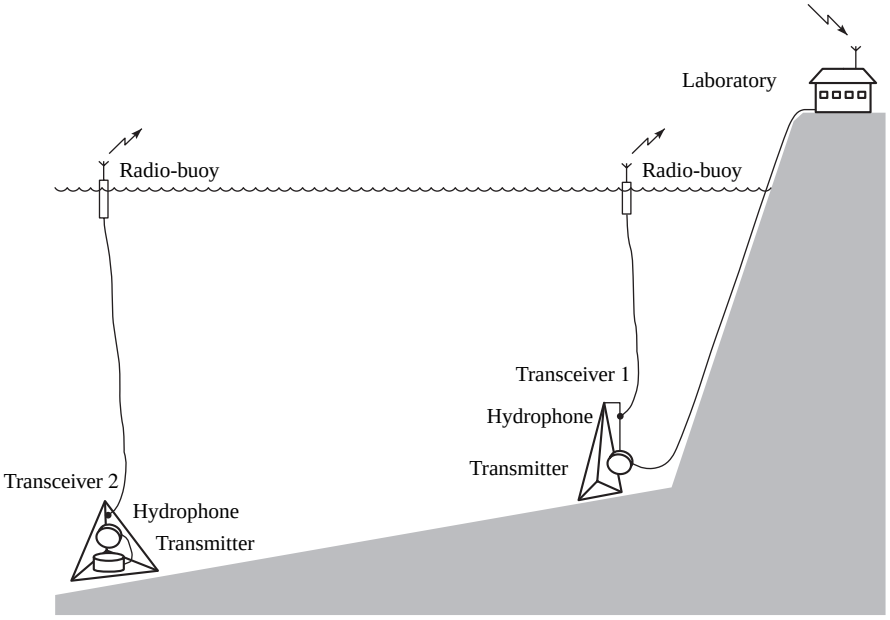

Fig. 2. Positions of the devices at the experimental site.

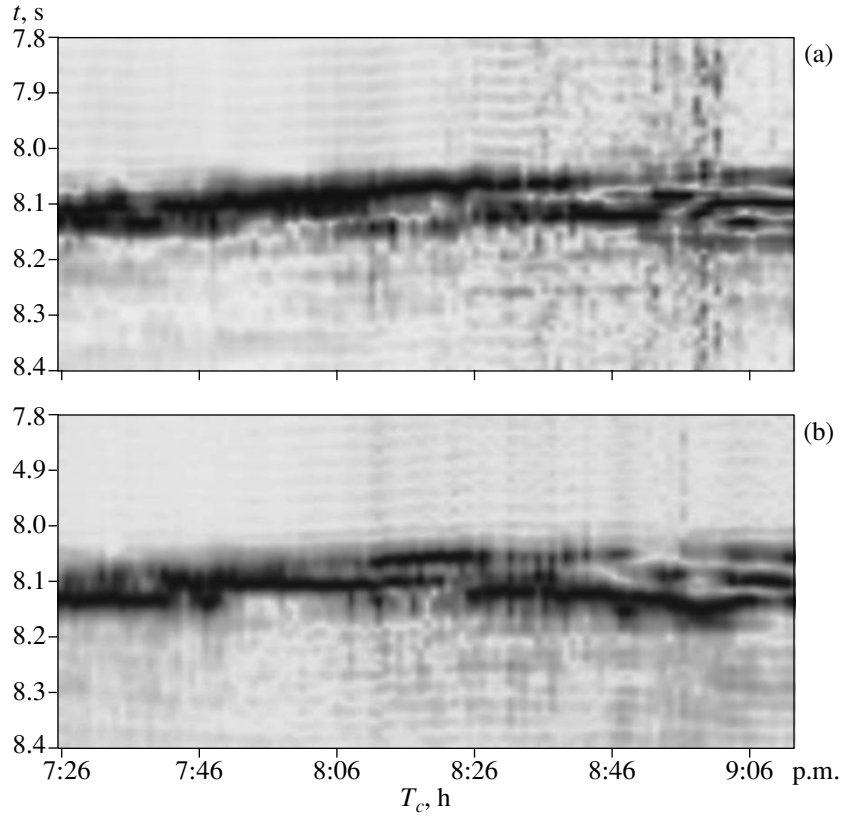

Fig. 3. Variations in the arrival times t of the sound signals versus time T_c of the day: (a) path P1–P2; (b) path P2–P1.

At the experimental site, the water column was isothermal from the surface to the bottom, with a slight negative gradient in the vertical temperature distribution during the tide-caused intrusion of cold waters to the shelf.

Every minute, the transceivers transmitted the M-sequences which were shifted relative to each other by 30 s to eliminate the interference caused by their own emissions. Figure 3 shows the variations in the arrival times of the sound signals that were received in

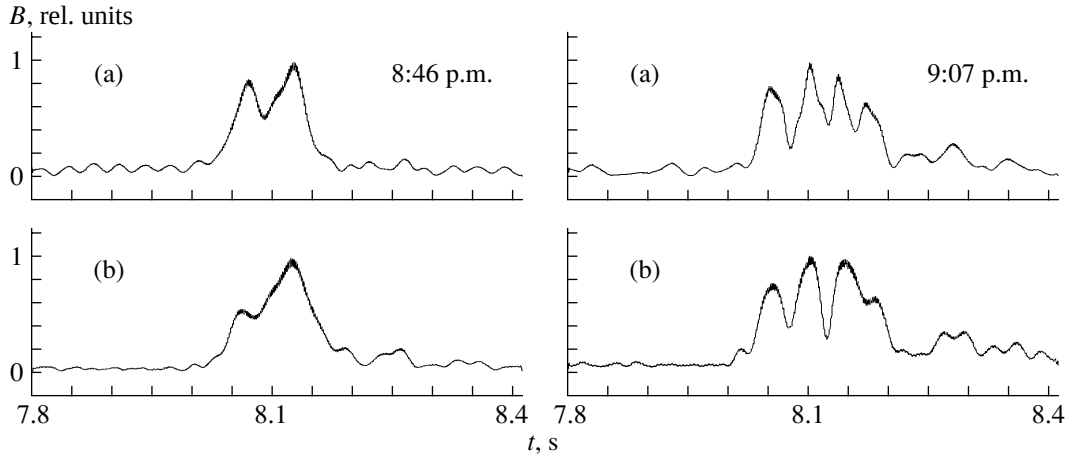

Fig. 4. Normalized cross-correlation function B in the range of signal arrival times t for two times T_c of the day (see Fig. 3) and two propagation paths: (a) path P1–P2; (b) path P2–P1.

the opposite-direction sounding at the time of the maximal velocities of the tide-caused water flow. The amplitudes of the cross-correlation function of the transmitted and received signals are represented by the brightness picture. The cross-correlation maximums served to determine the arrival times. The comparison of the two dependences shows that the main features of the time structure of the sound field are the same for the sound propagation against and along the flow: the reciprocity principle is valid. Figure 4 shows two fragments of these dependences that more obviously exhibit the reciprocity of the process and display the time shift between the arrivals of the signals propagating in opposite directions.

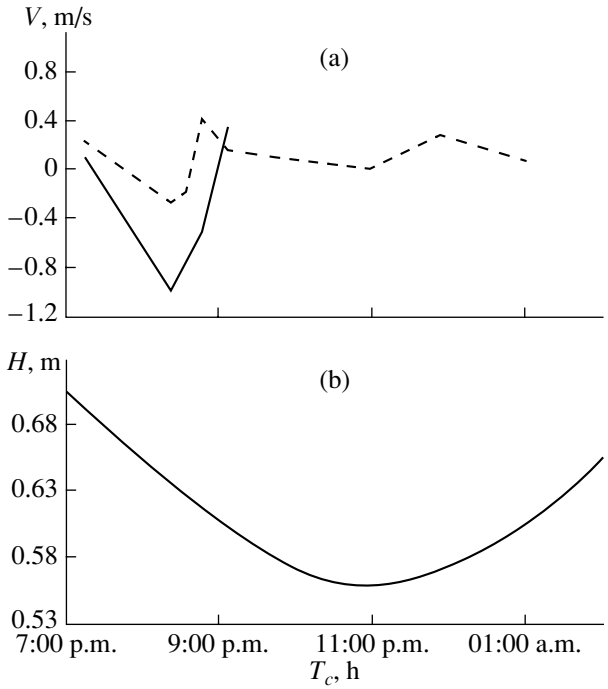

Fig. 5. Dependences on time T_c of the day: (a) for the component of the velocity of current V in the direction of signal propagation for the whole waveguide (the solid curve) and for the near-bottom layer (the dashed curve); (b) for the tide height H.

In Fig. 5, the component of the velocity of current along the propagation direction and the tide height are plotted versus time. The values of the velocity were calculated according to the aforementioned formulas for two signal arrivals: the first one formed by the rays propagating in the whole water layer and the second one formed by the rays propagating in the near-bottom layer of colder water. The positive and negative values correspond to the water flows towards and away from the coast, respectively. The minimal velocity was observed at ebb-tide (11 p.m.), and the maximal one corresponded to high tide (8:20 p.m.). As one would expect, the velocity is lower in the near-bottom layers than in the upper ones. The data obtained in the experiment agree well with the features of the dynamic processes in the water bulk of this region of the ocean, which were established in long-term oceanographic studies.

In the experiment that was carried out in the middle of October 1999, the sea medium was sounded by the complex signals (an M-sequence with the 250-Hz central frequency) every four hours, with the use of the sound source mounted on transceiver 1 (Figs. 1 and 2). The signal was received by the single hydrophone located at point P3, at a distance of 15 km, again, 1 m above the bottom. The received signals were transmitted to the coastal station through a radio-channel.

In the shelf region where the transmitting and receiving systems were located, the situation was governed by an irregular semidiurnal tide, with the associated variations in temperature and salinity. At high tide,

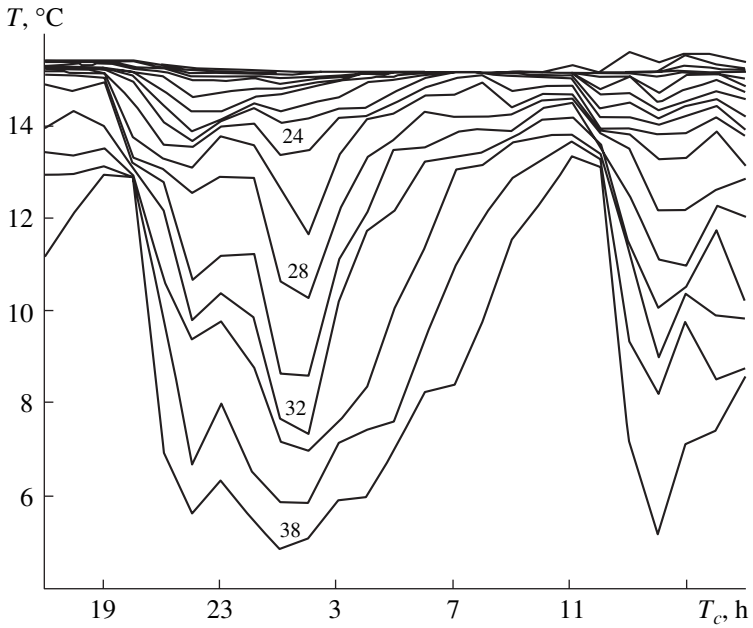

Fig. 6. Variations in the water temperature T°C versus time T_c of the day. The parameters of the curves are the depths (in meters).

starting from the 16-m horizon, warm coastal waters were replaced by colder and saltier sea waters. In this process, the temperature variations reached 10°C in the lower layers. Figure 6 shows the time dependence of the water temperature at different depths.

Figure 7 illustrates the 24-hour variations in the normalized cross-correlation function of the transmitted sound signal and that received at point P3. As mentioned above, these variations are related to those in the times of signal propagation along different paths. The maximal values of the propagation velocity, as measured for the main part of the signal power, correspond to 6:52 a.m. and 6:52 p.m., these times coinciding with those of ebb-tides, that is, with the moments of the isothermal water stratification caused by the withdrawal of the cold salty water. One can see that the propagation velocity is higher at 6:52 a.m., at the moment of the main tide (the daily phase). The latter fact characterizes the sensitivity of the proposed method, because, at 6:52 p.m., the vertical temperature distribution has a higher negative gradient, and, hence, more of the signal energy travels through the near-bottom water layer with a lower sound speed. The latest arrivals of the main signal energy are observed at 2:52 and 10:52 p.m. These values also agree with the ray theory, because they correspond to the tide phases of the highest negative gradient in the vertical temperature distribution. Hence, at these times, the rays travel along the longest paths near the bottom, in the layers with the minimal sound speed.

To analyze the effect of fine phenomena of smaller time scales on the sound propagation, we performed a one-hour-long session of sounding with a repetition rate of 30 s. The calculated cross-correlation functions and the signal arrival times are shown in Fig. 8. The time dependence shown exhibits pronounced effects of a wave process having a period of about 20 min. One can assume that, in this case, the sound field was influenced by internal waves, because the previously measured [7, 8] periods of internal waves have the same values.

Thus, the method of sounding the sea medium by complex signals revealed some features in the sound field formed under the influence of the dynamic hydrophysical processes. So, the conclusion can be drawn that the proposed method and its instrumental implementation are promising for solving the inverse problems in coastal regions. The arrival times of ray groups or modes depend on the vertical and horizontal distributions of the sound speed, which, in turn, are governed by the temperature and salinity distributions, as well as by the direction and velocity of the current. In data processing, the r.m.s. error is no higher than 2 ms, which is low enough to measure the water temperature to an accuracy of 1°C and the velocity of the current to an accuracy of 0.1 m/s. The presence of several arrivals of the ray groups (two to four in our experiments), which travel through different layers of the waveguide, allows one to estimate the fields of temperatures and currents in the vertical plane.

The simplicity, mobility, and low cost of the developed technique support its practical use in solving applied problems. The proposed tomographic systems can significantly improve the technical properties of the surfacing-and-drifting oceanographic buoys, which

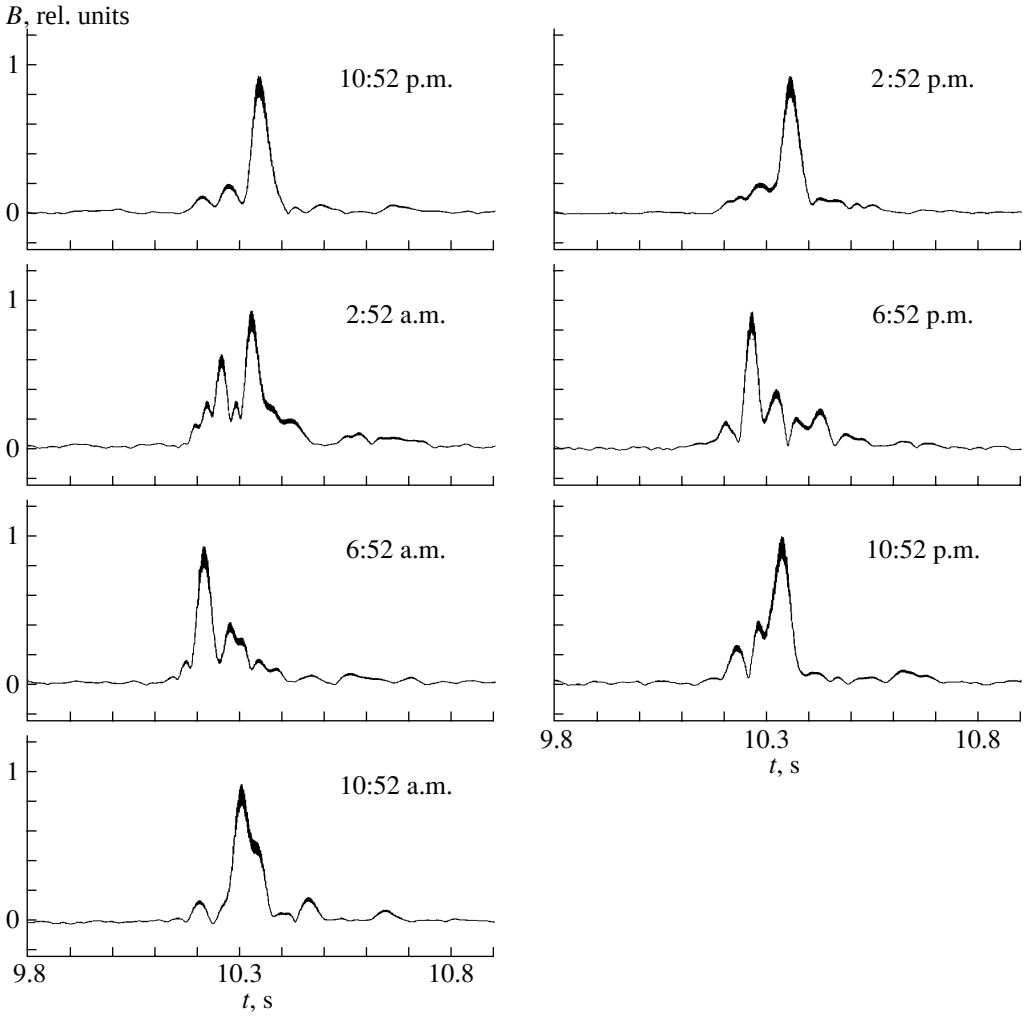

Fig. 7. Twenty-four-hour' variations in the normalized cross-correlation function B of the transmitted signal and that received at the point P3 for the range of the signal arrival times t.

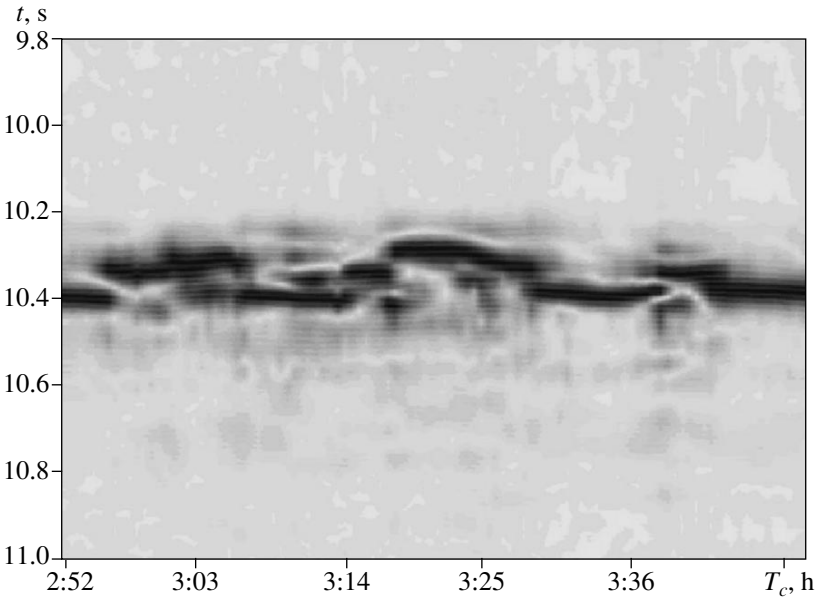

Fig. 8. Variations in the arrival time t of the sound signals versus time of the day T_c.

now are being set into practice in the United States and Japan (the ARGO Program—Array Real-Time Geostrophic Oceanography). The use of the proposed technique seems to be most advantageous on shallow-water shelves and in regions with complicated ice environments.

ACKNOWLEDGMENTS

This work was supported by the International Project of the Russian and Chinese Foundations for Basic Research (no. 99-05-39140) and the Joint American-Russian Project JESAEX (the Japan/East Sea Acoustics Experiment).

REFERENCES

1. A. N. Gavrilov, in *Proceedings of the VIII School–Seminar of Academician L.M. Brekhovskikh "Acoustics of the Ocean"* (GEOS, Moscow, 1999), p. 7.
2. O. A. Godin, D. Yu. Mikhin, and D. R. Palmer, Izv. Ross. Akad. Nauk, Fiz. Atmos. Okeana **36** (1), 141 (2000).
3. H. A. DeFerrari and H. B. Nguyen, J. Acoust. Soc. Am. **79**, 299 (1986).
4. D. B. Chester, P. Malonotte-Rizzoli, and H. A. DeFerrari, J. Geophys. Res. **96**, 7023 (1991).
5. V. A. Akulichev, V. V. Bezotvetnykh, S. I. Kamenev, *et al.*, Prib. Tekh. Eksp., No. 6, 112 (2000).
6. L. M. Lyamshev, Dokl. Akad. Nauk SSSR **138** (3), 575 (1961) [Sov. Phys. Dokl. **6**, 410 (1961)].
7. A. N. Serebryanyĭ, Okeanologiya (Moscow) **35** (4), 497 (1995).
8. V. A. Akulichev, V. V. Bezotvetnykh, S. I. Kamenev, *et al.*, in *Proceedings of the Seventh Western Pacific Regional Acoustics Conference (WESTPRAC VII), Kumamoto, Japan, 2000*, Vol. 2, p. 1159.

Translated by E. Kopyl

Acoustical Physics, Vol. 48, No. 1, 2002, pp. 107–109. Translated from Akusticheskiĭ Zhurnal, Vol. 48, No. 1, 2002, pp. 120–122.

SHORT COMMUNICATIONS

Analysis of the Natural Vibrations of Circular Piezoceramic Plates of Variable Thickness

N. F. Ivina

Makarov Pacific Naval Institute, ul. Kamskaya 6, Vladivostok, 690062 Russia

e-mail: helicot@mail.primorye.ru

Received December 12, 2000

Circular piezoceramic plates are widely used in modern acoustic instruments. The study of circular plates of a conventional shape (of uniform thickness and constant radius, see Fig. 1a) is the subject of many publications, e.g., [1–3]. From the experiment [1], it has been known that, in the case of thickness vibrations, the distribution of the normal displacement component at the flat surfaces of a circular plate is not uniform (piston-like), as would follow from the one-dimensional theory, but is oscillatory in nature. The solutions corresponding to the experimental data were obtained later using the variational method [2] and the finite-element method (FEM) [3]. The vibrations characterized by a cophased distribution of the axial displacement component at the $z = l$ plane and a dominance of this component over the radial one were called quasi-thickness vibrations [3]. It was shown that the quasi-thickness vibrations are formed by the fourth, seventh, tenth, thirteenth and subsequent modes at certain values of the piezoelectric plate thickness l/a. For each of these modes, there exist the optimal plate dimensions l/a at which the dynamic electromechanical coupling coefficient (DCC) is maximal.

The oscillatory nature of the distribution of the normal displacement component at the flat surfaces of a piezoelectric plate results in the fact that the DCC of the quasi-thickness vibrations of piezoelectric plates is lower than the static coupling coefficient of thickness vibrations k_t calculated by the one-dimensional theory. The DCC amounts to $0.7k_t$ for the plates made of the first-type piezoceramics and to $0.8k_t$ for the second-type piezoceramic plates [3, 4]. It is obvious that the oscillations of the normal displacement component are caused by the presence of a cylindrical surface confining the plate in the radial direction. By varying the shape of this surface, i.e., by using a plate of variable rather than uniform thickness, an effort could be made to reduce the oscillations of the normal displacement component (to smooth out its distribution) and to increase the DCC of the quasi-thickness vibrations.

Two technologically simple modifications of variable-thickness piezoelectric plates, symmetric about the plane $z = 0$, are shown in Figs. 1b and 1c. For brevity of further discussion, we call the plate shown in Fig. 1b the convex piezoelectric plate, as distinct from the concave one in Fig. 1c. A common piezoelectric plate is confined by the coordinate surfaces $z = \pm l$ and $r = a$ in the cylindrical coordinate system; its thickness is defined by the dimensionless ratio l/a. The minimal radius of the variable-thickness piezoelectric plate is a, and the maximal one is $a + h$. The deviation of plate shape from the conventional one can be described by the dimensionless ratio h/a or $h/l = \tan\alpha$.

To investigate the possibilities for improving the behavior of the thickness vibrations of piezoelectric plates, other variable-thickness plates were also considered. We call the piezoelectric plate shown in Fig. 1d the biconvex piezoelectric plate, as distinct from the biconcave one in Fig. 1e. The minimal thickness of the variable-thickness plate is equal to the thickness of the common plate $2l$. The maximal thickness of the variable-thickness piezoelectric plate is $2(l + b)$. The deviation of the shape of the variable-thickness plate from the common one can be described by the dimensionless ratio b/l or $b/a = \tan\beta$.

In the analysis of natural vibrations of piezoelectric plates, the following boundary conditions are assumed to be satisfied. The whole surface of the piezoelectric plate is free from mechanical stresses. Over the flat or conical surfaces confining the plates in the axial direction, thin equipotential electrodes are applied. The polarization vector is parallel to the z axis. At the surfaces free from electrodes, the normal component of the electric induction is equal to zero.

It is well known [3–5] that, at given boundary conditions for the analysis of the resonance (short circuit) and antiresonance (idling) regimes, the FEM leads to matrix eigenvalue problems of high dimensionality. The solution of these problems provides the eigenvalues, i.e., the resonance and antiresonance frequencies, and the eigenvectors, i.e., the nodal displacements. Knowing the resonance eigenvalues and eigenvectors, the DCC (k) can be calculated for any vibration mode

1063-7710/02/4801-0107$22.00

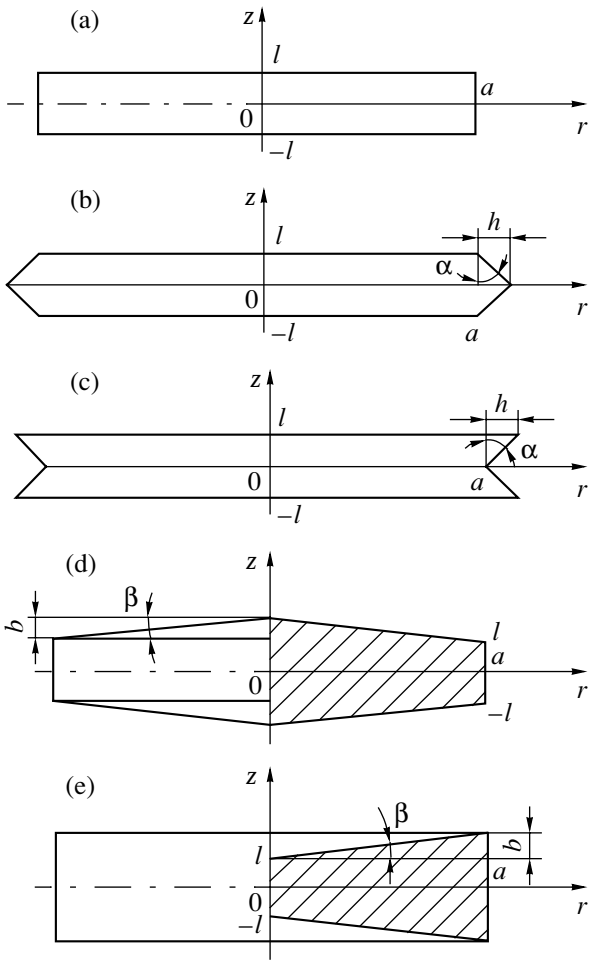

Fig. 1. Piezoelectric plates: (a) with a constant radius and a uniform thickness; (b, c) with a variable radius, including the (b) convex and (c) concave ones; and (d, e) with a variable thickness, including the (d) biconvex and (e) biconcave plates.

as the ratio of the mutual energy to the geometric mean of the elastic energy and the electric one.

The natural frequency spectra were calculated for the resonance and antiresonance cases in a wide range of geometric dimensions for all indicated types of piezoelectric plates of unconventional shapes made of ceramics of various compositions. The dependences of the DCC on the geometric dimensions and on the distribution of the displacements (the vibration mode) were also analyzed. The optimal geometric dimensions of piezoelectric plates, at which the DCC of quasithickness vibrations became maximal, were determined.

Consider, for example, one of the typical variants for a convex plate (Fig. 1b) made of the TsTBS-3 ceramics with the parameters corresponding to the reference data [6]. The maximal DCC of the tenth mode of quasi-thickness vibrations in a common piezoelectric plate, $k = 0.277$, is attained at the optimal thickness $l/a = 0.15$. The distribution of the displacement components for this case is shown in Fig. 2 (curves *1* and *2*). In this figure, the abscissa represents the numbers of equidistant nodal points in the range $r/a \in [0, 1]$ at the flat surface of a piezoelectric plate. The axial and radial displacement components normalized to the axial component at the center of the plate are plotted as ordinates. When proceeding to the convex piezoelectric plate, the modes of natural vibrations and, correspondingly, the distributions of the displacements change considerably. The distribution of the axial component of the displacement is smoothed out, and the radial component is reduced; at $h/a = 0.2$, the axial component of the displacement has a monotonic distribution. At the optimal geometric dimensions, the DCC of the tenth mode reaches the value $k = 0.339$ and increases by $\delta_{10} = 22.4\%$ relative to the common piezoelectric plate.

Now, we formulate the main conclusions and practical recommendations concerning the utilization of variable-radius piezoceramic plates made of piezoceramics of various compositions.

For the first-type piezoceramics (TsTBS-3, TsTSNV-1, and TsTS-19), the convex piezoelectric plates like the plate shown in Fig. 1b is advisable. Then, it is possible to increase the DCC of the quasi-thickness vibrations up to the value $k \approx 0.8k_t$, i.e., in this index, the first-type piezoceramics approaches the second-type one. In addition, in this case, it is possible to considerably improve the distribution of the normal displacement component at the flat surface of the piezoelectric plate (up to a monotonic distribution) and to reduce the radial displacement component. The use of concave piezoelectric plates made of the first-type ceramics provides a less considerable improvement in the displacement distributions and a small increase in the DCC.

For the second-type piezoceramics (NBS-1, TBKS, and TBK-3), the manufacture of a piezoelectric plate in the form of the convex plate deteriorates the characteristics of quasi-thickness vibrations. The manufacture of a piezoelectric plate in the form of the concave plate improves the distributions of the displacement components at the radiating surface, but the DCC increases by only 2–4%.

The biconvex shape of a piezoelectric plate made of the TsTBS-3 ceramic raises the DCC of the three first quasi-thickness modes by 10–23% and improves the distribution of the normal displacement component at the radiating surface. Each individual quasi-thickness mode has its own optimal geometry of the variable-thickness piezoelectric plate, which provides the maximal DCC. The increase in the DCC of quasi-thickness modes that is achieved with the use of a biconvex piezoelectric plate varies for different modes and decreases with increasing mode number.

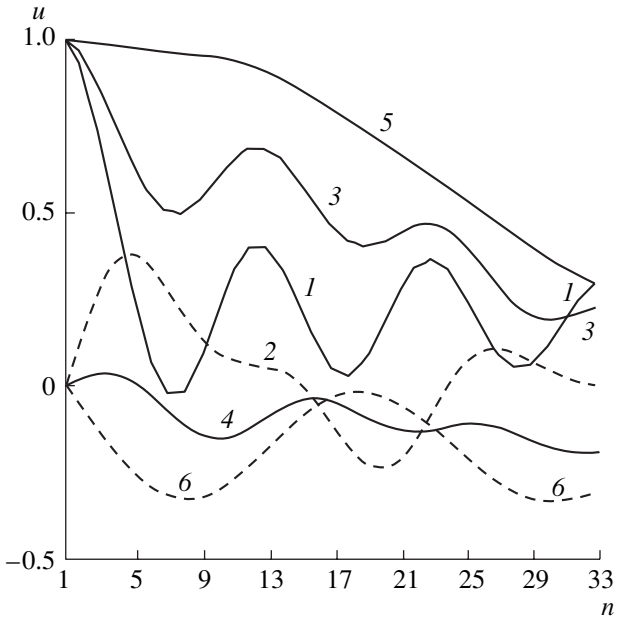

Fig. 2. Distributions of the (*1*, *3*, *5*) axial and (*2*, *4*, *6*) radial components of the displacement at the flat surface of a convex variable-radius piezoelectric plate: l/a = (*1*, *2*) 0.15 and (*3*–*6*) 0.16; h/a = (*1*, *2*) 0, (*3*, *4*) 0.16, and (*5*, *6*) 0.2; k = (*1*, *2*) 0.277, (*3*, *4*) 0.337, and (*5*, *6*) 0.339.

Now, we formulate the main recommendations for the utilization of variable-thickness circular piezoelectric plates made of piezoceramics of various compositions.

The DCC of quasi-thickness vibrations can be increased solely with the help of a biconvex piezoelectric plate, whereas a biconcave plate fails to produce this effect.

A greater increase in the DCC can be achieved with a piezoelectric plate made of the first-type piezoceramics (e.g, TsTBS-3), whereas a piezoelectric plate made of the second-type piezoceramics (e.g., NBS-1) allows only a slight increase in the DCC of the fourth mode.

REFERENCES

1. *Physical Acoustics: Principles and Methods*, Ed. by W. P. Mason (Academic, New York, 1964; Mir, Moscow, 1966), Vol. 1, Part A.
2. R. Holland and E. P. Eer Nisse, *Design of Resonant Piezoelectric Devices* (MIT Press, Cambridge, 1969).
3. N. F. Ivina, Akust. Zh. **35**, 667 (1989) [Sov. Phys. Acoust. **35**, 385 (1989)].
4. S. M. Balabaev and N. F. Ivina, *Computer Simulation of Vibrations and Radiation of Finite Bodies: The Finite-Element and Boundary-Element Methods* (Dal'nauka, Vladivostok, 1996).
5. J.-C. Debus, B. Debus, and J. Coutte, J. Acoust. Soc. Am. **103**, 3336 (1998).
6. *Piezoceramic Transducers*, Ed. by S. I. Pugachev (Sudostroenie, Leningrad, 1984).

Translated by A. Kruglov

Acoustical Physics, Vol. 48, No. 1, 2002, pp. 110–117. Translated from Akusticheskiĭ Zhurnal, Vol. 48, No. 1, 2002, pp. 123–130.

HISTORY OF RUSSIAN UNDERWATER ACOUSTICS

Experimental Study of the Prereverberation Times in Deep-Water and Surface Sound Channels

N. V. Studenichnik

Andreev Acoustics Institute, Russian Academy of Sciences, ul. Shvernika 4, Moscow, 117036 Russia

e-mail: vadov@akin.ru

Received December 27, 1999

Abstract—Experimental data on the volume and surface prereverberation are presented. The main prereverberation features and parameters are considered, and the mechanism and theory of the phenomenon are discussed. The range dependences of the prereverberation times are analyzed for different ocean regions and for distances from 180 to 1500 km. Quantitative data on the prereverberation times are presented. The widths of the scattering diagrams are estimated for the underwater and surface sound channels. © *2002 MAIK "Nauka/Interperiodica".*

In studying the fine structure of the sound field in the Black Sea, the author of this paper discovered the phenomenon of prereverberation. It consists in that, in the amplitude–time structure of the sound field in an inhomogeneous stratified waveguide, a reverberation-type background exists that precedes the arrival of the main signal governed by the deterministic parameters of the sound channel. Later, prereverberation was studied in other ocean regions, both with fully insonified and zone structures of the sound field, including moderate latitudes and tropical regions of the Pacific, Atlantic, and Indian oceans. The measured space–time dependences were identical for all regions. In view of the general character of the phenomenon in different conditions of the natural waveguides, the determination of the nature of prereverberation and a theoretical justification of this phenomenon have become topical. For this reason, as the amount of the experimental data collected for different regions of the Ocean increased, the new results were repeatedly discussed at scientific conferences and seminars. However, no reasonable physical explanation was found for a long time, mainly because the prereverberation phenomenon does not obey the classical theory of sound propagation in a stratified ocean [1]. Only 16 years after the discovery of the phenomenon, did the author of this paper manage to fully explain the prereverberation [2, 3] in the framework of the simplest model of the waveguide in the form of a surface channel with wind waves at its upper boundary (this theory is not presented in the aforementioned publications). By that time, the main features of the sound field, including the prereverberation components, had been studied in detail for different waveguides. Some of these results can be found in [2–8]. To explain the phenomenon, apart from the appropriate waveguide model, one should find the rays along which the prereverberation signals arrive, then, determine the propagation trajectories of the regular and scattered components of the sound field, and, finally, prove that the travel time of the background signals is smaller than that of the main signal governed by the deterministic conditions. In addition, it is necessary to prove that, within the time interval of adjacent ray cycles, prereverberation is formed by two pairs of unique arrivals, which are asymmetric in the associated cycle lengths and scattering angles. The latter fact is not quite obvious for an underwater sound channel. However, with the model of a surface channel with a wavy upper boundary, the feasibility of the observed prereverberation features seems to be quite natural. As a result of the analysis, it becomes clear that the prereverberation in an underwater sound channel is governed by the same mechanism, the volume inhomogeneities being the scatterers in this case. There are few publications on prereverberation. In addition to the aforementioned publications [2–8], one should mention the paper [9] that, as a matter of fact, reports on the prereverberation components (they are called "noise components" by the authors) for two deep-water ocean regions without zone structure of the sound field. In foreign publications, there are no special studies aimed at identifying the regular and prereverberation components. Kibblewhite and Denham [10] report that the regular component of the sound field is accompanied by a noise, which precedes it and exists some time after the regular component terminates. The recent publications include three papers [11–13]. However, these studies deal with the coherence of the integral levels of the sound field, without resolving in time and identifying the regular and random components.

By analyzing a large body of experimental data obtained in different ocean regions, a number of features were established [2–8] that are inherent in the regular and scattered components of the sound field:

(1) Prereverberation is represented by an incoherent sound field that is caused by the scattering from volume or surface inhomogeneities and that precedes the arrival of the main refracted signals. In contrast to reverbera-

tion, which is mainly associated with back-scattering, prereverberation is formed by forward sound scattering.

(2) While reverberation is a decaying process, prereverberation grows in its amplitude and reaches the maximal level at the moment of arrival of the main signal, when it virtually merges with this signal. The ratio of the prereverberation and the signal level can reach 0.1–1.0 at long ranges.

(3) As the range becomes longer, the duration of prereverberation increases proportionally to the cycle number and can reach several hundreds of milliseconds at distances of several hundreds of kilometers. The maximal duration of prereverberation is limited by the difference in the arrival times of the adjacent components. When the characteristic angles (at which the rays cross the channel axis) decrease and the regular components transform into the scattered prereverberation ones, the arrivals of the coherent and incoherent signals are equally probable in the vicinity of the channel axis, and these signals overlap in time. Instead of a discrete structure that is distinctly quantized in time and arrival angles [4–6], the sound field takes the form of a noise-like process with a uniform probability distribution of the amplitudes, angles, and arrival times, within relatively wide limits of their variations. The sound field becomes fully incoherent.

(4) Within the first ray cycle, the signals that arrive along the rays touching the bottom exhibit no prereverberation. The latter can exist only for the rays that produced two or more refraction cycles. If the sound field has a zone structure, prereverberation is weakly pronounced at distances up to those where the zones overlap, and it is absent at the extremum points and in the caustic zones.

(5) The angular diagrams of the volume and surface forward scattering (the phenomena causing prereverberation) reach ±0.5°–2.5° in their widths at a level of –30 dB.

(6) The deterministic signals can be accompanied by prereverberation, which also manifests itself after their arrivals. In this case, the signal shape is nearly symmetric due to the prereverberation components caused by the side scattering [3].

To illustrate the fundamental features of the sound field in underwater waveguides and the mechanism of prereverberation formation, we consider a surface channel with a wavy upper boundary. Let the sound source and the receiver be at the channel axis. Figure 1 shows the ray pattern that demonstrates the process of the sound field formation and the accompanying prereverberation. If the surface is flat and the channel thickness is finite, the transmitting point (O) and the receiving point (A) can be connected by a set of refracted rays that are strictly quantized in their arrival angles and times and that produce 1, 2, … full cycles. In the case at hand, for an arbitrary distance, the angle and time quantization can be analytically expressed in the form that represents a strictly discrete sequence in the arrivals of the deterministic components [3]. In the only possible situation, the boundary ray *1*, which corresponds to the maximal velocity, will be the first to arrive at the point A. This ray carries no prereverberation signal. Ray *3* arrives second: it produces two full cycles. Later, the rays arrive that produce three and more full cycles. If the surface is rough, the rays that do not obey the quantization condition for the deterministic waveguide can also arrive at the point A. In advance of ray *3*, the rays can arrive at point A that are scattered by the surface and are asymmetric in their lengths and arrival angles, namely: rays *2* and *2*', as well as rays *4* and *4*', which have equal mean propagation velocities and which undergo one surface reflection each. Their scattering diagrams are limited within the grazing angles $\Delta\alpha = \alpha_2 - \alpha_1$. Any other combination of the scattered rays with more reflections leads to prereverberation for the subsequent signal components. If the difference in the arrival angles tends to zero and, hence, the cycle lengths of rays *2* and *2*', *4* and *4*', respectively, become equal, the prereverberation components transform into the deterministic ray *3*. In an underwater sound channel, the mechanism of prereverberation is the same. The only difference consists in that, in this case, the volume inhomogeneities are the scatterers. For the surface channel with a linear sound speed profile, a simple expression was obtained in [4] for the dependence of the relative duration of prereverberation on the range within the first boundary cycle. In accordance with the sea state and the concentration of the volume inhomogeneities, changes occur in the frequency-dependent absolute levels of the sound field, in the scattering diagram, and in the prereverberation duration.

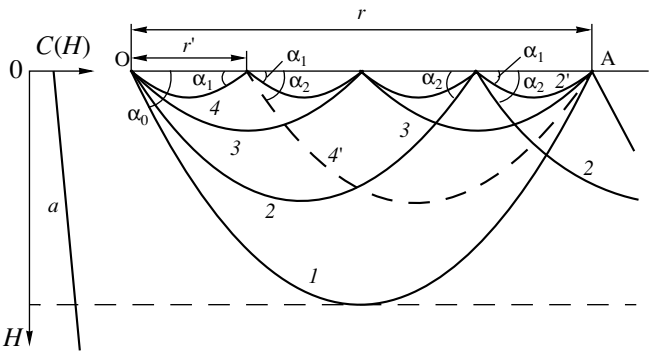

Fig. 1. Sound speed profile and ray pattern illustrating the mechanism of the prereverberation formation in a surface channel. The source and the receiver are both at the channel axis; *r* is the distance, *H* is the depth, and *a* is the relative sound speed gradient.

Let us consider typical structures of the sound field in an underwater sound channel to analyze the behavior of both the components and the whole signal. To study the fundamental characteristics of prereverberation, we use the data obtained in autumn, in the Black Sea where both underwater and stable surface channels were present. The sea depth was 2000 m, the depth of the

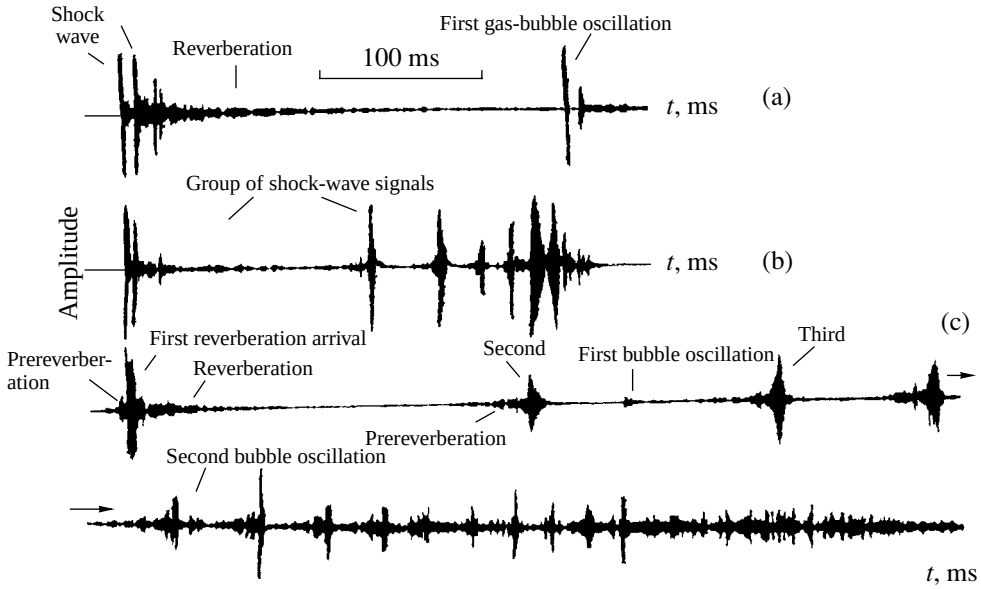

Fig. 2. Oscillograms of the explosion-generated signals in the underwater sound channel at the distances (a) 130 m, (b) 37, and (c) 140 km. The depth of explosions is 35–40 m, the reception depth is 60 m, and the frequency is 3 kHz.

channel axis was 60 m. The sound speeds were 1460 m/s at the axis, 1500 m/s near the surface, and 1505 m/s near the bottom. With such a difference in the sound speeds near the surface and the bottom, the refracted rays reaching the surface were those with the grazing angles from 0° to 5° at the distances 34–40 km, and the difference in the departure angles was ±2°. Explosive charges of 25 kg were used as the sound sources. The charges were detonated under the discontinuity layer, at depths of 30–40 m, where the sound speed was 1470–1474 m/s. The signals were received at a depth of 35 m. The analyzed frequency was 3 kHz, and the bandwidth was 20%. The signals received at the sea states of Beoufort 2–3 were photorecorded directly from the electron-ray tube, in a linear scale. The film was pulled at a velocity of 326 mm/s. Figure 2 shows the space–time structures of the signal amplitude, including the individual components of the sound field. The curves correspond to the high-frequency band of the signal propagating in the waveguide with the aforementioned parameters. The illustrations cover the near-field zone (130 m), the distance of the first boundary cycle (37 km), and the zone of full insonification (140 km).

In the near-field zone, single signals of the shock wave and those of the first gas-bubble oscillation can be seen. The period of this oscillation is 275 ms. At the frequency at hand, the ratios of the amplitudes of the shock wave and the first bubble oscillation are within 20–25 dB. In the records, the signals of the shock wave, which correspond to the direct and surface-reflected components, are limited in their amplitudes by 20–22 and 10–12 dB, respectively. The signals of the gas-bubble oscillation were not limited in the records. At small distances, the leading edge of the signal is sharp: the signal level rapidly increases. The signal is followed by the surface reverberation of a considerable duration and a high level. The volume reverberation, which can be seen between the direct and the surface-reflected signals, has the level that is by 10 dB lower than that of the surface reverberation. The same amplitude ratios are characteristic of the signals of the first gas-bubble oscillation.

In an underwater waveguide, the signals usually arrive in the form of quartets characterized by relatively close arrival times. At the distance 37 km, where the deep boundary ray reaches the reception point and where all signal components allowed by the waveguide at hand exist, the first components arrive at the surface, and, just as in the near-field zone, they are followed by a high-level reverberation. Again, the level of these components sharply increases. The subsequent signals are purely refractive ones: they produce two or more full cycles and interact with neither the surface nor the bottom. Pronounced noise-like components occur before each of these signals, and the leading edges of the deterministic components are less sharp. The level of the noise-like components increases and reaches its maximum at the moment of the arrival of the main signal. Due to these properties, these components are called prereverberation. The reverberation following the refracted components is much weaker. It is difficult to resolve the signal quartets in time because of the small depths of the transmitter and the receiver. The first arrival is the only one that is partially resolved (into signal pairs).

At the distance 140 km, the first and second signals are separated by an interval, which has increased approximately in proportion with distance (full propor-

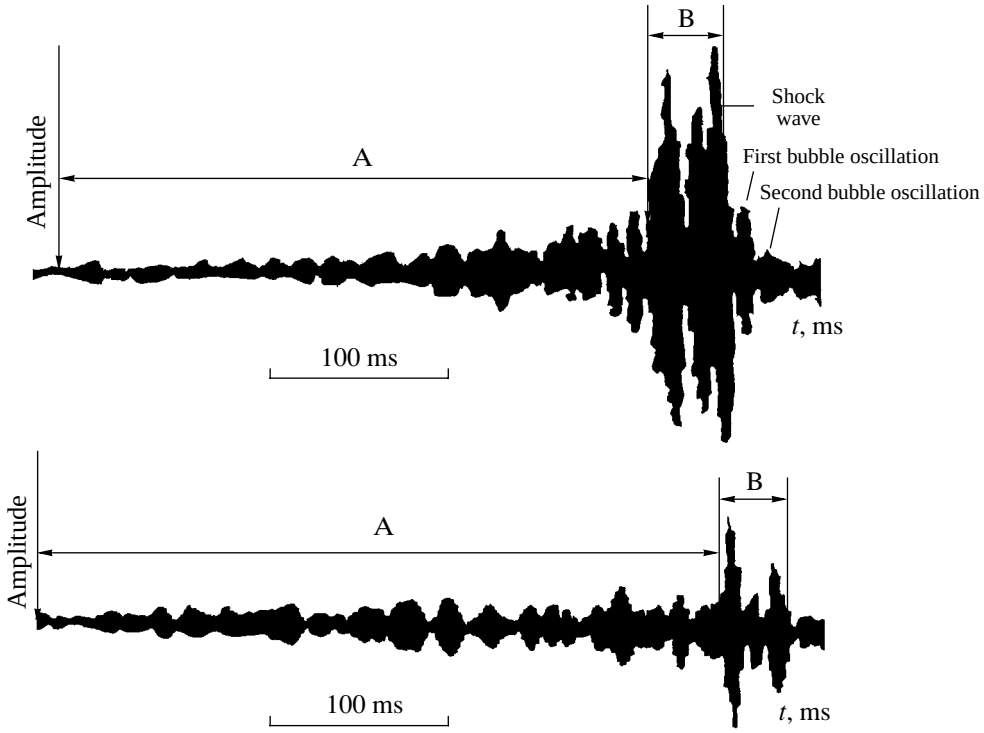

Fig. 3. Fragments of the oscillograms obtained for the signals in the surface sound channel of the north-western Pacific at the distances 290 and 390 km. The depth of explosions is 300 m, the reception depth is 200 m; A is the prereverberation and B is the main signal. The amplitudes are shown on a linear scale.

tionality exists only at the distances that are multiples of the refraction cycles and at fixed characteristic angles). The time structure of the arrivals is changed. The first signal reaching the surface has a pronounced reverberation and prereverberation of small duration. Subsequent signals, which are separated in time, are accompanied by a prereverberation of a considerable level. At the moment of the arrival of the deterministic signals, the prereverberation amplitude has a value of 0.3–0.4 relative to the maximal level. The prereverberation times are within 40–60 ms. The first signal has a prereverberation duration of 12 ms, because it propagates somewhat above the bottom (40 m). As the range increases, the near-axis components loose their regular properties because of the growing effect of prereverberation: they transform into random components that overlap in time and have equal levels. The sound field becomes totally diffuse, with a uniform distribution of phases and amplitudes for the characteristic angles within ±5° and the arrival times within 200–300 ms.

Figure 3 shows fragments of the oscillograms corresponding to the components of the sound field (the signal quartets) generated by the explosive sound sources at distances of 290 and 390 km. These data were obtained in conditions close to those of a surface sound channel. The frequency is 500 Hz. The grazing angles are 13–14° near the surface. The shown records are obtained in the central part of the Pacific Ocean, at northern latitudes, with the path length 1000 km, at sea states of Beoufort 2–3 to 5–7. The path had a latitudinal orientation and passed behind the Impair Mounts, along the surface isotherms with the temperature 15–16°C of the upper water layers at the 45° latitude. The path began at 173° E and terminated at 175° W. The channel axis was shallow: 40 to 100 m. At distances up to 500 km from the reception point, the near-surface sound speed was 1490 m/s; at 1000 km, it increased to 1495 m/s. At the same time, the near-axis sound speed changed from 1450 m/s at the reception point to 1464 m/s at the terminal point of the path (distance 1000 km). At the depth 5000 m (near the bottom), the sound speed was 1542 m/s. The 25-kg explosive charges were used in the experiment. The explosion depth was 300 m, the reception depth was 200 m. The ocean depth was mainly lower than 5000 m along the path, but exceeded 6000 m at the reception point. For the 300-m source depth (the sound speed 1460–1468 m/s), a powerful surface channel existed with the difference 50–55 m/s in the sound speeds near the surface and the bottom. In these conditions, the signals reaching the surface were those whose grazing angles were within 0° to 15.5°, with ray cycles 45–73 km in length. The prereverberation components have levels of 0.3–0.4 relative to the maximum of the deterministic components. The duration of prereverberation is 330–400 ms. The levels of reverberation are 8–10 dB lower than those of the prereverberation. In

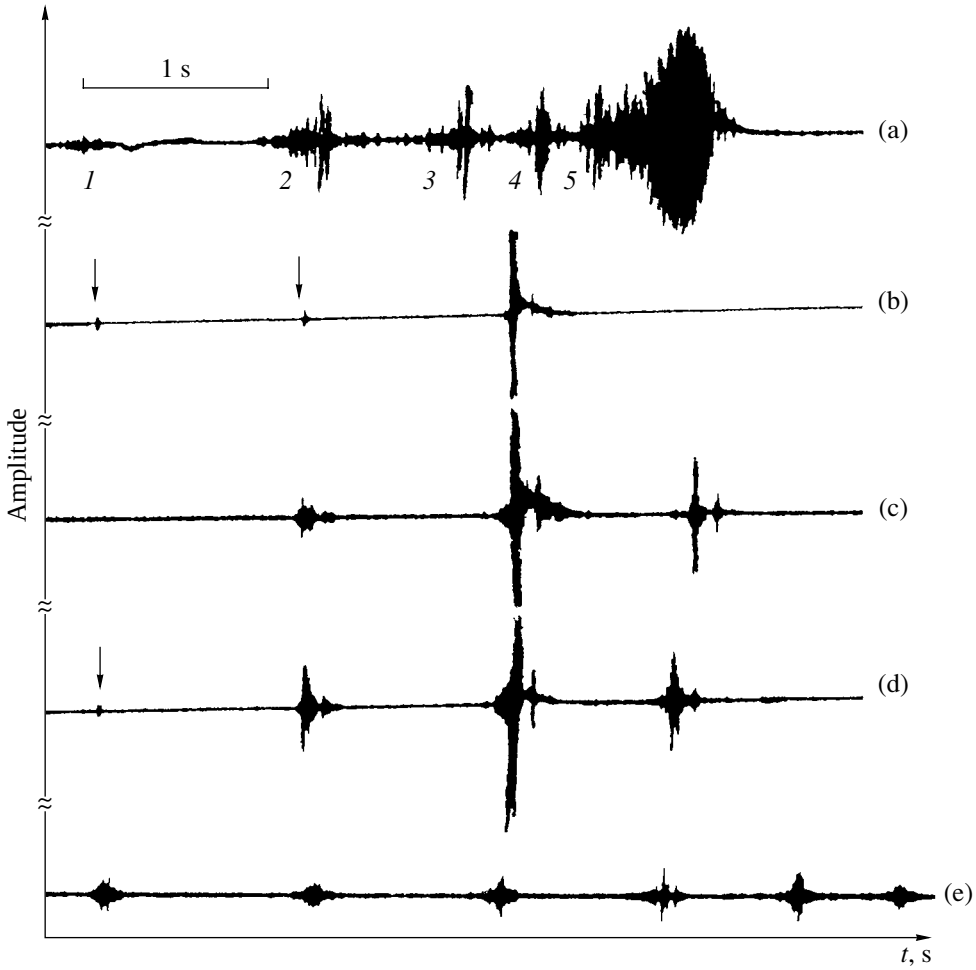

Fig. 4. Oscillograms illustrating the amplitude and space–time structures of the signals in the northern and central regions of the Pacific Ocean at the frequency 400 Hz. (a) The northern region: the distance is 500 km and the explosion and reception depths are each 100 m. (b–e) The central region: the reception depth is 200 m and the distance is (b) 400, (c) 590, (d) 735, and (e) 1500 km; the explosion depth is (b–d) 100 and (e) 200 m. The amplitudes are shown on a linear scale.

a number of records, signal forms close to symmetric were observed. In such situations, the reverberation-type tales of the signals are governed by both reverberation components (of small amplitude) and prereverberation ones (side-scattering). The associated levels depend on the angles between the propagation directions of the sound waves and the wind waves at the surface.

To illustrate the time structure of the sound field and the prereverberation properties in the convergence zones, the data are presented that were obtained in the tropical region of the Pacific Ocean and in the subtropical region of the Atlantic Ocean. The oscillograms of the signals received in different ocean regions are shown in Fig. 4. To compare the amplitude-time structures of the sound field in the convergence zones of tropical latitudes and in fully insonified zones of moderate latitudes, Fig. 4a shows a record of the full system of signals received in the north-western part of the Pacific Ocean. The path length was 500 km, the frequency was 400 Hz. The components of the sound field, both separate and overlapped in time, can be seen. For this set of explosions, the oscillograms of the individual components are shown in Fig. 3 in more detail. The four initial arrivals of the signal quartets that are separated in time propagate in the waveguide with surface reflections. The time-overlapped terminal part of the record is constituted by purely refracted signals that propagate near the channel axis without surface reflections. The total duration of the signal is 3.5 s. The near-axis noise-like irregular part of the signal, which is formed by the components with the characteristic angles ±11°–12° and influenced by the prereverberation components, has the duration 800 ms. The prereverberation time of the separated components is within 100–350 ms. The first signal quartet, which precedes the subsequent ones by 1.26 s and is reflected from the surface at grazing angles of 16°, is 15–20 dB weaker than the subsequent quartets and has a significant coherent part. The levels of the incoherent near-surface components, which

overlap in time, are 5–6 dB higher than the levels of the individual components.

Figures 4b–4e present the amplitude and space–time structures of the sound field for the Pacific Ocean (south-west of the Hawaii Islands), at the propagation distances 400–1500 km. In the experiment, 25-kg charges were exploded at the depth 100 m. The distances were 200 m to 1500 km. The signals were received at the depth 200 m and analyzed at the frequency 400 Hz. The sound speed profile was typical of tropical ocean regions. The thickness of the surface sound channel was 60–70 m. The sound speeds were 1538 m/s near the surface, 1490 m/s at the channel axis (1000 m), 1542 m/s near the bottom (5000 m), and 1520 m/s at the horizons of transmission and reception (200 m each). With the zone structure of the sound field, the records exhibit arrivals that are distinctly separated in time by 1–1.14 to 0.55 s, and an amplitude difference up to 30 dB. At the distance 400 km, only the refracted signal of the shock wave that produces six full cycles can be seen. There are also two gas-bubble oscillations with a period of 100 ms. Bottom reflections are absent. The convergence zones begin to overlap at the distances 450–500 km. At 400 km, two forerunners can be seen with advance times of 1.1 s. The forerunners are caused by the arrivals of the scattered signals from the surface channel. Within the frequency band determined by the channel parameters, the refracted signals that reach the surface in every cycle are captured by the waveguide (because of the scattering from the wavy surface), propagate in it, and, after surface reflections, penetrate below the discontinuity layer thereby reaching the receiver. Their amplitudes usually are 30–40 dB below the generating components. The prereverberation components are weakly pronounced. Their advance times are not higher than 30–40 ms, and the levels are 30–40 dB lower than those of the deterministic components. At distances of 590–1500 km, the number of signals increases to six. The prereverberation is most pronounced for the second components, at the distances 590 and 735 km. The prereverberation time reaches 120 ms, and the level is not higher than 0.10–0.15 relative to the levels of the deterministic components. Other components have lower times and levels of prereverberation. The only exception is the distance 1500 km (the 25th–30th convergence zones) where some components have prereverberation times as high as 150 ms and amplitudes up to 0.3–0.4 of the maximal value. At both moderate and tropical latitudes, the difference in the arrival times of the first and second signals is 1.1–1.26 s. The doubled difference in the arrival times of the refracted components determines the wavelength corresponding to the critical frequency of the waveguide. Hence, in the Pacific Ocean with the depth 5000 m, this frequency is 0.4–0.45 Hz, depending on the sound speed profile.

To analyze the field structure in the convergence zones of the Atlantic Ocean, we consider the records obtained on the path 740 km long. The path passed through the deep-water Canary Hollow, to the south-west of Madeira Island, and was oriented towards the Great Meteor Bank. The sea depths were 5000–6000 m. The sound speed profile exhibited a deep axis of the sound channel and a monotone decrease in the sound speed from the surface to 1700 m; at deeper horizons, the speed slowly increased. The profile was close to parabolic. As a result, the near-surface convergence zones were rather short. The sound speed was 1520 m/s near the surface, 1497 m/s at the channel axis, and 1542 m/s near the bottom (5000 m). The surface waveguide was 30–40 m in thickness. As in the aforementioned experiments, the sound sources were the 25-kg explosive charges. The depth of explosions was 150 m, the reception depth was 50 m. Figure 5 shows the sound field structure obtained at the frequency 400 Hz in the first (70 km), second (130 km), and combined 11th and 12th (740 km) convergence zones. At distances up to 600–670 km, the structure consists of single signals (the signal quartets). At ranges as long as 740 km, the convergence zones (the 11th and 12th ones) begin to overlap. At the distance 70 km, in addition to the signals of the shock wave (limited by 7–8 dB) and those of the first bubble oscillation, one can see twofold bottom-

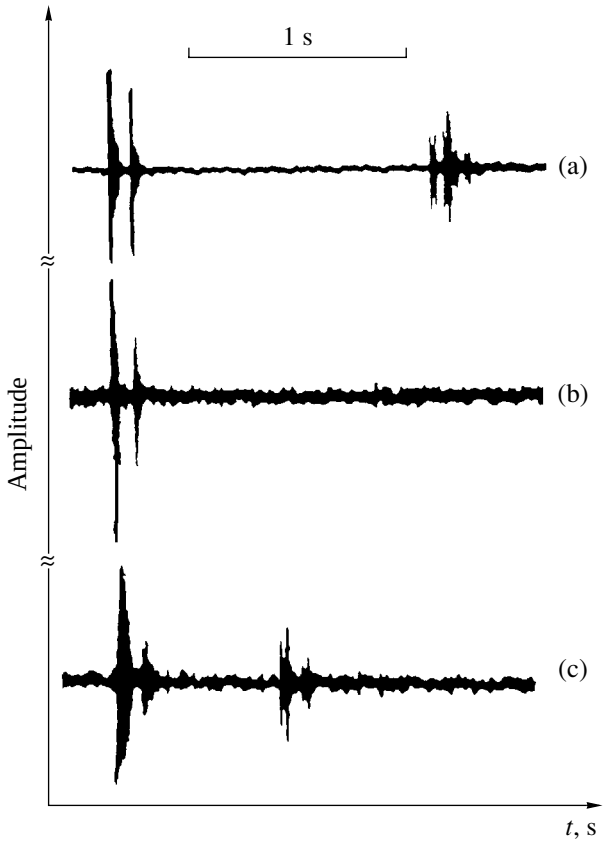

Fig. 5. Oscillograms illustrating the amplitude and space–time structures of the signals in the Atlantic Ocean. The frequency is 400 Hz; the explosion depth is 150 m; the reception depth is 50 m; and the distance is (a) 70, (b) 130, and (c) 740 km. The amplitudes are shown on a linear scale.

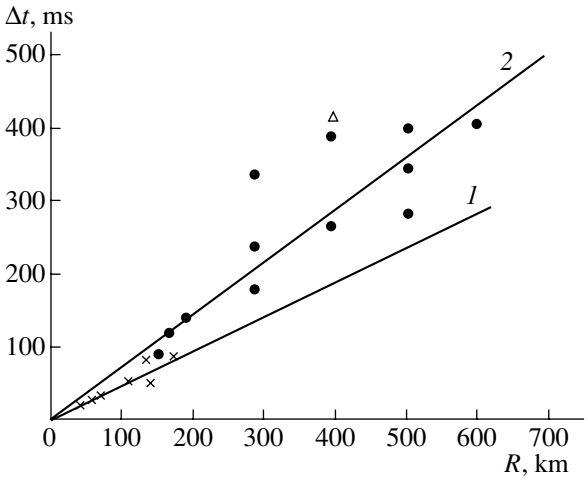

Fig. 6. Range dependences of the prereverberation duration in the underwater (crosses) and surface (dots) sound channels. The triangle corresponds to the data by Popov and Tyurin [9].

surface reflections, with a delay of 1.4 s. At greater distances, only one refraction signal is present in each record. The bottom reflections are absent at this frequency. In a broad frequency band, the coefficient of bottom reflection is not higher than 0.1–0.15. As was mentioned above, at the distance 740 km, there are two signals that correspond to the 11th and 12th convergence zones. The difference in their delay times is 730 ms, which corresponds to 1 ms/km. Hence, the critical frequency of the channel is 0.67 Hz in contrast to 0.4–0.45 Hz in the Pacific Ocean at the same depth (5000 m). At the frequency 400 Hz, the difference in the levels of the shock wave and the first bubble oscillation is 8–12 dB. According to the records shown, in this region of the Atlantic Ocean, no prereverberation manifests itself in the convergence zones with the sound levels from –20 to –40 dB. This fact can be primarily attributed to the high stability and uniformity of the sound speed profile along the path, to the monotonic character of the vertical sound speed gradient in the upper and lower layers of the ocean, and to the signal reception in the vicinity of the caustic. The broadening of the convergence zone boundaries follows the Airy function. When receiving the signal at deep horizons (200–300 m) outside the caustic zone, the prereverberation is also insignificant and has a duration of less than 10–20 ms. At the distance 740 km (the 12th convergence zone, the 2nd group of signals in Fig. 5c), the rays of the ray quartet are separated in time. The separation of the quartet components can also be noticed in the bottom reflections (Fig. 4a).

Figure 6 shows the averaged range dependences of the duration of volume prereverberation for the underwater sound channel of the Black Sea and the surface channel of the north-western Pacific, i.e., for the regions where prereverberation is most pronounced. Line *1* (crosses) approximates the average increase in the prereverberation level in the underwater channel, and line *2* (dots) corresponds to the surface channel. The prereverberation time was calculated starting from the moment when the prereverberation level became higher than the noise level and ending with the moment when the deterministic component arrived. The level difference was 20–35 dB. The plot illustrates the prereverberation times for the signals whose characteristic angles are within 7–11° in the underwater channel and 10–13° in the surface channel. For smaller characteristic angles, the prereverberation increase is limited by the difference in the arrival times of the deterministic components.

From the time dependences of the prereverberation amplitude obtained above, we calculated the scattering diagrams for the underwater and surface channels. Evidently, it was impossible to determine the prereverberation duration for the distances longer than 600 km in the Pacific Ocean, because, at such ranges, the deterministic and surface-scattered components rapidly decayed and then vanished. The near-axis components that do not touch the surface are present at distances up to 1000 km at frequencies up to 1000 Hz. The forward-scattering diagrams were calculated for the channels at hand. With the aforementioned grazing angles, the width of the scattering diagram of volume prereverberation is within ±0.5°, and the corresponding value for the surface prereverberation reaches ±2.5°. The side field was limited by the levels –20 to –35 dB relative to the level of the specular component.

The described experimental data on the sound fields in the underwater waveguides and the analysis of the field structure and stability show the variety of the field properties in different ocean regions.

ACKNOWLEDGMENTS

The work was supported by the Russian Foundation for Basic Research, project no. 98-05-64302.

REFERENCES

1. L. M. Brekhovskikh, *Waves in Layered Media*, 2nd ed. (Nauka, Moscow, 1973; Academic, New York, 1980).
2. N. V. Studenichnik, in *Abstracts of the 9th All-Union Acoustic Conference* (Inst. of Acoustics, USSR Academy of Sciences, Moscow, 1977), Section D-IV, p. 45.
3. N. V. Studenichnik, in *Proceedings of the Third Seminar on Statistical Acoustic Models of the Ocean* (Inst. of Acoustics, USSR Academy of Sciences, Moscow, 1981), p. 48.
4. L. M. Brekhovskikh, Yu. P. Lysanov, and N. V. Studenichnik, Dokl. Akad. Nauk SSSR **239** (1), 211 (1978).
5. N. V. Studenichnik, in *Proceedings of the Fourth Seminar on Statistical Acoustic Models of the Ocean* (Inst. of Acoustics, USSR Academy of Sciences, Moscow, 1982), p. 19.

6. N. V. Studenichnik, in *Proceedings of the Thirteenth All-Union School–Seminar* (Inst. of Acoustics, USSR Academy of Sciences, Moscow, 1984), p. 29.
7. N. V. Studenichnik, Akust. Zh. **43**, 283 (1997) [Acoust. Phys. **43**, 245 (1997)].
8. N. V. Studenichnik, in *Proceedings of the School–Seminar of Academician L.M. Brekhovskikh* (GEOS, Moscow, 1998), p. 330.
9. R. Yu. Popov and P. G. Tyurin, in *Abstracts of the 9th All-Union Acoustic Conference, Section IV* (Inst. of Acoustics, USSR Academy of Sciences, Moscow, 1977), p. 85.
10. A. C. Kibblewhite and R. N. Denham, J. Acoust. Soc. Am. **45**, 944 (1964).
11. M. Badiey, J. Simmen, and S. Forsythe, J. Acoust. Soc. Am. **101**, 3361 (1997).
12. P. H. Dahl, W. J. Plant, B. Nutzel, *et al.*, J. Acoust. Soc. Am. **101**, 2583 (1997).
13. P. H. Dahl and W. Plant, J. Acoust. Soc. Am. **101**, 2596 (1997).

Translated by E. Kopyl

Acoustical Physics, Vol. 48, No. 1, 2002, pp. 118–119. Translated from Akusticheskiĭ Zhurnal, Vol. 48, No. 1, 2002, pp. 131–132.

INFORMATION

4th Russian Research-Engineering Conference "State of the Art and Problems of Navigation and Oceanography"

The 4th Russian Research-Engineering Conference "State of the Art and Problems of Navigation and Oceanography" was held on June 6–9, 2001 in St. Petersburg. It was organized by the State Research Navigational-Hydrographical Institute (SRNHI) of the Defense Ministry of the Russian Federation together with the St. Petersburg Maritime Assembly, Leningrad District Office of the Krylov Research-Engineering Society of Shipbuilders, Institute of Problems of Mechanics, Russian Academy of Sciences, Russian Public Institute of Navigation, Russian Hydrographical Society, and Radio Navigation Interstate Council with support from the City Administration of St. Petersburg. Such conferences have been regularly held since 1992.

The conference Organizing Committee was headed by the Commander of SRNHI, Doctor of Engineering, Corresponding Member of the Transport Academy, Rear Admiral S.P. Alekseev.

The wide scope of the conference was presented in more than 170 papers delivered within the framework of eight sections. Four of the sections were largely devoted to acoustic methods and devices: Section 2 Autonomous Navigation Systems and Complexes, Section 5 Hydrography and Nautical Cartography, Section 6 Means and Methods of Marine Geophysics, and Section 7 Oceanographic Research.

The importance of designing new means of oceanographic and geophysical monitoring is evident. For example, research activities in the Gulf of Finland aimed at the development of transportation and communications demand new generation equipment. These activities include engineering-geological research to determine the routes for the North-European pipeline and the Russian–Finnish optical-fiber communication cable.

In 1998, the International Hydrographical Organization developed a new version of standards, S-44 for hydrographical works, which reflect stricter requirements on the precision of the sea bottom profiling for both solving economics problems and providing for general navigation safety. For example, a mandatory total survey of navigation routes, approaching channels, and harborages with the help of multibeam underwater acoustic systems is indicated.

Therefore, new hydrographical systems both existing and under development and their conformity to new trends were brought to the attention of conference participants.

Sonar systems for various hydrographical applications, e.g., mapping of the bottom profile of large areas (Institute of Radio Engineering and Electronics, Russian Academy of Sciences) and the mapping of morphological features of the bottom relief and coastline (Shirshov Oceanology Institute, Russian Academy of Sciences), were widely presented. A review paper from the Morfizpribor Central Research Institute and SRNHI on modern trends in the development of equipment for the remote profile survey of soil aroused considerable interest. In the paper, primary attention was paid to wideband underwater acoustic profilographs, which would satisfy the requirements of modern geomonitoring, e.g., would solve the problem of bottom stratification with the resolution of layers 0.2–0.4 m.

Prospects for the development of a new generation of automated hydrographical systems on the basis of double-frequency and multichannel echo-sounders (SRNHI) were discussed. Such systems will provide the opportunity to abandon the obsolete hydrographical practice of bottom profiling by measuring in tacks using a single-beam echo-sounder.

In underwater acoustic support for mapping and monitoring, important problems involve automation, the combination of acoustic techniques with other methods (e.g., with geomagnetic survey), data interpreting, error minimization, and, finally, the development of appropriate software [papers presented by SRNHI, Institute of Radio Engineering and Electronics (Russian Academy of Sciences), Institute of Oceanology (Russian Academy of Sciences), the Elektropribor Central Research Institute, the Briz Research Institute, and the Kurs Central Research Institute].

For example, a system approach is suggested for the important problem of bottom measurement: a measuring complex includes not only an echo-sounder but also receiving equipment for satellite navigation, a mapping system, and equipment for monitoring ship position. The conference proceedings demonstrated that such a system approach is now a common standard for underwater acoustic bottom survey. The main problems are the increase in the measurement efficiency and the possibility of the soil classification. For these purposes, a measuring system may be equipped with a profilograph and a side-scan sonar. However side-scan sonars do not

1063-7710/02/4801-0118$22.00

always meet the requirements, because they lack vertical selectivity and the sea depth cannot be determined with their help. Measurement efficiency can be considerably increased with the help of multibeam echosounders, which are already used extensively outside Russia.

Appropriate software is now being developed to increase survey efficiency. For example, one of presented software packages (Institute of Radio Engineering and Electronics, Russian Academy of Sciences) is used to solve the problems of the determination of soil type and to simultaneously present the results of the operation of a profilograph and a side-scan sonar in a form convenient for the further classification of the bottom by an operator.

The interest in systems, which could solve the problem of the remote classification of bottom sediments by acoustic methods, is not surprising. It seems that successful research in this area is possible with the correct implementation of foreign experience (such systems already exist in Australia and the United States), while proceeding from simplified to detailed classification models based on geoacoustic parameters of the actual sea bottom. Moreover, now, with the development of system integration, it is better to combine the remote acoustic methods with contact soil sampling rather than to separate the two approaches.

Considerable attention at the conference was given to the techniques for the transmission and reception of wide-band (super-wide-band) signals and FM signals and to the numerical processing techniques. The signal bandwidth that is sufficient for solving the problems of bottom monitoring and the monitoring of wind waves is a distinctive feature of photoacoustic sources exited remotely at the sea surface by laser radiation. A paper from the Andreev Acoustics Institute was devoted to the demonstration of the measurement capacities of this type of source.

Acoustic solutions for navigation problems were also proposed. For example, a paper from the Morfizpribor Central Research Institute presented new modifications of the known correlation hydroacoustic instrument for the measurement of ship velocity. Expressions for the space-time correlation function of a signal scattered by the sea bottom were calculated in the framework of one of the phenomenological models of a scattering bottom.

Lately, at all conferences on fundamental and applied oceanology, interest is centered on various aspects of the development of oceanografic databases. Work on the maintenance of databases on longterm oceanological observations, their development, and their adjustment to the requirements of the Unified System of Information on the Situation in the Ocean is being conducted at SRNHI. Certain organizational problems are connected with the sharp cutback of information during the 1990s and also with the natural necessity to transfer the initial data obtained earlier from old magnetic media to CD-ROM.

A very important issue brought up in papers and discussions was the relationship between the development costs of a new generation of equipment and the costs of the modernization of the equipment currently used by hydrographic, pilot, and other services. For example, equipping echo-sounders with separate digital units for communication with the data acquisition and processing equipment provides an opportunity for hydrographical service to work with the equipment that is currently at hand for several more years until the new equipment becomes available. The experience in the modernization of underwater acoustic equipment, which was accumulated by the Gidromaster Moscow research-technological company was approved by the audience.

The international status of the conference was characterized by the presence of researchers and experts from Poland, Germany, the United States, and China. Foreign companies manufacturing underwater acoustic equipment actively promoted their products through informative presentations and seminars.

S. V. Egerev

Translated by M. Lyamshev

Acoustical Physics, Vol. 48, No. 1, 2002, pp. 12–17. Translated from Akusticheskiĭ Zhurnal, Vol. 48, No. 1, 2002, pp. 16–21.

Characteristics of Thermal Acoustic Radiation as a Source of Acoustic Signals

A. A. Anosov[1, 2] and V. I. Pasechnik[1]

[1] *ELDIS Research Center, Institute of Radio Engineering and Electronics, Russian Academy of Sciences, Starosadskiĭ per. 8, Moscow, 101000 Russia*

[2] *Sechenov Medical Academy, Moscow*

e-mail: passech@orc.ru

Received February 21, 2001

Abstract—A linear dependence of the output voltage of an acoustic thermometer on the temperature difference between the source and the piezoelectric transducer is demonstrated experimentally. The constant component of the output voltage is determined by the noise temperature of the receiving device. The main feature of the thermal acoustic radiation as a source of acoustic signals is that the signal is represented not by the total thermal radiation of the object, which is proportional to the absolute temperature of the latter, but by the part of this radiation that is proportional to the temperature difference between the object and the transducer. © *2002 MAIK "Nauka/Interperiodica".*

The possibility of designing a passive acoustic thermotomograph for biomedical applications is much discussed in the literature [1–8]. Investigations of the parameters of thermotomograph sensors, i.e., acoustic thermometers or sensors of thermal acoustic radiation, are conducted for this purpose [1, 9–13]. Nevertheless, many fundamental problems of the physics of thermal acoustic radiation remain unsolved. The main problem is how to take into account the contribution of the noise produced by a heated body and by a piezoelectric transducer to the measured signal.

Measurements of thermal acoustic radiation are fundamentally limited because of the necessity to take into account the self-radiation of a transducer. A body heated to the temperature T must emit radiation with the intensity proportional to this quantity [12]. However, a piezoelectric transducer (a receiver of radiation) also has a definite temperature T_{TR}, and, therefore, it must also emit thermal radiation determined by this temperature. As a result, two radiation fluxes propagate towards each other in the medium adjacent to the transducer, and the total flux of radiation is determined by their difference. If the body temperature is higher than the temperature of the piezoelectric transducer, $T > T_{TR}$, the radiation flux is incident on the transducer from outside; if $T < T_{TR}$, the transducer emits into the surrounding medium; and if the temperatures are equal, $T = T_{TR}$, the total radiation flux is equal to zero. The measured quantity is the so-called acoustic brightness temperature T_A [9, 12] defined as the temperature of a black acoustic body that creates the same flux of acoustic radiation as the object under investigation. This temperature is proportional to the mean square of the sound pressure $\overline{p^2}$ measured by the transducer. It is still not quite clear how to connect the values of T_A with the temperatures of the object and the transducer. A similar problem was considered theoretically for a flux of thermal electromagnetic radiation [14]. Such studies for acoustic radiation have not been performed yet.

As there is no clear understanding of the mechanism of the acoustic signal formation owing to thermal acoustic radiation, it is difficult to interpret the results of temperature measurements using a correlation technique [5, 15]. With this method of reception, electric voltages from two piezoelectric transducers are recorded separately, and then they are multiplied and averaged. As a result, the so-called acoustic brightness temperature of the correlation signal T_{AC} is measured. Two results are obtained experimentally:

(1) the peak value of the correlation signal T_{AC} is proportional to the temperature difference $T - T_{TR}$;

(2) the increments of the acoustic brightness temperatures T_{A1}^M and T_{A2}^M measured using a modulation technique by the first and second sensors separately are also proportional to the same quantity.

The values of the correlation coefficient $R = T_{AC}/\sqrt{T_{A1}^M T_{A2}^M}$ estimated according to these data reached 0.6–0.7.

The first of these results does not seem evident. If the intensity of the thermal radiation of a body is determined by its absolute temperature, then, by analogy with the measurement of a noise signal from active sources, it is natural to expect that the peak value of the correlated signal will be proportional to the value of T rather than $T - T_{TR}$. Thus, here we have a disagreement

between the experimental data and theoretical estimates. The clarification of the origin of this disagreement is also important in practice, since the differences in the signal values by a factor of several tens can strongly affect the possibility of solving the inverse problems of passive acoustic thermotomography [5].

The first step in solving the problem on the specific features of thermal acoustic radiation as an acoustic signal must be the investigation of signals obtained in the case of uncorrelated reception. In [9, 16], to measure the thermal acoustic radiation intensity, its source (a body with the temperature T) was placed into a basin with the temperature T_{AQ}, where a piezoelectric transducer with the temperature T_{TR} coinciding with the basin temperature T_{AQ} was positioned. Already, one of the first studies of acoustic thermography [16] demonstrated that the signal obtained at the output of an acoustic thermometer increases when a body with a temperature higher than the basin temperature T_{AQ} occurs in its range of vision, and decreases when the temperature of this body is lower than T_{AQ}. It was found that the signal magnitude is proportional to the temperature difference $T - T_{AQ}$. Later on, this result was confirmed in [9, 12]. However, because of the peculiarities of the modulation scheme of the reception of thermal acoustic radiation, which was used in these studies, it was impossible to give an unambiguous answer to the question of whether the acoustics brightness temperature is determined by the temperature difference $T - T_{TR}$.

To describe the signals measured by an acoustic thermometer, a semi-empirical formula was suggested in [10] for the mean square of the electric voltage $\overline{u^2}$ detected at the piezoelectric transducer. This formula contains a term depending on the temperature difference between an object and a transducer $T - T_{TR}$. However, there is no strict derivation of this formula.

The purpose of this paper is the measurement of the dependence of the acoustic brightness temperature on the thermodynamic temperatures of a source of thermal acoustic radiation and a transducer and to obtain the corresponding theoretical expression describing this dependence.

Let us consider the distinctive features of the modulation scheme of measurement [9, 12] to select the optimal scheme of the experiment. A body with the temperature T was placed in a basin with the temperature T_{AQ}. A piezoelectric transducer with the temperature T_{TR} coinciding with the basin temperature was also positioned in the basin. A flux of thermal acoustic radiation was periodically interrupted with a frequency of several hertz. Thermal acoustic radiation from the object arrived at the piezoelectric transducer during one of the half-periods, and thermal acoustic radiation from the basin arrived during another half-period. The difference between the signals obtained during the two half-periods was measured.

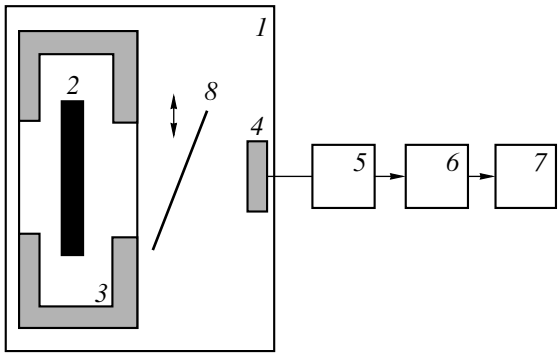

Fig. 1. Experimental setup: (*1*) a basin filled with water; (*2*) a plasticine bar; (*3*) a cuvette with foam-plastic walls and acoustically transparent windows, which is also filled with water; (*4*) a piezoelectric transducer; (*5*) an amplifier; (*6*) a square-law detector; (*7*) a personal computer; and (*8*) a reflecting duralumin plate.

Let us show that the dependence of the signal magnitude on the basin temperature that is recorded in the case of the modulation reception does not permit unambiguous interpretation. In [9, 12], the body under investigation and the basin were treated as two independent objects and the intensities of their thermal radiations were compared. The temperature of the piezoelectric transducer was taken into account only to the extent that it determined the intrinsic noise of the transducer. The fact that it had the same temperature as the basin did not provide grounds to believe that the signal proportional to the difference between the temperatures of the object and the piezoelectric transducer ($T - T_{TR}$) was recorded. Thus, the question of what is the quantity measured by the receiver of thermal acoustic radiation remains open.

From a practical point of view, this ambiguity does not affect the results of temperature measurements with the use of a noncorrelation technique. It is always possible to calibrate a receiving device according to several values of the object temperature and obtain a unique relation between the mean square of the voltage $\overline{u^2}$ picked up from a piezoelectric transducer and the object temperature T. Nevertheless, as mentioned above, this question is of key importance for correlation measurements.

To eliminate the ambiguity connected with the modulation reception, we measured thermal acoustic radiation using a nonmodulation technique (Fig. 1). The measurements were conducted in (*1*) a $40 \times 28 \times 30$-cm^3 basin filled with water. The source of thermal acoustic radiation was (*2*) a wide plasticine bar (the absorption coefficient of ultrasound in plasticine at the frequency about 2 MHz is 5 cm^{-1} [12]), which played the role of an acoustic "black" body. The bar was positioned in (*3*) a cuvette (a thermostat) with thick foam-plastic walls and acoustically transparent windows. The cuvette was also filled with water. The temperatures of

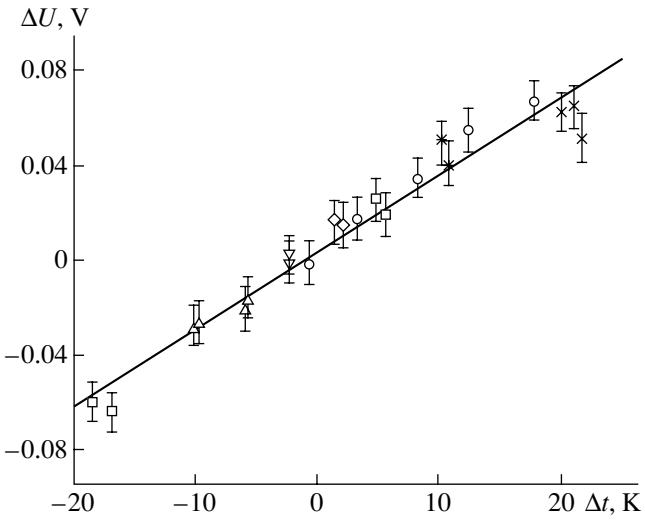

Fig. 2. Dependence of the voltage increment $\Delta U = U_O - U_C$ obtained in detecting the signals from the black body U_O and the basin U_C on the temperature difference Δt between the black body and the basin for different values of the basin temperature: (○) 29.1, (×) 30.0, (∗) 34.5, (□) 39.2, (◇) 44.4, (▽) 42.2, and (△) 40.5°C.

the basin and the cuvette were changed independently in the experiment in the range ~20–45°C. The temperatures were monitored by mercury thermometers with a precision of 0.2°C.

The radiation receiver was (*4*) a circular flat piezoelectric receiver with the radius a = 5 mm that was placed in the basin. The piezoelectric transducer was equipped with one quarter-wave layer, electrically loaded by a coupling transformer, and tuned to the frequency 2.2 MHz. The temperature of the piezoelectric transducer coincided with the temperature of the basin. The sound pressure produced by the thermal acoustic radiation from the basin with the cuvette was transformed into electric voltage by the piezoelectric transducer. The total signal also included the intrinsic noise of the piezoelectric transducer.

An electric signal was fed through (*5*) an amplifier with the transmission band 200 kHz to the input of (*6*) a square-law detector made using an MLT04 Analog Devices microcircuit. The resulting output voltage U proportional to the square of voltage at the output of the piezoelectric transducer $\overline{u^2}$ was averaged by a low-frequency filter of the first order with the time constant τ = 1 s and then stored during t = 20 s in (*7*) a PC with the help of an L-154 interface card (L-card SoftWare Lab Limited, Russia). The nonmodulation scheme of measurement preserves the constant component of the signal (whereas in the case of the modulation reception of an acoustic signal, this component vanishes). This, in its turn, dismisses the question of whether we measure the temperature of the piezoelectric transducer or the basin temperature.

To eliminate the drift of the output signal due to the piezoelectric transducer and the amplifier, we placed (*8*) a reflecting duralumin plate across the signal path. If the plate is removed, the signal from the black body is detected (position "open," the plate removed, $U = U_O$). If the plate is replaced, the signal from the basin is measured, $U = U_C$ (position "closed," the plate covers the acoustic window of the cuvette). The changes from the "open" to "closed" positions and back were performed with a period of several tens of seconds, which allowed us to correct the setup drifts and determine the voltage difference for the two aforementioned plate positions more precisely. We called this voltage difference the voltage increment $\Delta U = U_O - U_C$. Naturally, the increments were much smaller than each of the measured voltages U_O and U_C.

The dependences of the voltage increment ΔU on the temperature difference Δt between the black body and the piezoelectric transducer $\Delta t = T - T_{TR}$ are given in Fig. 2. If the temperature difference Δt is positive, the temperature of the black body is higher than the basin temperature, and if it is negative, the basin temperature is higher than the temperature of the black body. Various signs in Fig. 2 indicate the experimental data obtained at different basin temperatures in the range 29–45°C. The line approximating the given data is also shown in the figure.

The errors σ in the measured voltage increment ΔU, which are shown in Fig. 2, were determined taking into account the number of independent readings $N = t/2\tau$ during the time t: $\sigma = \sqrt{2/N}\,\sigma_m$, where σ_m is the rms error of measurement of the voltages U_O and U_C, and the factor $\sqrt{2}$ is connected with the fact that the voltage difference was calculated.

One can see that the data obtained can be approximated by a linear function $\Delta U = (A \pm \delta A)\Delta T$, where the mean value of the angular coefficient A has the meaning of the steepness of the transformation AT to the electric signal and δA is the error of its determination. Using the least squares method, one obtains $A \pm \delta A$ = 3.3 ± 0.3 mV/K.

The dependence of the voltage U_C measured by the piezoelectric transducer in the case of a closed shutter is given in Fig. 3 to evaluate the constant component of the signal and its drift. In this case, the changes of the output voltage are connected with the setup drifts. One can see that drifts constitute the value of the order of 10 mV while the average value is $U_0 \approx 2.37$ V. When the piezoelectric transducer was disconnected from the input amplifier, the noise level was U_A = 0.4 V, which is the contribution of the amplifier noise to the measured signal.

Thus, with allowance for the effect of the setup drifts and the signal noise, the mean square of the output voltage $\overline{u^2}$ of an acoustic thermometer consists of a large "base" and a term depending linearly on the tem-

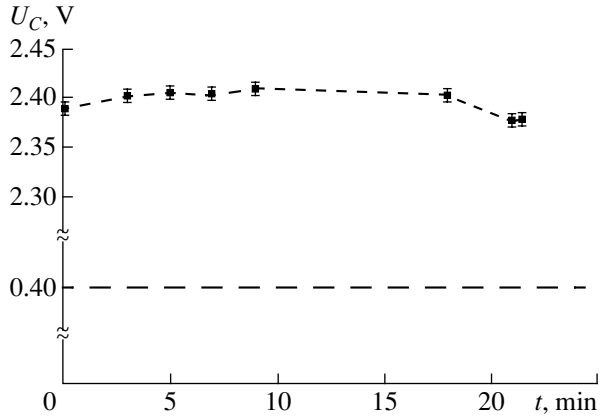

Fig. 3. Time dependence (drift) of the constant component U_C of the signal at the basin temperature 29.5 ± 0.5°C. The voltage of 0.4 V is the contribution of the amplifier noise to the measured signal.

perature difference between the object and the transducer $T - T_{TR}$:

$$\overline{u^2} = B + A(T - T_{TR}). \quad (1)$$

Now, let us turn to the analysis of the results. A semi-empiric formula for the mean square of the voltage $\overline{u^2}$ picked up from the output of the piezoelectric transducer has the form [10]

$$\overline{u^2} = k_B[4T_{TR}\mathrm{Re}Z + (K_2^2 z_2/S)(T - T_{TR})]\Delta f, \quad (2)$$

where k_B is the Boltzmann constant, ReZ is the real part of the complex electric output impedance of the transducer, K_2 is the magnitude of the coefficient of the pressure-to-voltage transformation, z_2 is the specific acoustic impedance of the medium under investigation, S is the area of the piezoelectric transducer, and Δf is the transmission band of the receiver. The temperature difference $T - T_{TR}$ is present in this formula in an explicit form, but this term was introduced artificially in [10].

Let us demonstrate that Eq. (2) can be derived strictly by the consideration of an equivalent electric circuit of a piezoelectric transducer as a six-terminal [17], as shown in Fig. 4. We consider a piezoelectric transducer with the specific acoustic impedance z_{TR} in contact with a damper (with the acoustic impedance $Z_1 = Sz_1$, where z_1 is the specific acoustic impedance) at one (rear) side (the 1–1 connectors) and with the medium under investigation with the acoustic impedance $Z_2 = Sz_2$ at the other side (the 2–2 connectors). In the general case, the piezoelectric transducer is connected with the medium under study through a matching layer with a specific acoustic impedance z_3. The forces F_1 and F_2 producing the pressures $p_1 = F_1/S$ and $p_2 = F_2/S$, respectively, affect the two inputs of the piezoelectric transducer.

We attribute all losses in the piezoelectric transducer to the damper, as it was done before [9]. In this case, the acoustic elements of the piezoelectric transducer are determined, first, by the acoustic properties of the transducer material (the quarter-wave coupling layer): $Z'_{TR} = z_{TR}S/j\sin(\pi\lambda_{ATR}/\lambda_{TR})$ ($Z'_3 = z_3 S/j\sin(\pi\lambda_{A3}/2\lambda_3)$), $Z''_{TR} = jz_{TR}S\tan(\pi\lambda_{ATR}/2\lambda_{TR})$ ($Z''_3 = jz_3 S\tan(\pi\lambda_{A3}/4\lambda_3)$), where j is the imaginary unit and λ_{TR} (λ_3) and λ_{ATR} (λ_{A3}) are the acoustic wavelength and the wavelength at the antiresonance frequency f_A in the piezoelectric transducer (in the quarter-wave layer), and, second, by the piezoelectric properties of the transducer: the coefficient $n = k_T\sqrt{2Sz_{TR}f_A C_0}$ of force-to-voltage transformation and the negative capacitance $-C_0/n^2$, where k_T is the coefficient of electromechanical coupling and C_0 is the transducer capacitance.

In such a circuit, the mean square of the voltage at the transducer output (the out–out connectors) can be represented as a sum of independent signals supplied to the transducer due to the thermal acoustic radiation from the medium and the damper:

$$\overline{u^2} = k_B[(K_2^2 z_2/S)T + (K_1^2 z_1/S)T_{TR}]\Delta f, \quad (3)$$

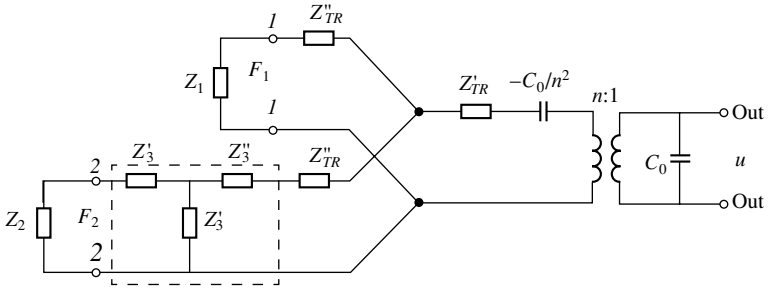

Fig. 4. Equivalent circuit of a piezoelectric transducer. The circuit of a coupling layer between the piezoelectric transducer and the medium under investigation is encircled by a dashed line. $F_1(F_2)$ is the force affecting the piezoelectric transducer from the side of the damper (the medium); u is the voltage at the transducer output; Z'_{TR} and Z''_{TR} (Z'_3 and Z''_3) are the circuit elements determined by the acoustic properties of the acoustic transducer (the coupling layer); Z_1 and Z_2 are the acoustic resistances of the damper and the medium; C_0 is the capacitance of the piezoelectric transducer; and n is the coefficient of the force-to-voltage transformation.

where K_1^2 is the square of the magnitude of the coefficient of transformation of effective pressure in the damper to electric voltage.

Using the theory of four-terminals for noise signals, it is possible to demonstrate the equivalence of Eqs. (2) and (3). In particular, at the antiresonance frequency, for a piezoelectric transducer without a quarter-wave layer, we have $\mathrm{Re}Z = \frac{k_T^2}{\pi^2}\frac{2z_{TR}}{f_A C_0(z_1 + z_2)}$ and $K_1^2 = K_2^2 = \frac{k_T^2}{\pi^2}\frac{8z_{TR}S}{f_A C_0(z_1 + z_2)^2}$, and with a quarter-wave layer, we have $\mathrm{Re}Z = \frac{k_T^2}{\pi^2}\frac{2z_{TR}}{f_A C_0(z_1 + z_3^2/z_2)}$, $K_1^2 = \frac{k_T^2}{\pi^2}\frac{8z_{TR}S}{f_A C_0(z_1 + z_3^2/z_2)^2}$, and $K_2^2 = \frac{k_T^2}{\pi^2}\frac{8z_{TR}z_3^2S}{f_A C_0 z_2^2(z_1 + z_3^2/z_2)^2}$. The majority of these formulas were obtained using other equivalent circuits of piezoelectric transducers [9, 11].

Thus, two approaches to the description of the reception of thermal acoustic radiation are possible. According to Eq. (2), the source is represented by the intrinsic noise of the piezoelectric transducer due to both the loss in the transducer itself and the loss for radiation and by the signal determined by the difference between the temperatures of the object and the transducer. In the case of a negative value of this signal, when $T < T_{TR}$, energy is carried away from the transducer. At the same time, according to Eq. (3), we can assume that the signal measured at the transducer output is formed by two independent sources. The first of them is thermal acoustic radiation of the medium under investigation, and the second one is similar radiation from the damper. The intensities of these signals are determined by the absolute temperatures of these objects. Both approaches are equivalent and lead to the same expressions. However, the information on the existence of the object appears only when the object temperature is different from the transducer temperature. Therefore, we can conclude that, in the case of the detection of thermal acoustic radiation, the signal is determined not by the total thermal radiation of the object, which is proportional to T, but only by its part that is proportional to the difference $T - T_{TR}$.

The described analysis provides an opportunity to evaluate the noise temperature T_N of an acoustic thermometer, which determines its threshold sensitivity. It is necessary to note that the measured quantity, i.e., the mean square of the voltage, $\overline{u^2}$, is virtually independent of the acoustic load of the piezoelectric transducer. If we remove the medium under investigation, i.e., put the piezoelectric transducer in air, the second terms in Eqs. (2) and (3) that are proportional to $T - T_{TR}$ and T, respectively, vanish and the first terms change. If we detect the signal within the whole transmission band of the piezoelectric transducer, the resulting value of the mean square of the voltage $\overline{U^2}$ for the electrically unloaded piezoelectric transducer considered above will be $\overline{U^2} = (8k_T^2/\pi^2)\, k_B T_{TR}/C_0$ [11].

Thus, if the temperatures of the medium under investigation and the piezoelectric transducer coincide, the resulting signal $\overline{U^2}$ barely changes when the medium is changed, e.g., in the case of such a fundamental change as the replacement of water by air. This signal actually determines the noise temperature of an acoustic thermometer.

Expression (2) provides an opportunity to estimate theoretically the noise temperature $T_{N_{TR}}$ of a piezoelectric transducer. These estimates yield reasonable results: $T_{N_{TR}} \le 2T_{TR}$ [9, 18]. The results given in Figs. 2 and 3 provide an opportunity to evaluate experimentally the noise temperature T_N of an acoustic thermometer. According to Eq. (1), it is the ratio of the constant term B to the transformation steepness A [10]:

$$T_N = B/A. \tag{4}$$

It is easy to find that, with allowance for the amplifier noise, the noise temperature of an acoustic thermometer is T_N = 720 K, while in the absence of the amplifier noise, $T_{N_{TR}} \approx 600$ K. It should be noted that the noise temperature of a piezoelectric transducer is approximately two times higher than its thermodynamic temperature and the contribution of the amplifier noise is 17%. Previously, these quantities were measured using indirect methods [9, 13, 18]. The given estimates coincide with our results obtained earlier [18] and are close to the results obtained by Gerasimov, Mirgorodskiĭ, and Peshin [13] using a different method.

It should be noted that Eq. (1) is obtained for the case of a black body covering the whole aperture of the piezoelectric transducer. A decrease in the thermal source dimensions leads only to a decrease in the transformation steepness A.

Thus, the linear dependence of the voltage increment on the temperature difference between the source and the transducer, which is predicted by Eq. (2), is proved experimentally. The constant component of the signal obtained at the output of the piezoelectric transducer determines the noise temperature of the receiving device. The main feature of the thermal acoustic radiation as a source of acoustic signals is that the signal is represented not by the total thermal radiation of an object, which is proportional to the absolute temperature T of this object, but by the part of this radiation that is proportional to the temperature difference between the object and the transducer, $T - T_{TR}$.

ACKNOWLEDGMENTS

This work was supported by the Russian Foundation for Basic Research, project no. 00-02-16370.

REFERENCES

1. E. V. Krotov, S. Yu. Ksenofontov, A. D. Mansfel'd, *et al.*, Izv. Vyssh. Uchebn. Zaved., Radiofiz. **42** (5), 479 (1999).
2. V. A. Burov and E. E. Kasatkina, Akust. Zh. **43**, 162 (1997) [Acoust. Phys. **43**, 135 (1997)].
3. A. I. Chmill, V. V. Gerasimov, Yu. V. Guluaev, *et al.*, in *Acoustical Imaging*, Ed. by S. Lees (Plenum, New York, 1997), Vol. 23, pp. 77–86.
4. R. A. Kruger, D. R. Reinecke, and G. A. Kruger, Med. Phys. **26**, 1832 (1999).
5. V. I. Pasechnik, A. A. Anosov, and K. M. Bograchev, Biomed. Radioelektron., No. 2, 3 (1999).
6. K. M. Bograchev and V. I. Pasechnik, Akust. Zh. **45**, 742 (1999) [Acoust. Phys. **45**, 667 (1999)].
7. V. I. Passechnik, A. A. Anosov, and K. M. Bograchev, J. Acoust. Soc. Am. **105**, 1209 (1999).
8. Brian Fowlkes, J. Acoust. Soc. Am. **101**, 3120 (1997).
9. V. I. Pasechnik, Akust. Zh. **36**, 718 (1990) [Sov. Phys. Acoust. **36**, 403 (1990)].
10. V. I. Pasechnik, Akust. Zh. **39**, 140 (1993) [Acoust. Phys. **39**, 70 (1993)].
11. A. A. Anosov and V. I. Pasechnik, Akust. Zh. **39**, 207 (1993) [Acoust. Phys. **39**, 110 (1993)].
12. V. I. Passechnik, Ultrasonics **32**, 293 (1994).
13. V. V. Gerasimov, V. I. Mirgorodskiĭ, and S. V. Peshin, Zh. Tekh. Fiz. **65** (5), 149 (1995) [Tech. Phys. **40**, 489 (1995)].
14. S. M. Rytov, Yu. A. Kravtsov, and V. I. Tatarskiĭ, *Introduction to Statistical Radiophysics*, Part 2: *Random Fields* (Nauka, Moscow, 1978).
15. A. A. Anosov, M. A. Antonov, and V. I. Pasechnik, Akust. Zh. **46**, 28 (2000) [Acoust. Phys. **46**, 21 (2000)].
16. V. I. Mirgorodskiĭ, V. I. Pasechnik, S. V. Peshin, *et al.*, Dokl. Akad. Nauk SSSR **297** (6), 1370 (1987) [Sov. Phys. Dokl. **32**, 1021 (1987)].
17. V. I. Domarkas and R.-I. Yu. Kazhis, *Control-and-Measurement Piezoelectric Transducers* (Mintis, Vilnius, 1975), pp. 48–69.
18. A. A. Anosov, A. V. Erofeev, and V. I. Pasechnik, in *Proceedings of IV Session of the Russian Acoustical Society "Acoustic Measurements: Methods and Means"* (Moscow, 1995), pp. 32–34.

Translated by M. Lyamshev

Acoustical Physics, Vol. 48, No. 1, 2002, pp. 18–23. Translated from Akusticheskiĭ Zhurnal, Vol. 48, No. 1, 2002, pp. 22–27.

Acoustic Anisotropy and Birefringence in Fibre-Reinforced Composite Materials

G. Busse*, I. Yu. Solodov, R. Stoessel*, and J. Schuetz***

** Department of Nondestructive Testing, Institute for Polymer Testing and Science, Stuttgart University, Pfaffenwaldring 32, Stuttgart, 70563 Germany*

***Department of Physics, Moscow State University, Vorob'evy gory, Moscow, 119899 Russia*

e-mail: solodov@acs465a.phys.msu.su

Received March 15, 2001

Abstract—All nine elastic moduli of an orthotropic composite material, namely, polypropylene reinforced with glass fiber, are determined from the measured values of the bulk acoustic wave velocities along specific directions in the planes of symmetry of the material. These data are used to calculate the angular dependences of phase velocities, polarization vectors, and directions of ray velocities of bulk waves in the composite. It is demonstrated that the difference in the velocities of shear waves polarized along and across the glass fiber gives rise to an acoustic birefringence and can lead to an elliptical polarization of waves. The measurement of the phase velocities of shear waves as functions of the wave polarization is suggested as a method for the determination of the fiber orientation in a composite material. © *2002 MAIK "Nauka/Interperiodica".*

The anisotropy of acoustic wave propagation in fiber-reinforced composites provides an opportunity to determine such important structural parameters of these materials as the fiber content, its orientation, etc., by measuring the characteristics of the bulk waves propagating in them. These characteristics must include not only the conventional anisotropy of the propagation velocity [1, 2], but also other parameters of acoustic waves (the velocity and direction of energy transfer, the polarization, etc.), which strongly depend on the propagation direction in both single crystals and composite materials. In this connection, acoustic polarization measurements for shear waves are of importance. These measurements are the subject of active recent investigations [3–5], but, in contrast to optics, they have not yet found wide application in nondestructive testing. In particular, this is true for the effect of birefringence of shear acoustic waves [6], which can serve as the source of information on the structural anisotropy of polymers and composites.

This paper analyzes the experimental potentialities of the birefringence polarization technique by using a well-known composite material, namely, sheet polypropylene reinforced with glass fiber, as an example. The analysis is preceded by the calculation of the anisotropy of acoustic wave propagation with the use of the values of the elastic moduli, which are determined for this material from the measurements of the phase velocities of bulk waves propagating in it.

The investigated composite material is an orthotropic material with three mutually orthogonal planes of symmetry normal to the x, y, and z axes. This material is characterized by a set of nine independent elastic moduli c_{ijkl} ($i, j, k, l = 1, 2, 3$). The propagation parameters of acoustic waves are determined by solving the Christoffel equation [7]

$$(c_{ijkl}n_j n_l - \rho c^2 \delta_{ik})u_k = 0, \tag{1}$$

where n_j and n_l are the components of a unit vector along the propagation direction, ρ is the material density, c is the phase velocity, and δ_{ik} is the Kronecker delta. A nontrivial solution to the system of equations (1) exists with the constraint

$$\left|c_{ijkl}n_j n_l - \rho c^2 \delta_{ik}\right| = 0 \tag{2}$$

and has the form

$$u_k = U_0 p_k, \tag{3}$$

where the components of the polarization vector p_k are the respective minors of the matrix given by Eq. (2), and U_0 is the acoustic wave amplitude.

The analysis of Eq. (2) shows that the values of all six diagonal components of the matrix of elastic moduli (c_{11}, c_{22}, c_{33}, c_{44}, c_{55}, and c_{66}) can be determined by measuring the phase velocities of longitudinal and transverse waves of respective polarizations, which propagate along the three basic directions, x, y, and z (the fiber orientation). To calculate the remaining three independent components of the matrix c_{ijkl} (c_{12}, c_{13}, and c_{23}), it is possible to use the measurements of the phase velocity of only longitudinal waves along the diagonal directions in the symmetry plane of the composite.

The phase velocities of bulk acoustic waves were measured in the samples of glass-fiber-reinforced sheet polypropylene with a thickness of about 4 mm and a

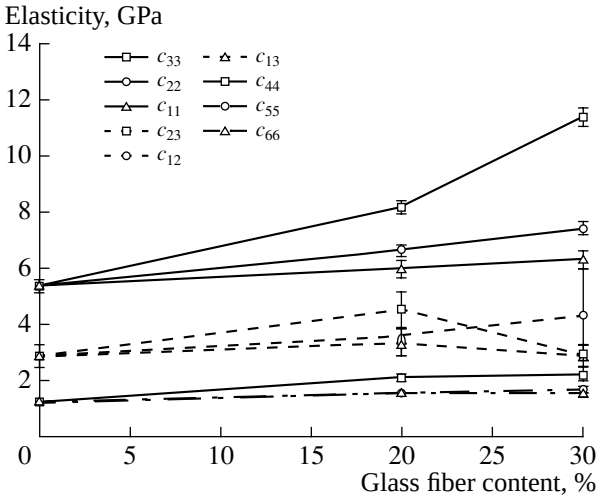

Fig. 1. Dependences of the elastic moduli of glass-fiber-reinforced polypropylene on the glass fiber content.

glass fiber content from 0 to 30%. Six cuts of the composite were prepared to determine all nine elastic moduli: three cuts along the basic directions, *x*, *y*, and *z*, and three 45° cuts in the symmetry planes. A standard pulsed technique using transmission and reflection was used to measure the delay of a radio-frequency pulse in the 2–10-MHz frequency range. In this frequency range, the dispersion of acoustic waves that is related to the molecular structure of the polymer matrix, is absent and the values of the phase velocity do not depend on frequency [1]. The error of the measurement of the pulse delay by a digital oscilloscope did not exceed 10 ns. Longitudinal waves were excited by ZTL ceramic transducers (the Krautkramer company), and *YX*-cut quartz plates were used to generate shear waves. The contact between a transducer and the sample surface was established using a layer of epoxy resin, which provided an opportunity to change (and analyze) the polarization of shear waves by rotating the transmitting (or receiving) transducer. A considerable number of measurements were conducted for each orientation to make the error of the phase velocity determination less than ~1%. The results of calculating the elastic moduli by Eq. (2) using the measured values of the phase velocities of acoustic waves for samples of glass-fiber-reinforced polypropylene with different glass fiber contents are given in Fig. 1. One can see that the elastic matrix without glass fiber is almost isotropic: $c_{11} = c_{22} = c_{33}$, $c_{44} = c_{55} = c_{66}$, and $c_{12} = c_{23} = c_{13} \approx c_{11} - 2c_{44}$. The introduction of glass fiber leads to the formation of an orthotropic composite with the longitudinal and shear elasticities (the diagonal components c_{ijkl}) increasing with the growth of fiber content. The maximal increase in elasticity (c_{33}) is observed, naturally, along the glass fiber direction (the *z* axis). At the same time, the values of the nondiagonal components (c_{13} and c_{23}) decrease with the growth of the fiber content from 20 to 30% (Fig. 1). Such behavior is physically analogous to a decrease in the Poisson's ratio in the case of increasing rigidity of a material, which usually occurs in the case of solids.

The values obtained above for the elastic moduli of glass-fiber-reinforced polypropylene were used to calculate the phase velocities and the polarization of acoustic waves in the planes of symmetry of the material by using Eqs. (2) and (3). The results of calculation for the *xz* plane (the *x* axis is directed along the thickness of a polypropylene sheet) of a sample with a 30% fiber content are given in Fig. 2.

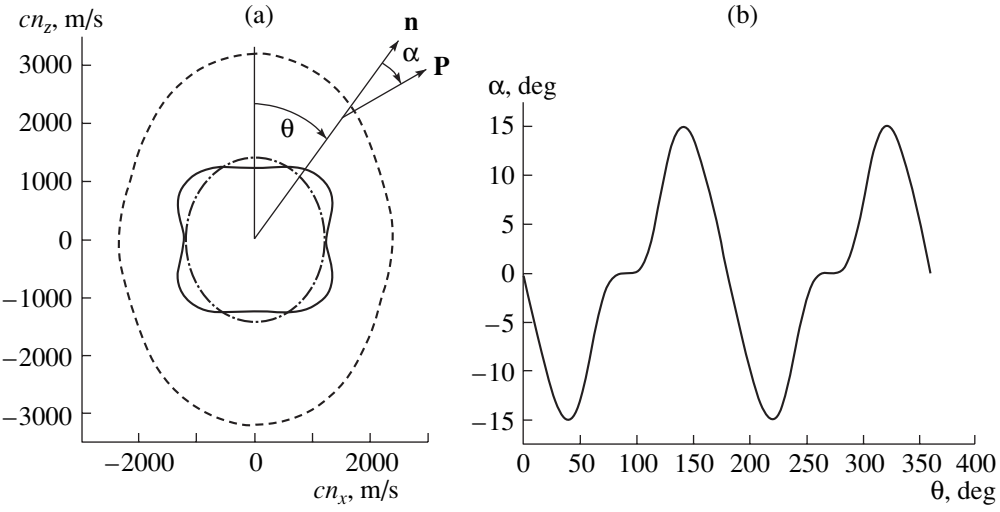

Fig. 2. (a) Anisotropy of the phase velocity in the *xz* plane of 30% glass-fiber-reinforced polypropylene: (----) a quasi-longitudinal wave; (—) a quasi-shear wave; and (–·–·–) a purely shear wave with polarization along the *y* axis. (b) Angle of deviation of the polarization of quasi-longitudinal waves from the propagation direction in the *xz* plane of 30% glass-fiber-reinforced polypropylene.

A purely shear wave (polarized normally to the propagation plane) and also quasi-longitudinal and quasi-shear (polarized in the propagation plane) waves can exist in an arbitrary direction in the symmetry plane. According to Fig. 2a, a strong anisotropy of the phase velocity (≅50%) is observed for a quasi-longitudinal wave. For shear waves in this plane, there are two acoustic axes near the reinforcement direction. Since the polarization vectors for quasi-longitudinal and quasi-shear waves are mutually orthogonal, it is possible to conclude from the data given in Fig. 2b that the polarization vectors of both waves can deviate from the propagation direction within the angles up to 15°. A strong acoustic anisotropy of glass-fiber-reinforced polypropylene is also confirmed by the calculation of the anisotropy of the ray velocity: the angles of deviation of the ray velocity from the propagation direction (δ) for quasi-longitudinal waves exceed 20°, and for quasi-shear waves, they can exceed even 30°, which can lead to a noticeable displacement of the beams of bulk waves in the nonsymmetric directions of the composite. It is characteristic that in this case the dependence $\delta(\theta)$ for quasi-longitudinal waves is completely analogous to the dependence shown in Fig. 2b, which is typical of all anisotropic media [7]: in the case of quasi-longitudinal waves in the directions of pure polarization, the ray velocity coincides with the wave normal ($\delta = 0$). This rule is not true for quasi-shear waves: according to the calculations, near the directions of pure polarization of shear waves, the value of δ reaches 20°–30°.

Figure 2a demonstrates that two shear waves with slightly different phase velocities and the polarizations parallel and perpendicular to the reinforcement direction (the *z* axis) are allowed in the direction of the *x* axis (across the thickness of a composite sheet). Hence, if we set an arbitrary polarization in the plane of the sheet (the *yz* plane) at the shear wave transducer, the excited shear wave will be split into two waves:

$$\begin{aligned}\mathbf{u}_T(x, t) &= U_{T_y}\mathbf{e}_y\sin(\omega t - k_2 x)\\ &+ U_{T_z}\mathbf{e}_z\sin(\omega t - k_3 x),\end{aligned} \tag{4}$$

where k_2 and k_3 are the wave numbers of the shear waves polarized along the *y* and *z* axes, respectively, and $\mathbf{e}_y$ and $\mathbf{e}_z$ are the unit vectors of polarization of these waves. The wave amplitudes in Eq. (4) depend on the orientation of the transmitting transducer: $U_{T_y} = U_T\cos\beta$ and $U_{T_z} = U_T\sin\beta$, where β is the orientation angle of the transmitting transducer and U_T is the displacement amplitude at the radiator. Since k_2 and k_3 differ to a certain extent according to Fig. 2, the oscillations in the plane $x = d$, after being transmitted through a sample with the thickness *d*, have the form

$$\begin{aligned}\mathbf{u}_T(d, t) &= (U_T\cos\beta)\mathbf{e}_y\sin\omega t\\ &+ (U_T\sin\beta)\mathbf{e}_z\sin(\omega t + \Delta\varphi),\end{aligned} \tag{5}$$

where the phase shift is $\Delta\varphi = d(k_2 - k_3)$. According to Eq. (5), glass-fiber-reinforced polypropylene acts as a polarizing plate that changes the polarization of shear waves depending on the strength of birefringence ($\Delta\varphi$).

If an analogous shear transducer is used for the detection of the resulting displacement, it is possible to determine the amplitude (V_0) and phase (ψ) of its output signal from Eq. (5):

$$V_0 = U_T\sqrt{\cos^2\beta\cos^2\gamma + \sin^2\beta\sin^2\gamma + 2\sin\beta\cos\beta\sin\gamma\cos\gamma\cos\Delta\varphi}, \tag{6}$$

$$\psi = \arctan\frac{\sin\beta\sin\gamma\sin\Delta\varphi}{\cos\beta\cos\gamma + \sin\beta\sin\gamma\cos\Delta\varphi}, \tag{7}$$

where γ is the angle between the direction of polarization of the receiving transducer and the *y* axis of the composite. The results of calculating $V_0(\gamma)$ and $\psi(\gamma)$ for $\beta = 45°$ and different values of $\Delta\varphi$ are shown in Figs. 3a and 3b.

The case $\Delta\varphi = 0$ corresponds to the propagation of a linearly polarized wave in an isotropic solid: the output signal of a phase plate naturally vanishes in the case of the orthogonal position of the radiator ($\beta = 45°$) and the receiver ($\gamma = 135°$) (Fig. 3a), and its phase changes stepwise to 180° as it passes through this position (Fig. 3b).

At $\Delta\varphi = 90°$, we have a circular polarization: the amplitude of the output signal does not depend on γ (Fig. 3a) and the phase grows linearly ($\varphi = \gamma$) with the receiver rotation (Fig. 3b). The intermediate values of $\Delta\varphi$ correspond to the elliptical motion of the medium particles. In this case, the minimums and maximums in Fig. 3a characterize the positions of the minor and major semiaxes of the ellipse, respectively. For $\Delta\varphi < 90°$, the ellipse is oriented along the direction of the radiator polarization ($\beta = 45°$), and for $\Delta\varphi > 90°$, the major semiaxis of the ellipse is rotated through 90°. Comparing Figs. 3a and 3b, we see that the steepest portions of the phase characteristic ($\gamma \cong 135°$) correspond to the position of the minor axis of the ellipse. This proves the theoretical prediction [7] that the sector velocity of a particle is constant in the case of elliptical motion: the angular velocity of a medium particle is large near the minor axis and decreases with distance from the rotation center.

In the case of the constant thickness *d* of a sample, the strength of birefringence depends on the frequency and the difference in the phase velocities of the waves polarized along the *y* and *z* axes and propagating through the composite thickness. The velocity of these

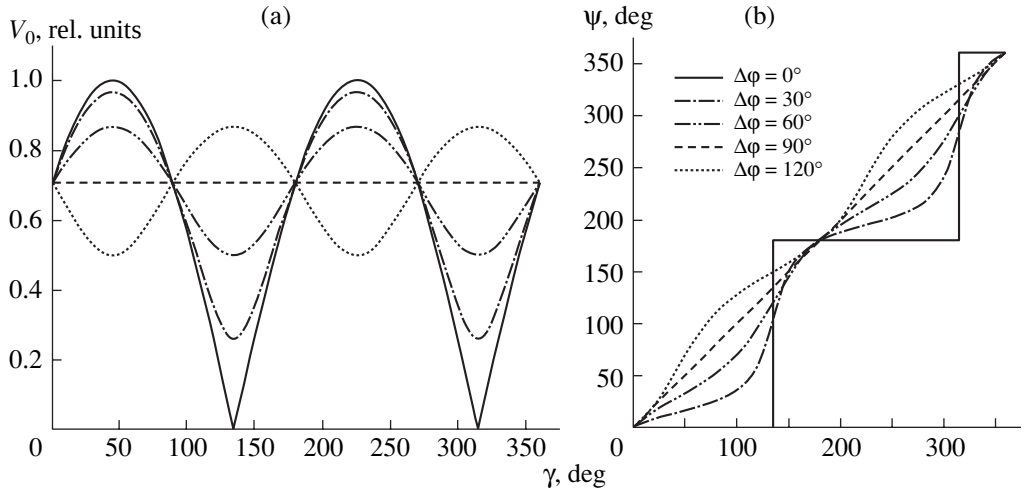

Fig. 3. Dependences of the (a) amplitude and (b) phase of the output signal on the orientation of the receiving transducer for different values of the birefringence strength.

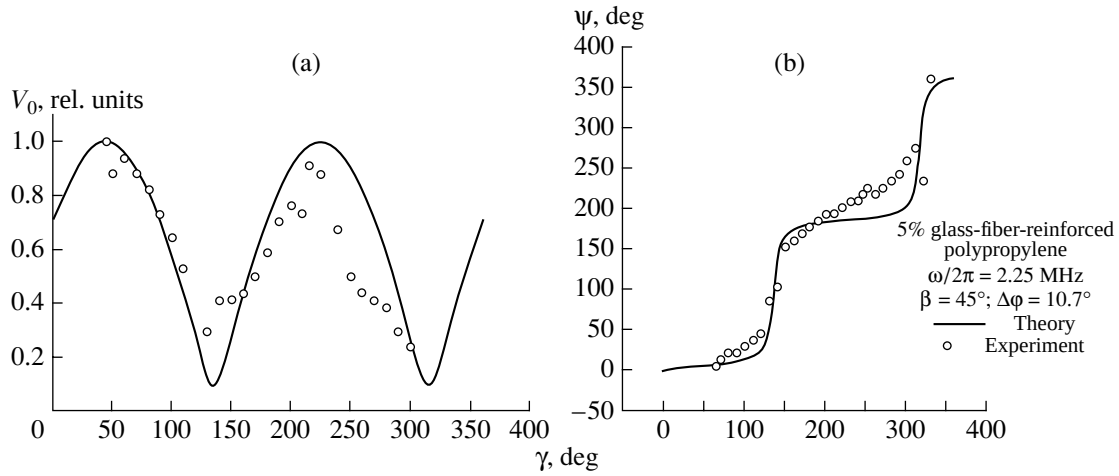

Fig. 4. Dependences of the (a) amplitude and (b) phase of the output signal on the orientation of the receiving transducer for a weakly birefringent sample of 5% glass-fiber-reinforced polypropylene.

waves is determined by the values of the elastic moduli c_{55} and c_{66}. The difference between these moduli vanishes as the concentration of glass fiber decreases (Fig. 1). At $\omega/2\pi \approx 2$ MHz, the 5% glass-fiber-reinforced polypropylene can be considered as a weakly birefringent medium: $\Delta\varphi \cong 11°$ at $d = 4$ mm, and the trajectory of particle motion is an elongated ellipse with the ratio of semiaxes about 1/10.

The experimental dependences of the amplitude and phase of the output signal on the angle of orientation of the receiving transducer are given in Figs. 4a and 4b. The deep amplitude modulation (Fig. 4a) and the step-like change of the signal phase (Fig. 4b) observed experimentally show that, in the case of a 5% glass-fiber-reinforced polypropylene sample, the ellipse of displacements is very strongly elongated along the direction of the radiator oscillations. One can see good general agreement of the experiment with the calculations conducted using Eqs. (6) and (7). Some scatter of single experimental points is apparently connected with the instability of the acoustic contact at the rotation of the receiving transducer.

A more pronounced manifestation of birefringence was observed in a 5% glass-fiber-reinforced polypropylene sample at the frequency 10 MHz. In this case, a composite sheet is a strongly birefringent medium: the calculated value is $\Delta\varphi \cong 48°$, and the expected ratio of the ellipse semiaxes is approximately equal to 1/2 according to Eq. (5). One can see from Figs. 5a and 5b that in this case the experimentally observed depth of the amplitude modulation of the output signal is much smaller and the phase of this signal changes almost linearly. Satisfactory agreement of experimental data with the calculations in Fig. 5 proves that the polarization of

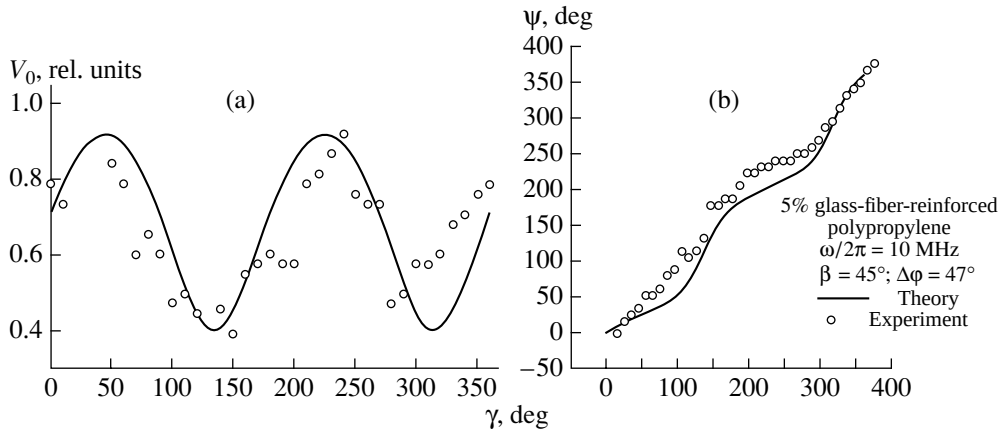

Fig. 5. Dependences of the (a) amplitude and (b) phase of the output signal on the orientation of the receiving transducer in the case of strong birefringence.

shear waves in glass-fiber-reinforced polypropylene changes qualitatively from linear to almost circular because of the birefringence.

Acoustic birefringence and the observed effects of elliptical polarization are caused by the difference in the phase velocities of shear waves with orthogonal polarizations and manifest themselves only in anisotropic media. Such an anisotropy in composites is caused by the effect of the fiber, which leads to different values of the shear rigidity of the material in the case of its deformation along and across the reinforcement direction. This provides the possibility of acoustically diagnosing the fiber orientation by measuring the velocity of shear waves (or the delay time $\Delta\tau$) as a function of their polarization. The results of such measurements for 30% glass-fiber-reinforced polypropylene are given in Fig. 6. To obtain these data, the radiator and the receiver were positioned coaxially ($\gamma = \beta$) and rotated synchronously in the sample plane. The angular position of the minimum in the curve of Fig. 6 (the velocity maximum) indicates the fiber direction, and the maximum in this curve corresponds to the orthogonal direction.

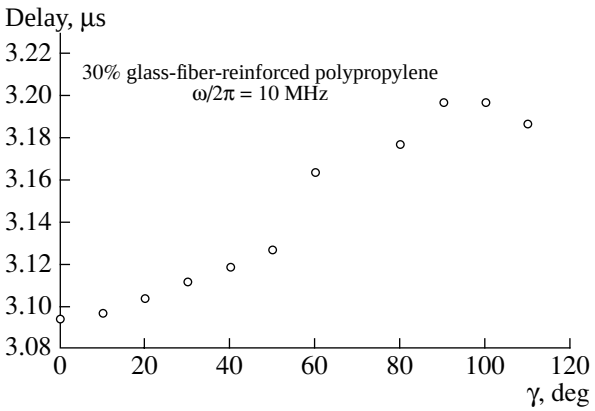

Fig. 6. Dependence of the delay time of the output signal of the receiving transducer on the polarization of shear waves.

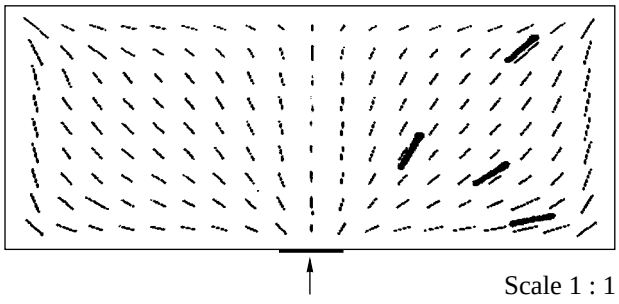

Fig. 7. Determination of the local orientation of glass fiber in a polyamide sample: (—) acoustic measurements and (----) measurements with the electromagnetic polarization technique.

Analogous measurements of $\Delta\tau(\gamma)$ were conducted for another composite material, glass-fiber-reinforced polyamide, with the local orientation determined preliminarily by the electromagnetic polarization technique [8]. Its local orientation varied strongly for different points of the sample (Fig. 7). The data of acoustic measurements given in this figure demonstrate that the method of acoustic birefringence provides the opportunity to determine the local orientation of a fiber with sufficiently high precision. The spatial resolution of measurements is determined by the size of the transducers, which was about 1 cm in our experiments.

In conclusion, it is necessary to note that the studied polarization effects in glass-fiber-reinforced polypropylene must be typical for a wide class of uniaxial fiber-reinforced composites. Similar acoustic anisotropy and effects of birefringence can arise due to internal mechanical stress. In this case, the sample can

behave like a polarizing plate, and the polarization of shear waves will depend on the value and orientation of stress.

REFERENCES

1. K. J. Newell, A. N. Sinclair, Y. Fan, and C. Georgescu, Res. Nondestruct. Eval. **9**, 25 (1997).
2. K. Y. Kim, T. Ohtani, A. R. Baker, and W. Sachse, Res. Nondestruct. Eval. **7**, 13 (1995).
3. D. Fei and D. Hsu, QNDE **18**, 1385 (1999).
4. D. Fei and D. Hsu, QNDE **19**, 1159 (2000).
5. Probing Fiber Orientation in Composites Using Transverse Ultrasound, CNDE News **12** (1), 3 (2001).
6. B. A. Auld, *Acoustic Fields and Waves in Solids* (Wiley, New York, 1973), Vol. 1.
7. F. I. Fedorov, *Theory of Elastic Waves in Solids* (Plenum, New York, 1968).
8. R. Steegmuller and L. Diener, Nondestr. Test. Eval. **13**, 203 (1997).

Translated by M. Lyamshev

Acoustical Physics, Vol. 48, No. 1, 2002, pp. 24–33. Translated from Akusticheskiĭ Zhurnal, Vol. 48, No. 1, 2002, pp. 28–38.

Long-Range Sound Propagation in the Norwegian Sea

R. A. Vadov

Andreev Acoustics Institute, Russian Academy of Sciences, ul. Shvernika 4, Moscow, 117036 Russia
e-mail: vadov@akin.ru

Received December 25, 2000

Abstract—The data of repeated experiments on the long-range propagation of explosion-generated and cw signals in the Norwegian Sea in summer conditions (with a fully-developed underwater sound channel) are presented. These data are used to analyze the spatial and time structures of the sound field, as well as to estimate the attenuation coefficient at frequencies within 63–630 Hz and to determine its frequency dependence. The spatial variability of the propagation conditions is analyzed on the basis of the experimental data obtained for the propagation of explosion-generated signals along a 815-km-long path crossing the Norwegian and Lofoten Hollows. © *2002 MAIK "Nauka/Interperiodica"*.

A specific feature of the water characteristics in the Norwegian Sea is their spatial variability governed by the currents that exist in this region [1–3]. Through the Faeroe-Scotland Trough, warm and high-saline waters of the Atlantic Ocean arrive at the Norwegian Sea. Because of the permanent influx of these waters, the near-surface temperature approaches 5–15°C, and the salinity is close to 35‰. From the north and north-west, cold arctic waters intrude that reach deep horizons in their mixing with the Atlantic waters. The salinity of the deep waters is about 34.9‰, and their temperature is as low as –1°C. Towards the north (along the Norwegian coastline), water currents are branched from the Gulf Stream and produce counterclockwise rotations. The directions of the local currents and the depth that is reached by them are strongly influenced by the general bottom relief. The bed of the Norwegian Sea has a rough relief. The central part of this sea is occupied by the Norwegian Hollow (with 2900–3500-m depths) and the Lofoten Hollow (with 2800–3200-m depths) [2]. According to the publications, the bottom sediments of the central deep-water part of the Norwegian Sea are represented by terrigenic aleurite silts. The sediments have a layered structure. Interlayers of different hardness, viscosity, and consistence occur. The highest density characterizes the viscous sediments that are enriched with a fine-grained clay-like bottom material.

In summertime (July to September), experiments were repeatedly performed by the Andreev Acoustics Institute to study the sound attenuation and to determine the space–time variability and the intensity structure of the sound field in the underwater sound channel (UWSC) of the deep-water Norwegian Sea. The main experiments were carried out with explosive sound sources on the propagation path that crossed the Norwegian and Lofoten hollows from south-west to north-east. In the southern part of the sea (the region of the Norwegian Hollow), the vertical structure of the water column had the following features. The upper mixed layer reached depths of 20–40 m. The temperature in this layer was 7–8°C, the salinity was 35.0–35.1‰, and the sound speed gradient varied from –0.4 to +0.03 1/s. At depths of 20–40 to 50–60 m, a pronounced temperature discontinuity layer was observed. As the depth increased, the water temperature decreased from 7–8 to 3.5–5.5°C. The sound speed gradient in the discontinuity layer varied from –0.5 to –0.8 1/s. At deeper horizons, the temperature decreased more slowly. At depths of 100–200 to 300–400 m, a layer existed, within which the depth dependence of the sound speed (under the effect of the slight decrease in the water temperature) was nearly compensated by the hydrostatic gradient. At the depths 300–400 to 600–700 m, the temperature decreased to 0°C, and the sound speed gradient remained within –0.02 to –0.03 1/s. At lower depths, the temperature monotonically decreased to –0.8 to –1.5°C near the bottom. At such depths, the hydrostatic gradient predominates, and the lower boundary of the UWSC is formed, its axis being at the depth 400–600 m. Figure 1a shows a vertical sound speed profile $c(z)$ that is characteristic of the Norwegian Hollow. At the surface, the sound speed is by 18–20 m/s lower than at the bottom (with a sea depth of about 3.5 km) and by 18–25 m/s higher than at the UWSC axis.

Figure 1b shows a vertical sound speed profile $c(z)$ that is characteristic of the northern part of the sea (the region of the Lofoten Hollow). In contrast to the southern part of the sea, the UWSC axis here is at the depth 800–1100 m. The difference in the sound speeds at the bottom (with a sea depth of about 3.3 km) and at the UWSC axis is about 35 m/s. The value of the sound speed at the surface is 10–15 m/s lower than at the bottom. In some curves $c(z)$ obtained in the measurements that accompanied the acoustical experiments, a relative maximum was observed at depths of ~350–400 m in the southern and ~500–600 m in the northern parts of the

path. The sound speed at these depths was 1–3 m/s higher than at 150–200 m and 7–9 m/s higher than at the axis of the main UWSC. Thus, in some cases, an additional weakly pronounced underwater sound channel existed that could capture rays crossing its axis at angles smaller than 3°–3.5° (in comparison with 10° for the main UWSC).

To study the spatial structure of the point-source sound field within the kilohertz frequency band, towed piezoceramic transmitting transducers were used. In these experiments, a continuous noise signal was transmitted within a 1/3-octave band. The sound sources were towed along paths 80–100 km in length. The minimal distance between the corresponding points was no higher than 200–400 m. The latter fact allowed us to perform mutual calibration of the transmitting and receiving systems, which is required to subsequently recalculate the measured sound levels to the anomaly of sound propagation. The aforementioned experiments were carried out both in the northern and southern parts of the Norwegian Sea.

According to one such experiments performed in the region of the Norwegian Hollow, with a 95-m source depth, the nearest boundary of the first convergence zone was at a 41-km distance for a 20-m receiver depth, at 36 km for a 150-m receiver depth, and at 31.5 km for 600 m. The propagation anomaly reached 12–16 dB at the beginning of the zone. At horizons deeper than 300–400 m, the convergence zone broke down into two half-zones, the nearest boundary of the second half-zone was 42.5 km from the source for the 600-m receiving horizon. Figure 2a illustrates the range dependence of the propagation anomaly for the 600-m depth of the receiver.

According to a similar experiment performed in the region of Lofoten Hollow, with a 95-m source depth, the nearest boundary of the first convergence zone was 43.5 km for a 150-m receiver depth and 36.5 km for 1000 m. The propagation anomaly reached 12–15 dB at the beginning of the zone. At horizons deeper than 500–600 m, the convergence zone again broke into two half-zones. The nearest boundary of the second half-zone was 52 km from the source for the 1000-m receiving horizon. Figure 2b illustrates the range dependence of the propagation anomaly for the 150-m receiver depth in this region.

The spatial structures of the sound field intensity are different for the northern and southern parts of the Norwegian Sea.

At low frequencies (10–300 Hz), experiments were also carried out with the use of cw sources that could not be towed. In these studies, vertical structures of the sound field were measured at different distances from the source. The transmitter was usually at a 100–200-m depth in such measurements. The results obtained at closer (about 1 km) distances were used to calibrate the sound source. At small distances, the measured vertical structure agrees well with the calculations. However, at

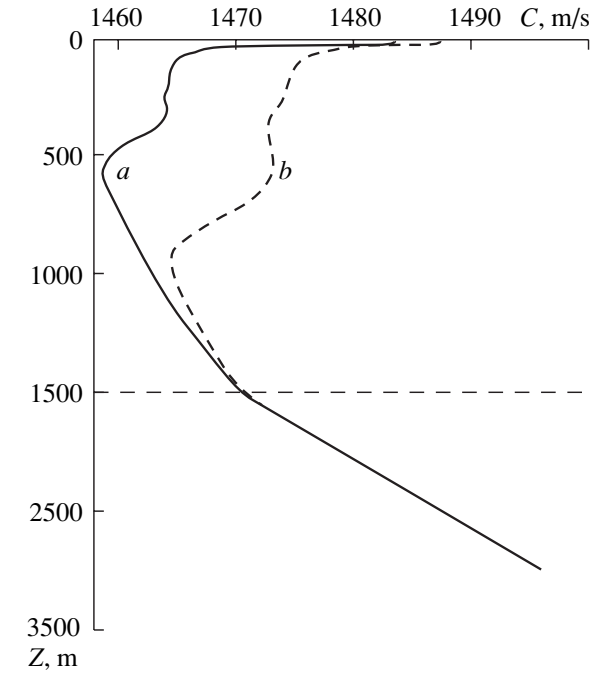

Fig. 1. Vertical sound speed profiles typical of (*a*) the Norwegian Hollow and (*b*) the Lofoten Hollow.

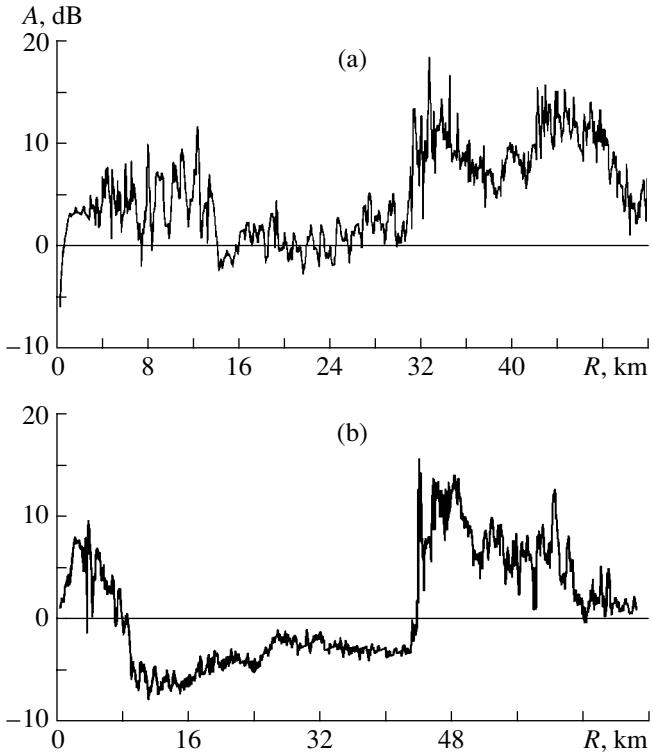

Fig. 2. Propagation anomaly versus the distance. Experimental data obtained in the regions of (a) the Norwegian Hollow (the source and receiver depths are 90 and 600 m, respectively) and (b) the Lofoten Hollow (90 and 150 m, respectively).

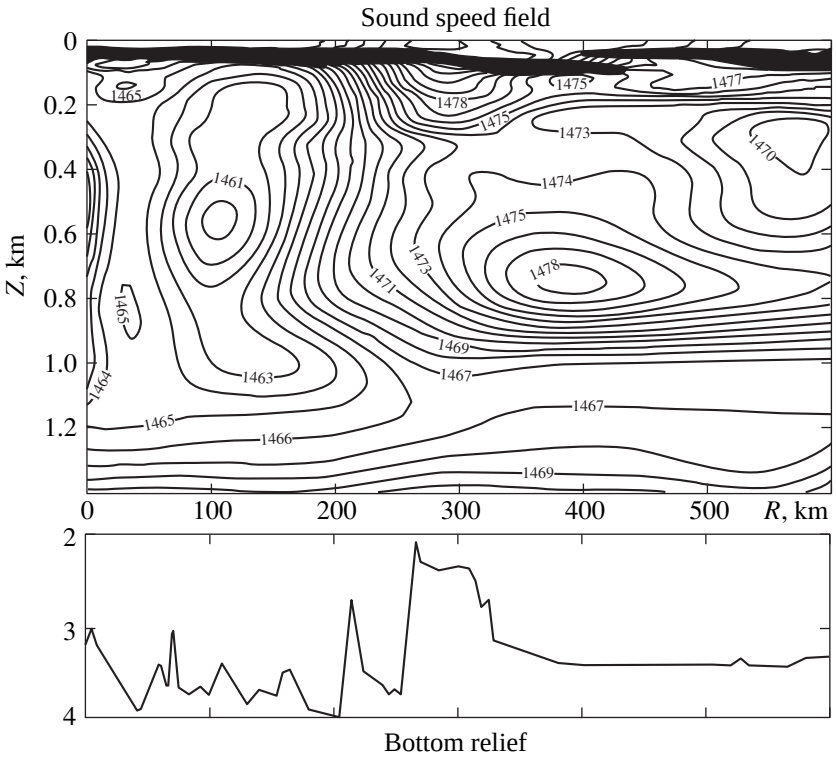

Fig. 3. Sound speed field and the bottom relief on the path of long-range propagation of explosion-generated signals. The values of the speed of sound (in m/s) are indicated by the numbers on isolines.

long ranges (more than 40–50 km), we failed to obtain good agreement between the experimental and calculated vertical structures of the sound field. But the experimental values of the propagation anomaly at the frequencies 16–250 Hz, upon being averaged over a layer of 100–200 m, agreed well with the horizontal structure of the sound field that was calculated for the 150-m receiver depth using the ray-approximation computer code developed by Vagin [4]. In analyzing the vertical structure of the sound field, a characteristic period of interference was found. In a number of measurements, the vertical structure was obtained nearly simultaneously at different frequencies. For each fixed distance from the source, the spatial interference period was inversely proportional to the frequency of transmission.

In experimenting with the explosive sound sources, the receiving vessel was drifted at 220–230 nautical miles to the north of the Faeroes. The transmitting vessel went a heading of about 45° away from the receiving one in the north-eastern direction. In these measurements, a path 650–815 km in length was surveyed. Figure 3 shows the results of echo-sounding along the propagation path. In the region of reception, the sea depth was 3000–3900 m. At a distance 200 km from the receiver (at the boundary between the Norwegian and Lofoten Hollows), a sharp bottom rise existed: the sea depth decreased from 4000 to 2700 m. At longer distances, the sea depth again increased to 3700–3850 m and did not change within the path fraction of about 50 km. Then, the sea depth sharply decreased to 2100 m and did not exceed 2400 m within the next 50-km-long fraction of the path. At longer distances, the path crossed the Lofoten Hollow.

Along the path of long-range propagation, up to ten hydrological observations were usually performed. Figure 3 shows an example of such measurements. When the distance from the reception point increases to about 150–200 km, the UWSC axis lowers from 500–600 to 1000–1100 m. At the distances longer than 150–200 km, two UWSC axes were observed. The axis depth of the second (weakly pronounced) UWSC was 250–400 m. In experimenting at the boundary between the Norwegian and Lofoten Hollows, rather sharp changes occurred in the structure of the sound speed field. The sites of the changes correlate well with those of the bottom rises determined by the echo sounding.

In experimenting on this path, the water temperature was also measured at the depths 40 to 400 m, with the use of TZO-2 expandable thermosensors. Totally, 24 sensors were dropped from the transmitting vessel, equidistantly along the path. Figure 4 presents the measured temperature field. Considerable changes in the temperature field can be seen at the distances 200–250 km. These changes are somewhat more intricate than those in the sound speed field (measured at nine points). At this part of the path, the horizontal (along the path) temperature

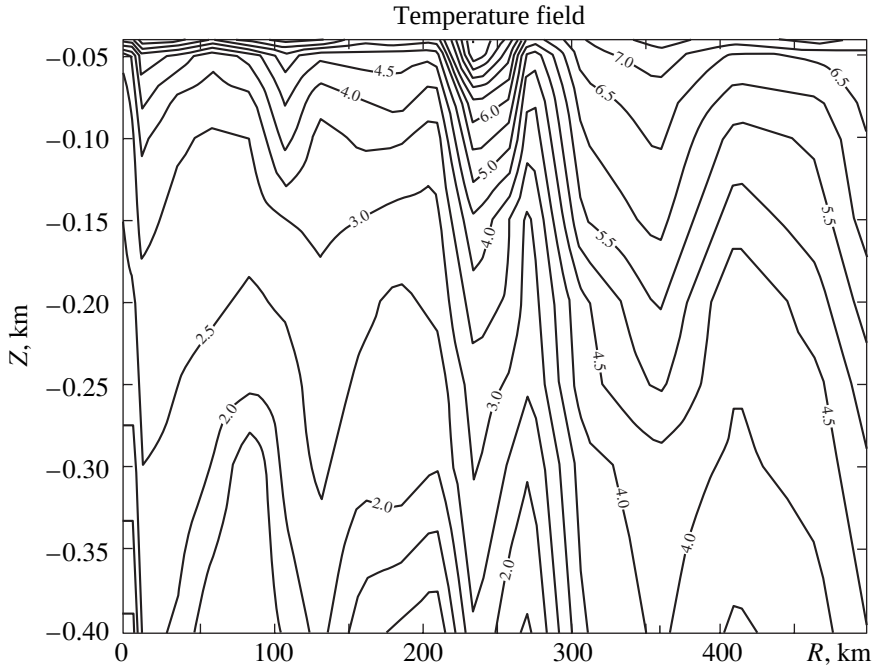

Fig. 4. Temperature field on the path of long-range propagation of explosion-generated signals, as measured by TZO-2 expandable thermosensors. The temperature values (in °C) are indicated by the numbers on the isolines.

gradients reached 0.15–0.2 deg/km at depths of 100–150 m.

According to the publications (e.g., [2]), in some regions of the Norwegian Sea, the Polar Front is observed in the form of a narrow zone of high horizontal temperature gradients. The front occurs at the boundary between the warm Norwegian and cold East-Icelandic currents. The researchers also argue that the long-standing changes in the front position can be mainly attributed to the variations in the intensity of the currents, as well as to the features of the large-scale atmospheric circulation. In the experiments performed on the same path in other years, less sharp changes in the temperature and sound speed fields were observed.

Let us consider the experimental data obtained in the environment illustrated by Figs. 3 and 4 in more detail. In total, 180 charges were exploded on the path. Pressure-sensitive detonators were used as the charges dropped from the vessel. They exploded at a depth of 300 m (with the period about 10 ms of the gas-bubble fluctuation). At the moment of each explosion, the distance between the vessels was determined by the propagation time of the sound signal. The explosion-generated signals were received by omnidirectional systems deployed to the depths 150 and 600 m. The received signals were magnetic-tape recorded. At the laboratory, the signals were reproduced and, upon preliminary filtering (the antializing filter has a 2.5-kHz cutoff frequency), converted to a digital form with 10-kHz sampling frequency by a 12-bit A/D converter.

First, the time structure of the explosion-generated signals was analyzed. Figure 5 shows this structure for the signals received at the depths 150 and 600 m, at distances 18 to 50 km from the source. All signals are normalized to their maximal levels. At the distances up to 45 km, in addition to "purely water-path" signals, signal quartets can be seen that are once reflected from the bottom (in the figure, they are the last to arrive becoming closer to the main group of the water-path signals as the distance increases). At the distances at hand, the experimental time structure of the signals agrees well with that calculated by using the computer code developed by Tebyakin [5]. The bottom-reflected signals differ from the water-path ones in their shapes and specific positions in the time structure of the total multiray signal. While the singly bottom-reflected signals have rather high amplitudes, twice and triply bottom-reflected signals (received at 50–70-km distances) become negligibly small in comparison with the water-path ones. Signals reflected from the sea surface were also observed. These signals are much more difficult to detect and identify.

Upon propagating in the UWSC, the explosion-generated signal becomes protracted in time. The extent of signal protraction is governed by the propagation conditions, which are specific for the region, that is, by the multiray character of propagation. Figure 6 presents the range dependence of the signal duration for reception depths of 150 m (dots) and 600 m (asterisks). In experimental evaluation of the signal duration, elementary bottom-reflected signals were ignored. At distances longer than 20–40 km, the signal duration at the hori-

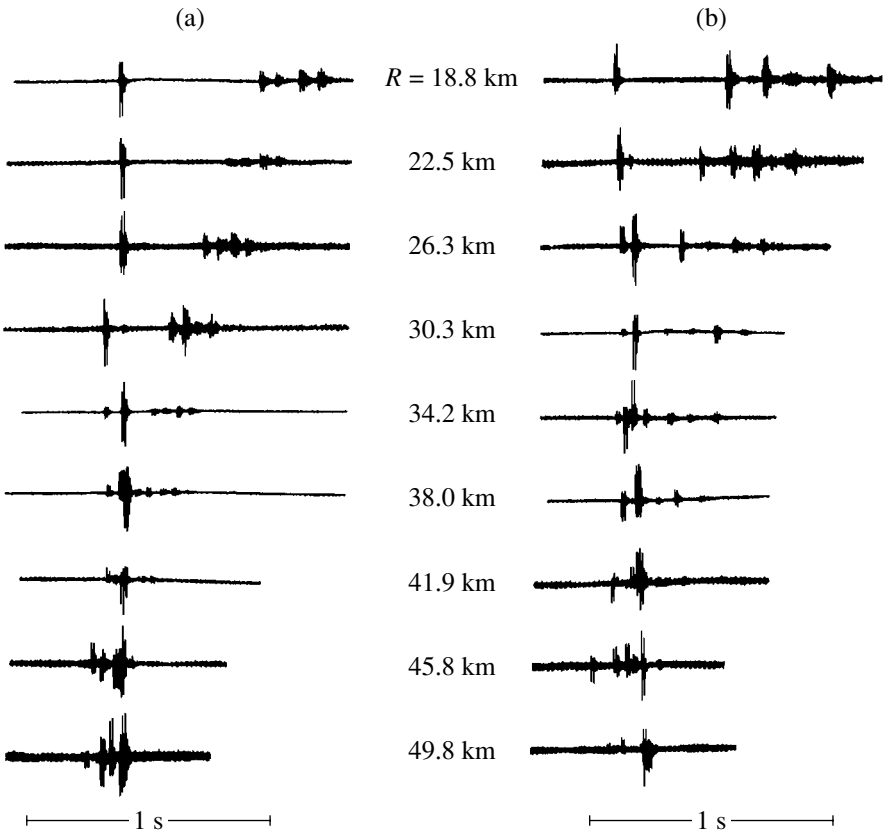

Fig. 5. Time structure of the exlosion-generated signals received at distances from 18 to 50 km with a 300-m source depth; the reception depths are (a) 150 and (b) 600 m.

zon 150 m is usually 40–60 ms lower than at 600 m. At 250–300-km distances, the range dependence of the signal duration is rather regular. With a periodicity about 43–44 km, maximums are observed that precede the bottom-caused cutoff of the signals, which most widely deviate from the UWSC axis. At distances longer than 300 km (after the path crosses the boundary between the Norwegian and Lofoten hollows), the periodicity of the maximums is violated.

At the initial fraction of the path (the region of the Norwegian Hollow), the change in the duration of the total signal is on average proportional to the distance with the proportionality factor $K = \sim 0.0015$ s/km. According to our other experiments, in other regions of the Ocean this factor is much higher (with the exception of the eastern part of the Central Atlantic) [6]. In the experiment under discussion, the depth of the sound source (300 m) differs from that of the UWSC axis. However, according to the measurements, the difference in the sound speeds was no higher than 1–2 m/s at these two horizons, which is not enough to cause a significant increase in the proportionality factor. According to the calculated time structure of the sound field in the Norwegian Hollow (including the surface-reflected signals), the theoretical value of factor K agrees well with the experimental one for 600- and 300-m reception and transmission depths, respectively. For the source depth 600 m (at the UWSC axis), the factor K proves to be only 10–20% higher.

Unfortunately, we failed to determine the factor K for the region of the Lofoten Hollow from the data of the experiment at hand. The information on the signal protraction is distorted in these data. The explosion-generated signals that arrive from this part of the path exhibit a noticeable cut-off because of the bottom rise between the two hollows.

The time of signal protraction is a fairly rough characteristic of time relations in the multiray signal. To describe the time structure of the sound field in the UWSC in more detail, Ewing and Worzel [7] proposed the so-called t–R diagram (t is the time advance for the signal propagating over an individual ray relative to the signal propagating along the UWSC axis, and this advance corresponds to the given distance R). For a classical UWSC, when the source and receiver are at the same horizons, the t–R diagram is represented by many triplets of curves. The central curve in each triplet characterizes the t–R relation for the rays that made an integer number of full cycles in space; the side curves correspond to the rays that differ from a full-cycle ray by a half-cycle. The adjacent triplets of curves differ from each other by a single full cycle.

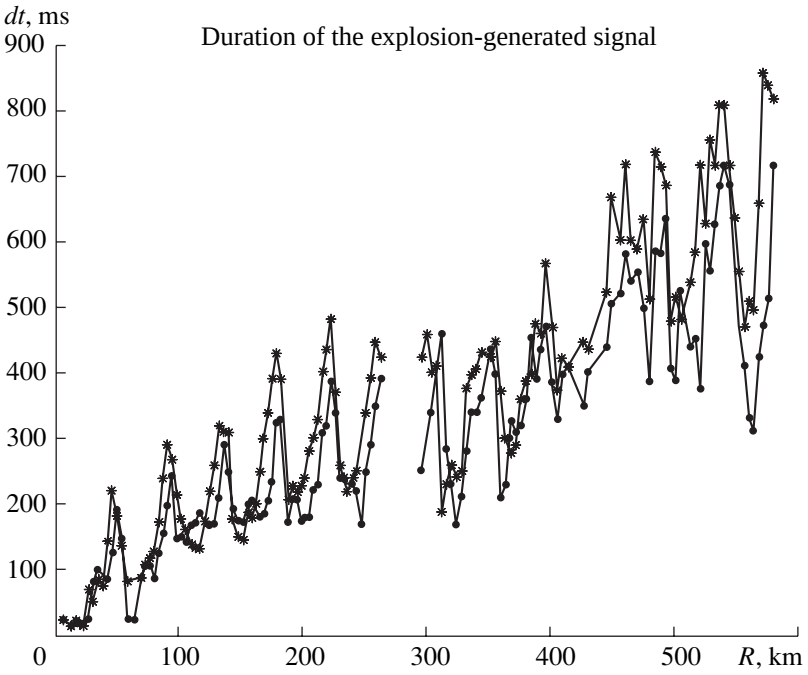

Fig. 6. Duration of the explosion-generated signal versus the distance for the reception depths 150 m (asterisks) and 600 m (dots).

Although the *t–R* diagrams are quite informative, they are rather cumbersome and not convenient for correlating the sound field structures formed in different regions of the Ocean. For this purpose, a more compact, reduced *t–R* diagram, which consists of a single curve characterizing the *t–R* relation for the rays that made a single full cycle, was proposed [8]. With the appropriate choice of the scales (t/N and R/N) for an arbitrary ray that makes an arbitrary number N of full cycles, such a curve determines the propagation times for all typical signal quartets, along with the relative delays in the arrival times for the adjacent signal quartets.

Figure 7 shows a fragment of the reduced *t–R* diagram obtained from the experiment in the Norwegian Sea. To plot the diagram, the explosion-generated signals were analyzed that arrived from the distances 10 to 225 km (the values of N varied from 1 to 5). The quartets with time-separated signals arrive from the distances that are multiples of 41–47 km. With the experimental data obtained in the Norwegian Sea, it is not easy to interpret the resulting reduced *t–R* diagram. In the multiray signals received at shorter distances from the source, in addition to the purely water-path signals, the surface-reflected ones are present that cannot always be unambiguously identified. However, the calculations showed that the signals of the typical quartets, which are well resolved at the distances 40–45, 85–90 km, and so on, are the surface-reflected ones. This fact is indirectly confirmed by the phase relations between the signals. The measured (frequency-independent) phase shift for the signals of a quartet, which differ by a single surface reflection from each other, proved to be about 180°. Thus, the *t–R* diagram obtained in the experiments under discussion differs from the diagrams presented in [8] for other regions of the Ocean in that the latter diagrams were plotted by neglecting the effect of the bottom and surface reflections on the time structure of the sound field. No quartets of time-separated water-path signals were observed in the time structure of explosion-generated signals propagating in the Norwegian Sea.

In the UWSC of the Norwegian Sea, the geometric dispersion of the signal was estimated from the data of its frequency filtering. The explosion-generated signal received from a certain distance was filtered in 1/3-octave bands that covered the 63–250 Hz range. The time structures of the signal filtered in different frequency bands were correlated for the same time intervals. Signals received from different distances were analyzed. No noticeable dispersion was detected for any of these signals. The group velocity calculations performed with the wave-approximation computer code [9] led to the same conclusion: the geometric dispersion is rather weak, if any.

From the experimental data, the coefficients of sound attenuation were estimated for the frequency band 63–630 Hz. As a rule, one determines the attenuation coefficient in the ocean by the deviation of the experimental sound field decay from the cylindrical law of the geometric spread. With explosion-generated signals, the sound field is characterized by the following

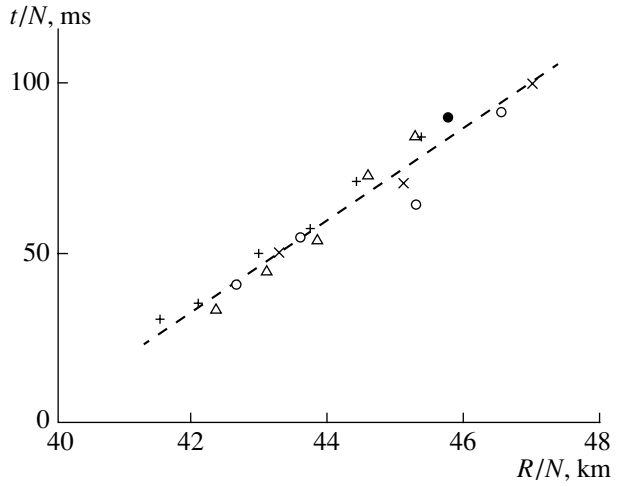

Fig. 7. Fragment of the reduced t–R diagram for the distances R/N = 41–49 km. The region of the Norwegian Hollow. The experimental values of t/N correspond to N = (●) 1, (×) 2, (○) 3, (+) 4, and (△) 5.

quantity that is equivalent to the signal energy within the frequency band Δf:

$$E_f = \int_0^T p_f^2(t)dt,$$

where T is the signal duration and $p_f(t)$ is the sound pressure in the explosion-generated signal, which is normalized to the frequency band Δf. In the computer signal processing, the equivalent quantity can be obtained from the power spectrum of the signal. For the spectral analysis of the experimental data, a set of computer codes was developed to determine the decay law of the explosion-generated signals, the attenuation coefficients at individual frequencies, and the frequency dependence of attenuation.

As a result of the signal processing performed for the signals that were received at the horizons 150 and 600 m, the laws governing the decay of the sound field levels with distance were obtained. The values of the attenuation coefficient at different frequencies were determined based on the deviations of the experimental decay curves from the cylindrical law for the path fraction 50–815 km. At frequencies higher than 400 Hz, the most distant boundary of the path was chosen from the condition of sufficiently high signal level above the noise (at least 8–10 dB). At about 200 km from the reception point, the boundary between the Norwegian and Lofoten hollows was located, at which rather sharp changes in the profile $c(z)$ took place. The signals arriving from distances longer than 200 km were partially screened by the bottom rise. The sound speed at the depth about 2400 m (corresponding to the bottom rise) were nearly the same as near the surface. In this case, only the purely water-path rays contributed to the signal energy. The signals reflected from the surface were attenuated by the additional bottom reflection (during experimentation, the wind speed was 8–12 m/s, the sea state was Beoufort 4–6).

Figure 8 shows the experimental decays for the sound field level, upon introducing corrections for the cylindrical law of geometrical spread, at the frequencies 63, 160, and 315 Hz for the 600-m receiver depth. At 80–160-km distances, a considerable (6–8 dB) increase was observed in the sound field level. For the 150-m receiver depth, a similar increase exists at the distances 250–300 km. The calculations with the use of the Vagin ray-approximation computer code [4] confirmed the experimentally observed increase in the sound field level for 80–160-km distances (with the 600-m receiver depth). It is worth mentioning that the location of this increase agrees well with the position of the core of cold waters (see Fig. 3).

In Table 1, the attenuation coefficients are summarized that are directly estimated from the deviation of the sound level decay from the cylindrical law. At frequencies higher than 400 Hz (the data marked with asterisks), the attenuation was estimated for the path fraction bounded by the 600-km limiting distance. This limitation is determined by low signal-to-noise ratios at higher frequencies.

For the signals received at the 600-m depth, an additional estimate was obtained for the sound attenuation at the path fraction bounded by the distances 200 and 815 km. In this case, the fraction between 80 and 160 km, where a local increase in the signal level occurred, was eliminated from the consideration. Here, the decay of the 63–100-Hz signals was slower than the cylindrical one. Earlier, we repeatedly observed similar deviations from the cylindrical law at low frequencies at which the sound attenuation in sea water is relatively weak. These deviations can be attributed to the redistribution of the sound energy in depth due to the range-dependent changes in the profile $c(z)$ [10]. The fact is worth mentioning that the attenuation coefficients determined from the decay law for the 600-m horizon differ on the average by 5–6 dB/km for the path fractions 50–815 and 200–815 km. This difference is nearly frequency independent and seems to be caused by nothing but the increased sound field level within the 80–160-km path fraction.

Strictly speaking, a direct determination of the attenuation coefficient by the deviation of the sound level decay from the cylindrical law is incorrect for the experiment at hand. In this case, in spite of the guided sound propagation, one cannot speak of the cylindrical law of the geometric spread: the medium deviates appreciably from a horizontally layered structure. If the medium characteristics change along the path and the law of the geometric spread cannot be established to a sufficient accuracy, one should use the so-called differential method [11] to estimate the attenuation coefficient. This method is based on two assumptions. First, the law of the geometric spread is unknown, but it is the

Table 1. Directly determined attenuation coefficients

f, Hz	Attenuation coefficient (dB/km) for a reception depth of 150 m	Attenuation coefficient (dB/km) for a reception depth of 600 m		Absorption coefficient (dB/km) calculated according to Eq. (2)
	50–815 km	50–815 km	200–815 km	
63	0.002	0.003	−0.003	0.00024–0.00026
80	0.0031	0.0036	−0.002	0.00038–0.00041
100	0.0041	0.005	−0.00015	0.0006–0.00065
125	0.0043	0.0054	0.001	0.00093–0.001
160	0.0052	0.009	0.0043	0.0015–0.0016
200	0.0078	0.010	0.005	0.0023–0.0025
250	0.0106	0.0132	0.0067	0.0035–0.0038
315	0.0115	0.0168	0.0122	0.0054–0.0058
400	0.0181*	0.0278*	0.0220*	0.0084–0.0089
500	0.0246*	0.0336*	0.0346*	0.0122–0.0130
630	0.0262*	0.0498*	0.0370*	0.0175–0.0190

same for whole frequency band under study. Second, the frequency dependence of the attenuation coefficient obeys a power law with a zero constant component. The sound levels at individual frequencies are normalized to the level at a single frequency, which is considered as a reference one. Thus, the unknown law of the geometric spread can be eliminated. From the normalized decay at each frequency, the differential attenuation coefficient is determined, and this coefficient can be shown to be equal to the difference in the values of the total attenuation coefficient at two frequencies: the frequency under analysis and the reference one. By approximating the frequency dependence of the differential attenuation coefficient by a power-law function and omitting the free term, we arrive at the following expression for the total attenuation coefficient:

$$\beta = a f^n. \quad (1)$$

This technique was first used in [12]. We implemented it in a computer code for processing the experimental data and repeatedly used it to estimate the sound attenuation in complex hydrological environments. With approximation of the sound field level (at a certain frequency) normalized to that at the reference frequency (160 Hz) by an exponential law, there no need to choose a path fraction with uniform hydrological characteristics. To estimate the attenuation coefficient with the differential method, we used the sound signals received at the distances between 50 and 650–815 km from the source. Figure 9 shows the range dependences of the experimental sound field levels normalized to the corresponding values measured at the reference frequency (160 Hz). These dependences illustrate the advantages of the differential method: the local increases in the sound field level, which are caused by the changes in the hydrological characteristics along the path, are absent in the curves.

To describe the frequency dependence of sound attenuation by Eq. (1) with the frequency measured in kilohertz and the attenuation coefficient measured in decibels per kilometer, we determined the following values of the parameters:

(i) for the 600-m reception depth, $a = 0.0524$ and $n = 0.925$;

(ii) for the 150-m reception depth, $a = 0.0438$ and $n = 0.99$.

The resulting expressions yield close values for the attenuation coefficient. Table 2 presents the attenuation coefficients determined by the differential method.

For the sake of comparison, the last columns of Tables 1 and 2 contain the absorption coefficients calculated according to the formula given in [13]:

$$\alpha = \frac{A_B f}{f/f_{rB} + f_{rB}/f} + \frac{A_{MgSO_4} f}{f/f_{rMgSO_4} + f_{rMgSO_4}/f} + K f^2, \quad (2)$$

where f is the frequency in kilohertz, $K = 1.42 \times 10^{(-8 + 1240/T)}$ dB/km kHz^2, $f_{rMgSO_4} = 1.125 \times 10^{(9 - 2038/T)}$ kHz, $A_{MgSO_4} = 62.5ST \times 10^{-6}$ dB/km kHz, $f_{rB} = 37.9S^{0.8} \times 10^{-780/T}$ kHz, $A_B = 1.65S \times 10^{(4 + 0.78\mathrm{pH} - 3696/T)}$ dB/km kHz, S is the salinity in parts per thousand, T is the temperature in Kelvin degrees, and pH is the effective value of the hydrogen ion exponent.

The first term in Eq. (2) characterizes the relaxation absorption associated with boron, the second corresponds to the relaxation absorption associated with magnesium sulfate, and the third determines the freshwater sound absorption.

In calculating the absorption coefficient for the Norwegian Sea, we specified the following parameters of

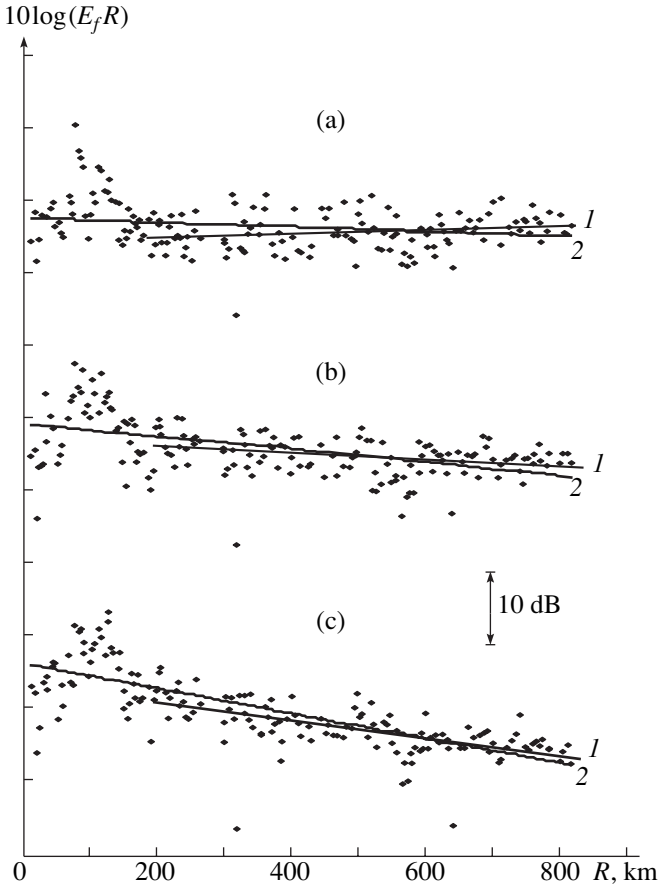

Fig. 8. Experimental decays of the sound field level corrected for the cylindrical law of the geometric spread. The reception depth is 600 m. The frequencies are (a) 63, (b) 160, and (c) 315 Hz. The decay is approximated by an exponential function for the intervals of distances from the source (*1*) 200–815 and (*2*) 50–815 km.

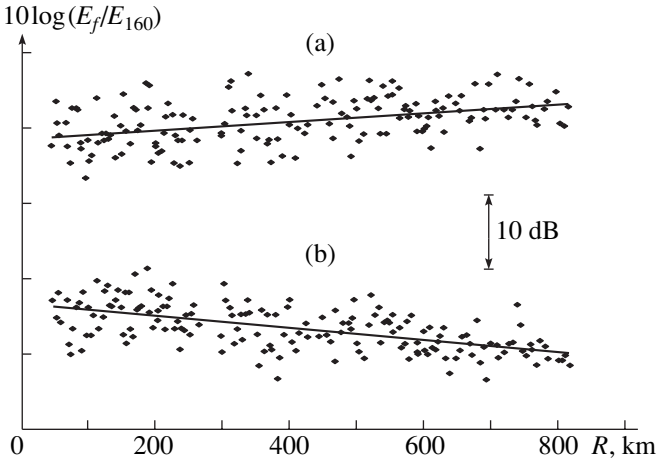

Fig. 9. Experimental decays of the sound field level normalized to the corresponding level at the reference frequency (160 Hz). The reception depth is 600 m. The frequencies are (a) 63 and (b) 315 Hz.

the water medium: T = 272.5°K, S = 35.2‰, and pH = 8.15–8.2.

For the Norwegian Sea, the experimental values of the attenuation coefficient are by a factor of 1.5–2.5 higher than the predicted values of the absorption coefficient at the frequencies 400–630 Hz and 10 to 20 timed higher than the values predicted for the low frequencies (63–100 Hz).

A possible reason for that high values of the attenuation coefficient is the sound scattering by thermal inhomogeneities like thin-layered structures in the ocean. In [14], based on the analysis of a large body of experimental data on the hydrological parameters for the north-western part of the Pacific Ocean, a conclusion is drawn that the aforementioned inhomogeneities are generated in the ocean regions that are influenced by the Kamchatka current. In such regions and in the areas that are close to them, typical limits are determined for the variations of the mean square refractive index: $\mu^2 \approx 10^{-5}$–10^{-7}.

The Norwegian Sea is strongly influenced by the cold East-Greenland Current and by a branch of the warm North-Atlantic Current. To explain the values of the attenuation coefficient obtained in our experiment for a frequency of about 500 Hz by the sound scattering from the fine-structure inhomogeneities of the medium, it is sufficient to substitute $\mu^2 \approx 10^{-7}$ into the expressions given in [15] with the vertical and horizontal inhomogeneity sizes of about 1 and 150 m, respectively.

In the literature, the fractal nature of the fine-structure inhomogeneities of the ocean is discussed. The sound scattering by such inhomogeneities leads to a power-law dependence of the low-frequency attenuation [16]. With certain parameters of a fractal, the exponent in the frequency dependence of attenuation can be obtained that agrees with the results of our experiment. The fractal parameters for the Norwegian Sea noticeably differ from those chosen earlier [11] to describe the experimental data on the sound attenuation in the Greenland Sea, for instance. This difference can be explained by nothing but the regional features of thin-layered structures (scatterers), which are responsible for the increased attenuation (in comparison with absorption) of sound in sea water.

Generalizing the analysis of experimental data described above, we can draw the conclusion that the features of sound propagation in the Norwegian Sea are fairly intricate. In particular, profound changes occur in the propagation conditions when the path crosses the boundary between the Norwegian and Lofoten hollows, these changes correlating with the bottom rise (oceanologists repeatedly observed the correlation between the positions of different ocean fronts and the bottom relief [17]). The hydrological data presented above determine the position of the front zone at the moment of experimenting with long-range propagation of the explosion-generated signals. However, these data are

Table 2. Attenuation coefficients determined by the differential method

Frequency, Hz	Attenuation coefficient (dB/km) for a reception depth of 150 m		Attenuation coefficient (dB/km) for a reception depth of 600 m		Absorption coefficient (dB/km) calculated according to Eq. (2)
	experiment	Eq. (1)	experiment	Eq. (1)	
63	0.0030	0.0028	0.0044	0.0041	0.00024–0.00026
80	0.0044	0.0036	0.0050	0.0051	0.00038–0.00041
100	0.0050	0.0045	0.0063	0.0062	0.0006–0.00065
125	0.0050	0.0056	0.0068	0.0077	0.00093–0.001
160	0.0058	0.0072	0.0103	0.0096	0.0015–0.0016
200	0.0083	0.0089	0.0115	0.0118	0.0023–0.0025
250	0.0125	0.0111	0.0145	0.0146	0.0035–0.0038
315	0.0122	0.0140	0.0182	0.0180	0.0054–0.0058
400	0.0180	0.0177	0.0229	0.0225	0.00840–0.0089
500	0.0250	0.0221	0.0273	0.0276	0.01220–0.0130
630	0.0261	0.0277	0.0338	0.0342	0.01750–0.0190

insufficient to estimate the horizontal gradients of temperature and the speed of sound in the front zone and to describe the front zone itself in detail.

The presented experimental data give an insight into the formation of the spatial and time structures and the intensity structure of the sound field in this rather peculiar region of the ocean.

The analysis of the experimental data on sound attenuation in the Norwegian Sea leads to the conclusion that the role of sound scattering by the thermal inhomogeneities of the medium (of the type of a thin-layered structure) is significant. This mechanism can override the sound absorption in the ocean medium (including the relaxation processes associated with boron). When ascribing the fractal nature to the scattering, one should take into account that the differences in the fractal parameters, which lead to certain frequency dependences of attenuation (that are different for different ocean regions), can be used to estimate the regional variability of the conditions of sound propagation in the UWSC.

ACKNOWLEDGMENTS

This work was supported by Russian Foundation for Basic Research, project no. 99-02-18359.

REFERENCES

1. V. F. Sukhoveĭ, *Seas of the Global Ocean* (Gidrometeoizdat, Leningrad, 1986).
2. B. S. Zalogin and A. N. Kosarev, *Seas* (Mysl', Moscow, 1999).
3. R. W. Firebridge and Takashi Ichie, in *Oceanographic Encyclopedia* (Gidrometeoizdat, Leningrad, 1974).
4. A. V. Vagin, *A Report of the Acoustics Institute, USSR Acad. Sci.* (Moscow, 1974).
5. V. P. Tebyakin *et al.*, *A Report of the Acoustics Institute, USSR Acad. Sci.* (Moscow, 1990).
6. R. A. Vadov, Akust. Zh. **40**, 992 (1994) [Acoust. Phys **40**, 880 (1994)].
7. M. Ewing and J. Worzel, in *Sound Propagation in the Ocean* (Inostrannaya Literatura, Moscow, 1951).
8. R. A. Vadov, Akust. Zh. **40**, 930 (1994) [Acoust. Phys. **40**, 824 (1994)].
9. K. V. Avilov, M. Yu. Galaktionov, and L. A. Ivanitskaya, in *Proceedings of UDT-94 Conference, London, 1994*.
10. R. A. Vadov, in *Problems of the Ocean Acoustics* (Nauka, Moscow, 1984), pp. 31–42.
11. R. A. Vadov, Akust. Zh. **46**, 47 (2000) [Acoust. Phys. **46**, 37 (2000)].
12. M. J. Sheehy and R. Halley, J. Acoust. Soc. Am. **29**, 494 (1957).
13. R. A. Vadov, Akust. Zh. **46**, 624 (2000) [Acoust. Phys. **46**, 544 (2000)].
14. I. D. Rostov, Candidate's Dissertation in Geography (Vladivostok, 1985).
15. Yu. P. Lysanov and I. A. Sazonov, Akust. Zh. **39**, 697 (1993) [Acoust. Phys. **39**, 366 (1993)].
16. Yu. P. Lysanov and L. M. Lyamshev, in *Proceedings of the Fourth European Conference on Underwater Acoustics, Rome, 1998*, p. 801.
17. K. N. Fedorov, *Physical Nature and Structure of Oceanic Fronts* (Gidrometeoizdat, Leningrad, 1983).

Translated by E. Kopyl

Acoustical Physics, Vol. 48, No. 1, 2002, pp. 34–38. Translated from Akusticheskiĭ Zhurnal, Vol. 48, No. 1, 2002, pp. 39–43.

Transformation of Elastic Wave Energy to the Energy of Motion of Bodies

A. I. Vesnitskiĭ† and E. E. Lisenkova

Institute of Mechanical Engineering, Nizhni Novgorod Branch, Russian Academy of Sciences, ul. Belinskogo 85, Nizhni Novgorod, 603024 Russia

e-mail: wvs@dynamo.nnov.ru

Received August 7, 2000

Abstract—The motion of a body along an elastic guide under the effect of an incident wave is considered. An equation describing the longitudinal motion of a body along an arbitrary guide is derived from the laws governing the energy and momentum variations for the case when the incident wave generates a single reflected wave. The equations that describe the motion of a body along a string and along a beam corresponding to the Bernoulli–Euler model are considered as examples. The process of the body acceleration along a beam of the aforementioned type is investigated. For the subcritical velocities, the law governing the motion of the body and the ratio of the kinetic energy variation to the energy supplied to the body are determined. *© 2002 MAIK "Nauka/Interperiodica".*

The statement that waves exert some pressure on the bodies impeding their free propagation was first formulated by L. Euler. Being an opponent of the corpuscular theory of light, in 1746, he published a paper [1] in which he explained the elongation of cometary tails observed with decreasing distance to the Sun by the pressure produced by light waves, whereas his opponents attributed this effect to the bombardment of atmosphere by particles of light. In 1873, Maxwell proposed a theoretical explanation for the effect of the wave pressure and derived a formula for calculating the pressure exerted by electromagnetic waves on a stationary obstacle [2]

$$F = \Phi/c, \tag{1}$$

where Φ is the wave energy flux and c is the propagation velocity of electromagnetic waves. Experimentally, the wave pressure was first observed by Dvorak in 1876 [3]. He insonified acoustic resonators suspended from threads and used the angles made by the threads with the vertical to measure the pressure produced by the sound waves. The results of his experiments were interpreted by Rayleigh [3], who developed the theory of sound wave pressure in the framework of the adiabatic approximation. In 1902, after the famous experiments by P.N. Lebedev [4], which revealed the pressure produced by light waves, Rayleigh and Larmor independently put forward the idea that any wave motion of any origin produces a certain pressure on the bodies that impede its free propagation [5, 6]. The studies of the pressure effect caused by mechanical waves, which were initiated by Rayleigh and Larmor, were continued by E. Nicolai. In 1912–1925, he considered a set of problems on the interaction of transverse waves excited in a string with its moving supports [7, 8].

Interest in a closer consideration of the effect of wave pressure has revived recently in connection with attempts to explain the parametric instability of the second kind in systems with moving supports [9, 10], as well as the effects of wave formation in the presence of loads moving along elastic guides [11]. It was found that the energy required for the excitation of pulses in the first case and the wave generation in the second is taken from the energy of the translational motion of the supports and the loads, respectively, and that this energy transformation occurs via the force caused by the pressure of waves [12]. The problem of taking into account the pressure of waves is especially important for the design and use of railroads [13]. When a train moves with a speed 200 km/h or higher, elastic waves can be excited in the railway bed and in the surrounding ground [14, 15]. The pressure produced by these waves makes the major contribution to the tractive resistance.

Let us estimate the pressure exerted by waves of different physical origins on a stationary obstacle. If the obstacle absorbs the incident wave, the pressure will be determined by Eq. (1), where $c = \omega/k$ is the phase velocity, ω is the frequency, k is the wave number, and Φ is the wave source power, provided that the whole wave energy flux generated by the source is incident on the obstacle. The corresponding estimates are presented in the table. To make the comparison more convenient, for all kinds of waves given in the table, the source powers are assumed to be identical and equal to 10^4 W.

Evidently, the pressure produced by low-frequency gravity waves, as well as by transverse waves in beams, chains, crawler belts, and plates, is comparable with the

† Deceased.

forces that drive the machines. This explains the interest by researchers in the development of machines and mechanisms based on the wave motion concept, including those transforming the wave energy to the translational energy of bodies.

Let us consider the motion of a body of mass m along an elastic guide (Fig. 1) under the effect of pressure produced by a wave incident on this body. If the body does not move in the transverse direction, the wave does not penetrate behind it, and we can consider the case of perfect reflection. Then, the problem under study can be identified with the problem of a collision of two bodies. One of them is represented by the body moving along the elastic guide, and the other is represented by the wave, which can be characterized by the wave momentum [12]. We assume that the incident wave generates a single reflected wave propagating in the direction opposite to that of the incident wave. For such an interaction, the laws governing the energy and momentum variations have the following differential form:

$$\begin{aligned} d\varepsilon_0 - d\varepsilon &= mvdv + Fdl, \\ dp_0 - dp &= mdv + Fdt. \end{aligned} \tag{2}$$

Here, $v = \dot{l}(t)$ is the velocity of travel of the mass m; $dl = vdt$; ε_0 and p_0 are the energy and momentum of the incident wave; ε and p are the energy and momentum of the reflected wave; and F is the friction force, which has the form

$$F = F_0 \operatorname{sgn} v + \delta v, \tag{3}$$

where F_0 and δ are the constants characterizing dry and viscous friction, respectively.

We assume that the wave incident on the body has the frequency ω_0, and the frequency of the reflected wave ω varies slowly so as to satisfy the condition

$$|d\omega/dt| \ll \omega^2. \tag{4}$$

In this case, the energy and the wave momentum averaged over the period are related as follows [16]:

$$\varepsilon_0 = c_0 p_0, \quad \varepsilon = cp, \tag{5}$$

where $c_0 = \omega_0/k_0$ and $c = \omega/k$ are the phase velocities of the incident and reflected waves, respectively.

Assuming that relationships (5) are also valid in the small, from Eqs. (2) we obtain the following equation describing the motion of the body along the guide:

$$m\frac{dv}{dt} = \frac{(c + c_0)}{c_0(c + v)}\frac{d\varepsilon_0}{dt} - F. \tag{6}$$

We note that, in deriving Eq. (6), instead of the law governing the momentum variation, one can use the so-called law of conservation of the number of wave energy quanta, which has the form $\varepsilon/\omega = \varepsilon_0/\omega_0 = \text{const}$ in the case of a perfect reflection with a single reflected wave [16], and the law of the double Doppler effect,

Table

Waves	Velocity c, m/s	Pressure F, N
Electromagnetic waves in vacuum	3×10^8	3.3×10^{-5}
Sound waves in metal	5×10^3	2
Sound waves in air	3×10^2	3.3×10^1
Low-frequency gravity waves	10^{-1}–1	10^4–10^5
Low-frequency transverse waves in beams, chains, crawler belts, and plates	1–10	10^3–10^4

which relates the frequencies of the incident and reflected waves.

To calculate the possible types of motion of bodies under the forces caused by the elastic wave pressure, it is convenient to preset either the wave source power Φ_0 when the wave is fed by a force source or the wave energy density h_0 when the wave is fed by a displacement source. Taking into account that the wave energy flux incident on a moving body is equal to $(\Phi_0 - vh_0)|_{x = l(t)}$ and the wave flux through a stationary cross-section (i.e., the source power Φ_0) is related to the wave energy density h_0 by the formula $\Phi_0 = v_{gr}h_0$, where $v_{gr} = \left.\frac{d\omega}{dk}\right|_{\omega = \omega_0}$ is the wave energy flow velocity (i.e., the group velocity of the incident wave), we obtain the expression

$$d\varepsilon_0 = (1 - v/v_{gr})\Phi_0|_{x = l(t)}dt = (v_{gr} - v)h_0|_{x = l(t)}dt.$$

Then, Eq. (6) can be represented in the form

$$\begin{aligned} m\frac{dv}{dt} &= \frac{(c + c_0)}{c_0(c + v)}(1 - v/v_{gr})\Phi_0|_{x = l(t)} - F \\ &= \frac{(c + c_0)}{c_0(c + v)}(v_{gr} - v)h_0|_{x = l(t)} - F. \end{aligned} \tag{7}$$

Equation (7) is derived under the natural assumption that the incident wave catches up with the moving body, i.e., $v_{gr} > v$. Otherwise, no interaction will occur between the body and the wave.

To determine the group and phase velocities involved in Eq. (7), it is necessary to know the dependence of the frequency on the wave number. This dependence is obtained either from the dynamic equa-

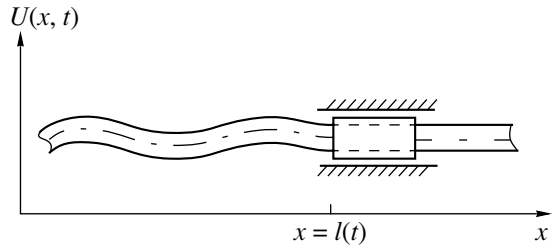

Fig. 1. Motion of a mass along an elastic guide.

tion of the elastic guide in the form of the dispersion equation

$$f(\omega, k) = 0, \tag{8}$$

or from the experiment. It is necessary to take into account that the frequency and the wave number of the incident wave are related to the frequencies and wave numbers of the secondary (reflected and transmitted) waves:

$$\omega - vk = \omega_0 - vk_0. \tag{9}$$

This relationship expresses the condition that the frequencies of all secondary waves are equal to the frequency of the incident wave in the moving coordinate system ($x' = x - vt$, $t' = t$). Among all solutions to the system of equations (8) and (9), only those corresponding to the energy flow away from the moving body, i.e., those with the group velocity satisfying the condition $d\omega/dk < v$, will describe the reflected waves.

The first term on the right-hand side of Eq. (7) represents the force caused by the wave pressure (F_{pr}), the presence of which was first mentioned in [5–7]. It can easily be shown that, in the case of total reflection [for which Eq. (7) was derived], this force is proportional to the reflection coefficient (Φ_1/Φ_0) at the boundary [17]:

$$F_{pr} = \frac{v_{gr}h_0(c + c_0)}{c(c_0 - v)}(1 + v/v_{gr1})\frac{\Phi_1}{\Phi_0}. \tag{10}$$

Here, Φ_1 is the reflected energy flux and v_{gr1} is the group velocity of the reflected wave.

If we choose the guide in the form of a string for which $c = c_0 = d\omega/dk = \omega_0/k_0 = \sqrt{N/\rho}$ (where N is the string tension and ρ is the density per unit length of the string), Eq. (7) will take the form of the equation derived in [12] from the corresponding nonlinear boundary-value problem

$$m\frac{dv}{dt} = 2\frac{c_0 - v}{c_0 + v}h_0 - F.$$

The solution of this equation was studied in detail in [18–20].

Let us consider the transformation of the flexural wave energy to the energy of the motion of bodies. For this purpose, we choose the guide in the form of a beam corresponding to the Bernoulli–Euler model.[1] Transverse vibrations of such a beam are described by the equation

$$\gamma u_{xxxx} + \rho u_{tt} = 0,$$

where γ is the flexural rigidity of the beam and ρ is its density per unit length. Representing the solution to this equation in the form $u(x, t) = u_0\cos(\omega t - kx + \varphi_0)$ (where u_0 and φ_0 are constant values), we obtain the following dispersion equation [Eq. (8)] for flexural waves [23]:

$$\gamma k^4 - \rho\omega^2 = 0. \tag{11}$$

From this equation, we obtain

$$v_{gr} = 2c_0, \quad c_0 = (\gamma/\rho)^{1/4}\omega_0^{1/2},$$

where ω_0 is the frequency of the incident wave. Solving Eqs. (9) and (11) in combination, we find that, in the velocity interval $v_1 < v < v_2$ (where $v_1 = -2(\sqrt{2} + 1)c_0$ and $v_2 = 2(\sqrt{2} - 1)c_0$), a near-boundary oscillation and a travelling reflected wave whose phase velocity is $c = c_0 - v$ must occur. In all other cases, the number of reflected waves is greater, and these cases are beyond the scope of our paper.

As for the wave energy transferred by the incident wave, with allowance for Eq. (11), its density can be represented as $h_0 = \frac{1}{2}(\rho u_t^2 + \gamma u_{xx}^2) = \frac{1}{2}\rho\omega_0^2u_0^2 = \text{const}$. Then, from Eq. (7), we obtain

$$m\frac{dv}{dt} = \left(2 - \frac{v}{c_0}\right)^2 h_0 - F$$

$$\left(-2(\sqrt{2} + 1) < \frac{v}{c_0} < 2(\sqrt{2} - 1)\right).$$

Let us consider the solution of this equation for some particular cases. First, we assume that the friction force is negligibly small ($F = 0$). Then, after integrating the equation $dv/dt = (2 - v/c_0)^2h_0/m$ with allowance for the initial condition $v(0) = v_0$, we derive

$$v = v_0 + 2\frac{h_0}{m}\left(2 - \frac{v_0}{c_0}\right)t\Big/\left[1 + \frac{h_0}{mc_0}\left(2 - \frac{v_0}{c_0}\right)t\right]. \tag{12}$$

From this expression, it specifically follows that the longitudinal component of the beam reaction to the body (the wave pressure) is equal to

$$F_{pr} = \left(2 - \frac{v_0}{c_0}\Big/\left[1 + \frac{h_0}{mc_0}\left(2 - \frac{v_0}{c_0}\right)t\right]\right)^2 h_0.$$

The subsequent integration yields the law that governs the motion of the body

$$l(t) = 2c_0t - \frac{mc_0^2}{h_0}\ln\left|1 + \frac{h_0}{mc_0}\left(2 - \frac{v_0}{c_0}\right)t\right| + l(0).$$

Since we consider the interval $-2(\sqrt{2} + 1) < \frac{v}{c_0} < 2(\sqrt{2} - 1)$, the time within which the above formulas are valid is as follows:

$$t < t^* = 2(\sqrt{2} - 1) - \frac{v_0}{c_0}\Big/\left[\frac{2\sqrt{2}h_0}{mc_0}\left(2 - \frac{v_0}{c_0}\right)(\sqrt{2} - 1)\right].$$

[1] This model is widely used in mechanics [21, 22]. However, the attention is usually concentrated on the dynamic behavior of the system under the effect of moving loads or on the interaction of flexural waves with fixed supports.

Taking into account that the energy supplied to the moving mass is equal to

$$\varepsilon_0 = \int_0^t (S_0 - vh_0)dt = h_0 \int_0^t (2c_0 - v)dt$$
$$= mc_0^2 \ln\left|1 + \frac{h_0}{mc_0}\left(2 - \frac{v_0}{c_0}\right)t\right|,$$

from Eq. (12) we obtain $v = 2c_0 + (v_0 - 2c_0)\exp\left(-\frac{\varepsilon_0}{mc_0^2}\right)$. The dependence corresponding to this formula is shown in Fig. 2.

We can also calculate the ratio of the kinetic energy variation to the energy supplied to the body, i.e., the efficiency $\eta = m(v^2 - v_0^2)/(2\varepsilon_0)$ $(t < t_*)$. Setting $v_0 = v(0) = 0$ and taking into account Eq. (12), we determine the acceleration efficiency $\eta = 8h_0^2 t^2 / \left[m^2 c_0^2 \left(1 + \frac{2h_0 t}{mc_0}\right)^2 \ln\left|1 + \frac{2h_0 t}{mc_0}\right| \right]$, where $t < t_*$. Expressing it through the energy of the incident wave, we obtain

$$\eta = 2\left(\exp\left(\frac{\varepsilon_0}{mc_0^2}\right) - 1\right)^2 / \left[\frac{\varepsilon_0}{mc_0^2}\exp\left(\frac{2\varepsilon_0}{mc_0^2}\right)\right].$$

Figure 3 represents the dependence of the efficiency on the reduced energy of the incident wave. One can see that, for the case under consideration, the efficiency does not exceed 0.7. All solutions are obtained within approximation (4)

$$mc_0\omega_0\left(1 - \frac{v}{c_0}\right)^3 / \left[2h_0\left(2 - \frac{v}{c_0}\right)^2\right] \gg 1$$
$$\left(\frac{v}{c_0} < 2(\sqrt{2} - 1)\right).$$

The presence of the friction force given by Eq. (3) leads to the existence of several types of motion [18]. If the force caused by the wave pressure is smaller than the friction force, the motion of the object will terminate within a finite time interval. If these forces are comparable, the motion will be intermittent. Finally, the motion of the object will be continuous if the force acting on it is sufficiently strong. For the latter case, in the framework of the approximation specified above, we obtain

$$v = c_0\sqrt{K}\frac{1 + A_1\exp(2\beta t)}{1 - A_1\exp(2\beta t)} + 2c_0 + \frac{c_0^2\delta}{2h_0},$$
$$l(t) = c_0\left(\left(2 + \frac{c_0\delta}{2h_0} + \sqrt{K}\right)t - \frac{\sqrt{K}}{\beta}\ln\left|\frac{1 - A_1\exp(2\beta t)}{1 - A_1}\right|\right).$$

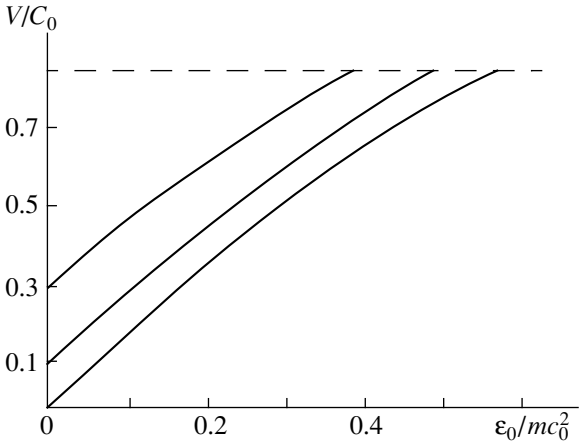

Fig. 2. Dependence of the velocity of travel of a mass on the energy of the incident wave for different initial conditions.

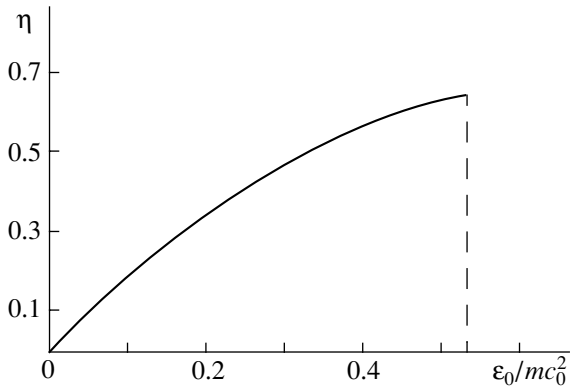

Fig. 3. Qualitative dependence of the efficiency on the reduced energy of the incident wave.

Here, $A_1 = 2 - \frac{v_0}{c_0} + \frac{c_0\delta}{2h_0} + \sqrt{K} / \left[2 - \frac{v_0}{c_0} + \frac{c_0\delta}{2h_0} - \sqrt{K}\right]$, $K = \frac{c_0^2}{4}\left(\frac{8}{c_0} + \frac{\delta}{h_0}\right)\frac{\delta}{h_0} + \frac{F_0}{h_0}$, and $\beta = \frac{h_0\sqrt{K}}{mc_0}$.

Thus, for distributed systems with objects moving along them, it is possible to determine some important quantities from the laws governing the energy and momentum variations without solving the corresponding nonlinear boundary-value problems.

ACKNOWLEDGMENTS

This work was supported by the Russian Foundation for Basic Research (project no. 00-01-00344) and the Federal Special-Purpose Program Integratsiya.

REFERENCES

1. L. Euler, *Historie de l'Académie Royale* (Berlin, 1746), Vol. 2, p. 117.

2. J. C. Maxwell, Selected Works on the Electromagnetic Field Theory (Inostrannaya Literatura, Moscow, 1954).
3. J. W. Strutt (Lord Rayleigh), *The Theory of Sound*, 2nd ed. (Macmillan, London, 1896; GITTL, Moscow, 1944), Vol. 2.
4. P. N. Lebedev, *Light Pressure* (Akad. Nauk SSSR, Moscow, 1963), pp. 368–390.
5. D. Rayleigh, Philos. Mag., Ser. 6, **3** (15), 338 (1902).
6. I. Larmor, *Radiation*, in *Encyclop. Br.* (1902), Vol. 32.
7. E. L. Nicolai, Izv. S.-Peterb. Politekh. Inst. **18** (1), 49 (1912).
8. E. L. Nicolai, Philos. Mag., Ser. 6, **49**, 171 (1925).
9. A. I. Vesnitskiĭ and A. I. Potapov, Prikl. Mekh. **11** (4) (1975).
10. A. I. Vesnitskiĭ and S. V. Krysov, Pis'ma Zh. Tekh. Fiz. **3** (19), 1032 (1977) [Tech. Phys. Lett. **3**, 423 (1977)].
11. A. I. Vesnitskiĭ, S. V. Krysov, S. A. S'yanov, and G. A. Utkin, Preprint No. 160, NIRFI (Radiophysical Research Inst., Gorki, 1982).
12. A. I. Vesnitskiĭ, L. É. Kaplan, and G. A. Utkin, Prikl. Mat. Mekh. **47** (5), 863 (1983).
13. A. I. Vesnitskiĭ and A. V. Metrikin, Usp. Fiz. Nauk **166** (10), 1044 (1996) [Phys.–Usp. **39**, 983 (1996)].
14. A. V. Metrikine and K. Popp, Eur. J. Mech. A/Solids **18** (4), 679 (1999).
15. A. S. J. Suiker, A. V. Metrikine, and R. de Borst, J. Sound Vibr. **240**, 1 (2001).
16. A. I. Vesnitskiĭ and E. E. Lisenkova, Akust. Zh. **41**, 209 (1995) [Acoust. Phys. **41**, 178 (1995)].
17. M. B. Vinogradova, O. V. Rudenko, and A. P. Sukhorukov, *The Theory of Waves* (Nauka, Moscow, 1979).
18. A. I. Vesnitskiĭ and G. A. Utkin, Dokl. Akad. Nauk SSSR **302** (2), 810 (1988).
19. E. E. Lisenkova and S. B. Malanov, Izv. Ross. Akad. Nauk, Mekh. Tverd. Tela, No. 5, 45 (1995).
20. N. V. Derendyaev and I. N. Soldatov, Prikl. Mat. Mekh. **61** (4), 703 (1997).
21. M. Ichikowa, Y. Miyakowa, and A. Matsuda, J. Sound Vibr. **230**, 493 (2000).
22. G. V. Rao, Trans. ASME, J. Vibr. Acoust. **122** (3), 281 (2000).
23. *Vibration in Engineering*, Ed. by V. V. Bolotin (Mashinostroenie, Moscow, 1978), Vol. 1.

Translated by E. Golyamina

Acoustical Physics, Vol. 48, No. 1, 2002, pp. 39–45. Translated from Akusticheskiĭ Zhurnal, Vol. 48, No. 1, 2002, pp. 44–51.

Correlation Structure of the Sound Field Produced in a Deep Ocean by a Near-Surface Sound Source

O. P. Galkin and S. D. Pankova

Andreev Acoustics Institute, Russian Academy of Sciences, ul. Shvernika 4, Moscow, 117036 Russia

e-mail: bvp@akin.ru

Received December 28, 2000

Abstract—Experimental data obtained by studying the sound field produced in the first and second convergence zones by an omnidirectional pseudonoise source operating in the kilohertz frequency range at a depth of ~10 m are presented. The measurements of the cross correlation and the time spectra are performed for the signals received from different directions in the vertical plane by one narrow-beam, 40-m array and by two such arrays with the array centers positioned at different depths (200 and 450 m). The results of the experiments show that, for the signals arriving over different ray paths, the cross-correlation coefficients and the fluctuations of the time spectra obtained by using the reception at one depth and at two different depths are practically identical. © *2002 MAIK "Nauka/Interperiodica".*

To predict theoretically the sound field structure in different parts of the oceanic waveguide so as to obtain the sound field characteristics close to reality is a rather difficult task, especially in the complex acoustic conditions of the oceanic medium. In this connection, the need arises in reliable experimental measurements and in the comparison of their results with the corresponding calculations. Recently, the interest of many researchers in experiments of this kind has quickened [1–3]. In particular, full-scale measurements were carried out near caustics and at large distances from the source with the use of large-aperture vertical arrays. However, such measurements are usually performed with pulsed signals whose carrier frequencies are about several tens or hundreds of hertz. For these frequencies, the design of narrow-beam arrays with low enough sidelobe levels to study the fine structure of the sound field (e.g., the angular and time spectra of the received signals) is highly complicated, if not impossible. We note that the angular spectrum is understood as a set of the arrival angles of the signal in the vertical plane, and the time spectrum is a set of the differences in the arrival times of one signal by different rays paths.

In our previous publications [4–7], we studied the cross-correlation and spectral characteristics of broadband pseudonoise signals in the kilohertz frequency band in the case of their reception by narrow-beam vertical arrays (with a main lobe width of ~2° at the mean frequency) in different situations. For example, we studied the fine structure of the sound field at large distances from the source for a single reception point (in multipath propagation conditions) and for reception points spaced at several tens of kilometers along the acoustic track, in the regions of the sound field caustics and in their vicinities, in the presence of considerable space-time variations of the sound velocity because of the Gulf Stream, and even in the case of the signal reception at the points lying in different oceans with the use of the data recorded in different years.

In this paper, we consider the variability of the correlation characteristics and the time spectra of signals received at relatively large depths (200–450 m) from a near-surface omnidirectional source of sound lying at a depth of about 10 m. In this situation, unlike the case of a large transmission depth, even in the underwater sound channel conditions, the characteristics of the signals can be strongly affected by the agitated ocean surface and by the source depth variations due to the roll of the transmitting ship. Thus, in the situation under study, the correlation and spectral characteristics of the received signals can depend not only on the sound scattering by random inhomogeneities of the water column, but also on the scattering by the agitated ocean surface.

To estimate the effect produced by the inhomogeneities of the refractive index of the water column on the fluctuations of the time of signal propagation $(\sigma_\tau)_1$ over the water ray paths, i.e., along the rays that undergo no surface or bottom reflections, one can use the formula [8]

$$(\sigma_\tau)_1 = \left(\frac{\pi^{1/2}}{2c^2}\langle\mu^2\rangle\bar{a}r\right)^{1/2},$$

where $\langle\mu^2\rangle$ is the mean square fluctuation of the refractive index, $\bar{a}$ is the mean diameter of random inhomogeneities on the acoustic track, c is the velocity of sound, and r is the distance. We note that this formula yields the upper estimate, because it is derived on the assumption that the inhomogeneities of the medium occur along the whole propagation path of the signal, both in the upper layers of the ocean and in the deep

water layers. If we assume that the whole waveguide is filled with large inhomogeneities characterized by the size $\bar{a} = 115$ m and the maximal value $\langle\mu^2\rangle = 270 \times 10^{-10}$, the calculation by the aforementioned formula yields the value $(\sigma_\tau)_1 < 0.3$ ms for the distances within ~55–70 km, which are considered in this study. Taking into account that the dimensions of the inhomogeneities and the mean square fluctuation of the refractive index vary with depth (in the upper layers of the ocean, $\bar{a} = 1.5$–1.9 m and $\langle\mu^2\rangle = (16$–$22) \times 10^{-10}$, whereas in the lower layers, $\bar{a} = 110$–115 m and $\langle\mu^2\rangle = (100$–$270) \times 10^{-10}$ [9]) and, hence, different kinds of inhomogeneities occur on the signal propagation path (because of the vertical refraction), we can take the equivalent size of random inhomogeneities throughout the propagation path to be $\bar{a} \cong 40$ m and the mean square fluctuation to be $\langle\mu^2\rangle = 50 \times 10^{-10}$ [10]. Then, we obtain the estimate $(\sigma_\tau)_1 < 0.07$ ms. Thus, for the distances under consideration, the inhomogeneities of the water column should not cause any noticeable changes in the time spectra or any decorrelation of signals received at different angles in the vertical plane.

Since, in the experiment, the source of sound was submerged to a small depth (~10 m), a much stronger effect on the cross correlation of signals and on the temporal variations of the time spectra should be produced by the agitated ocean surface. Therefore, we estimate the possible mean square fluctuations of the propagation time due to the signal reflection from the surface, $(\sigma_\tau)_2$, by the formula for the variance [11]

$$(\sigma_\tau)_2^2 = 4N\frac{\sin^2\alpha}{c_0^2}\left\{\sigma^2 + \frac{2\gamma^4}{r_\alpha^2}\right.$$

$$\left.\times\left[r_{2\alpha}^2 r_{3\alpha}^2 + \frac{N^2-1}{12}D_\alpha^2\left(r_\alpha^2 - 6r_{2\alpha}r_{3\alpha} + \frac{3N^2-7}{20}D_\alpha^2\right)\right]\right\}.$$

Here, N is the number of reflections from the upper boundary of the waveguide; α is the grazing angle formed by a ray and the flat (unperturbed) surface; c_0 is the sound velocity near the surface; σ^2 and γ are the variance of the displacements and the rms slope angle of the surface, respectively; D is the ray cycle length; r is the source–receiver distance along the ray at no swell; $r_2 = r_h + (N-1)D/2$ and $r_3 = r_z + (N-1)D/2$, where r_h and r_z are the horizontal projections of the ray taken between the reflection point and the source and between the reflection point and the receiver, respectively; and the subscript α indicates a derivative with respect to the angle α.

For a wind speed of 6–7 m/s and wind waves of about Beaufort 3 (rms displacement of the water surface $\sigma \cong 0.19$–0.26 m), the estimate of the rms slope angle of the rough surface γ by the formulas given, e.g., in [12] yields a value of about 0.6°–0.7°. The calculation of $(\sigma_\tau)_2$ by the formula presented above shows that (see, e.g., [11]), for the distances 50–70 km, the rms fluctuations of the difference in the signal arrival times corresponding to different ray paths do not exceed 1–1.5 ms, even when the grazing angle of the incident sound wave (relative to the flat surface) is ~10°.

The change that occurs in the frequency spectrum of a signal at its reflection from the rough surface should cause a decorrelation of signals propagating over different ray paths. However, a number of experimental studies [4, 6, 7] provide (in the case of a small number of reflections) correlation coefficients no less than 0.4 and variations of the time spectra no greater than 1.6 ms, even for a Rayleigh parameter close to unity. In the case of a near-surface sound source, the decorrelation presumably should be greater because of the stronger effect of the source depth variation due to the roll of the transmitting ship.

The experiment was carried out in a deep-water region of the Atlantic Ocean (sea depth $H = 5180$ m) in March 1980 by the research ships *Petr Lebedev* and *Sergeĭ Vavilov*.[1] The transmitting ship was maintained at a fixed point by an electrical motor, and the receiving ship lay to. As a result, the distance between the ships varied steadily from 58 to 66 km during the measurements in the first convergence zone and from 119 to 126 km during the measurements in the second convergence zone.

The hydrological conditions were characterized by the sound velocity profile $c(z)$ shown in Fig. 1a, and the weather conditions were characterized by wind speed 5–6 m/s and wind waves corresponding to Beaufort 2–3 (rms height of waves was ~0.1–0.19 m). A continuous pseudonoise signal was generated in the frequency band 0.8–1.3 kHz at a source depth of ~10 m. The signal was received by two 40-m vertical arrays whose centers were at the depths 200 and 450 m. Each of these arrays consisted of 296 hydrophones, which were combined into 74 nonequidistant centers, and had an outer diameter of 5 cm. The signals intended for the cross-correlation processing were simultaneously received by two directional patterns formed by either one or two arrays. The deviation of the arrays, which had ~700 kg weights at their ends, from vertical was controlled by special clinometers or estimated by the difference in the arrival angles of the signals, one of which was reflected from the bottom and the other from the bottom and the surface. During the experiments, the deviation from vertical did not exceed ±1°. The angular resolution of the arriving signals in the vertical plane was ~2° at the mean frequency of the aforementioned frequency band, and the resolution in the arrival time was 2 ms.

The sound field produced by a near-surface sound source is known to be characterized by narrower convergence zones (all other conditions being equal). However, when the signals are received in these zones,

[1] The unique set of transmitting and receiving systems used in the experiment was developed under the supervision of A.M. Dymshits at the Morfizpribor Central Research Institute.

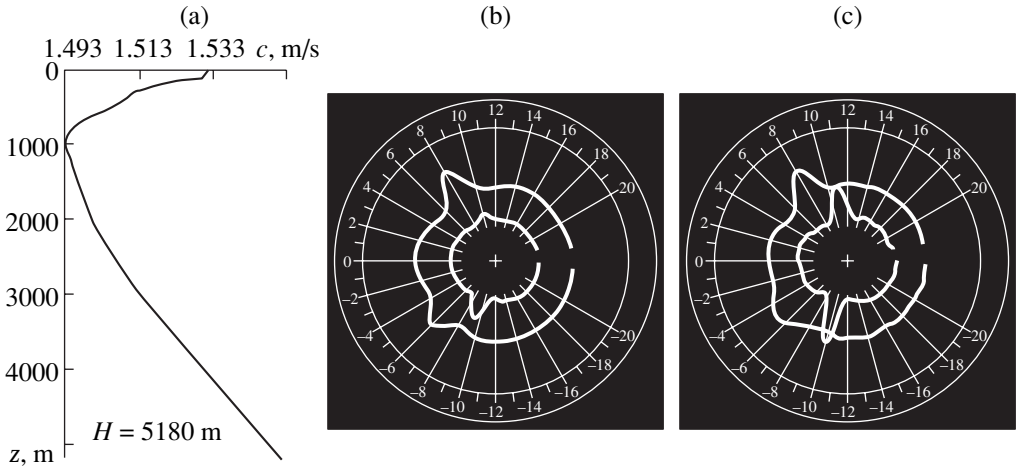

Fig. 1. (a) Sound velocity profile $c(z)$ and (b, c) the angular spectra of the sound field [in the middle of the (b) first and (c) second convergence zones].

they can arrive at the depths specified above both from below (by rays with negative arrival angles) and from above (by rays with positive arrival angles).

Figures 1b and 1c present the angular spectra of signals received at different depths in the middle of the first and second convergence zones. The photographs showing the responses of the arrays to the arriving signals were made using a sector scan indicator in the beam scanning mode within the angular range ±20°C, which was "stretched" on the screen to approximately 310°C. The outer and inner scans refer to the reception depths 200 and 450 m, respectively. At both reception depths, signals with both positive and negative arrival angles α were observed. In the middle of the first convergence zone, the signals arrived at the angles $\alpha_1 = +8°$ and $\alpha_2 = -6°$ for $z = 200$ m and $\alpha_1 = +10°$ and $\alpha_2 = -9°$ for $z = 450$ m; in the middle of the second convergence zone, the arrival angles were $\alpha_1 = +8°$ and $\alpha_2 = -5°$ for $z = 200$ m and $\alpha_1 = +11°$ and $\alpha_2 = -10°$ for $z = 450$ m. It should be noted that from the response at the indicator, i.e., from the dependence of the amplitude on the angle in the vertical plane, one can derive information not only on the direction of the arriving signals, but, based on the width of the response, also on the number of signals received from a given direction. If the width of the response does not exceed ~2°, i.e., corresponds to the main lobe width of the array, the arriving signal can be naturally considered as a single-ray one. Otherwise, there is reason to believe that there are several signals that arrive along this direction to the reception point with their arrival angles being unresolved by the array.

The signal processing provided the values of the cross-correlation coefficient $|R|$ for the signals simultaneously received by the directional patterns of one or two arrays aimed at different angles in the vertical plane. The current values of $|R|$ were calculated using an averaging time of 1.024 s at 12- to 20-s intervals. The measurements were performed for signals with different pairs of arrival angles: $\alpha_1, \alpha_2 > 0$ (both signals arrive from above), $\alpha_1, \alpha_2 < 0$ (both signals arrive from below), and $\alpha_1 > 0$ and $\alpha_2 < 0$ (one signal arrives from above, and the other from below). The results of the measurements were used to obtain the time spectra, i.e., the sets of differences in the arrival times of signals within the observation interval. For each two- to three-minute-long signal record, six to fourteen measurements were taken. Although the duration of each single record was small, it was long enough for the distance between the transmitting and receiving ships to vary and also for the source depth to vary with a ship roll period of about 10 s; in addition, within a single record, changes occurred in the field structure, which, in particular, can be seen in Fig. 2. This figure shows several records for the signals received by the two arrays positioned at different depths (200 and 450 m). The abscissa axis represents the observation time t, and the ordinate axis represents the difference τ in the arrival times of the signals with the arrival angles α_1 and α_2 at which the main lobes of the arrays were aimed. The distances between the transmission and reception points are indicated at the top of the plots. Figures 2a and 2b show the time spectra of the signals received in the first convergence zone at the distances from 60 to 66 km, and Fig. 2c shows the time spectra for the signals received in the second convergence zone at the distances 119.5–126 km. Dots of different shapes shown in Fig. 2 represent different values of the cross-correlation coefficients $|R|$ of the received signals: (∗) $0.8 \le |R| \le 1.0$, (×) $0.6 \le |R| < 0.8$; (○) $0.4 \le |R| < 0.6$; and (●) $0.2 \le |R| < 0.4$. Despite the rather small width of the main lobe of each of the arrays ($\Delta\alpha_{0.7} \cong 2°$), in some cases signals arriving over different rays with close grazing angles fell within it. The signals that were unresolved in angle but resolved in the arrival time gave rise to several correlation peaks and, hence, to several components in the time spectra.

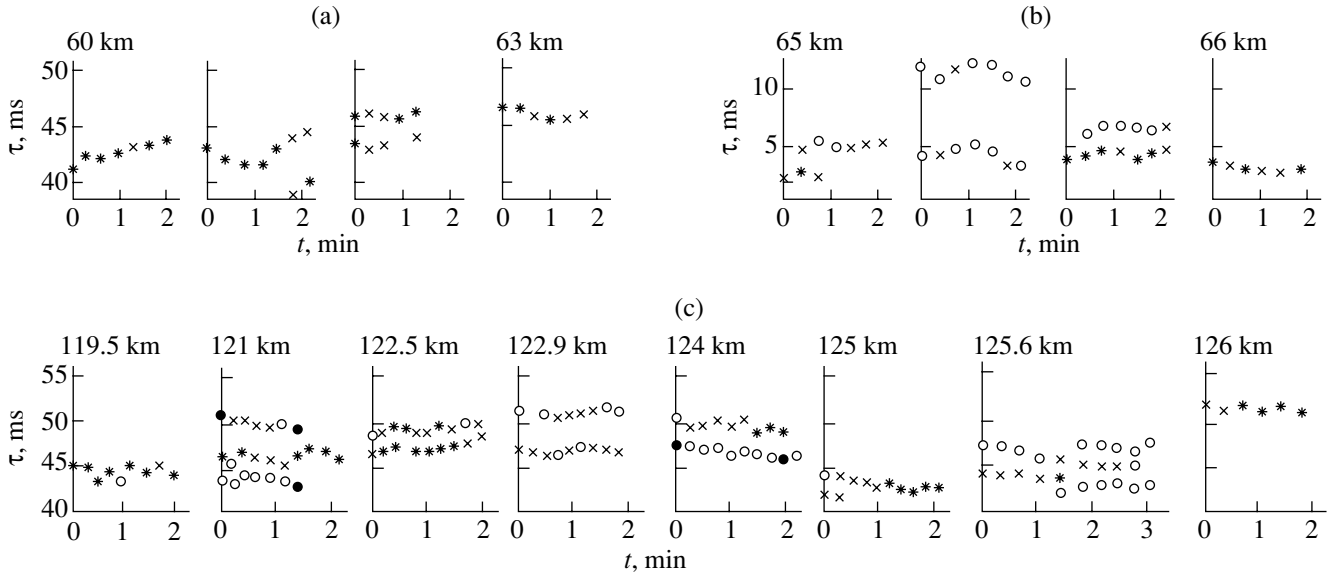

Fig. 2. Time spectra of signals for reception at different depths (α_1 and α_2 are for z = 200 and 450 m, respectively): in the first convergence zone for the arrival angles $\alpha_1 \cong$ (a) –6° and (b) +8° and $\alpha_2 \cong$ (a) –10° and (b) +11°; (c) in the second convergence zone for $\alpha_1 \cong -5°$ and $\alpha_2 \cong -10°$.

Within the first half of the first convergence zone (Fig. 2a), the mean values of the time delays τ increased from ~42 to ~46 ms as the distance increased by 3 km, and the values of the cross-correlation coefficient varied from $|\bar{R}_{\max}| = 0.81$ at the distance $r \sim 60$ km to $|\bar{R}_{\max}| = 0.70$ at $r \sim 63$ km. In the second half of the first convergence zone (Fig. 2b), two signals instead of one fell within one of the directional patterns in most cases, which resulted in the formation of two branches of τ in the time spectra. For the time spectrum component with maximal correlation coefficients, the mean values of τ varied insignificantly (from ~5 to ~3 ms) and the maximal correlation coefficient $|\bar{R}_{\max}|$ varied from 0.64 ($r \sim$ 65 km) to 0.76 ($r \sim 66$ km).

In the second convergence zone at the distances from 119.5 to 126 km, several signals fell within practically every directional pattern of the receiving systems. Therefore, in most cases, several delay values were simultaneously observed in the time spectra (Fig. 2c). The time delays τ between the signals that provided the maximal values of the cross-correlation coefficient $|R_{\max}|$ varied from ~44 to ~52 ms. The values of the maximal correlation coefficients $|R_{\max}|$ varied from 0.59 to 0.83.

When more than one signal fell within the main lobe of the directional pattern, the determination of the cross-correlation coefficient for the received signals resulted in several values of $|R|$ instead of one. In such a situation, the signals arriving over different ray paths played the role of "signal" interference for each other and reduced the correlation coefficient $|R|$ for each individual signal. If the difference in the arrival times of the signals exceeded 2 ms, the "signal" interference was an additive one. In this case, to take into account the interfering effect of the time resolved signals that fell within the directional pattern by propagating over each (ith) ray, we calculated the corrected correlation coefficient under the assumption that the levels of the arriving signals are equal: $|R_\Sigma| = \sqrt{\sum_i |R_i|^2}$. For the records presented in this paper, its mean values $|\bar{R}_\Sigma|$ vary from 0.68 to 0.88 in the first convergence zone and from 0.66 to 0.92 in the second convergence zone.

Figures 3–5 present (from top to bottom) the data on the positions of the reception points of the propagation track (variations in the distance r during the experiment), the aiming angles of the directional patterns in the vertical plane (angles α at which the directional patterns of the arrays were directed), the correlation coefficients $|\bar{R}|$ for one of the components of the time spectra with the maximal value of $|R_{\max}|$ together with the mean values of the corrected correlation coefficients $|\bar{R}_\Sigma|$ indicated by asterisks (*), and the differences in times of the signal arrivals τ over all rays falling within the directional pattern. The abscissa axis represents the observation time t in minutes. The fluctuations of the time differences $\pm\sigma_\tau$, i.e., the rms deviation from the mean value of τ, are shown by vertical segments in the plots of $\tau(t)$.

Figure 3 corresponds to a single-depth reception, i.e., to a simultaneous reception of signals by two directional patterns of the same array. The depth at which the receiving array is positioned is indicated at the top of each column of plots. Figure 3a presents the results obtained by measuring the aforementioned characteris-

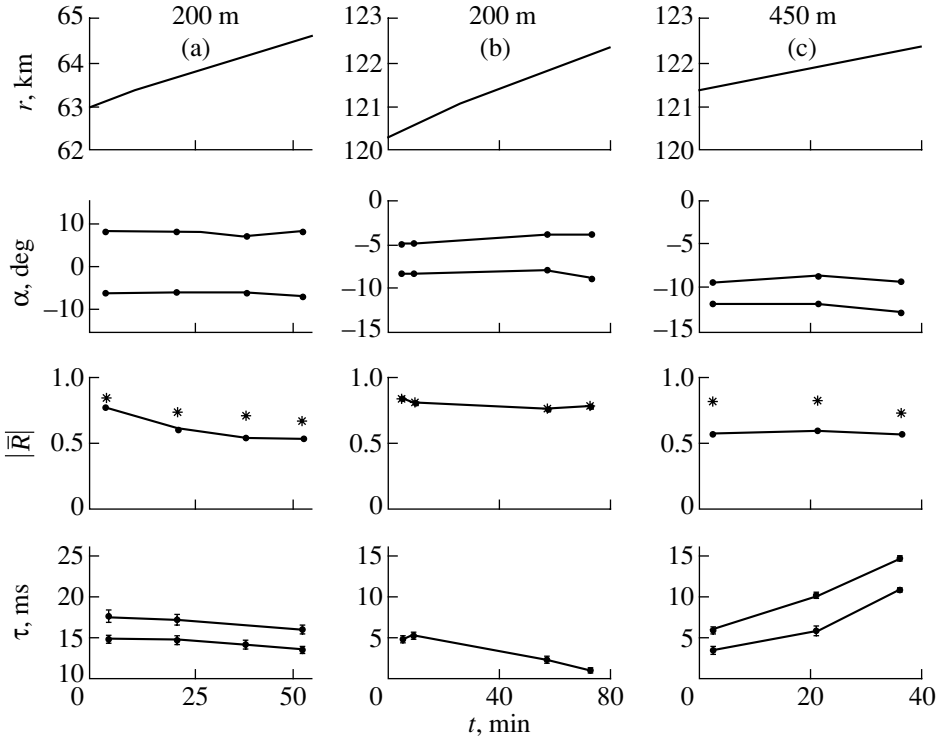

Fig. 3. From top to bottom: variations of the distance r, the arrival angles α, the mean values of the correlation coefficients $|\bar{R}|$, and the arrival time differences τ in the case of the reception at a single depth in (a) the first and (b, c) the second convergence zones. The reception depth is (a, b) 200 and (c) 450 m.

tics in the first convergence zone with the receiving array center positioned at a depth of 200 m. The correlation and time characteristics were measured between the signals received at the angles α equal to ~+8° and ~–6°. As one can see from the plot $\tau(t)$, the time spectrum contains two components (~15 and ~18 ms), which indicates that one of the directional patterns simultaneously received two signals whose arrival angles are close to each other, so that these signals cannot be resolved. At the beginning of the second convergence zone at the same depth 200 m (Fig. 3b), each of the directional patterns, which were turned to the angles α close to –5° and –8°, received one signal. Therefore, the time spectrum $\tau(t)$ contains only one component, and the measurements of the correlation coefficient reveal a single correlation peak. In this case, naturally, we have $|\bar{R}_{\max}| \equiv |\bar{R}_\Sigma|$. At a reception depth of 450 m (Fig. 3c), for the signals with the arrival angles ~–12° and ~–9°, each time spectrum $\tau(t)$ proves to have two components and the correlation functions have two correlation peaks. The smooth variations observed in Figs. 3a–3c for the mean values of the time differences τ within the observation interval t (40 to 80 min) are mainly related to the variations of the distance between the transmission and reception points.

Different data characterizing the experimental conditions (the distance r, the depth of the vertical array center h, and the aiming angles of the major maximums of the directional patterns α_1 and α_2) and the results obtained from the single-depth reception (the mean value of the maximal correlation coefficients $|\bar{R}_{\max}|$, the number of correlation peaks n, the corrected cross-correlation coefficient $|\bar{R}_\Sigma|$, and the rms deviation of the arrival time differences σ_τ) are presented in Table 1.

Now, we consider the results obtained using the different-depth reception, i.e., the signal reception by two arrays positioned at different depths. Figure 4 presents the plots for the signals received in the first convergence zone. The center of one array is at a 200-m depth, and the center of the other is at a 450-m depth. The angles α of the signal arrivals at the depths 200 and 450 m are denoted by dots and crosses, respectively. The characteristics of the received signals were measured for different angles α. At the beginning of the experiment (within 145 min), negative values of the arrival angles were used for both reception depths (~–7° for 200 m and ~–9° for 450 m), whereas at the end of the experiment (within the last 50 min), one angle was negative (~–6° at 200 m) and the other was positive (~+11° at 450 m).

Figure 5 corresponds to the measurements performed in the second convergence zone with the different-depth reception. As in the experiments in the first convergence zone, negative arrival angles were selected at the beginning ($\alpha_1 \cong -7°$ for the depth 200 m and $\alpha_2 \cong$

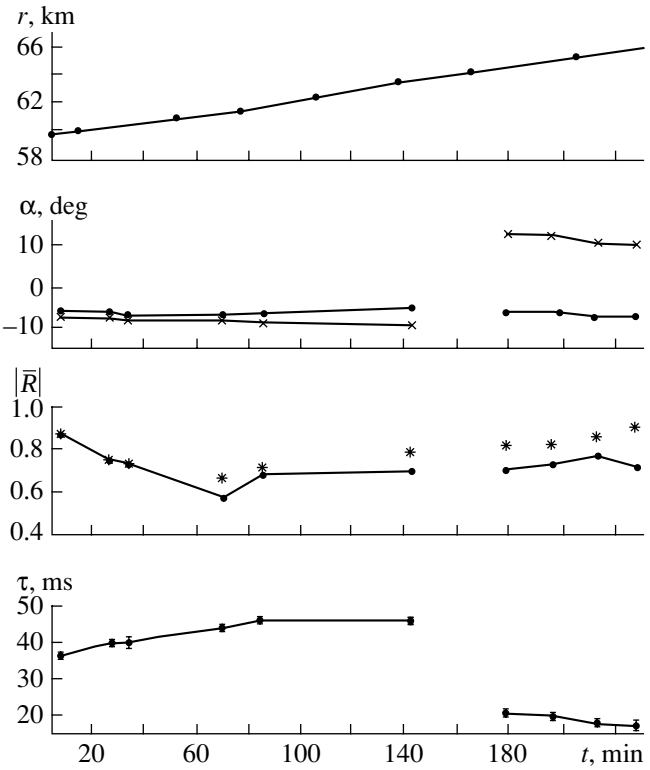

Fig. 4. From top to bottom: variations of the distance r, the arrival angles α, the mean values of the correlation coefficients $|\bar{R}|$, and the arrival time differences τ for the reception at two different depths in the first convergence zone. The reception depths are (●) 200 and (×) 450 m.

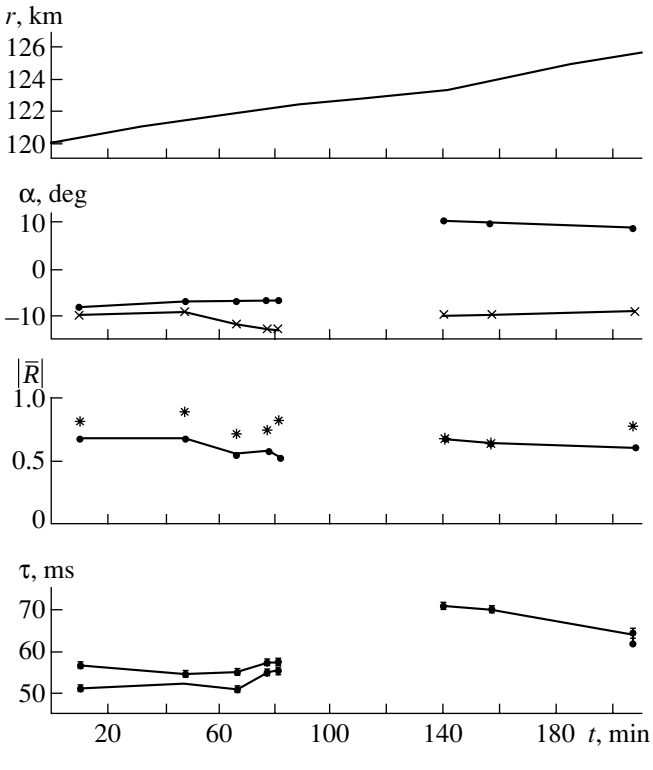

Fig. 5. From top to bottom: variations of the distance r, the arrival angles α, the mean values of the correlation coefficients $|\bar{R}|$, and the arrival time differences τ for the reception at two different depths in the second convergence zone. The reception depths are (●) 200 and (×) 450 m.

–11° for 450 m), and then, one positive ($\alpha_1 \cong +10°$ for 200 m) and one negative angle ($\alpha_2 \cong -10°$ for 450 m) were used.

The data characterizing the experimental conditions and the results obtained in the case of the different-depth reception are presented in Table 2.

Thus, the studies of the correlation characteristics of continuous broadband (with a bandwidth of 500 Hz) signals received at distances up to 130 km from a sound source positioned near the ocean surface showed that the maximal correlation coefficients fall within 0.53 to 0.87 (the corrected values fall within 0.60 to 0.91, respectively). The same values of $|\bar{R}_{max}|$ and $|\bar{R}_\Sigma|$ are typical of a source positioned at a large depth (see, e.g., [4, 5]). As for the fluctuations of the differences in the arrival times σ_τ of signals generated by a near-surface source, in accordance with the theoretical estimates presented above, they are often greater (up to 1.25 ms) than the corresponding fluctuations observed for the signals propagating in water without reflections, which are not affected by the ocean surface and by the variations of the source depth due to the roll of the transmitting ship (up to 0.3–0.5 ms).

In closing, we note that, for narrow-beam reception in the vertical plane (~2°) both at a single depth (200 or 450 m) and at two different depths (200 and 450 m), the values of the cross-correlation coefficients of the received signals are mainly determined by the angular resolution of the signals by the receiving system rather than by the near-surface position (~10 m) of the source. When several signals with close arrival angles are received, the increase in the number of correlation

Table 1

r, km	h, m	α_1, deg	α_2, deg	$\lvert\bar{R}_{max}\rvert$	n	$\lvert\bar{R}_\Sigma\rvert$	σ_τ, ms
63.0–64.6	200	~+8	~–6	0.53–0.77	2	0.67–0.85	0.40–0.73
120.3–122.3	200	~–5	~–8	0.76–0.83	1	0.76–0.83	0.25–0.39
121.4–122.3	450	~–12	~–9	0.56–0.59	2	0.71–0.82	0.27–0.52

Table 2

r, km	h = 200 m α_1, deg	h = 450 m α_2, deg	$\lvert\bar{R}_{max}\rvert$	n	$\lvert\bar{R}_{\Sigma}\rvert$	σ_τ, ms
59.8–63.3	~–7	~–9	0.58–0.87	2–3	0.66–0.87	0.11–1.25
64.8–65.9	~–6	~+11	0.71–0.78	2	0.83–0.91	0.39–0.88
65–66	~+8	~+11	0.64–0.76	1–2	0.66–0.88	0.36–0.67
119.5–126.0	~–5	~–10	0.59–0.83	1–3	0.66–0.92	0.32–0.53
120.1–122.2	~–7	~–11	0.55–0.69	2–3	0.71–0.82	0.16–0.48
123.3–125.8	~+10	~–10	0.61–0.68	1–2	0.65–0.78	0.34–0.88

peaks (in the cross-correlation function) is accompanied by a decrease in their magnitudes according to the number of arriving signals and their relative intensities. This occurs for all spatial arrangements of the transmitting–receiving systems. Only the values of the rms deviations of the arrival time differences between signals arriving over different ray paths prove to be greater for a near-water source than for a source positioned at a large depth.

ACKNOWLEDGMENTS

This work was supported by the Russian Foundation for Basic Research (project no. 00-02-17694).

REFERENCES

1. P. F. Worcester, B. D. Cornuelle, M. A. Dzieciuch, *et al.*, J. Acoust. Soc. Am. **105**, 3185 (1999).
2. J. A. Colosi, E. K. Scheer, S. M. Flatte, *et al.*, J. Acoust. Soc. Am. **105**, 3202 (1999).
3. J. A. Simmen, S. M. Flatte, H. A. De-Ferrari, *et al.*, J. Acoust. Soc. Am. **105**, 3231 (1999).
4. O. P. Galkin and S. D. Pankova, Akust. Zh. **41**, 216 (1995) [Acoust. Phys. **41**, 184 (1995)].
5. O. P. Galkin and S. D. Pankova, Akust. Zh. **44**, 57 (1998) [Acoust. Phys. **44**, 44 (1998)].
6. O. P. Galkin and S. D. Pankova, Akust. Zh. **45**, 59 (1999) [Acoust. Phys. **45**, 52 (1999)].
7. O. P. Galkin and S. D. Pankova, Akust. Zh. **45**, 479 (1999) [Acoust. Phys. **45**, 426 (1999)].
8. N. G. Kuznetsova and L. A. Chernov, Vopr. Sudostr., Ser. Akust., No. 15, 5 (1982).
9. S. D. Chuprov and R. F. Shvachko, in *Acoustics of the Ocean*, Ed. by L. M. Brekhovskikh (Nauka, Moscow, 1974), pp. 573–581.
10. N. G. Kuznetsova, Vopr. Sudostr., Ser. Akust., No. 11, 89 (1978).
11. V. P. Akulicheva and V. M. Frolov, Akust. Zh. **32**, 742 (1986) [Sov. Phys. Acoust. **32**, 465 (1986)].
12. E. A. Kopyl, in *Problems of the Ocean Acoustics* (Nauka, Moscow, 1984), pp. 143–153.

Translated by E. Golyamina

Acoustical Physics, Vol. 48, No. 1, 2002, pp. 46–49. Translated from Akusticheskiĭ Zhurnal, Vol. 48, No. 1, 2002, pp. 52–55.

Experimental Study of Ultrasonic Velocity in Dispersive Media

E. N. Dyatlova, I. S. Kol'tsova, and Mukel Maysun

St. Petersburg State University, ul. Ul'yanovskaya 1, St. Petersburg, 198904 Russia

e-mail: apvear@paloma.spbu.ru

Received March 29, 2001

Abstract—The results of an experimental study of the velocity of ultrasonic waves propagating at a 3 MHz frequency in suspensions of glass spheres in water are presented for a wide range of concentrations. It is shown that, from the variations in the concentration coefficient of the velocity of ultrasonic waves, one can extract information on the structural rearrangements in the suspension and, in the range of low concentrations, information on the elastic moduli of individual microparticles. *© 2002 MAIK "Nauka/Interperiodica".*

Dispersive media are widespread in nature, and, therefore, they are the subject of numerous theoretical and experimental studies, including those based on the measurements of the velocity and attenuation of ultrasonic waves. The propagation velocity of ultrasonic waves is related to one of the basic properties of materials, elasticity. As is well known, the dynamic elasticity of an inhomogeneous medium is determined by the elastic parameters of the matrix and the disperse phase; their structural parameters, such as size, form, and concentration; and the exchange processes between the phases [1–11].

This paper is devoted to the experimental study of the concentration dependence of the velocity of ultrasonic wave propagation in suspensions of spherical glass particles in the range of volume concentrations from fractions of a percent to 55%, that is, to the concentrations at which a globular porous structure is formed [12, 13].

By using a histogram of glass particles, which was determined by measuring the sizes of 1000 spheres with a microscope, we determined the mean size characterizing the maximal fraction of glass spheres (10 μm), as well as the minimal (3 μm) and the maximal (40 μm) sizes. The suspensions were sounded by ultrasonic waves with a frequency of 3 MHz. The velocity was measured by a pulse-phase method with a variable base, which uses the interference of two signals with a path-length difference being a multiple of $\lambda/2$ in the sample under study [14]. The accuracy of measurements was about 1%. For all sizes of particles, the condition $kR \ll 1$ was satisfied, where k is the wave number and R is the radius of a particle.

The results of measuring the velocity of ultrasonic wave propagation in suspensions in the whole range of particle concentrations are presented by curve *1* in Fig. 1. As is seen, in the region of low concentrations $n \in$ 0.1–10%, the velocity of ultrasonic waves decreases with the increase in the particle concentration. In this region, the concentration coefficient of velocity is negative $\partial c/\partial n < 0$. At concentrations higher than 10%, the dependence of the velocity of ultrasonic waves on the concentration changes. In the 10–20% range of concentrations, the curve reaches its minimum and the concentration coefficient tends to zero $\partial c/\partial n \sim 0$. On further growth of the particle concentration in the suspension, the velocity of ultrasound begins to rise. The concentration coefficient of velocity becomes positive $\partial c/\partial n > 0$. At a concentration ~45%, the velocity of ultrasonic waves in the suspension reaches the values comparable with the velocity in a pure matrix and then becomes even higher.

A negative concentration coefficient of the ultrasonic velocity in the region of low concentrations was observed in suspensions of ferromagnetic particles and in water with gas bubbles of sizes much smaller than resonant. In the first case, this effect was explained by the dominant role of the additive density of the suspension, and in the second case, by the dominant role of the additive compressibility [15, 16]. In the suspensions of glass spheres, the negative concentration coefficient of ultrasonic waves in the region of low particle concentrations up to 10% is most likely associated with the dominant role of the additive density of the suspension, as in suspensions of ferromagnetic particles.

Calculations and direct observations with a microscope showed that the change in the character of the concentration dependence of the ultrasonic velocity takes place in the regions of structural rearrangements. In the concentration range 0.1–10% ($\partial c/\partial n < 0$), the distance between the particles is $r_{mn} > 2R$ and the number of interparticle contacts is $\gamma = 0$. It is the region of existence of isolated particles almost uniformly distributed in the matrix. In the concentration range 10–20% ($\partial c/\partial n \sim 0$), the distance between the particles is $r_{mn} <$

$2R$, and the cluster aggregations appear with double and triple interparticle contacts. When the concentration exceeds 20%, a globular porous structure begins to form and the number of interparticle contacts grows with concentration and reaches a value of $\gamma \approx 6$. A similar sensitivity to structural rearrangements in suspensions of glass spheres was observed in the study of the concentration dependence of the attenuation constant for ultrasonic waves [7].

The theories describing the propagation of acoustic waves in disperse systems are based on the model of microinhomogeneous media [18]. The additivity of the density $\langle\rho\rangle = (1-n)\rho_1 + n\rho_2$, the heat capacity at constant pressure $\langle c_p\rangle = (1-n)c_{p1} + nc_{p2}$, the coefficient of thermal expansion $\langle\alpha\rangle = (1-n)\alpha_1 + \alpha_2$, and the isothermal compressibility $\langle\beta\rangle = (1-n)\beta_1 + n\beta_2$ is assumed to be valid. Here, index 1 designates a liquid medium, the index 2 designates a solid medium, and n is the volume concentration of the disperse phase. The coefficient of adiabatic compressibility in the absence of exchange processes between the phases of a disperse system is also additive: $\langle\beta_a\rangle = (1-n)\beta_{a1} + n\beta_{a2}$. In this case, the Laplacian velocity of ultrasonic waves is determined by the expression

$$c_{ll} = (\langle\rho\rangle\langle\beta_a\rangle)^{-\frac{1}{2}}. \quad (1)$$

However, in the case of the propagation of ultrasonic waves in heterogeneous systems, the processes of the energy transfer between the phases occur at the phase boundaries, which results in an additional loss of acoustic energy and calls for corrections to the Laplacian velocity of ultrasonic waves.

In particular, due to the distinction between the thermal parameters of disperse phases, acoustic waves propagating in dispersive media excite temperature waves at the phase boundaries. The heat transfer processes produced by these waves depend on the relation between the size of the particles and the temperature wavelength. For $k_T R < 1$, where $k_T = \sqrt{\frac{\omega\rho c_p}{2\kappa}}$ is the wave number of the temperature wave, within the time equal or less than half-period of the ultrasonic wave, an equalization of temperatures of the disperse phases will occur in the zones of both compression and rarefaction of the acoustic wave. In this case, the velocity of ultrasonic waves and the correction to it Δc_T are calculated by the formula

$$c = c_{ll} + \Delta c_T = c_{ll} - \frac{n}{2} T_0 c_{ll}^3 \langle\rho\rangle \rho_2 c_{p2} \left(\frac{\alpha_1}{\rho_1 c_{p1}} - \frac{\alpha_2}{\rho_2 c_{p2}}\right)^2, \quad (2)$$

where Δc_T is the correction to the Laplacian velocity.

When the size of particles is much greater than the temperature wavelength $k_T R \gg 1$, the temperature gradient between phases is retained in the zone of both compression and rarefaction. Then, the velocity of ultrasound and the correction to it are calculated by the formula

$$c = c_{ll} + \Delta c_T = c_{ll} - \frac{3n}{2R\sqrt{2\omega}} T_0 c_{ll}^3 \langle\rho\rangle \times \left(\frac{\alpha_1}{\rho_1 c_{p1}} - \frac{\alpha_2}{\rho_2 c_{p2}}\right)^2 \frac{1}{(\kappa_1\rho_1 c_{p1})^{-\frac{1}{2}} + (\kappa_2\rho_2 c_{p2})^{-\frac{1}{2}}}, \quad (3)$$

where κ is the thermal conductivity coefficient and T_0 is the equilibrium temperature [1, 20].

As is seen from Eqs. (2) and (3), Δc_T is negative, i.e., the heat exchange process reduces the magnitude of the Laplacian velocity of sound.

An additional attenuation and a correction to the velocity of acoustic waves will be caused by the viscosity waves arising at the phase boundaries in the case of the propagation of ultrasonic waves in dispersive media. For the suspensions under study, this correction to the velocity can be computed by using Rytov's theory:

$$c = c_{ll} + \Delta c_\eta,$$

$$\Delta c_\eta = c_{ll} \frac{a\xi\sqrt{\xi}(1 + b\sqrt{\xi})}{(1+\sqrt{\xi})^2 + \xi(1+b\sqrt{\xi})^2 - a\xi\sqrt{\xi}(1+b\sqrt{\xi})}, \quad (4)$$

where

$$\xi = \frac{\omega\rho}{\eta} R^2, \quad a = \frac{2}{9} n \left(\frac{\rho_2 - \rho_1}{\rho_1}\right)^2,$$

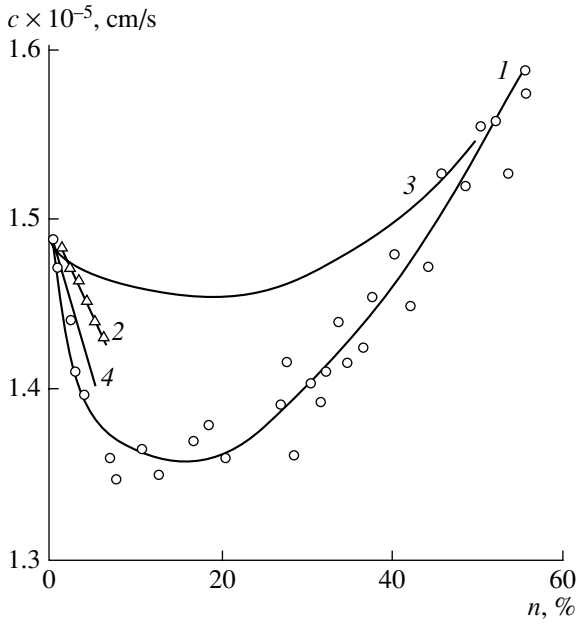

Fig. 1. Dependence of the propagation velocity of ultrasonic waves on the concentration of particles at a frequency of 3 MHz: (*1*) glass spheres, (*2*) ferrite particles [15], (*3*) the theoretical values of c_{ll} for glass particles, and (*4*) the values of c_{ll} with the corrections Δc_T and Δc_η.

Table

Substance	Parameters					
	density $\rho \times 10^3$ kg/m^3	heat capacity $c_p \times 10^{-2}$ J/kg K	thermal conductivity κ W/m K	coefficient of compressibility $\beta \times 10^{-10}$ Pa^{-1}	coefficient of thermal expansion $\alpha \times 10^{-4}$ K^{-1}	viscosity $\eta \times 10^{-3}$ Pa s
Water	0.998	41.9	0.63	4.56	1.82	1.01
Glass	2.32	6.3	1.34	0.15	2.82×10^{-2}	

and

$$b = \frac{2}{9}\left(\frac{\rho_1 - 2\rho_2}{\rho_1}\right).$$

The values of the parameters needed for calculating c_{ll}, Δc_T, and Δc_η are given in the table [19]. In the calculations, we used the mean size of particles determined from the histogram for the suspensions under study.

The results of calculating the velocity c_{ll} by Eq. (1) are displayed by curve *2* in Fig. 1. As seen from the figure, the theoretical concentration dependence of the velocity of ultrasonic waves calculated by Eq. (1) for a suspension of glass particles qualitatively coincides with the experimental curve: $\partial c/\partial n < 0$ in the range of concentrations $n \in$ 1–10%, $\partial c/\partial n \approx 0$ at concentrations $n \in$ 10–20%, and $\partial c/\partial n > 0$ beginning from the concentration $n \approx 20\%$. However, the numerical values differ appreciably.

The theoretical models described in the literature [1–3, 20] make it possible to compute the corrections Δc_T and Δc_η to the velocity of ultrasonic waves in dispersive media on condition that $r_{mn} \gg 2R$, where r_{mn} is the distance between the particles. For the suspensions under study, this condition is satisfied for the concentrations up to 10%. For these suspensions, $k_{T_1} R = 0.1$ and $k_{T_2} R = 0.3$, and, consequently, for calculating Δc_T and Δc_η, one can use Eqs. (2) and (4). The theoretical values of the velocity c_{ll} obtained by taking into account the corrections Δc_T and Δc_{ll} are in good agreement with the experimental data (curve *3* in Fig. 1).

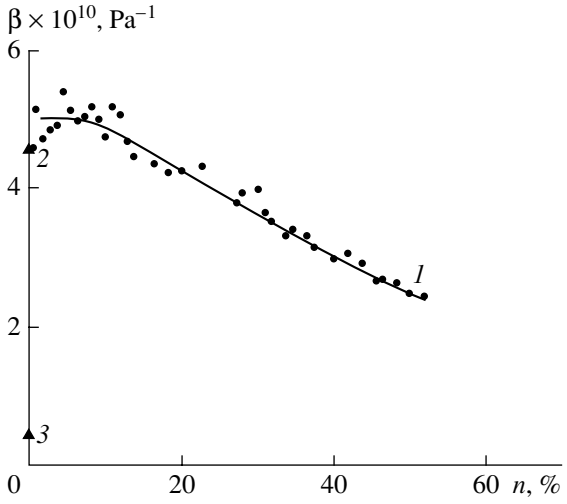

Fig. 2. Dependence of the compressibility of the suspension on the concentration of particles: (*1*) the effective compressibility of the suspension of glass spheres, (*2*) the coefficient of compressibility of water, and (*3*) the coefficient of compressibility of glass.

The calculations allowed us to choose the range of concentrations in which it is possible to compute the coefficient of compressibility of particles by Eq. (1) from the experimentally measured velocity of ultrasonic waves without consideration for the corrections Δc_T and Δc_η. For the studied suspensions, the corrections Δc_T and Δc_η are small in the range of concentrations $n \in$ 0.01–2%. For this range, having measured the density of the glass spheres, which coincided with the density of solid glass accurate to the third decimal place, we calculated the coefficient of compressibility of the particles: $\beta_2 \approx 11 \times 10^{-10}$.

Figure 2 shows the coefficient of the effective compressibility versus the concentration for the investigated suspensions (curve *1*). The values of the coefficient of compressibility of water (point *2*) and solid glass (point *3*) are also presented. From the figure, it is seen that the mean value of the effective compressibility of suspensions of glass spheres in the range of concentrations of 0–10% exceeds the compressibility of water, which is caused by the relatively high compressibility of particles.

The formal application of Eq. (1) for calculating the compressibility at concentrations $n > 10\%$, i.e., when the distance between the particles becomes less than their size and interparticle contacts occur giving rise to a porous globular structure, reveals a decrease in the effective compressibility of the suspension with the increasing number of interparticle contacts and closeness of the packing of the particles.

Thus, by measuring the propagation velocity of ultrasonic waves in suspensions in the range of low concentrations, it is possible to obtain information on the elastic moduli of individual microparticles, whereas, such measurements in the range of high concentrations provide information on the effect of structural rearrangements in the ensemble of particles on the effective elastic parameters of the suspension.

REFERENCES

1. M. A. Isakovich, Zh. Éksp. Teor. Fiz. **18** (10), 905 (1948).
2. S. M. Rytov, V. V. Vladimirskiĭ, and M. D. Galanin, Zh. Éksp. Teor. Fiz. **8** (5), 210 (1938).
3. I. A. Ratinskaya, Akust. Zh. **8**, 210 (1962) [Sov. Phys. Acoust. **8**, 160 (1962)].
4. J. R. Allegra and S. A. Hawley, J. Acoust. Soc. Am. **51**, 1545 (1971).
5. Avtar S. Ahja, J. Appl. Phys. **44**, 1545 (1973).
6. M. A. Biot, J. Acoust. Soc. Am. **34**, 1254 (1962).
7. I. A. Chaban, Akust. Zh. **39**, 362 (1993) [Acoust. Phys. **39**, 190 (1993)].
8. M. F. Poujol-Pfefer, J. Sound Vibr. **184**, 665 (1995).
9. A. K. Mukhopadhyay and K. K. Phani, J. Mater. Sci. Lett. **18**, 1759 (1999).
10. Liee Jiatiang, Vino Mao, and Sun Zwigang, JEEE Ultrason. **2** (3), 1299 (1996).
11. M. D. Collins, J. F. Lingevith, and W. L. Sigmann, Wave Motion **25** (3), 265 (1997).
12. A. L. Éfros, *Physics and Geometry of Disorder* (Nauka, Moscow, 1982), p. 175.
13. S. I. Kol'tsov and N. G. Roslyakova, *Porous Materials* (Leningr. Tekhnol. Inst., Leningrad, 1987), p. 66.
14. H. McSkimin, in *Physical Acoustics: Principles and Methods*, Ed. by W. P. Mason (Academic, New York, 1964; Mir, Moscow, 1966), Vol. 1, Part A.
15. V. M. Polunin, in *Ultrasound and Physical-Chemical Properties of Materials* (KGPI, Kursk, 1979), Issue 13, pp. 151–154.
16. J. W. Leander, in *Proceedings of 4th European Congress on Underwater Acoustics, Rome, 1998*, Vol. 1, p. 113.
17. I. S. Kol'tsova and M. Maisun, Akust. Zh. **43**, 362 (1997) [Acoust. Phys. **43**, 310 (1997)].
18. M. A. Isakovich, Usp. Fiz. Nauk **129** (3), 531 (1979) [Sov. Phys.–Usp. **22**, 928 (1979)].
19. *Physical Quantities. Handbook*, Ed. by I. S. Grigor'ev and E. Z. Meĭlikhov (Énergoatomizdat, Moscow, 1991).
20. Yasuhide Fukumoto, Phys. Rev. A **46**, 4905 (1992).
21. Yu. I. Petrov, *Clusters and Small Particles* (Nauka, Moscow, 1986), p. 367.

Translated by A. Svechnikov

Acoustical Physics, Vol. 48, No. 1, 2002, pp. 50–53. Translated from Akusticheskiĭ Zhurnal, Vol. 48, No. 1, 2002, pp. 56–60.

Experimental Study of the Motion of Liquid Droplets in a Capillary under Vibration

Yu. M. Zaslavskiĭ

Institute of Applied Physics, Russian Academy of Sciences, ul. Ul'yanova 46, Nizhni Novgorod, 603950 Russia

e-mail: zaslav@hydro.appl.sci-nnov.ru

Received July 10, 2000

Abstract—Results of an experimental study of the motion of small droplets in a capillary are discussed. The translational velocity of small droplets is studied as a function of the level and frequency of vibration acting together with a static force on the droplet–capillary system. The results are presented in the form of a set of curves, which reveal the nonlinear mechanical features of the system under consideration. The experiments confirm the previously developed theoretical model [7] based on the hysteresis dependence of the surface tension forces on the velocity of the meniscus motion. © *2002 MAIK "Nauka/Interperiodica".*

The mechanisms of the effect of vibration on fluid-containing porous media, which results in the convection or filtration of the fluid components, are much discussed in the literature in connection with the practical problems of increasing the efficiency of hydrocarbon extraction from the interior of the earth, as well as with some technological problems. The studies are usually concerned with the most common cases of completely liquid-saturated media. Particular interest is attracted to the processes determined by the contacts of two or more liquid phases that differ in skeleton wetting, as well as to analysis of the effect of the gaseous phase on the fluid flow in pores [1–6].

This paper describes an experiment demonstrating the specific effects that arise under the combined action of a static force and a low-frequency vibration in a droplet–capillary system, which consists of a glass capillary with a liquid droplet inside and with air in front and behind the droplet. Such a system models the effect of the surface tension that occurs at the meniscuses separating liquid fractions of different types with different wetting properties in the capillaries of porous media.

A theoretical study of the dynamics of small droplets placed in a cylindrical capillary and subjected to the two aforementioned types of external action was carried out earlier [7]. On the basis of a simplified model equivalent to the droplet–capillary system, an equation was derived to describe the motion of a small droplet partially wetting the capillary walls. The solution to this equation allows one to determine the possible complex movements of the center of mass of the droplet, i.e., to predict different specific types of droplet motion. In the cited paper, attention is concentrated on the motion features related to the surface tension forces that arise at the meniscuses of the droplet and lead to the effects characteristic of systems with dry, i.e., Coulomb, friction [8]. One of these features is as follows: in the presence of vibration, the external force level that is necessary for disturbing the droplet from its equilibrium position becomes lower than the corresponding static force threshold observed in the absence of vibration. Another feature is the experimentally observed difference between the dependences of the translational velocity of the droplet on the vibration amplitude for the case of its increase or decrease, when the region of the reconstruction includes a force threshold corresponding to either the departure of a stationary droplet from its equilibrium position or the termination of the translational motion of a moving droplet. It should be noted that the difference is observed between the threshold values themselves, which will be seen from the experimental dependences presented below. In addition, it is worth noting the existence of other experimental data that cannot be described by the simplified model, which points to the possibility of the presence of unknown physical mechanisms that make the behavior of the dynamic system under study more complicated.

Therefore, it is of interest to describe in more detail the experimentally observed characteristics, specifically, the dependence of the translational velocity of the droplet on the frequency of vibration at constant amplitude and the dependence of this velocity on the amplitude of vibration at constant frequency. From the point of view of the specific features of these dependences, the low-frequency region is of most interest.

The experimental studies of the effect of vibration were performed using a vibration-testing machine (RFT DDR), which provided the vibrational acceleration with the amplitudes 0–30 m/s^2 in the frequency range 10–100 Hz. The vibrational acceleration was controlled by a KB-10 accelerometer (RFT DDR). The static force was represented either by the gravity force

1063-7710/02/4801-0050$22.00

when the capillary was set in the vertical position or by the force due to the excess air pressure supplied to one end of the capillary when it was in the horizontal position. In the latter case, the excess air pressure was controlled by a liquid-column manometer. To provide a translational velocity of about several centimeters per second for a 5–10 mm long droplet in a horizontal capillary with an inner diameter of ~1 mm, it is necessary to maintain a pressure difference of ~20 mm water column. Approximately the same average values of the droplet "flow" velocity are obtained under the effect of the gravity force acting on the droplet disturbed from its equilibrium position. Two types of liquid were studied in the experiment: distilled water and a 50% solution of glycerol in water. For the vertically oriented capillary where the weight of the droplet played the role of the external static force, we used the liquid of the second type, and for the horizontally oriented capillary with a pneumatic external action, we used the liquid of the first type. It should be noted that, to avoid the distorting effect of the surface film, which in every preceding experiment partially or fully covered the inner surface of the channel behind the moving droplet, we took special measures that prevented the formation of such a film, and the measurements were performed with a clean inner wall of the capillary. We note that the visually observed effect of the film formation is more prominent for higher velocities of the droplet motion at which a greater portion of the droplet mass is left on the wall, i.e., the droplet mass decreases more substantially. Therefore, in the experiment, the translational velocities were maintained so as not to exceed 3–4 cm/s.

Let us first consider the data obtained from the experiments with a droplet of the 50% solution of glycerol in water. Initially, the droplet was in equilibrium. After the vibration-testing machine was turned on, when the vibration level exceeded a certain threshold, the droplet began to move with a translational velocity depending on the vibration amplitude and frequency under the effect of gravity and vibration. In this series of experiments, the vibration-testing machine produced vertically polarized vibrational accelerations of the capillary, which was mounted on its platform so that the longitudinal capillary axis was strictly vertical. Figure 1 presents a family of curves *1–6* obtained under vibrations with the frequencies 20, 30, 40, 50, 60, and 70 Hz. The horizontal axis in the plot corresponds to the vibrational acceleration amplitude measured by the accelerometer (KB-10) with a sensitivity of 1 mV/m/s^2, and the vertical axis corresponds to the translational velocity of the droplet. The latter was measured by the conventional method of determining the time interval (by a stopwatch) within which the droplet traveled a reference distance. The estimates show that, in these measurements, the vertical scatter of the experimental points due to the measurement error does not exceed 0.25 cm/s.

One can easily see that the experimental results support some theoretical inferences made in [7], specifically, the statement that the translational velocity increases as the frequency of vibrations becomes lower. The same refers to the increase that was observed in the motion onset threshold with increasing vibration frequency: this effect agrees well with the results of the aforementioned theoretical study.

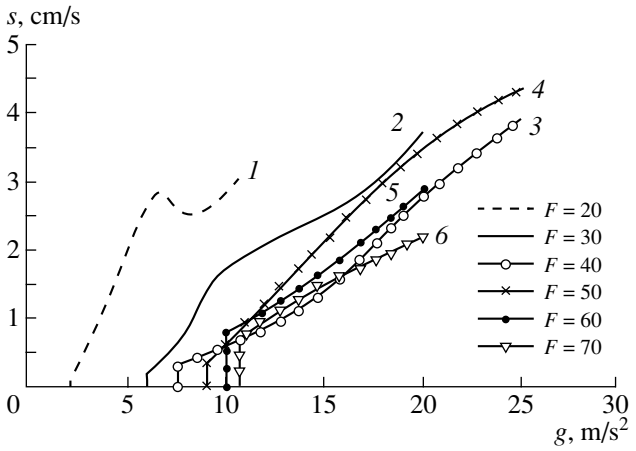

Fig. 1. Dependence of the translational velocity of the droplet (a 50% solution of glycerol in water) on the vibrational acceleration amplitude for the vibration frequencies (*1*) 20, (*2*) 30, (*3*) 40, (*4*) 50, (*5*) 60, and (*6*) 70 Hz.

In the cited paper [7], it was found that the motion onset threshold can be estimated by the formula

$$(y\omega^2)_{\text{thr}} = \frac{2\sigma}{\rho L r}(\cos\theta_- - \cos\theta_+) - g, \qquad (1)$$

where g = 9.8 m/c^2 is the acceleration of gravity; the difference between the cosines of the contact angles, $\cos\theta_- - \cos\theta_+$, characterizes the uncertainty interval of the static moisture contact angle of the meniscus bounding a semi-infinite liquid column in the capillary (see Fig. 2 showing the qualitative dependence of the cosine of the meniscus contact angle on the velocity of the droplet motion from [9]); $\theta_{\mp}$ denotes the limiting static values of the moisture contact angle, which correspond to the meniscus velocity tending to zero for the positive and negative meniscuses; σ is the surface tension constant at the liquid–wall boundary; ρ is the density of the liquid; L is the droplet length; r is the inner radius of the capillary; ω is the vibration frequency; and y is the amplitude of the capillary wall displacement under vibration.

The hysteresis observed in Fig. 2 for the moisture contact angle of a stationary (i.e., in the static position) meniscus determines a nonlinear type of motion of a small droplet when its length exceeds the capillary diameter by no more than an order of magnitude. Substituting the specific values of the parameters in Eq. (1) by taking them from the reference data and from the experiment (on the basis of the presented curves), we estimate the aforementioned uncertainty interval of the cosine of the moisture contact angle as 0.3–0.5.

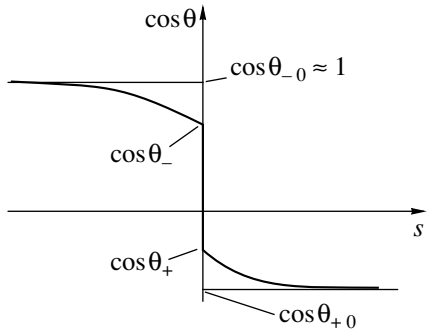

Fig. 2. Dependence of the cosine of the moisture contact angle at the rigid wall on the velocity for the cases of the positive ($s > 0$) and negative ($s < 0$) meniscuses bounding a semi-infinite liquid column.

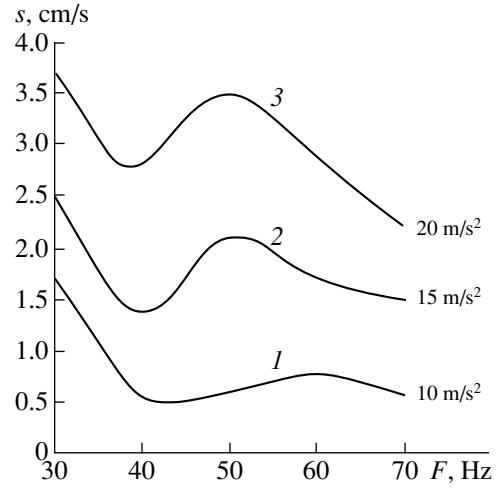

Fig. 3. Dependence of the translational velocity of the droplet (a 50% solution of glycerol in water) on the vibration frequency for the vibrational acceleration amplitudes (*1*) 10, (*2*) 15, and (*3*) 20 m/s^2.

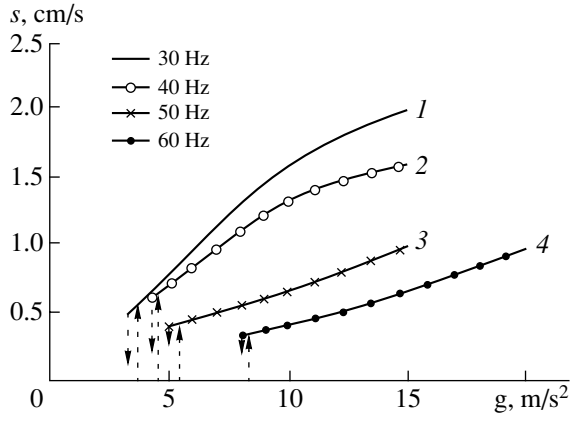

Fig. 4. Dependence of the translational velocity of the droplet (distilled water) on the vibrational acceleration amplitude for the vibration frequencies (*1*) 30, (*2*) 40, (3) 50, and (*4*) 60 Hz.

Recall that these values are obtained by approximating curves *1–6* shown in Fig. 1 to the zero velocity value. Similar values were obtained in the earlier studies [9, 10] based on the optical observation of the meniscus shape, but this method is much more difficult to realize in the experiment.

A distinctive feature of the experimental data obtained in this series of experiments is the decrease in the mean slope of the amplitude dependences with increasing frequency, which can be seen from the curves presented in Fig. 1. This experimental fact still has no rigorous theoretical explanation, although general physical considerations point to the possible effect of the Stokes friction forces that act over the whole lateral droplet surface being in contact with the wall rather than only in the meniscus region, as in the proposed simplified model. Therefore, in more adequate models to be developed, the role of the near-wall viscosity should be corrected.

Figure 3 presents the dependences of the translational velocity on the vibration frequency at constant levels of vibrational acceleration: curves *1*, *2*, and *3* correspond to the vibrational acceleration amplitudes 10, 15, and 20 m/s^2, respectively. In this figure, the velocity decreases with increasing frequency on the average, but all three curves exhibit local minimums and maximums in the frequency interval 40–60 Hz.

The second series of experiments was performed with a water droplet in an identical capillary oriented horizontally. The vibrations were polarized along the horizontal capillary axis. This configuration was obtained by rotating the vibration-testing machine through a right angle from the initial position. In this case, the static action was provided by excess air pressure on one side of the droplet. The excess pressure in the compression vessel over the atmospheric pressure was ~15–16 mm water column, which was somewhat below the threshold value corresponding to the onset of uniform motion of the center of mass of a 15–20 mm long droplet. The application of a certain vibration level causes the droplet to leave its equilibrium position, whereas, in the absence of vibration, the equilibrium is not disturbed. Figure 4 shows the dependences of the translational velocity on the amplitude of the vibrational acceleration for the frequencies 30, 40, 50, and 60 Hz (curves *1–4*, respectively). As in the previous series of experiments, higher velocities of the droplet motion correspond to lower frequencies. At the same time, the curves obtained in this series of experiments are characterized by smaller average slopes, as compared to the experiments with a 50% glycerol solution droplet. However, the essential difference from the previous series of measurements is not the quantitative difference in the velocities of motion or in the slopes of the corresponding dependences, but the following fact: the second series of measurements revealed a difference between the vibration level at which the droplet changes from the state of rest to motion with increasing

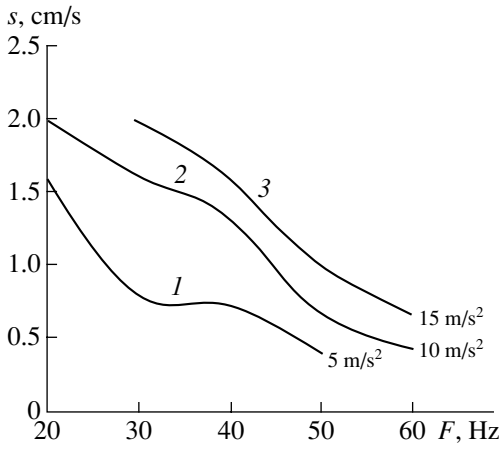

Fig. 5. Dependence of the translational velocity of the droplet (distilled water) on the vibration frequency for the vibrational acceleration amplitudes (*1*) 5, (*2*) 10, and (*3*) 15 m/s^2.

vibrational acceleration and the level at which the translational motion of the droplet terminates as the vibration level decreases. This difference is relatively small, but it is detected in the experiment. The threshold value corresponding to the transition from rest to motion is higher than the threshold value for the inverse process. This can be seen from the splitting in the left parts of the curves shown in Fig. 4, where the directions of the variation of the vibrational acceleration amplitude are indicated by arrows.

In Fig. 5, curves *1–3* represent the frequency dependences of the translational velocity of the center of mass of the water droplet in the presence of a combined effect produced by the vibration and pneumatic action, when their "total" level exceeds the critical value. One can see the same tendency for a general decrease in the velocity with increasing frequency, as well as local minimums and maximums at the frequencies specified above.

On the whole, the experimental studies of the translational velocity of liquid droplets in a capillary as a function of the amplitude and frequency of applied vibration, which were performed in the presence of static forces of different nature for different liquids, reveal a non-Newtonian (Bingham) [11] "rheology" in the droplet–capillary system. This result is explained by the fact that, along with the presence of forces of different physical origins, the dominant factor is the surface tension acting on the droplet meniscuses, as well as the specific hysteresis behavior of the velocity of motion as a function of the external action, which is inherent in the nature of the surface tension forces.

From the practical point of view, the experimental results presented above can be essential in analyzing the processes of the artificial drying of partially fluid-saturated materials and in developing methods for the intensification or stimulation of oil recovery by vibroseismic techniques.

ACKNOWLEDGMENTS

I am grateful to S.V. Birin for the assistance in the experiments. The work was supported by the Russian Foundation for Basic Research (project no. 97-02-17537).

REFERENCES

1. V. P. Dyblenko, R. N. Kamalov, R. Ya. Sharifullin, and I. A. Tufanov, *Productivity Raising and Reanimation of Wells Using the Effect of Vibration* (Nedra, Moscow, 2000).
2. V. N. Nikolaevskiĭ, *Geomechanics and Fluid Dynamics with Applications to the Problems of Gas and Oil Pools* (Nedra, Moscow, 1996).
3. P. M. Roberts and A. Sharma, J. Acoust. Soc. Am. **105**, 1385 (1999).
4. A. Sharma and P. M. Roberts, EOS Trans. Am. Geophys. Union **79** (45), F895 (1998).
5. S. M. Gadiev, Sh. K. Gimatudinov, K. S. Konenkov, and Yu. A. Kuzmichev, Izv. Vyssh. Uchebn. Zaved., Neft' Gaz, No. 9, 25 (1997).
6. R. F. Ganiev, A. E. Ukrainskiĭ, and K. V. Frolov, Dokl. Akad. Nauk SSSR **306** (4), 803 (1989) [Sov. Phys. Dokl. **34**, 519 (1989)].
7. V. S. Averbakh, S. N. Vlasov, and Yu. M. Zaslavskiĭ, Izv. Vyssh. Uchebn. Zaved., Radiofiz. **43** (2), 155 (2000).
8. I. I. Blekhman, *Vibration Mechanics* (Nauka, Moscow, 1994; World Sci., Singapore, 2000).
9. B. V. Zheleznyĭ, Dokl. Akad. Nauk SSSR **207** (3), 647 (1972).
10. W. Rose and R. W. Heins, J. Colloid Sci. **17**, 39 (1962).
11. Yu. P. Ampilov, *Absorption and Scattering of Seismic Waves in Inhomogeneous Media* (Nedra, Moscow, 1992).

Translated by E. Golyamina

Acoustical Physics, Vol. 48, No. 1, 2002, pp. 54–61. Translated from Akusticheskiĭ Zhurnal, Vol. 48, No. 1, 2002, pp. 61–69.

Piston-Type Radiator in a Soft Screen in the Pekeris Waveguide

N. V. Zlobina and B. A. Kasatkin

Institute of Marine Technology Problems, Far East Division, Russian Academy of Sciences, ul. Sukhanova 5a, Vladivostok, 690950 Russia

e-mail: kasatkas@marine.febras.ru

Received November 10, 2000

Abstract—A model problem is considered for a radiator in the form of a circular disk with a given pressure jump at its surface. The radiator is inserted in a soft screen coinciding with the upper boundary of the Pekeris waveguide. A series expansion of the sound field in normal modes is obtained. A numerical analysis of the radiation impedance and its components that are responsible for the radiation into the waveguide and into the halfspace is carried out. © *2002 MAIK "Nauka/Interperiodica".*

The well-known problem of low-frequency radiation in free space has certain specific features when the radiator operates in a shallow sea. In this case, the low efficiency of radiation decreases additionally because of the inefficient distribution of the radiated power between the waveguide and the halfspace. Numerical estimates of the components of the radiation impedance that are responsible for the radiation into the waveguide and the halfspace were obtained earlier [1, 2] for a vertical cylindrical radiator in a rigid screen in the Pekeris waveguide. According to these estimates, when a radiator of size $l \sim 1$ m operates in a frequency range of 50–100 Hz near the surface of a waveguide with a depth $h = 100$ m and with a sandy bottom, 80–90% of the power radiated by this source is lost in the sea bottom instead of remaining in the waveguide.

The objective of this paper is to obtain similar numerical estimates for model radiators of a different type, which correspond to actual radiators and radiation conditions at low frequencies. As a model radiator, we consider a circular disk with a given pressure jump at its surface. The radiator is inserted in a soft screen whose surface coincides with the upper boundary of the Pekeris waveguide. By its geometry, such a source can be assigned to radiators of the piston type, although the piston-type distribution of the particle velocity at its surface exists only at low frequencies.

By the boundary function type, such a radiator is close to an explosive source and, in this sense, is of certain interest. Note that, in the literature, the operation of a piston radiator has been considered only when it is inserted in a rigid screen coinciding with the boundary of a waveguide with perfectly rigid walls [3]. However, such a model radiator has limited application in hydroacoustics.

The boundary problem is written as

$$\Delta\varphi(r, z) + k_1^2\varphi(r, z) = 0,$$

$$z = 0, \quad p(z) = \begin{cases} p_0, & r \le a \\ 0, & r > a, \end{cases} \tag{1}$$

$$z = h, \quad p - Z_{\text{in}} v_z = 0, \quad Z_{\text{in}} = \frac{\rho_2 c_2}{\cos\theta_2},$$

where $\varphi(r, z)$ and $p(r, z)$ are the velocity potential and the sound pressure in the waveguide, $z \in (0, h)$, $k_1 = \omega/c_1$, ρ_1 and c_1 are the density and the sound velocity in the waveguide, ρ_2 and c_2 are the density and the sound velocity in the halfspace, Z_{in} is the input impedance of the halfspace, θ_2 is the refraction angle, p_0 is the pressure developed by the piston, a is the piston radius, and ω is the circular frequency.

Applying the Hankel transformation to solving problem (1), we obtain its solution as the following improper integral

$$\varphi(r, z) = \frac{p_0}{\rho_1 c_1}\frac{a}{ik_1}\int_0^\infty J_1(\xi a)\frac{\varphi(\xi, z)}{\Delta}J_0(\xi r)d\xi, \tag{2}$$

where $\Delta = \cos x + i\rho_{12}\dfrac{k_{32}}{k_{31}}\sin x$, $\rho_{12} = \dfrac{\rho_1}{\rho_2}$, $x = k_{31}h$, $k_{31}^2 = k_1^2 - \xi^2$, $k_{32}^2 = k_2^2 - \xi^2$, $k_2 = \omega/c_2$, ξ is the parameter of the integral transformation, and

$$\varphi(\xi, z) = \cos k_{31}(h - z) + i\rho_{12}\frac{k_{32}}{k_{31}}\sin k_{31}(h - z).$$

Using the known relationships [4]

$$J_0(x) = \frac{1}{2}[H_0^{(1)}(x) + H_0^{(2)}(x)], \quad H_0^{(1)}(-x) = -H_0^{(2)}(x),$$

$$J_1(x) = \frac{1}{2}[H_1^{(1)}(x) + H_1^{(2)}(x)], \quad H_1^{(1)}(-x) = H_1^{(2)}(x),$$

one can transform solution (2) to the form

$$\varphi(r, z) = \begin{cases} \dfrac{p_0}{\rho_1 c_1}\dfrac{a}{2ik_1}\displaystyle\int_{-\infty}^{\infty}\frac{J_1(\xi a)\varphi(\xi, z)}{\Delta}H_0^{(2)}(\xi r)d\xi \\ r \geq a \\ \dfrac{p_0}{\rho_1 c_1}\dfrac{a}{2ik_1}\displaystyle\int_{-\infty}^{\infty}\frac{J_0(\xi r)\varphi(\xi, z)}{\Delta}H_1^{(2)}(\xi a)d\xi \\ r \leq a. \end{cases} \tag{3}$$

In estimating the field in the waveguide $z \in (0, h)$, we use as the upper (physical) list of the Riemann surface the one where for the root $k_{32} = \sqrt{k_2^2 - \xi^2}$ the radiation condition $\mathrm{Re}\, k_{32} \geq 0$ is satisfied. In this case, the discrete part of the solution in the region $r \leq a$, according to the residue theorem, is given by

$$\varphi(r, z) = \frac{p_0}{\rho_1 c_1}\frac{\pi a_1}{2k_1}\left\{\sum_n \frac{x_n \varphi_n(\xi_n, z)}{\xi_n h E_n}J_0(\xi_n r)H_1^{(2)}(\xi_n a)\varepsilon_n + i\frac{2}{\pi a_1}\frac{\cos(k_1(h-z)) + i\rho_{12}c_{12}\sin(k_1(h-z))}{\cos(k_1 h) + i\rho_{12}c_{12}\sin(k_1 h)}\right\},$$

where

$$a_1 = \frac{a}{h}, \quad c_{12} = \frac{c_1}{c_2},$$

$$\varepsilon_n = \begin{cases} 1 \text{ for ordinary normal waves } (\mathrm{Im}\, k_{32,n} < 0,\ \mathrm{Im}\,\xi_n = 0) \\ \text{and generalized normal waves } (\mathrm{Im}\, k_{32,n} > 0,\ \mathrm{Im}\,\xi_n = 0), \\ 2 \text{ for leakly normal waves} \\ (\mathrm{Re}\, k_{32,n} > 0,\ \mathrm{Im}\, k_{32,n} > 0;\ \mathrm{Re}\,\xi_n > 0,\ \mathrm{Im}\,\xi_n < 0), \end{cases} \tag{4}$$

$$E_n = 1 - \frac{\sin(2x_n)}{2x_n} - i\rho_{12}\frac{\sin^2 x_n}{k_{32,n}h}.$$

The total piston radiation conductivity, Y_R, is then determined by the expression

$$\frac{1}{S}\int_S v_z(r, 0)dS = -F_0 Y_R, \quad S = \pi a^2,$$

$$F_0 = p_0 S, \quad Y_R = \frac{Y'_R}{\rho_1 c_1 S_1},$$

where $v_z = -\dfrac{\partial\varphi}{\partial z}$ is the normal component of the particle velocity. For the normalized conductivity Y'_R, we obtain the following expression

$$Y'_R = \frac{\pi}{4}\frac{a_1^2}{k_1 h}\sum_n \frac{x_n^2 \Phi_n}{\xi_n a E_n}H_1^{(2)}(\xi_n a)$$

$$+ i\frac{\sin(k_1 h) - i\rho_{12}c_{12}\cos(k_1 h)}{\cos(k_1 h) + i\rho_{12}c_{12}\sin(k_1 h)} = Y'_{12} + Y'_3 + Y'_4,$$

where

$$Y'_{12} = \frac{\pi}{8}\frac{a_1^2}{k_1 h}\sum_{\substack{n(1)\\ n(2)}}^{N^+ + N^-}\left\{\frac{x_n^2}{E_n}\Phi_n^2 - i\frac{x_n^2}{E_n}\frac{2N_1(\xi_n a)}{\xi_n a}\Phi_n\right\} \tag{5}$$

is the conductivity component responsible for the radiation by the system of the ordinary $n(1)$ and generalized $n(2)$ normal waves in the waveguide and N^- and N^+ are the numbers of the ordinary and generalized normal waves, respectively;

$$\Phi_n = \frac{2J_1(\xi_n a)}{\xi_n a} = \frac{2J_1(k_1 a \sin\theta_{1n})}{k_1 a \sin\theta_{1n}}$$

is the partial directional pattern of the piston, which corresponds to a normal wave with the angle of incidence θ_{1n};

$$Y'_3 = \frac{\pi}{2}\frac{a_1^2}{k_1 h}\sum_{n(3)}H_1^{(2)}(\xi_n a)\left[\frac{x_n^2 \Phi_n}{\xi_n a E_n}\right]$$

is the total conductivity component responsible for the radiation into the halfspace by the system of the leaky normal waves $n(3)$; and

$$Y'_4 = \frac{\rho_{12}c_{12}}{\cos^2(k_1h) + \rho_{12}^2c_{12}^2\sin^2(k_1h)} + i\frac{(1-\rho_{12}^2c_{12}^2)\sin(k_1h)\cos(k_1h)}{\cos^2(k_1h) + \rho_{12}^2c_{12}^2\sin^2(k_1h)}$$

is the total conductivity component responsible for the radiation into the halfspace by the liquid layer performing thickness vibrations in depth ($\xi = 0$).

The radiation impedance of the piston and its total conductivity are related by the standard relationship $Z_R = Y_R^{-1}$.

We now consider the results of numerical calculations assuming that $\rho_{12} = 1/1.6$ and $c_{12} = 1.5/1.75$, which corresponds to the impedance boundary between the water and the sandy bottom. Figure 1 exhibits the frequency dependence of individual components of the total conductivity of the piston with the geometric parameter $a_1 = 10^{-2}$. Note some specific features.

The component $\mathrm{Re}\,Y'_{12}$, responsible for the radiation into the waveguide, differs from zero at frequencies higher than the first critical frequency and has a clearly pronounced discrete form associated with the mode structure of the sound field in the waveguide. Its first maximum corresponds to the condition $k_1a = \pi/2$. This means that, for an observer located in the waveguide at a rather large distance, only one Fresnel zone fits within the radiator surface. A similar interpretation is valid for the following maxima corresponding to the condition $k_1a = \frac{\pi}{2}(2n+1)$ with their amplitudes decreasing with frequency.

As the geometric parameter a_1 increases, the maximum of the component $\mathrm{Re}\,Y'_{12}$ is shifted to the region of lower frequencies down to the first critical frequency. In this case, the maximal value of this component increases ($\mathrm{Re}\,Y'_{12,\max} \approx 0.1$–$0.15$).

At low frequencies, the reactive component $\mathrm{Im}\,Y'_{12}$ has an elastic character, but as the frequency increases, this component changes its sign and becomes an inertial reactance.

The component $\mathrm{Re}\,Y'_3$ is negative at low frequencies and becomes positive only at rather high frequencies. This means that the system of leaky normal waves is not self-sufficient to describe the energy characteristics of piston radiation into the halfspace. At low frequencies, the reactive component $\mathrm{Im}\,Y'_3$ has an inertial character, but as frequency increases, this component oscillates and remains an alternating quantity.

The interference character of both components is also related to the mode structure of the field in the halfspace. However, in the case under study, the system of leaky normal waves is used only for the formal description of the resonance properties of the liquid layer loaded by the halfspace with allowance for the inhomogeneous distribution of the field in the radial direction ($\xi_n \neq 0$, $\mathrm{Im}\,\xi_n < 0$).

The components $\mathrm{Re}\,Y'_4$ and $\mathrm{Im}\,Y'_4$ describe the resonance properties of the liquid layer, which performs one-dimensional thickness vibrations in depth ($\xi = 0$), and provide an additional description of the energy characteristics of the piston radiation into the halfspace. Averaged over the frequency domain, the active conductivity value $\langle \mathrm{Re}\,Y'_4 \rangle_\omega = \frac{2\rho_{12}c_{12}}{1+\rho_{12}^2c_{12}^2}$ corresponds to the energy transparency of the impedance boundary.

Figure 1d illustrates the frequency dependence of the total component $(Y'_3 + Y'_4)$ for which $\mathrm{Re}(Y'_3 + Y'_4) > 0$ everywhere in the domain of its definition. It is this total component that describes the piston radiation into the halfspace.

Figure 2 shows the frequency dependence of the components of the total radiation impedance Z_R of the piston for different values of the parameter a_1: $a_1 = 2 \times 10^{-3}$, 10^{-2}, and 10^{-1}. All three plots show that the strong interference variability of the total impedance components corresponds to the resonance properties of the liquid layer performing oscillations in depth. We can also note that the reactive component of the inertial character far exceeds the active component. As the frequency increases, the active component becomes greater than the reactive one; however, the latter does not vanish, at least, in the frequency interval under consideration.

Figure 3 exhibits the frequency dependences of the coefficient $K = \mathrm{Re}\,Y'_{12}/\mathrm{Re}(Y'_{12} + Y'_3 + Y'_4)$, which characterizes the ratio of the power radiated into the waveguide to the total power and, therefore, the efficiency of the piston radiator operation in the waveguide. All frequency dependences calculated for various values of the geometric parameter a_1 are similar in essence and differ in the frequency corresponding to the maximum of the coefficient K, this frequency being determined by the Fresnel rule. In Fig. 3c, one can see additional maximums corresponding to an odd number of Fresnel zones on the radiator surface for the case $a_1 = 0.1$.

The low efficiency of the piston radiation into the waveguide is easily understood, because, at very low frequencies, only a small number of energy-carrying normal waves of the $n(1)$ and $n(2)$ type are present in the whole set of normal waves, while, at rather high fre-

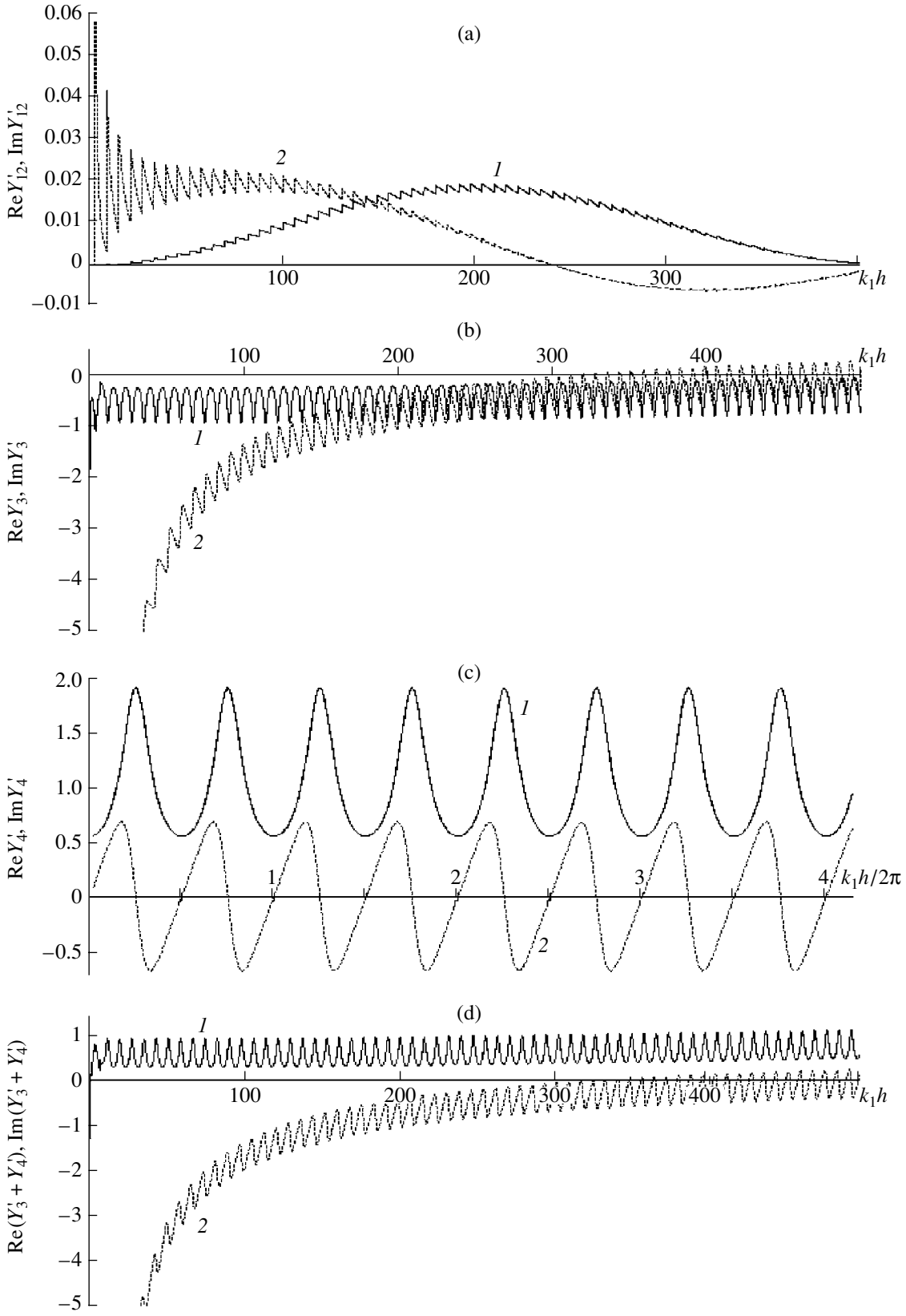

Fig. 1. Frequency dependences of the active and reactive components of the total conductivity of the piston for $a_1 = 10^{-2}$: (a) (*1*) $\mathrm{Re}\,Y'_{12}$, (*2*) $\mathrm{Im}\,Y'_{12}$; (b) (*1*) $\mathrm{Re}\,Y'_3$, (*2*) $\mathrm{Im}\,Y'_3$; (c) (*1*) $\mathrm{Re}\,Y'_4$, (*2*) $\mathrm{Im}\,Y'_4$; and (d) (*1*) $\mathrm{Re}(Y'_3 + Y'_4)$, (*2*) $\mathrm{Im}(Y'_3 + Y'_4)$.

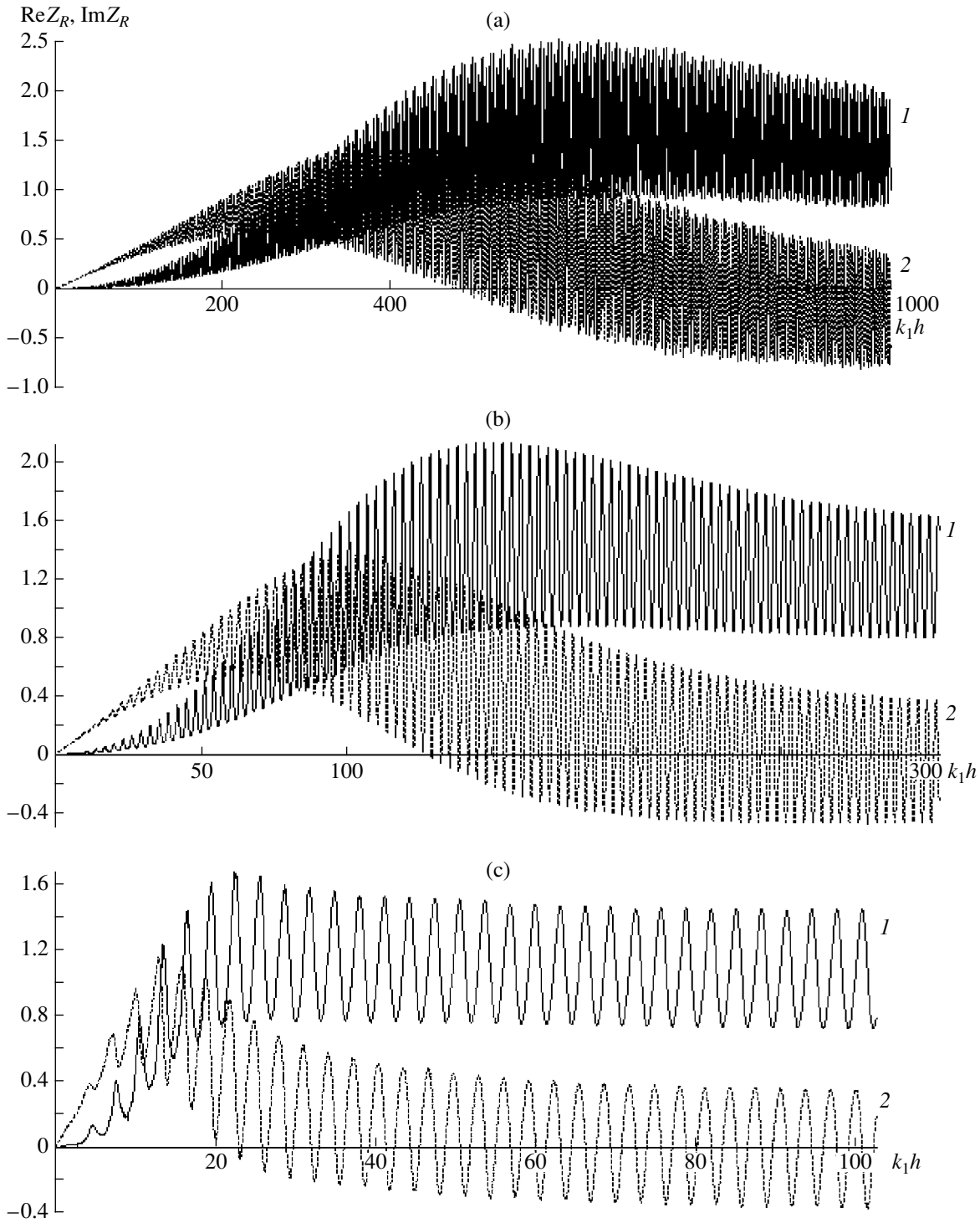

Fig. 2. Frequency dependences of the active and reactive components of the piston radiation impedance for a_1 = (a) 2×10^{-3}, (b) 10^{-2}, and (c) 10^{-1}: (*1*) ReZ_R and (*2*) ImZ_R.

quencies, the directional pattern of the piston becomes narrow and oriented toward the bottom. Therefore, the optimal situation is realized only when the condition $k_1a = \pi/2$ (i.e., $2a = \lambda/2$) is satisfied.

To analyze the piston radiator field in the waveguide, one can use the upper integral in Eq. (3). Applying the residue theorem again, we obtain the desired representation

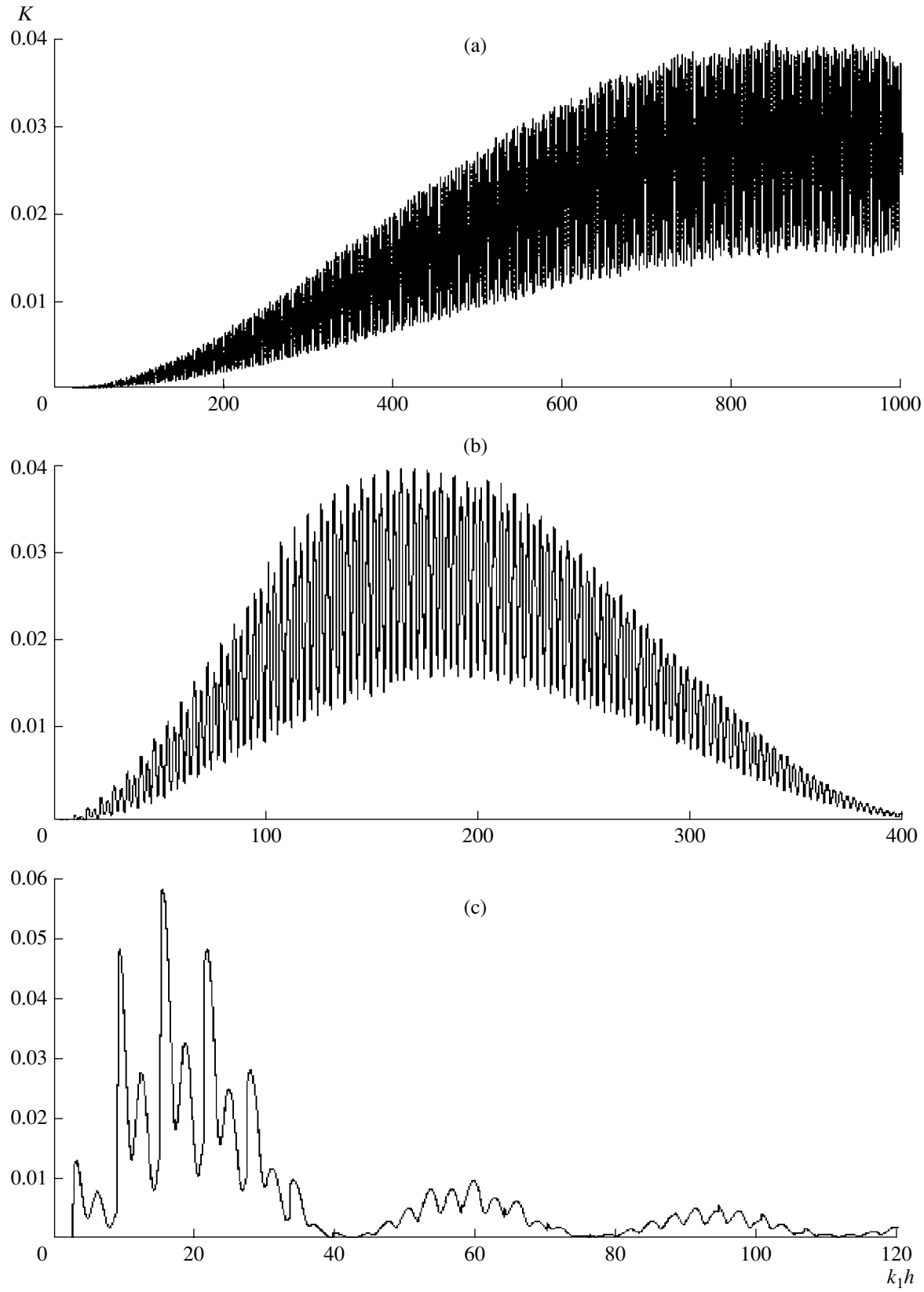

Fig. 3. Frequency dependence of the transfer coefficient K of the power radiated into the waveguide for a_1 = (a) 2×10^{-3}, (b) 10^{-2}, and (c) 10^{-1}.

$$\varphi(r, z) = \frac{p_0}{\rho_1 c_1}\frac{\pi a_1^2}{4k_1}\sum_n \frac{x_n \Phi_n}{E_n}\varphi_n(\xi_n, z)\varepsilon_n H_0^{(2)}(\xi_n r), \quad r > a. \tag{6}$$

In this case, the general solution, as well as solution (4), contain normal waves of the $n(1)$, $n(2)$, and $n(3)$ types.

Integrating the horizontal power flux corresponding to solution (6) over the waveguide cross section $z \in (0, h)$ at large distances $k_1 r \gg 1$, we obtain one more expression for the acoustic power radiated into the waveguide:

$$P_{\text{ac, 12}} = \frac{1}{2}F_0^2 \operatorname{Re}\tilde{Y}_{12}, \quad \tilde{Y}_{12} = \frac{1}{\rho_1 c_1 S}\tilde{Y}'_{12},$$

$$\operatorname{Re}\tilde{Y}'_{12} = \frac{\pi a_1^2}{8k_1 h}\sum_{n,m}\frac{\Phi_n \Phi_m x_n x_m}{E_n E_m}\sqrt{\frac{\xi_n}{\xi_m}}E_{nm}, \tag{7}$$

where

$$E_{nm} = \left[\frac{\sin(x_n - x_m)}{x_n - x_m} - \frac{\sin(x_n + x_m)}{x_n + x_m}\right]\cos((\xi_n - \xi_m)r),$$

and the summation involves only the normal waves of the $n(1)$ and $n(2)$ types.

The structure of solution (7) is such that the acoustic power corresponding to the total sound field cannot be represented as the sum of powers related to individual normal waves, which is the consequence of the nonorthogonality of the eigenfunctions $\varphi_n(\xi_n, z)$ within the interval $z \in (0, h)$. In addition, the power given by Eq. (7) retains the range dependence, but this dependence, being purely formal, is also caused by the interference interaction of the power fluxes corresponding to individual normal waves.

It is natural to assume that the component $\operatorname{Re}Y'_{12}$ given by formula (5) and the component averaged over the distance

$$\langle \operatorname{Re}\tilde{Y}_{12}\rangle_r = \frac{\pi a_1^2}{8k_1 h}\sum_n \frac{\Phi_n^2 x_n^2}{E_n^2}E_{1n}, \quad E_{1n} = 1 - \frac{\sin(2x_n)}{2x_n},$$

are equal to each other, because they correspond to the same power radiated into the waveguide. In fact, numerical estimates of these components confirm their close values. In this connection, the following interpretation of the generalized normal waves is possible.

It is known that the operator corresponding to boundary problem (1) is not self-adjoint. This means that, for the full description of the sound field in the Pekeris waveguide, one has to consider a boundary problem adjoint to problem (1) and the adjoint operator corresponding to it. The generalized normal waves of the family $n(2)$ are just a subset of the eigenfunctions of the adjoint operator with real propagation constants ($\operatorname{Im}\xi_n = 0$, $\operatorname{Im}k_{32,n} > 0$). The poles corresponding to the total set of the normal waves of $n(1)$, $n(2)$, and $n(3)$ types are located on the upper list of the Riemann surface for the root $k_{32} = \sqrt{k_2^2 - \xi^2}$ determined by the condition $\operatorname{Re}k_{32} \geq 0$. This condition determines its choice in the model problem under consideration.

It is should be noted that the cut $\operatorname{Re}k_{32} = 0$ was first used in [5] to analyze roots of the Stoneley–Scholte characteristic equation, which determines the surface waves at the boundary between liquid and solid halfspaces. In [6], the roots of the characteristic equation, which correspond to ordinary and generalized Stoneley–Scholte waves, were numerically analyzed, and the existence of the generalized Stoneley–Scholte waves was confirmed experimentally.

A closer examination of the generalized solutions and their application in solving various acoustical problems are described in [7]. The types of the generalized Stoneley–Scholte waves fully correspond to those studied theoretically and experimentally in [6].

Some properties of the generalized normal waves and their application for describing the operation of directional arrays in the Pekeris waveguide are given in [2]. Since the application of the generalized normal waves for describing the sound field in the Pekeris waveguide is unconventional, we present here some information about their structure and general properties. The most important property of the subset of ordinary and generalized normal waves of the $n(1)$ and $n(2)$ types is their generalized orthogonality within the whole domain of their definition $z \in (0, \infty)$, which formally expresses their energy independence. To clarify the relations of the generalized orthogonality, we introduce the vector functions $\mathbf{x}_n(p_n, v_{rn})$ describing the horizontal power fluxes (v_r is the radial component of the particle velocity)

$$\mathbf{x}_n^- = \begin{pmatrix} p_n^- \\ v_{rn}^- \end{pmatrix}, \quad p_n^- = \begin{cases} i\sin(k_{31,n}z)H_0^{(2)}(\xi_n^- r) \\ z \in (0, h), \quad n \in n(1) \\ i\sin(k_{31,n}h)e^{-ik_{32,n}(z-h)}H_0^{(2)}(\xi_n^- r) \\ z \in (h, \infty), \quad \operatorname{Im}k_{32,n} < 0; \end{cases} \tag{8}$$

$$\mathbf{v}_{rn}^- = \begin{cases} \xi_n^- \sin(k_{31,n}z)H_1^{(2)}(\xi_n^- r) \\ z \in (0, h), \quad n \in n(1) \\ \rho_{12}\xi_n^- \sin(k_{31,n}h)e^{-ik_{32,n}(z-h)}H_1^{(2)}(\xi_n^- r) \\ z \in (h, \infty), \quad \operatorname{Im}k_{32,n} < 0; \end{cases}$$

$$\mathbf{x}_n^+ = \begin{pmatrix} p_n^+ \\ v_{rn}^+ \end{pmatrix},$$

$$p_n^+ = \begin{cases} i\sin(k_{31,n}z)H_0^{(2)}(\xi_n^+ r) \\ z \in (0, h), \quad n \in n(2) \\ i\sin(k_{31,n}h)e^{-ik_{32,n}(z-h-L)}H_0^{(1)}(\xi_n^+ r) \\ z \in (h, \infty), \quad L \longrightarrow \infty, \quad \operatorname{Im}k_{32,n} > 0; \end{cases} \tag{9}$$

$$\mathbf{v}^{+}_{rn} = \begin{cases} \xi^{+}_n \sin(k_{31,n} z) \mathrm{H}^{(2)}_1(\xi^{+}_n r) \\ z \in (0, h), \quad n \in n(2) \\ \rho_{12} \xi^{+}_n \sin(k_{31,n} h) e^{-ik_{32,n}(z-h-L)} H^{(1)}_1(\xi^{+}_n r) \\ z \in (h, \infty), \quad L \longrightarrow \infty, \quad \mathrm{Im} k_{32,n} > 0. \end{cases}$$

With the adopted notation, the relationships of the generalized orthogonality for the normal waves of the $n(1)$ and $n(2)$ types have the canonical form

$$(\mathbf{x}_n, N\mathbf{x}_m) = E_n \delta_{nm}, \tag{10}$$

where $N = \begin{pmatrix} 0 & 1 \\ 1 & 0 \end{pmatrix}$ is the matrix operator of permutation, δ_{nm} is the Kronecker delta, $(n, m) \in n(1) \cup n(2)$, and

$$(\mathbf{x}, \mathbf{y}) = \frac{\pi r}{2h} \int_0^\infty \left(\sum_i x_i y_i^* \right) dz, \quad i = 1, 2.$$

With allowance for Eq. (10), the total power transferred by the normal waves of the $n(1)$ and $n(2)$ types in the horizontal direction is given by the expression

$$P_{\mathrm{ac},12} = \frac{1}{2}(p_0 S)^2 \mathrm{Re} Y_{12} = \frac{1}{2} \frac{p_0^2 S}{\rho_1 c_1} \frac{\pi a_1^2}{8 k_1 h} \sum_{\substack{n(1) \\ n(2)}}^{N^+ + N^-} \frac{x_n^2}{E_n} \Phi_n^2,$$

where the conductivity $\mathrm{Re} Y'_{12}$ fully coincides with definition (5) and the power is decomposed into a sum of components corresponding to individual normal (generalized normal) waves. The power (normalized) of each normal wave, or the norm of the corresponding vector-function $\mathbf{x}_n$, is determined as

$$E_n = E_{1n} \pm E_{2n}, \quad E_{1n} = 1 - \frac{\sin(2x_n)}{2x_n},$$

$$E_{2n} = \rho_{12} \frac{\sin^2 x_n}{\alpha_n h}, \quad k_{32,n} = \mp i \alpha_n, \quad \alpha_n > 0,$$

where the upper signs refer to the normal waves of the $n(1)$ type and the lower signs to the generalized normal waves of the $n(2)$ type. The components of the power flux $\pm E_{2n}$ correspond to inhomogeneous waves, which are an extension of the normal wave field from the waveguide to the halfspace. For $n(1)$-type normal waves, this extension is continuous (regular) in the sound pressure and in the normal component of the particle velocity, whereas for generalized normal waves, it is continuous only in the impedance but discontinuous (generalized) in the sound pressure and the normal component of the particle velocity.

The components of the power flux $\pm E_{2n}$ are almost completely compensated in the total field of normal waves in the halfspace. The range-averaged power transferred through the waveguide cross section $z \in (0, h)$ closely coincides with the power transferred through the cross section $z \in (0, \infty)$ of the layer–halfspace system. The exact and approximate relations between these quantities are as follows:

$$\langle \mathrm{Re} \tilde{Y}_{12} \rangle_r = \mathrm{Re} Y'_{12} + \frac{\pi a_1^2}{8 k_1 h} \left(\sum_{n(2)}^{N^+} \frac{\Phi_n^2 x_n^2}{E_n^2} E_{2n} - \sum_{n(1)}^{N^-} \frac{\Phi_n^2 x_n^2}{E_n^2} E_{2n} \right) \approx \mathrm{Re} Y'_{12},$$

where the power fluxes in the lower halfspace are better compensated the greater the number of normal (generalized normal) waves existing in the waveguide.

The description of the energy characteristics of normal waves only by the subset of $n(1)$-type waves is insufficient, because uncompensated power fluxes E_{2n} in the lower halfspace have no physical meaning: the power of a source located in the waveguide cannot be transferred though the boundary with a reactive input impedance when the incidence angle exceeds the critical one.

Estimating the operation of a piston radiator as a whole, we can note its low efficiency. The radiation into a waveguide is optimal when the size of the radiator is equal to the half-wavelength of the first critical frequency of the waveguide $\omega_{\mathrm{cr.}\,1}$; in this case, $a_{1,\,\mathrm{opt}} = 0.57$, $(k_1 h)_{\mathrm{cr.}\,1} = 2.74$, and $K_{\max} = 0.15$. For a radiator of an arbitrary size, the radiation efficiency is still lower: $K = (3–5)\%$. As the reflectivity of the water–sea bottom impedance boundary increases, the efficiency of the piston radiator operation also increases; for a rocky bottom, the coefficient K increases by a factor of 2.0–2.5.

REFERENCES

1. N. V. Zlobina, B. A. Kasatkin, and L. G. Statsenko, in *Acoustics of the Ocean: Proceedings of the VIII School–Seminar of Academician L.M. Brekhovskikh* (GEOS, Moscow, 2000), p. 118.
2. B. A. Kasatkin and L. G. Statsenko, *Energy and Field Characteristics of the Acoustic Arrays in Waveguides* (Dal'nauka, Vladivostok, 2000).
3. A. D. Lapin, Akust. Zh. **46**, 427 (2000) [Acoust. Phys. **46**, 367 (2000)].
4. L. M. Brekhovskikh, *Waves in Layered Media*, 1st ed. (Nauka, Moscow, 1957; Academic, New York, 1960).
5. J. H. Ansell, Pure Appl. Geophys. **194**, 172 (1972).
6. F. Padilla, M. de Billy, and G. Quentin, J. Acoust. Soc. Am. **106**, 666 (1999).
7. B. A. Kasatkin and N. V. Zlobina, *Nonclassical Solution of Classical Acoustical Problems* (Dal'nauka, Vladivostok, 2000).

Translated by Yu. Lysanov

Acoustical Physics, Vol. 48, No. 1, 2002, pp. 62–68. Translated from Akusticheskiĭ Zhurnal, Vol. 48, No. 1, 2002, pp. 70–76.

Near Field of a Low-Frequency Source of Forced Vibration on a Layered Biological Tissue

B. N. Klochkov

Applied Physics Institute, Russian Academy of Sciences, ul. Ul'yanova 46, Nizhni Novgorod, 603950 Russia
e-mail: klochkov@appl.sci-nnov.ru

Received October 2, 2000

Abstract—Results of a numerical calculation of the near acoustic field excited by a low-frequency source of forced vibration positioned on the surface of a layered biological tissue are presented. The latter is simulated by a soft tissue layer varying in thickness and overlying a solid halfspace. The spatial distribution of the acoustic field in the biological tissue is obtained. © *2002 MAIK "Nauka/Interperiodica".*

Investigation of a near acoustic field excited by a low-frequency source of forced vibration placed on the surface of a layered biological tissue is important from the point of view of determining the layered structure of the tissue (the layer thickness) and the elastic parameters (the shear moduli of the layers) depending on the tissue state. Attempts to determine the acoustomechanical parameters of a biological tissue and its structure are described in the literature [1–14]. Local and nonlocal quasistatic methods [5–9, 11, 14], wave methods [2–4, 9], and ultrasonic techniques for visualization of the elastic properties of tissues and for tomographic examinations [1, 10, 12, 13] are used in this case. This concerns, first of all, the soft tissues that are responsible for the functional state of a living body and also the hard tissues responsible for supporting the body and for defensive functions. Longitudinal ultrasonic waves, when used in tissues, usually provide information only on the layered nature of a tissue and its volume compressibility. Therefore, the studies of tissues by shear waves [3, 4, 9], including surface waves, are conducted to obtain information on the structure of layers and their shear elastic parameters. The successful studies are those of simple homogeneous samples in which known types of shear waves (e.g., rod waves), whose parameters involve the elastic modulus in an explicit analytical way, are excited.

The problem is much more complex in actual conditions when a layered structure is present with both soft and hard layers. Several types of waves occur in the wave field simultaneously, and the presence of the reactive component, the so-called near field, is essential. This is especially characteristic of soft (water-like) layers. It is difficult to separate the wave modes from the reactive component, and this is a separate problem. The acoustic field is mainly concentrated near the source, at a distance of several wavelengths, because of the strong damping both at the surface and in the depth of a soft tissue. An analytical representation relating the wave field to the structure and the viscoelastic properties of layers in such a system is cumbersome. A certain way out is the utilization of numerical methods of the wave field calculation and also the development of computational algorithms for the determination of the layer thickness, the elastic moduli, and other parameters on their basis. The calculation of low-frequency vibroacoustic fields is important also for the problems of the ultrasonic imaging of tissue structure and its viscoelastic properties [1, 3, 7–10]. As applied to layered biological tissues, a method for the numerical calculation of near acoustic fields produced by a surface source of forced vibrations along the surface of a tissue [15–20] and within it [15, 21, 22] was developed with averaging over the area of a vibrating stamp [17, 19] and without averaging. This method was used for describing the field of normal and tangential components of displacements [15–20], the propagation of surface waves [15–17, 19], and mechanical impedance [19, 21, 22]. It is necessary to note that, in the case of a three-layer model of a biological tissue, rather good agreement of the calculated frequency dependences of mechanical impedance with experiment was obtained [5, 6]. The calculation for the mechanical impedance of a gelatin layer [23] was conducted using the methods developed in [15–22], and an attempt was made to compare it with the measurements.

In this paper, we ignore the detailed structure of biological tissue and represent it as a two-layer medium with widely different shear moduli and with the internal layer being a halfspace. Primary attention is given to the numerical calculation of the near acoustic fields excited by a surface source of forced vibrations that is positioned on the soft external layer (a viscous water-like tissue) linked with a hard halfspace (a weakly dissipative elastic material), which is common for an endoskeleton (a bone inside). This paper presents the

1063-7710/02/4801-0062$22.00

results of calculating the frequency dependences of the displacement field for both normal and tangential components and the calculated spatial distribution of the displacement field over the surface of the tissue and in its depth. The method of integral representations of the Lamb type was used to calculate the near wave fields by analogy with similar calculations in seismology [24].

The excitation of elastic waves was conducted by a surface source of forced vibrations (a stamp) normally to the surface (the layered halfspace occupied the region $z \geq 0$, and the r axis was directed along the tissue surface from the stamp). It was assumed that the component of the stress tensor $\sigma_{zz} = \sigma_0 \exp(i\omega t)$ (σ_0 is the amplitude of the normal component of stress and ω is the frequency) was distributed uniformly over the circular surface area of radius a under the source. Beyond this area, $\sigma_{zz} = 0$, and the other component is $\sigma_{zr} = 0$ over the whole surface $z = 0$. On both sides of the contact surface of the layer and the halfspace $z = h$, the normal and tangential components W^n and W^t of the displacement vector must be equal by virtue of the assumed condition of a tight mechanical link, and the normal and tangential components of the stress tensor σ_{zz} and σ_{zr} must also be equal. In addition, it is assumed that the materials of the layer and the halfspace can be described by common linear equations of the Lame elasticity theory in the cylindrical coordinates r and z with allowance for dissipation in the soft medium within the framework of the Kelvin–Voigt model. The major parameters of a two-layer tissue are the Lame constants λ_n and μ_n and the density ρ_n; the index $n = 1$ corresponds to the parameters of the soft medium; μ_1 is an operator: $\mu_1 \Rightarrow \mu_1 + \mu_1' \partial/\partial t$, where μ_1' is the viscosity coefficient; and $n = 2$ corresponds to the hard medium.

By introducing the scalar and vector potentials and the Hankel transformation in the equations and boundary conditions, we obtain a set of algebraic equations with respect to the unknowns A, B, C, D, E, and F:

$$(2k^2 - k_{s1}^2)A + (2k^2 - k_{s1}^2)B - 2k^2\nu_1' C + 2k^2\nu_1' D = -\sigma_0 a J_1(ka)/(k\mu_1), \quad (1)$$

$$2k\nu_1 A - 2k\nu_1 B - k(2k^2 - k_{s1}^2)C - k(2k^2 - k_{s1}^2)D = 0, \quad (2)$$

$$\mu_1[(2k^2 - k_{s1}^2)e^{-\nu_1 h}A + (2k^2 - k_{s1}^2)e^{\nu_1 h}B - 2k^2\nu_1' e^{-\nu_1' h}C + 2k^2\nu_1' e^{\nu_1' h}D] = \mu_2[(2k^2 - k_{s2}^2)e^{-\nu_2 h}E - 2k^2\nu_2' e^{-\nu_2' h}F], \quad (3)$$

$$\mu_1[-2\nu_1 e^{-\nu_1 h}A + 2\nu_1 e^{\nu_1 h}B + (2k^2 - k_{s1}^2)e^{-\nu_1' h}C + (2k^2 - k_{s1}^2)e^{\nu_1' h}D] = \mu_2[-2\nu_2 e^{-\nu_2 h}E + (2k^2 - k_{s2}^2)e^{-\nu_2' h}F], \quad (4)$$

$$e^{-\nu_1 h}A + e^{\nu_1 h}B + \nu_1'[-e^{-\nu_1' h}C + e^{\nu_1' h}D] = e^{-\nu_2 h}E - \nu_2' e^{-\nu_2' h}F, \quad (5)$$

$$\nu_1(-e^{-\nu_1 h}A + e^{\nu_1 h}B) + k^2(e^{-\nu_1' h}C + e^{\nu_1' h}D) = -\nu_2 e^{-\nu_2 h}E + k^2 e^{-\nu_2' h}F, \quad (6)$$

where

$$\nu_n = \sqrt{k^2 - k_{pn}^2}, \quad \nu_n' = \sqrt{k^2 - k_{sn}^2},$$

$$k_{pn}^2 = \frac{\omega^2 \rho_n}{\lambda_n + 2\mu_n}, \quad k_{sn}^2 = \frac{\omega^2 \rho_n}{\mu_n},$$

and k is the propagation constant with respect to r.

Solving the set of equations (1)–(6) for the displacement components normal and tangential to the surface, we obtain rather cumbersome expressions in the form of integrals with respect to the tangential wave numbers k, which are the inverse Hankel transformations of the zeroth and first order [15–19]. We obtain for the soft layer

$$W^n(r, z) = \int_0^\infty [\nu_1(Be^{\nu_1 z} - Ae^{-\nu_1 z}) + k^2(Ce^{-\nu_1' z} + De^{\nu_1' z})]kJ_0(kr)dk, \quad (7)$$

$$W^t(r, z) = -\int_0^\infty [Ae^{-\nu_1 z} + Be^{\nu_1 z} + \nu_1'(De^{\nu_1' z} - Ce^{-\nu_1' z})]k^2 J_1(kr)dk, \quad (8)$$

where J_m is the Bessel function of order m. The values of the components W^n and W^t are determined numerically. It is well known that it is possible to obtain an asymptotic expression for integrals of this form at rather large distances from the source. The values of integrals (7) and (8) near the source can be determined only using numerical methods. It is necessary to keep in mind that the denominator of the integrand Δ [Δ is the determinant of the system of the boundary conditions of the sixth order (1)–(6)] has a finite number of zeros of the first order, which correspond to surface waves. The integration method taking into account the poles and the branch points is selected in such way that the energy flux in the waves is directed away from the source. At $z > h$, the waves must be either exponentially decaying or propagating in the direction of increasing z.

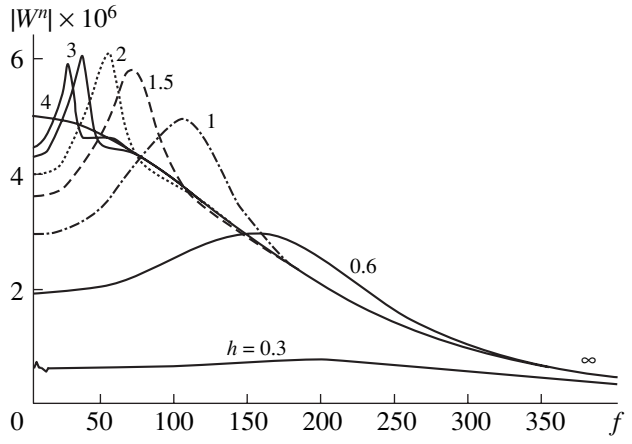

Fig. 1. Amplitude of normal displacements (in centimeters) at point 0 on a layered tissue as a function of frequency (in hertz) for various values of the soft layer thickness.

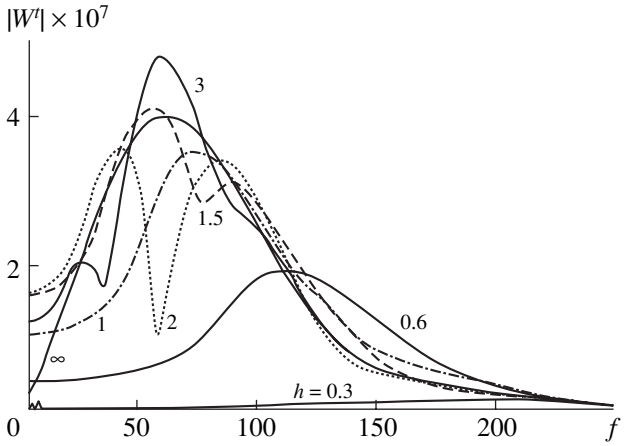

Fig. 2. Amplitude of tangential displacements (in centimeters) at point 1 on a layered tissue as a function of frequency (in hertz) for various values of the soft layer thickness.

The values of the parameters of the biological tissue layers were selected as follows [25]: $\lambda_1 = 2.67 \times 10^{10}$ dyn/cm^2, $\mu_1 = 5 \times 10^4$ dyn/cm^2, $\rho_1 = 1.05$ g/cm^3, and $\mu_1' = 25$ dyn/cm^2 for the soft layer; $\lambda_2 = 5.7 \times 10^{10}$ dyn/cm^2, $\mu_2 = 6.4 \times 10^{10}$ dyn/cm^2, and $\rho_2 = 1.6$ g/cm^3 for the hard halfspace. The source radius was $a = 0.5$ cm and the normal stress amplitude was $\sigma_0 = 1$ dyn/cm^2. The thickness of the soft layer was varied: $h = 0.3$, 0.6, 0.85, 1, 1.05, 1.1, 1.5, 2, 3, 4 cm and ∞ (a halfspace).

The values of the complex amplitudes of normal and tangential displacements were determined as the functions of the source frequency f for various distances from the source center along the surface. The results of calculation are given in Fig. 1 (the normal components of the displacement) and Fig. 2 (the tangential components of the displacement). The amplitude–frequency and phase–frequency characteristics of the wave field are most clearly defined and rather simple exactly at the point 0 ($r_0 = 0$, $z = 0$) under the stamp (Fig. 1). Characteristic resonance peaks are visible in the amplitude–frequency dependences for each layer thickness h. These peaks manifest themselves also in the phase–frequency dependence. In the case of a halfspace, the peak meets the ordinate axis $f = 0$. The following distinctive features of the influence of the layer thickness h are essential. As h increases, the peak shifts monotonically to the low-frequency region. Its value increases up to approximately $h = 2$ cm and then decreases starting from $h = 3$ cm and tending to the case of a halfspace. Additionally, the increase in h is accompanied by the narrowing of the resonance. If the layer thickness decreases below the value $h = 2$ cm, the peak becomes noticeably smaller and wider. In the case of rather high frequencies f, these layer effects vanish and the dependence of the displacement on frequency becomes close to the one in the case of the halfspace. In this case, the amplitude curves for rather thin layers are below the curve for the halfspace. Similar effects manifest themselves in the calculations of the tissue rigidity proportional to $1/W^n$ and also in the mechanical impedance [19]. In the case of averaging over the stamp area, the pattern exhibits little qualitative changes; whereas, quantitatively, a certain decrease in the average displacement is observed, the values of the average rigidity are somewhat higher, and the values of the average impedance are also greater. A characteristic frequency irregularity with sharp dips in the ranges 10–80 Hz and 100–150 Hz and around 300 Hz is observed in the amplitude–frequency dependence of the normal displacements at point 1 ($r_1 = 2.5$ cm, $z = 0$) [19]. The phase–frequency characteristic at point 1 is sufficiently monotonic, excluding the region around 300 Hz, the low-frequency range 10–80 Hz, and also the range about 150–180 Hz for $h = 0.85$ cm. The phase variation with frequency in the range 100–150 Hz is relatively large for all values of h. The indicated irregularity is characteristic of the complex near field produced by the vibration source at the tissue surface, while the corresponding curves are already noticeably smoother at point 2 ($r_2 = 4.5$ cm, $z = 0$). This is confirmed by special calculations of the spatial distribution of the vibration field [18, 21, 22].

An essential difference from the normal displacements is observed for the tangential displacements at point 1 (at point 0 under the stamp, the tangential displacements are equal to zero), which is connected with the resonance maximums and minimums at different frequencies depending on the thickness h (Fig. 2). The greatest dip is observed for the layer with $h = 2$ cm at the frequency f about 56 Hz (the split main resonance). At $h > 2$ cm, the dip depth decreases and it shifts towards lower frequencies; at $h < 2$ cm, the dip depth decreases also, but it shifts towards higher frequencies. In the case of a halfspace ($h = \infty$) and $h = 1$, 0.85, 0.6,

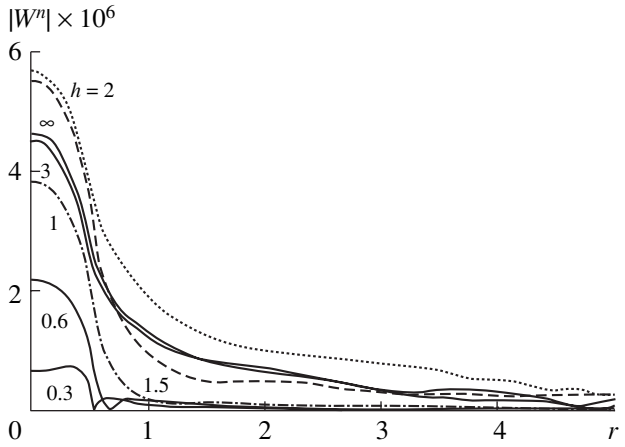

Fig. 3. Spatial distribution of the amplitude of normal displacements (in centimeters) over the surface of a layered tissue (distance in centimeters) for various values of the soft layer thickness at $f = 60$ Hz.

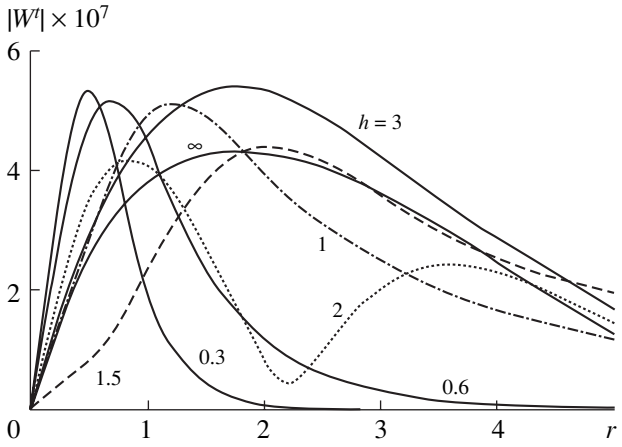

Fig. 4. Spatial distribution of the amplitude of tangential displacements (in centimeters) over the surface of a layered tissue (distance in centimeters) for various values of the soft layer thickness at $f = 60$ Hz.

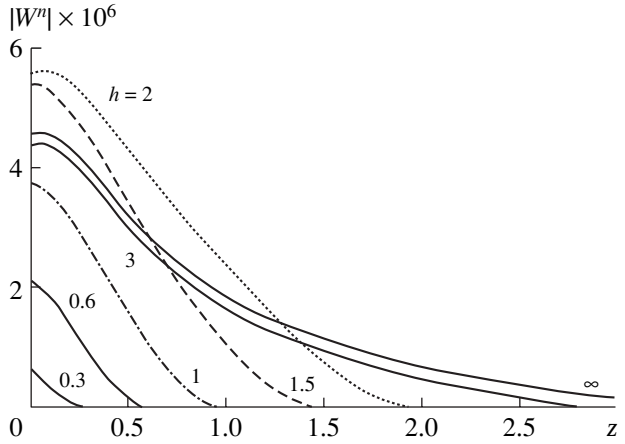

Fig. 5. Spatial distribution of the amplitude of normal displacements (in centimeters) within a layered tissue (depth in centimeters) for various values of the soft layer thickness at $f = 60$ Hz.

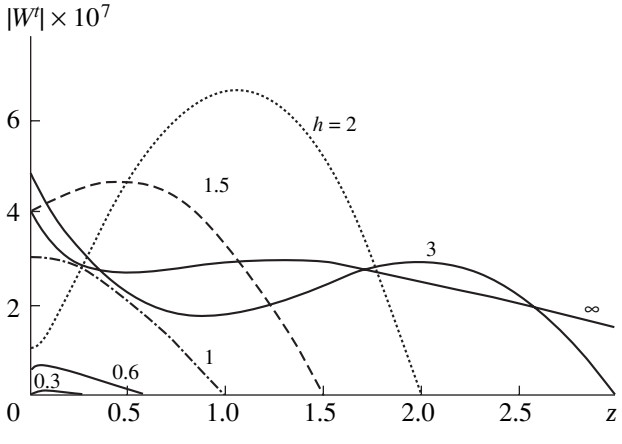

Fig. 6. Spatial distribution of the amplitude of tangential displacements (in centimeters) within a layered tissue (depth in centimeters) for various values of the soft layer thickness at $f = 60$ Hz.

and 0.3 cm, no dips are observed. This is reflected in the corresponding phase characteristics, a noticeable minimum being present at $f \approx 56$ Hz for $h = 2$ cm.

The spatial distribution of the near acoustic field produced by a surface source of forced vibrations positioned on a soft layered biological tissue (along its surface and within it) was calculated for the frequencies $f = 60$ and 70 Hz (Figs. 3–8) and also for $f = 130$ Hz at $h = 1$ and 2 cm [18, 21, 22]. The elastic near field along the surface (in r) is given in Figs. 3 and 4 for $z = 0$ and $f = 60$ Hz. The amplitudes of the normal components of displacement decrease relatively fast with the distance r from the vibrating stamp, the amplitude value for rather thick layers ($h \geq 1$ cm) being much higher than in the case of thin layers ($h < 1$ cm). The normal field is considerably large at the distances 0.5–1 cm. These laws are also reflected in the corresponding phase characteristics of the normal components, the phase change near the source in the case of thin layers being greater than for the thick layers. The amplitudes of tangential components near the source are much smaller in value than the amplitudes of normal components, and they behave nonmonotonically with varying the distance r. A peak is observed for all h, and, in the case of $h = 2$ cm, two peaks are present. The tangential field for thin layers $h = 0.3$ and 0.6 cm is concentrated near the source. The phase of the tangential components of displacements decreases with distance for all h, except for $h = 0.3$ and 1.5 cm. At the frequency $f = 130$ Hz, the elastic field behaves nonmonotonically, the interference effects being more pronounced for $h = 2$ cm than for $h = 1$ cm. On the average, the slopes of the

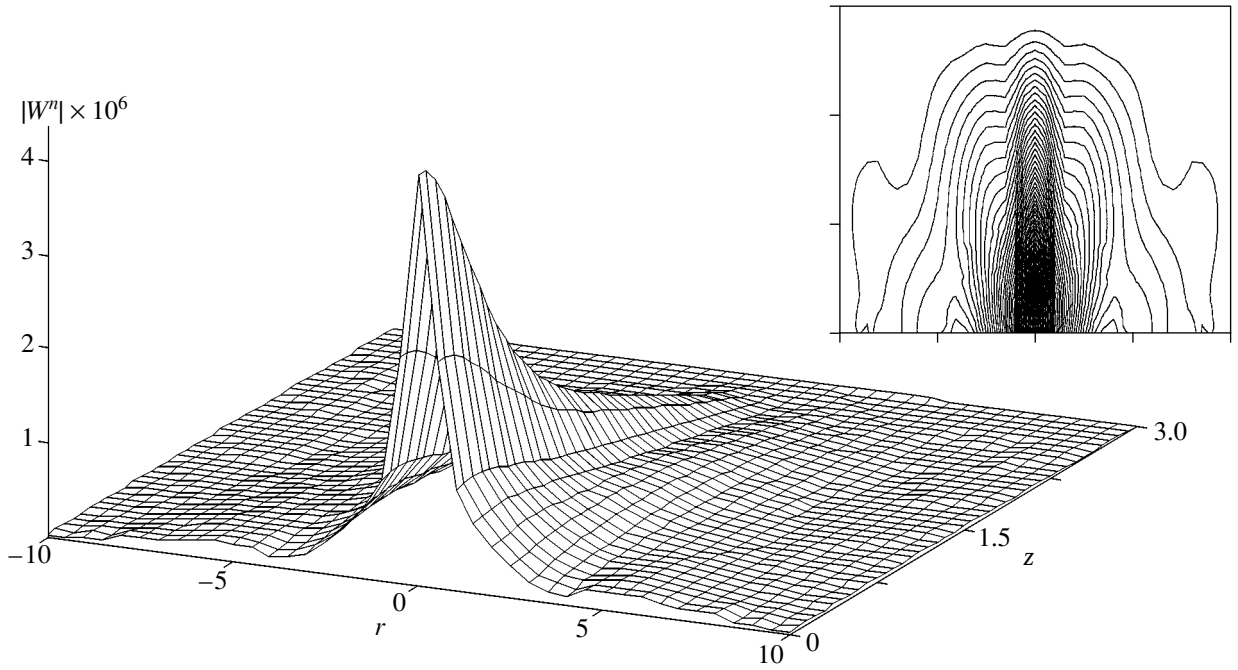

Fig. 7. Two-dimensional distribution of the amplitude of normal displacements (in centimeters) over the surface and in the depth of a layered tissue (in centimeters) for $h = 3$ cm and $f = 70$ Hz. The level curves (within the same limits in r and z) are shown at the top right of the figure.

amplitude curves obtained for these layers for each of the displacement components are rather close, and the skin-layer at this frequency is rather thin. From the corresponding phase dependences, it follows that the phase difference near the source is small for the layers with $h = 1$ and 2 cm, but it increases with distance. At the same time, the phase differences between the normal and tangential components of displacements behave nonmonotonically.

The distribution of the near acoustic field within the layered tissue (in z) for $f = 60$ Hz is given in Figs. 5 and 6. The amplitudes of normal displacements at $r = r_0$ within the tissue decrease with depth. An exception is a very narrow region near the source for $h = 2$ and 3 cm, where a small peak is present. In this case, the phases of normal components decrease noticeably with depth for the layers with $h > 1.5$ cm, whereas the phase variation is small within the layers with $h \le 1.5$ cm. The amplitudes of the tangential components of displacements at $r = r_1$ vary nonmonotonically with depth z for different h, the peak growing and shifting deeper with the increase in the layer thickness h up to $h = 2$ cm, and for $h = 3$ cm and $h = \infty$, the behavior is even more nonmonotonic: there are two zones of decrease and one zone of increase with depth. Simultaneously, the phases of the tangential components decrease with depth for the layers with $h > 1.5$ cm, and for $h \le 1.5$ cm, the phase variation is small.

The two-dimensional distribution (in r and z) of the elastic field of a surface source of vibrations is represented in Figs. 7 and 8 in the form of a surface and in the form of level curves for $f = 70$ Hz and $h = 3$ cm. A characteristic peak at the point of the source position is visible for the normal component of the displacement. Its behavior is nonmonotonic in r far from the source and in z near it (Fig. 7). The distribution of the level curves around the source is also visible. A more complex pattern is observed for the tangential component of the displacement: it is equal to zero at the point of the source position $r = r_0$, and when the distance from it increases, the tangential field exhibits several peaks, which is reflected in the plots of both the surface and the level curves (Fig. 8).

In conclusion, it should be noted that, from the described rather complete investigations of the near acoustic fields excited by a source of forced vibrations at the surface of a layered biological tissue, it follows that, in the low frequency range, it is possible to represent common tissues of a live body by a viscoelastic water-like layer rigidly bound with a hard elastic layer (in particular, a halfspace). A strong effect of the soft layer thickness on the frequency characteristics of the acoustic field is revealed. The spatial distributions of the acoustic field over the surface and within the tissue are obtained. Surface waves are convenient for the investigation of biological tissues and sensitive to their structural and functional changes. The results of this study allow us to hope for the possibility of solving the inverse problem, i.e., to determine the structure of a layered tissue (in particular, the layer thickness) and its

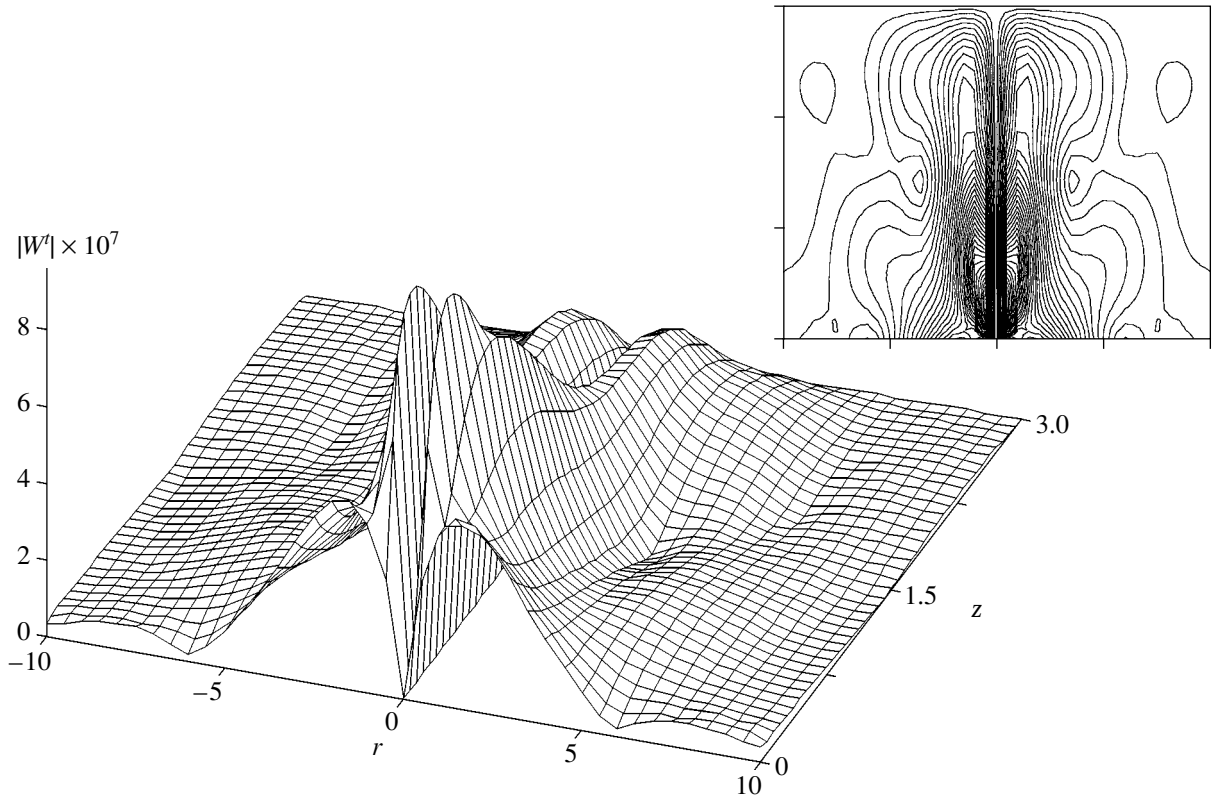

Fig. 8. Two-dimensional distribution of the amplitude of tangential displacements (in centimeters) over the surface and in the depth of a layered tissue (in centimeters) for $h = 3$ cm and $f = 70$ Hz. The level curves (within the same limits in r and z) are shown at the top right of the figure.

viscoelastic parameters from the characteristics of the transverse and longitudinal components of displacements in the near field in various types of layered tissues. This is important from the point of view of the evaluation of the state of a tissue as a complex reacting medium, as well as for the development of the foundations of linear tissue tomography utilizing surface waves.

ACKNOWLEDGMENTS

This work was supported by the Russian Foundation for Basic Research, project no. 97-02-18612.

REFERENCES

1. Y. Yamakoshi, J. Sato, and T. Sato, IEEE Trans. Ultrason. Ferroelectr. Freq. Control **37** (2), 45 (1990).
2. O. V. Rudenko and A. P. Sarvazyan, Biomed. Radioelektron., No. 3, 6 (2000).
3. A. P. Sarvazyan, O. V. Rudenko, S. D. Swanson, *et al.*, Ultrasound Med. Biol. **24** (9), 1419 (1998).
4. V. G. Andreev, V. N. Dmitriev, Yu. A. Pishchal'nikov, *et al.*, Akust. Zh. **43**, 149 (1997) [Acoust. Phys. **43**, 123 (1997)].
5. A. R. Skovoroda and S. R. Aglyamov, Mat. Model. **9** (8), 119 (1997).
6. A. R. Skovoroda and S. R. Aglyamov, Biofizika **43** (2), 348 (1998).
7. A. R. Skovoroda and S. R. Aglyamov, Biofizika **40** (6), 1329 (1995).
8. A. R. Skovoroda, Biofizika **45** (4), 723 (2000).
9. S. R. Aglyamov and A. R. Skovoroda, Biofizika **45** (6), 1137 (2000).
10. L. Gao, K. J. Parker, R. J. Lerner, and S. F. Levinson, Ultrasound Med. Biol. **22** (8), 959 (1996).
11. T. J. Royston, H. A. Mansy, and R. H. Sandler, J. Acoust. Soc. Am. **106**, 3678 (1999).
12. V. A. Burov, S. N. Sergeev, and O. D. Rumyantseva, Biomed. Radioelektron., No. 3, 61 (2000).
13. I. Yu. Demin, T. Sato, K. Kameyama, *et al.*, Akust. Zh. **41**, 508 (1995) [Acoust. Phys. **41**, 447 (1995)].
14. E. V. Bukhman, S. G. Gershman, V. D. Svet, *et al.*, Akust. Zh. **40**, 336 (1994) [Acoust. Phys. **40**, 306 (1994)].
15. R. Kh. Aksenova, V. A. Antonets, V. V. Kazakov, *et al.*, in Summary Report No. 01,860,087,893, Code "Kubik," IPF RAN (Inst. of Applied Physics, Russian Academy of Sciences, Nizhni Novgorod, 1991), pp. 7–72.
16. B. N. Klochkov and A. V. Sokolov, Akust. Zh. **40**, 270 (1994) [Acoust. Phys. **40**, 244 (1994)].
17. B. N. Klochkov and A. V. Sokolov, Akust. Zh. **41**, 512 (1995) [Acoust. Phys. **41**, 451 (1995)].

18. B. N. Klochkov and A. V. Sokolov, in *Book of Abstracts of XV Congress of the International Society of Biomechanics, 1995* (Jyvaskyla, Finland, 1995), p. 488.
19. B. N. Klochkov and A. V. Sokolov, Preprint No. 445, IPF RAN (Inst. of Applied Physics, Russian Academy of Sciences, Nizhni Novgorod, 1997).
20. B. N. Klochkov and A. V. Sokolov, in *Abstracts of Papers of IV All-Russian Conference on Biomechanics, Nizhni Novgorod, 1998*, p. 60.
21. B. N. Klochkov and A. V. Sokolov, in *Abstracts of Papers of II All-Russian Conference on Biomechanics, Nizhni Novgorod, 1994*, Vol. 2, p. 63.
22. B. N. Klochkov and A. V. Sokolov, in *Abstracts of Papers of Jubilee Scientific Conference Dedicated to 100-Year Anniversary of Radio and 50-Year Anniversary of Radiophysical Faculty* (Nizhni Novgorod State Univ., Nizhni Novgorod, 1995), p. 38.
23. E. V. Eremin and E. M. Timanin, Akust. Zh. **46**, 490 (2000) [Acoust. Phys. **46**, 421 (2000)].
24. W. Nowacki, *Teoria Sprezystosci* (PWN, Warszawa, 1970; Mir, Moscow, 1975).
25. V. A. Berezovskiĭ and N. N. Kolotilov, *Biophysical Characteristics of Human Tissue: A Handbook* (Naukova Dumka, Kiev, 1990).

Translated by M. Lyamshev

Acoustical Physics, Vol. 48, No. 1, 2002, pp. 69–75. Translated from Akusticheskiĭ Zhurnal, Vol. 48, No. 1, 2002, pp. 77–84.

Sound Diffraction by an Inhomogeneity in an Oceanic Waveguide

V. M. Kuz'kin

Wave Research Center, General Physics Institute, Russian Academy of Sciences, ul. Vavilova 38, Moscow, 119991 Russia

e-mail: gera@kapella.gpi.ru

Received December 25, 2000

Abstract—Sound diffraction by a moving inhomogeneity in a shallow sea is considered as applied to a shadow observation system. An expression for the perturbation formed by a group of in-phase excited normal modes is obtained in the WKB approximation. The perturbation characteristics are estimated depending on the shadow contour of the inhomogeneity and the observation conditions. A small-parameter model of diffraction is proposed in the framework of the averaged description of a multimode pattern of the diffraction shading. Conditions for the model applicability are formulated © *2002 MAIK "Nauka/Interperiodica"*.

INTRODUCTION

Development of a model, which provides an opportunity to analyze the results of a numerical calculation of the acoustic field diffraction by localized inhomogeneities in underwater sound channels, is very important for solving many problems of ocean acoustics. In particular, for inhomogeneity motion along the normal to a reference line connecting the source with the receiver, a simple physical model was suggested by Gorskiĭ *et al.* and Kuz'kin [1, 2]. This model agrees well with the results of numerical calculations and provides an opportunity to qualitatively understand and quantitatively estimate the characteristics of a perturbed field [3–6]. The fruitfulness of the utilization of this model in the problems of matched processing was demonstrated in earlier papers [2, 7, 8]. However, as numerical calculations [3, 9] show, this model is inadequate when an inhomogeneity crosses the reference line at an angle different from $\pi/2$. Therefore, it seems important to consider a more general case of inhomogeneity observation in the vicinity of the reference line with the use of the shadow scattered field.

This paper presents a theoretical analysis of this problem. The consideration is based on the isotropy of scattering in the vertical plane and on a "rather narrow" spectrum of eigenvalues.

QUALITATIVE CONSIDERATIONS

Let a stationary point source be positioned at the point $Q(\mathbf{r}_0, z_0)$ with the coordinates $\mathbf{r}_0 = (0, 0)$ and $z = z_0$, the geometric center of an inhomogeneity be positioned at the point $S(\mathbf{r}_s, z_s)$ with the coordinates $\mathbf{r}_s = (x_s, y_s)$ and $z = z_s$, and a stationary receiver, at the point $G(\mathbf{r}, z_r)$ with the coordinates $\mathbf{r} = (x_r, y_r)$ and z_r, where $\mathbf{r} = (x, y)$ is the radius-vector in the horizontal plane. We consider the case of monochromatic radiation with the frequency f and the motion of an inhomogeneity in the horizontal plane (at a fixed depth z_s) with a constant velocity v at an angle γ to the reference line. We understand that the angle γ is the angle between the vector of the velocity $\mathbf{v}$ of the inhomogeneity and the positive direction of the reference line (from the source towards the receiver), which is measured in the counterclockwise direction. We denote the horizontal distance between the source and the receiver by R and the distances from the point, at which the inhomogeneity crosses the reference line,

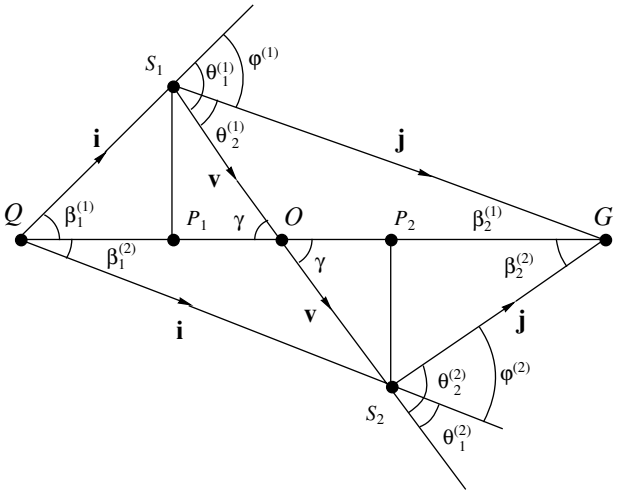

Problem geometry. Top view. (Q is the source, $S_{1,2}$ is the inhomogeneity, and G is the receiver.)

$QG = R$, $QO = R_1$, $OG = R_2$, $S_1P_1 = y^{(1)}$, $P_1O = x^{(1)}$, $S_2P_2 = y^{(2)}$, $OP_2 = x^{(2)}$, $QS_1 = r_s^{(1)}$, $S_1G = r_r^{(1)}$, $QS_2 = r_s^{(2)}$, and $S_2G = r_r^{(2)}$.

1063-7710/02/4801-0069$22.00 © 2002 MAIK "Nauka/Interperiodica"

to the source and the receiver, by R_1 and R_2, respectively ($R_1 + R_2 = R$). The figure presents the problem geometry for the angle $\gamma < \pi/2$. The upper indices 1 and 2 marking the distances $r_{s,r}$, x, y, and the angles $\beta_{1,2}$, $\theta_{1,2}$, φ refer to the cases of the inhomogeneity approaching the reference line and moving away from it, respectively.

Conditions for the sound propagation in the ocean are such [10, 11] that the field is effectively formed by a small number of constructively interfering groups of modes of the same type with close numbers. Further, as in [2], we assume that, within the range of numbers of the group of modes under consideration, the scattering in the vertical plane is isotropic (all directions of reradiation from the mode m of an incident wave into the mode μ of a scattered wave are equivalent) and the range of eigenvalues is "rather narrow." Assuming that the scattering is isotropic within the range of the Brillouin grazing angles of the propagating modes, we proceed to a considerably simplified model. Nevertheless, it allows us to reveal the influence of the oceanic medium on the characteristics of a perturbed field in an underwater sound channel and is rather close to actual conditions when the field is formed by a relatively small number of modes with close numbers.

In this case, under the assumption that the effects of multiple scattering are small [12] and the medium is locally inhomogeneous [13], the field diffracted by the inhomogeneity can be represented according to [14] in the form

$$\begin{aligned} &u_s(\mathbf{r}, z_r; 0, z_0) \\ &= F(\mathbf{j}, \mathbf{i}) u_1(r_s, z_s; 0, z_0) u_2(r_r, z_r; \mathbf{r}_s, z_s), \end{aligned} \tag{1}$$

where $F(\mathbf{j}, \mathbf{i})$ is the scattering amplitude describing the amplitude and phase of a scattered wave in the far wave field in the direction $\mathbf{j}$ on the condition that a plane wave propagating in the direction $\mathbf{i}$ is incident on the body;

$$\begin{aligned} u_{1,2} &= \frac{i}{4}\sqrt{\frac{2}{\pi}}\exp(-i\pi/4) \\ &\times \sum_{m,\mu} \frac{\exp(i\xi_{m,\mu} r_{s,r} - \kappa_{m,\mu} r_{s,r})}{\sqrt{\xi_{m,\mu} r_{s,r}}} \psi_{m,\mu}(z_{0,s}) \psi_{m,\mu}(z_{s,r}) \end{aligned} \tag{2}$$

are the fields of the point sources at the distance r_s from the source to the inhomogeneity and at the distance $r_r = |\mathbf{r} - \mathbf{r}_s|$ from the inhomogeneity to the receiver, respectively. Here, $\psi_m(z)$, ξ_m, and κ_m are the orthonormal eigenfunction, the propagation constant, and the modal attenuation coefficient of the mth mode. Different factors in Eq. (1) are separated in a convenient way. The diffraction effects are characterized by the scattering function F, and the waveguide propagation is reflected in the source functions u_1 and u_2.

Now, if we use the WKB asymptotics of eigenfunctions to describe the field of the point source produced by the in-phase excited group of modes, Eq. (1) can be reduced to the form [10]

$$u_s = A_s F(\mathbf{j}, \mathbf{i})(\xi_l^2 r_s r_r)^{-1/2} W_1 W_2 \exp(i\xi_l r - \kappa_l r), \tag{3}$$

where

$$A_s = \frac{i}{32\pi}[h_l(z_0) h_l^2(z_s) h_l(z_r)]^{-1/2} \left[\int_{-H}^{z_l} \frac{ds}{h_l(s)}\right]^{-2}, \tag{4}$$

$$r = r_s + r_r,$$

$$\begin{aligned} W_{1,2} &= (a_{1,2} + b_{1,2})\exp(-i2N\phi_{1,2}) \\ &+ (c_{1,2} + d_{1,2})\exp(i2N\phi_{1,2}). \end{aligned} \tag{5}$$

The following notations are used in Eqs. (4) and (5):

$$a_{1,2} = \frac{\sin\left[(2N+1)\left(\frac{\alpha r_{s,r}}{2} + \vartheta_{1,2}\right)\right]}{\sin\left(\frac{\alpha r_{s,r}}{2} + \vartheta_{1,2}\right)},$$

$$b_{1,2} = \frac{\sin\left[(2N+1)\left(\frac{\alpha r_{s,r}}{2} + \phi_{1,2}\right)\right]}{\sin\left(\frac{\alpha r_{s,r}}{2} + \phi_{1,2}\right)},$$

$$c_{1,2} = \frac{\sin\left[(2N+1)\left(\frac{\alpha r_{s,r}}{2} - \vartheta_{1,2}\right)\right]}{\sin\left(\frac{\alpha r_{s,r}}{2} - \vartheta_{1,2}\right)},$$

$$d_{1,2} = \frac{\sin\left[(2N+1)\left(\frac{\alpha r_{s,r}}{2} - \phi_{1,2}\right)\right]}{\sin\left(\frac{\alpha r_{s,r}}{2} - \phi_{1,2}\right)}, \tag{6}$$

$$\vartheta_{1,2} = \frac{\pi}{2}[D_l(z_{s,r}) + D_l(z_{0,s})],$$

$$\phi_{1,2} = \frac{\pi}{2}[D_l(z_{s,r}) - D_l(z_{0,s})],$$

$$\alpha = d\xi_l/dl = -2\pi/D_l.$$

Here, $h_l(z) = [(\omega/c(z))^2 - \xi_l^2]^{1/2}$ is the vertical component of the wave vector of the lth mode, in whose vicinity the neighboring modes are in phase; $\bar{z}_l$ is the upper turning point, which may also be located at the surface $z = 0$; H is the waveguide depth; D_l is the cycle length of the ray corresponding to the mode with the number l; $D_l(z)$ is the horizontal distance, which the ray travels from the upper turning point until it reaches the depth z; and N is the number of constructively interfering

modes. Estimates of their number can be found, e.g., in [10, 11].

In the WKB approximation, the field of a point source that is produced at the reception point by the in-phase excited group of modes is equal to [10]

$$u_0(r, z_r; 0, z_0) = A_0(\xi_l R)^{-1/2} W_0 \exp(i\xi_l R - \kappa_l R), \quad (7)$$

where

$$A_0 = \frac{\exp(i\pi/4)}{8}\sqrt{\frac{2}{\pi}}[h_l(z_0)h_l(z_r)]^{-1/2}\left[\int_{-H}^{z_l}\frac{ds}{h_l(s)}\right]^{-1},$$

$$W_0 = (a_0 + b_0)\exp(-i2N\phi_0) + (c_0 + d_0)\exp(i2N\phi_0).$$

Here,

$$a_0 = \frac{\sin\left[(2N+1)\left(\frac{\alpha R}{2} + \vartheta_0\right)\right]}{\sin\left(\frac{\alpha R}{2} + \vartheta_0\right)},$$

$$b_0 = \frac{\sin\left[(2N+1)\left(\frac{\alpha R}{2} + \phi_0\right)\right]}{\sin\left(\frac{\alpha R}{2} + \phi_0\right)},$$

$$c_0 = \frac{\sin\left[(2N+1)\left(\frac{\alpha R}{2} - \vartheta_0\right)\right]}{\sin\left(\frac{\alpha R}{2} - \vartheta_0\right)},$$

$$d_0 = \frac{\sin\left[(2N+1)\left(\frac{\alpha R}{2} - \phi_0\right)\right]}{\sin\left(\frac{\alpha R}{2} - \phi_0\right)},$$

$$\vartheta_0 = \frac{\pi}{2}[D_l(z_0) + D_l(z_r)], \quad \phi_0 = \frac{\pi}{2}[D_l(z_r) - D_l(z_0)].$$

Under the assumption $|u_0| \gg |u_s|$, the field perturbation u_0 determined as the difference between the amplitudes of the perturbed and unperturbed fields $\Delta u = |u_0 + u_s| - |u_0|$ can be written as

$$\Delta u = |u_s|\cos(\Theta_s - \Theta_0), \quad (8)$$

where

$$|u_s| = |A_s||F|(\xi_l^2 r_s r_r)^{-1/2}|W_1||W_2|\exp(-\kappa_l r) \quad (9)$$

is the magnitude of the scattered field and

$$\Theta_s = \xi_l r + \arg W_1 + \arg W_2 + \arg F + (\pi/2),$$
$$\Theta_0 = \xi_l R + \arg W_0 + (\pi/4) = \text{const} \quad (10)$$

are the phases of the scattered (Eq. (3)) and primary (Eq. (7)) fields, respectively. Here,

$$|W_i| = [(a_i + b_i)^2 + (c_i + d_i)^2 + 2(a_i + b_i)(c_i + d_i)\cos(4N\phi_i)]^{1/2}, \quad i = 1, 2; \quad (11)$$

$$\arg W_i = \arg\tan\left[\frac{(c_i + d_i) - (a_i + b_i)}{(c_i + d_i) + (a_i + b_i)}\tan(2N\phi_i)\right], \quad i = 0, 1, 2. \quad (12)$$

are the modulus and the argument of the complex function W_i.

According to Eq. (8), the complex envelope of the diffracted field is determined by the form of the function F describing the scattering with the slowly varying functions W_1 and W_2 superimposed upon it, the latter functions being determined by the waveguide character of propagation. This leads to the fact that, depending on the observation conditions, the envelope can exhibit "intricate" variations, thus, it can widely deviate from the form of the scattering function F. In particular, as one can see, the complex envelope is an even function relative to the time moment t_0 of crossing the reference line by the inhomogeneity, $\Delta u(t_0 - t) = \Delta u(t_0 + t)$, if

(a) the motion occurs along the normal to the reference line, or

(b) the reference line is crossed at the angles different from $\pi/2$ and $z_0 = z_r$, $R_1 = R_2 = R/2$.

In the case of any other geometry of the problem, the violation of the symmetry pattern must occur. The indicated distinctive feature of the perturbed field is confirmed by the results of numerical simulation [3–6, 9]. To make the following consideration more concise, it is convenient to adopt the time moment $t_0 = 0$ as the initial one and assume that $t < 0$ ($t > 0$) when the inhomogeneity approaches (or moves away from) the reference line. Without violation of generality, let us consider the distinctive features of the shadow observation system for the case shown in figure. It is clear that, for the angles γ and $\pi - \gamma$, the function $\Delta u(t)$ (Eq. (8)) represents the mirror reflections with respect to the moment $t_0 = 0$, all other conditions being equal:

$$\Delta u(\gamma, t \le 0) = \Delta u(\pi - \gamma, t \ge 0),$$
$$\Delta u(\gamma, t \ge 0) = \Delta u(\pi - \gamma, t \le 0).$$

SMALL-ANGLE APPROXIMATION

Let us describe the pattern of the shadow scattered field for the case when it is concentrated within a narrow angular region around the source–inhomogeneity direction (a small-angle approximation). We assume that the inhomogeneity is a body extended in the horizontal plane and characterized by the horizontal dimension $2l$ far exceeding the sound wavelength λ, $\lambda \ll 2l$. This means the smallness of the angular deviation φ (the figure), $\varphi \sim \lambda/2l \ll 1$, which allows us to

simplify Eq. (8) to a certain extent. The limitation from above for the value of the characteristic vertical dimension $2d$ is caused by the isotropy of the scattering in the vertical plane, and, in the conditions of waveguide propagation, it is reduced to the inequality [2]

$$2d \le \lambda/2\sqrt{1-(\xi_{l+N}/k)^2}, \tag{13}$$

where $k = 2\pi/\lambda$. In the small-angle approximation, the dependence of the modulus of the scattering function $F(\varphi)$ has a lobe structure, in which the near side-lobe amplitude does not exceed 0.2 of the main lobe amplitude, and the main lobe contains more than 90% of the energy scattered forward by the body. The width of the main lobe is equal to λ/l_* in order of magnitude, where $2l_* = 2l\sin(\gamma + \beta_1^{(1,2)})$ is the visible characteristic horizontal dimension of the inhomogeneity from the side of the source, i.e., its projection on the normal to the direction of wave incidence from the source. In the case $\tan\gamma \gg \tan\beta_1^{(1,2)}$, the projection is $2l_* \approx 2l\sin\gamma$. At $\varphi \longrightarrow 0$, the value of $|F(\varphi)|$ increases on the average and reaches the maximal value $F_0 = 4\pi\varepsilon_0(S_*/\lambda)$, where ε_0 is the constant depending on the wave dimensions and the acoustic properties of the inhomogeneity ($0 < \varepsilon_0 \le 1$), S_* is the area of the body projection onto the incident wave front at $\varphi = 0$. At $\lambda \ll 2d$, the constant is $\varepsilon_0 = 1$ and does not depend on the acoustic properties of the inhomogeneity [15].

To obtain a qualitatively correct diffraction pattern in the conditions of waveguide propagation, one can use approximate expressions for the scattering amplitude (see, e.g., [16, 17]), the applicability of which does not imply their validity in a homogeneous space. This statement is also confirmed by the results of the numerical simulation of the sound diffraction by a rigid spheroid extended in the horizontal plane for the case $\gamma = \pi/2$, which was performed using both approximate [4] and exact [6] expressions for the scattering amplitude. This is explained by the fact that, in bottom sound channels where different modes may have different absorption coefficients, the condition of the isotropy of scattering in the vertical plane [Eq. (13)] is much weaker than the analogous condition in a homogeneous medium, $2d \le \lambda/2$. In actual conditions, the shape of an inhomogeneity is usually not known exactly. At the same time, proceeding from the energy considerations, it is desirable to observe an inhomogeneity within the main lobe of the shadow scattered field, where almost the whole potentially possible energy scattered forward by the inhomogeneity is concentrated. This shows that the shape of an inhomogeneity is unimportant in the analysis of many diffraction problems. Therefore, for the sake of clarity, we restrict the following consideration to a rigid cylindrical body as an example.

According to [16], the scattering function for a circular cylinder can be written in the form

$$F = F_0\sin\gamma\frac{\sin\Omega}{\Omega}, \tag{14}$$

where $F_0 = 4\pi\varepsilon_0(S_0/\lambda)$, $S_0 = 4ld$ is the area of the shadow contour, $\Omega = \varepsilon_l l(\cos\theta_2 - \cos\theta_1)$, and $\theta_{1,2}$ are the angles in the azimuth plane between the directions of the incident (scattered) wave and the rotation axis of the body. From the figure, we obtain

$$\begin{aligned}\theta_1^{(1,2)} &= \gamma \pm \beta_1^{(1,2)}, \quad \theta_2^{(1,2)} = \gamma \mp \beta_2^{(1,2)},\\ \varphi^{(1,2)} &= \beta_1^{(1,2)} + \beta_2^{(1,2)}.\end{aligned} \tag{15}$$

If the condition

$$\tan\gamma \gg \tan\left|(\beta_1^{(1,2)} - \beta_2^{(1,2)})/2\right| \tag{16}$$

is satisfied, we obtain from Eq. (14) by taking into account Eq. (15):

$$F = F_0\sin\gamma\frac{\sin[\xi_l l\sin\gamma(\sin\beta_1^{(1,2)} + \sin\beta_2^{(1,2)})]}{\xi_l l\sin\gamma(\sin\beta_1^{(1,2)} + \sin\beta_2^{(1,2)})}.$$

At small angles $\beta_{1,2}^{(1,2)}$, this expression yields

$$F(t) = F_0\sin\gamma\frac{\sin\Phi(t)}{\Phi(t)}, \tag{17}$$

where

$$\Phi(t) = \frac{\xi_l l R v t\sin^2\gamma}{(R_1 + vt\cos\gamma)(R_2 - vt\cos\gamma)}.$$

It is necessary to note that, when the inhomogeneity crosses the reference line in the middle of the distance $R_1 = R_2$, the scattering amplitude proves to be an even function.

In the small-angle approximation, the distance $r_{s,r}$ in the factor $(r_s r_r)^{-1/2}$ in Eq. (9) and in the expressions for the magnitude (11) and phase (12) of $W_{1,2}$ can be assumed as equal to $r_{s,r} \approx R_{1,2} \pm vt\cos\gamma$. The quantity r in the argument of the cosine in Eq. (9) can be replaced by an approximate expression:

$$r \approx R + \frac{R(vt\sin\gamma)^2}{2(R_1 + vt\cos\gamma)(R_2 - vt\cos\gamma)}. \tag{18}$$

As we are interested in the region of the main lobe, we consider in more detail the case of small values of $x = vt\cos\gamma$. This provides an opportunity to linearize the magnitude and phase of the function $W_{1,2}$ with respect to the value of $W_{1,2}^{(0)}$, which corresponds to the inhomogeneity motion at the angle $\gamma = \pi/2$ to the reference line. Let us expand $a_{1,2}(x)$ [Eq. (6)] as a Taylor series in the

vicinity of the distances $R_{1,2}$ and consider only the first approximation:

$$a_{1,2} \approx a_{1,2}(R_{1,2}) + a'_{1,2}(R_{1,2})\nu t\cos\gamma = a^{(0)}_{1,2} + a^{(1)}_{1,2}\nu t\cos\gamma.$$

Writing similar expressions for $b_{1,2}$, $c_{1,2}$, and $d_{1,2}$ [Eq. (6)], we finally obtain

$$|W_{1,2}| = |W^{(0)}_{1,2}| \pm \frac{2W^{(1)}_{1,2}}{|W^{(0)}_{1,2}|}\nu t\cos\gamma,$$
$$\arg W_{1,2} = \arg W^{(0)}_{1,2} \pm \frac{w_{1,2}H^{(0)}_{1,2}}{1 + (H^{(0)}_{1,2})^2}\nu t\cos\gamma, \quad (19)$$

where

$$W^{(1)}_{1,2} = [(a^{(0)}_{1,2} + b^{(0)}_{1,2})(c^{(1)}_{1,2} + d^{(1)}_{1,2}) + (a^{(1)}_{1,2} + b^{(1)}_{1,2})(c^{(0)}_{1,2} + d^{(0)}_{1,2})]\cos^2(2N\phi_{1,2}),$$
$$w_{1,2} = \frac{2[(a^{(0)}_{1,2} + b^{(0)}_{1,2})(c^{(1)}_{1,2} + d^{(1)}_{1,2}) - (a^{(1)}_{1,2} + b^{(1)}_{1,2})(c^{(0)}_{1,2} + d^{(0)}_{1,2})]}{[(c^{(0)}_{1,2} + d^{(0)}_{1,2}) - (a^{(0)}_{1,2} + b^{(0)}_{1,2})][(c^{(0)}_{1,2} + d^{(0)}_{1,2}) + (a^{(0)}_{1,2} + b^{(0)}_{1,2})]}.$$

The values of $|W^{(0)}_{1,2}|$ and $\arg W^{(0)}_{1,2} = \arctan H^{(0)}_{1,2}$ in Eq. (19) are determined by Eqs. (11) and (12), in which the substitutions $a_i \longrightarrow a^{(0)}_{1,2}$, $b_i \longrightarrow b^{(0)}_{1,2}$, $c_i \longrightarrow c^{(0)}_{1,2}$, and $d_i \longrightarrow d^{(0)}_{1,2}$ must be made. The plus-sign in Eq. (19) refers to the lower index 1, and the minus-sign, to the lower index 2. Let us consider the characteristics of the perturbation given by Eq. (8).

(a) *Duration.* We determine the duration T as the duration of the main peak of the envelope $|u_s|$ [Eq. (9)] at the level of the zero value, where the majority of the energy is concentrated. We introduce the notation $\Delta R = R_2 - R_1$. We assume that

$$(\Delta R/R)^2 \ll 1, \quad \sin^2\gamma \gg (\lambda/2l)[1 + (|\Delta R|/R)]\cos\gamma, \quad (20)$$

i.e., the inhomogeneity crosses the reference line in the vicinity of the middle of the path at angles that are not too shallow. In these conditions, the duration determined by the main lobe width of the scattering function (17) is equal to

$$T = \frac{1}{l\nu}\left(\frac{L}{\sin\gamma}\right)^2, \quad (21)$$

where $L = (R_1R_2\lambda/R)^{1/2}$ is the radius of the first Fresnel zone at the moment of crossing of the reference line. In this case, the horizontal $x^{(1,2)}$ and vertical $y^{(1,2)}$ displacements of the inhomogeneity with respect to the point of crossing the reference line, which correspond to the half-width of the spike, are estimated as

$$x^{(1,2)}_* = y^{(1,2)}_*\cos\gamma, \quad y^{(1,2)}_* = \frac{L^2}{2l\sin\gamma}(1 \mp \nu),$$

where $\nu = (\lambda/2l)(\Delta R/R)(\cos\gamma/\sin^2\gamma)$. We note that condition (20) implies the validity of inequality (16). It is clear that these conclusions are not connected with the choice of the inhomogeneity model. One can also arrive at this result directly by assuming that the rational value of the angular sector of observation is determined by the relation $\max\varphi^{(1,2)} \sim \lambda/2l_*$ (figure).

(b) *Spectrum width.* If Eqs. (20) hold, the change of the phase of the field perturbation (8) [as it follows from Eqs. (10), (18), and (19)] is determined by the expression

$$\Theta(t) = \Theta_1(t) + \Theta_2(t), \quad (22)$$

where

$$\Theta_1(t) = -\pi\left(\frac{\nu t\sin\gamma}{L}\right)^2,$$
$$\Theta_2(t) = \left[\frac{w_2H^{(0)}_2}{1 + (H^{(0)}_2)^2} - \frac{w_1H^{(0)}_1}{1 + (H^{(0)}_1)^2}\right]\nu t\cos\gamma. \quad (23)$$

The initial phase is omitted in Eq. (22), its exact value being irrelevant in what follows. The component $\Theta_1(t)$ describing the quadratic dependence of the phase is caused by the Doppler effect (see below), and the component $\Theta_2(t)$ determining the linear dependence of the phase is related to the waveguide character of propagation. A constant frequency shift, which is determined by the linear phase variation, is equal to zero when the source and the receiver are positioned at the same horizontal level, $z_0 = z_r$, and the inhomogeneity crosses the reference line in the middle of the path ($R_1 = R_2$) or moves along the normal to the reference line ($\gamma = \pi/2$). The deviation of the instantaneous frequency during the time T is

$$\Delta\omega = \Theta'(-T/2) - Q'(T/2) = 2\pi(\nu/l),$$

so that the base m determining the complexity of the pulse form is equal to

$$m = \Delta\omega T = \left(\frac{L}{l\sin\gamma}\right)^2. \quad (24)$$

According to Eq. (24), in the case of large inhomogeneities, $l_* = l\sin\gamma \sim L$, the base value is small—of the order of unity. The pulse becomes simple, and its spectrum width is estimated as $\Delta f \approx 1/T = t\nu(\sin\gamma/L)^2$. By contrast, in the case of small inhomogeneities, $l_* \ll L$,

the base is large, because the scattered field has time to change considerably within the first Fresnel zone.

One can arrive at Eq. (23) for $\Theta_1(t)$ in a different way by considering the Doppler frequency shift. Indeed, in the case of a stationary receiver receiving the sound scattered by a moving inhomogeneity, the frequency ω of the received wave is equal to [19]

$$\omega_* = \omega_0 \frac{1-(v/c)\cos\theta_1}{1-(v/c)\cos\theta_2},$$

where ω_0 is the radiation frequency; c is the sound velocity in the medium; and θ_1 and θ_2 are the angles between the direction of the inhomogeneity velocity and the propagation directions of the initial and scattered waves, respectively (figure). If the inequality $v/c \ll 1$ and conditions (20) are satisfied, we obtain for the Doppler frequency

$$\omega(t) = \omega_* - \omega_0 = -2\pi\left(\frac{v\sin\gamma}{L}\right)^2 t, \qquad (25)$$

which coincides with the derivative of the phase $\Theta_1(t)$ given by Eqs. (23). The mechanism of the Doppler effect in the case of the inhomogeneity motion in the horizontal plane can be also described by a simple interference model. According to it, the intersection of two plane waves produces an interference pattern with the periodic spatial distribution of the intensity of the resulting field. The width of the interference band Λ in this case is given by the formula

$$\Lambda = \frac{\lambda}{2\sin(\beta/2)} = \frac{L^2}{v|t|\sin\gamma},$$

where $\beta = \beta_1 + \beta_2$ is the angle between the propagation directions of the primary and scattered waves (figure). The radiation scattered by an inhomogeneity moving in the interference field is intensity modulated. The modulation frequency is equal to the inverse value of the time of crossing a single interference band by the inhomogeneity:

$$\omega(t) = 2\pi(v\cos\chi/\Lambda),$$

where $v\cos\chi$ is the projection of the velocity vector onto the direction of the difference between the wave vectors of the scattered and incident waves ($\chi = (\pi/2) - \gamma$ in the case of the inhomogeneity approaching the reference line and $\chi = (\pi/2) + \gamma$ when it moves away from the reference line). The resulting expression coincides with Eq. (25) for the Doppler frequency shift.

AVERAGE PERTURBED FIELD

Let us consider the average pattern of a perturbed field Δu [Eq. (8)]:

$$\overline{\Delta u} = \frac{\overline{u_0 u_s^* + u_0^* u_s}}{2\sqrt{\overline{|u_0|^2}}} = \sqrt{\overline{|u_0|^2}}\,\overline{\cos(\Theta_s - \Theta_0)}, \qquad (26)$$

which is relevant in the application of extended vertical arrays. The overbar in Eq. (26) means averaging over the positions of the source, the inhomogeneity, and the receiver within the waveguide depth. In this case, it becomes possible to describe a multimode pattern of diffraction shading in the framework of the small-parameter model. The utilization of the small-parameter model in algorithms of matched filtering provides an opportunity to obtain the detection characteristics close to the potentially possible ones and predict the inhomogeneity parameters with a preset precision [1, 8, 20–22].

Let us use the representation of the direct and diffracted fields in the form of a mode expansion according to Eq. (2):

$$u_s = \frac{iF}{8\pi\sqrt{r_s r_r}} \sum_m^M \sum_\mu^M \frac{\exp[i(\xi_m r_s + \xi_\mu r_r)]}{\sqrt{\xi_m \xi_\mu}} \psi_m(z_0) \times \psi_m(z_s)\psi_\mu(z_s)\psi_\mu(z_r)\exp[-(\kappa_m r_s + \kappa_\mu r_r)],$$

$$u_0 = \frac{i}{\sqrt{8\pi}}\exp(-i\pi/4) \times \sum_n^M \frac{\exp(i\xi_n R)}{\sqrt{\xi_n R}} \psi_n(z_0)\psi_n(z_r)\exp(-\kappa_n R).$$

Then, we substitute these expressions into Eq. (26). In the process of averaging, we take into account the orthonormality of the eigenfunctions: $\int_{-H}^0 \psi_m(z)\psi_\mu(z)dz = \delta_{m\mu}$, where $\delta_{m\mu}$ is the Kronecker delta. Assuming that the eigenvalue spectrum is narrow, we can consider the slowly varying parameters ξ_m and κ_m as constant and equal to $\xi_l = 2\pi/\lambda$ and κ_l and factor them out from under the summation sign. If inequality (20) is valid, the quantity $r_{s,r}$ in the factor $1/\sqrt{r_{s,r}}$ and in the argument of the attenuation exponent can be replaced by the approximate value $R_{1,2}$. As a result, we obtain

$$\overline{\Delta u(t)} \approx \left(\frac{1}{4\pi H}\right)^2 \sqrt{M}\exp(i\pi/4) \times \frac{\lambda\exp(-\kappa_l R)}{\sqrt{R_1 R_2}} F(t)\cos\Theta_1(t), \qquad (27)$$

where the phase $\Theta_l(t)$ is determined according to Eqs. (23).

Let us introduce the variation coefficient

$$g = \sqrt{\overline{|u_s|^2}}/\sqrt{\overline{|u_0|^2}}$$

characterizing the contrast of the averaged diffraction pattern. The rms value of the primary field is equal to

$$\sqrt{\overline{|u_0|^2}} \approx (\sqrt{M}/4\pi)\sqrt{\lambda/R}\exp(-\kappa_l R),$$

so that from the comparison of Eqs. (26) and (27) we obtain

$$g \approx \frac{1}{4\pi H}\sqrt{\frac{\lambda R}{R_1 R_2}}F, \quad (28)$$

i.e., the variation coefficient reproduces the scattering amplitude of the inhomogeneity correct to the constant factor $\sqrt{\lambda R}/4\pi\sqrt{R_1 R_2}$. The maximal value of the variation coefficient (28) attainable at the moment $t = 0$ of crossing the reference line by the inhomogeneity is

$$g_{\max} \approx \frac{S_*}{HL}. \quad (29)$$

We note that the estimate (29) can be also obtained by proceeding from the Huygens–Fresnel principle, as it is demonstrated in [2, 18] for the case $\gamma = \pi/2$.

It should be also noted that, as one can see from Eqs. (21), (22), (24), and (29), in the particular case $\gamma = \pi/2$, we arrive at the expressions for the characteristics of a diffracted signal, which were proposed earlier in [1, 2, 18].

APPLICABILITY OF THE SIGNAL MODEL

The estimates presented above are based on the isotropy of scattering in the vertical plane [Eq. (15)] and on a rather narrow eigenvalue spectrum. Let us specify the second condition. If we repeat the reasoning used in [2] for the case $\gamma = \pi/2$, we arrive at analogous expressions

$$\Delta\xi/\xi_l < 1, \quad \Delta\xi/\xi_l < 1/m,$$

where $\Delta\xi = \xi_1 - \xi_M$ is the width of the spectrum of propagation constants and the base m is determined by Eq. (24).

CONCLUSION

The proposed model provides an opportunity to describe simply and directly the sound diffraction by localized inhomogeneities in oceanic waveguides and to estimate the effect of the observation conditions on the perturbed field without time-consuming numerical calculations. In particular, the relation between the perturbed field characteristics and the parameters of the problem geometry and the oceanic medium becomes absolutely clear. It is demonstrated that, when the reference line crossing angle differs from $\pi/2$, the specificity of the waveguide propagation manifests itself in a distortion of form and a frequency shift, as compared to free space, if the source and the receiver are located at different horizontal levels. A small-parameter model of diffraction is proposed in the framework of the averaged description of a multimode pattern of diffraction shading. It provides an opportunity to increase the efficiency of storing the signal responses from the elements of a vertical array by using the methods of matched filtering.

ACKNOWLEDGMENTS

This work was supported by the Russian Foundation for Basic Research, project no. 99-02-17671.

REFERENCES

1. S. M. Gorskiĭ, V. A. Zverev, A. L. Matveev, and V. V. Mityugov, Akust. Zh. **41**, 223 (1995) [Acoust. Phys. **41**, 190 (1995)].
2. V. M. Kuz'kin, Akust. Zh. **43**, 514 (1997) [Acoust. Phys. **43**, 440 (1997)].
3. V. A. Eliseevnin and Yu. I. Tuzhilkin, Akust. Zh. **41**, 249 (1995) [Acoust. Phys. **41**, 214 (1995)].
4. V. A. Grigor'ev and V. M. Kuz'kin, Akust. Zh. **41**, 410 (1995) [Acoust. Phys. **41**, 359 (1995)].
5. A. Sarkssian, J. Acoust. Soc. Am. **102**, 825 (1997).
6. V. A. Grigoriev, B. G. Katsnelson, V. M. Kuz'kin, and V. G. Petnikov, Phys. Vibr. **7** (3), 185 (1999).
7. V. A. Zverev, A. L. Matveev, and V. V. Mityugov, Akust. Zh. **41**, 591 (1995) [Acoust. Phys. **41**, 518 (1995)].
8. V. M. Kuz'kin, Akust. Zh. **46**, 515 (2000) [Acoust. Phys. **46**, 445 (2000)].
9. B. G. Katsnelson, V. A. Grigor'ev, V. M. Kuz'kin, and V. G. Petnikiov, J. Acoust. Soc. Am. **108**, 2486 (2000).
10. V. N. Kulakov, N. E. Mal'tsev, and S. D. Chuprov, Akust. Zh. **29**, 74 (1983) [Sov. Phys. Acoust. **29**, 41 (1983)].
11. A. L. Virovlyanskiĭ, Preprint No. 120, IPF AN SSSR (Inst. of Applied Physics, USSR Academy of Sciences, Gorki, 1985).
12. N. K. Uzunoglu and J. G. Fikioris, J. Acoust. Soc. Am. **72**, 628 (1982).
13. V. M. Kuz'kin, Akust. Zh. **47**, 483 (2001) [Acoust. Phys. **47**, 591 (2001)].
14. Yu. A. Kravtsov, V. M. Kuz'kin, and V. G. Petnikov, Akust. Zh. **30**, 339 (1984) [Sov. Phys. Acoust. **30**, 199 (1984)].
15. L. N. Zakhar'ev and A. A. Lemanskiĭ, *Wave Scattering by "Black" Bodies* (Sovetskoe Radio, Moscow, 1972).
16. A. I. Boĭko, Akust. Zh. **29**, 321 (1983) [Sov. Phys. Acoust. **29**, 189 (1983)].
17. N. B. Konyukhova and T. V. Pak, *Diffraction of a Plane Sound Wave by a Rigid Prolate Spheroid* (VTs AN SSSR, Moscow, 1985).
18. V. A. Zverev, Akust. Zh. **40**, 401 (1994) [Acoust. Phys. **40**, 360 (1994)].
19. *Ultrasound: A Small Encyclopedia* (Sovetskaya Entsiklopediya, Moscow, 1979).
20. J. V. Candy and E. J. Sullivan, in *Proceedings of 4th European Conference on Underwater Acoustics, Rome, Italy, 1998*, Vol. 1, p. 3.
21. P. M. De Kooter, in *Master's Thesis. Naval Postgraduate School* (Monterey, Calif., 1997).
22. K. B. Smith, J. Brune, and C. S. Chiu, in *Proceedings of 4th European Conference on Underwater Acoustics, Rome, Italy, 1998*, Vol. 1, p. 9.

Translated by M. Lyamshev

Acoustical Physics, Vol. 48, No. 1, 2002, pp. 76–80. Translated from Akusticheskiĭ Zhurnal, Vol. 48, No. 1, 2002, pp. 85–90.

Effect of an Intense Sound Wave on the Acoustic Properties of a Sandstone Bar Resonator. Experiment

V. E. Nazarov, A. V. Radostin, and I. A. Soustova

Institute of Applied Physics, Russian Academy of Sciences, ul. Ul'yanova 46, Nizhni Novgorod, 603950 Russia

e-mail: nazarov@hydro.appl.sci-nnov.ru

Received January 10, 2001

Abstract—Experimental results and a theoretical description are presented for the effect of an intense pumping wave on a weak wave in a sandstone bar resonator. From the amplitude dependences of the resonance frequency shift and of the nonlinear loss, which are measured for the weak wave in the presence of the intense one, it is inferred that sandstone exhibits a dissipative acoustic nonlinearity. *© 2001 MAIK "Nauka/Interperiodica".*

INTRODUCTION

When propagating in a medium, an elastic wave interacts with it causing a number of nonlinear effects, such as wave generation at combination frequencies, amplitude-dependent loss, change in the wave velocity, attenuation of sound by sound, amplitude limitation, and demodulation of high-frequency pulses. The intensity of these effects depends on the nonlinear properties of the medium and on the amplitude of the wave. Therefore, the investigation of these effects, including the reconstruction of the amplitude–frequency characteristics, contributes to revealing the mechanisms of acoustic nonlinearity and deriving the equations of state of the medium. All this forms the basis for the development of nonlinear methods of testing the structure and condition of the medium.

One of the principal problems arising in the analytical description of experiments involving nonlinear effects is the proper choice of the equation of state for the medium in which these effects are observed. Another no less important side of this problem is to set up the experiment so that the results can be used "to make statements independent of the existing theoretical concepts" [1]. In acoustics (and, hence, also in seismoacoustics), theoretical knowledge traditionally relies on the five- or nine-constant elasticity theory [2, 3]. However, this approach can only be applied to homogeneous solids. For microinhomogeneous media, which contain various inclusions (dislocations, grains, cracks, etc.), the equations of state are often nonanalytic and contain a fractional-power or hysteretic nonlinearity even in the case of relatively small strains (10^{-7} to 10^{-6}) [4–15]. The effective parameters of the acoustic nonlinearity of microinhomogeneous media are, as a rule, considerably greater than the nonlinearity parameters of homogeneous media and materials. All other factors being the same, the nonlinear effects are most pronounced in resonators, in which the amplitudes of elastic waves can be much higher than in an unbounded medium. Such experiments were carried out with some polycrystalline metals and rocks. It was found that, in addition to the hysteretic nonlinearity, these materials exhibit a dissipative acoustic nonlinearity [6, 11, 14, 16, 17]. In this connection, a search for new media that exhibit these properties is also a topical problem of nonlinear acoustics and seismoacoustics.

This paper presents the results of an experimental study and analytical description of the effect of an intense acoustic pumping wave on the characteristics of a sandstone resonator that are measured by a weak wave. The analysis of these results shows that sandstone exhibits a dissipative acoustic nonlinearity.

DESCRIPTION OF THE EXPERIMENT

A block diagram of the experimental setup is shown in Fig. 1. The experiment used a bar resonator (*1*) made of sandstone, which was taken from a core extracted at an oil and gas production site. The length L of the bar was 28 cm and its diameter was d = 2.5 cm. A piezoceramic vibrator (*2*) used to produce the weak wave was attached to the end face of the bar and to a massive (M = 2 kg) titanium concentrator (*3*) intended for producing the intense pumping wave. Therefore, the boundary condition at this face of the resonator was close to the boundary condition at a perfectly rigid surface. (The minimal level of the pumping wave exceeded the level of the weak wave by more than 30 dB.) A piezoelectric accelerometer (*4*) was attached to the other (free) end face of the bar. The mass of this device was sufficiently small, so that this boundary could be considered as acoustically soft. The eigenfrequencies of longitudinal vibrations of this resonator can be calculated as $F_n = C_0(2n - 1)/4L$, where C_0 is the velocity of the longitudinal wave in the bar and n is the index of the longitudinal mode. The signal produced by the accelerometer (*4*) was supplied to a spectrum analyzer (*5*) in order to measure the amplitude of the pumping wave, and,

1063-7710/02/4801-0076$22.00

through a rejection filter (*6*), which suppressed the pumping signal by 30 dB, this signal was also supplied to a frequency selective voltmeter (*7*) and an oscilloscope (*8*), which measured the amplitude A of the weak wave. At small excitation amplitudes, the eigenfrequencies of the first four longitudinal modes of the resonator were $F_1 \approx 2230$ Hz, $F_2 \approx 6800$ Hz, $F_3 \approx 10150$ Hz, and $F_4 \approx 13340$ Hz. Their Q factors were $Q_1 \cong 125$, $Q_2 \cong 130$, $Q_3 \cong 135$, and $Q_4 \cong 140$, respectively. These resonance frequencies correspond to the velocity of the longitudinal wave in the bar $C_0 \cong 2.5 \times 10^5$ cm/s.

EXPERIMENTAL RESULTS

In the experiment, a continuous weak wave at the fourth mode and a continuous intense pumping wave at the first mode were first excited in the resonator. Subsequently, the weak wave was excited at the first mode and the intense wave was excited at the fourth mode. This choice of frequencies of the intense and weak waves was determined primarily by the acoustic compatibility, i.e., by the condition that they could be received separately. The amplitude of the weak wave was maintained constant during the measurements. The amplitude of the pumping wave was increased, which caused the resonance conditions to be violated. Therefore, the frequency of this wave was varied so as to keep the pumping wave at resonance. Figures 2a and 2b show respectively the resonance curves for the weak wave at the fourth and first modes with the pumping wave amplitude at the first and fourth modes as a parameter. These figures show that an increase in the pumping wave amplitude ε_m shifts the resonance frequency and broadens the resonance curve for the weak wave. This effect is associated with a decrease in the Young modulus (or in the elastic wave velocity) and with a decrease in the Q factor of the resonator (or an increase in the nonlinear loss). The level of the combination frequency components (near the third and fifth resonator modes) were about 30 dB lower than the weak wave level. Therefore, these waves could not cause such a considerable decrease in the Q factor at the fourth and first modes of the resonator. Figure 3 shows the shift $\Delta F_{4,1}$ in the resonance frequency of the weak wave versus the strain amplitude due to the pumping wave. As seen in Fig. 3, $\Delta F_{4,1} \sim \varepsilon_m$. Figure 4 displays the relative amplitude $R = A/A_0$ of the weak wave (at resonance) versus the amplitude ε_m of the pumping wave (A_0 and A are the weak wave amplitudes at $\varepsilon_m = 0$ and $\varepsilon_m \neq 0$, respectively). From the dependences shown in Fig. 4, it follows that the relative amplitude R decreases with increasing ε_m.

ANALYTICAL DESCRIPTION OF THE EFFECT OF THE PUMPING WAVE ON THE WEAK WAVE

The nonlinear effects observed in the experiment, namely, the resonance frequency shift and the decrease in the Q factor of the resonator with increasing wave amplitude, are usually explained in the framework of the hysteretic nonlinearity model [4, 6–14]. In this paper, we will also try to analytically describe these effects in terms of the hysteretic equation of state

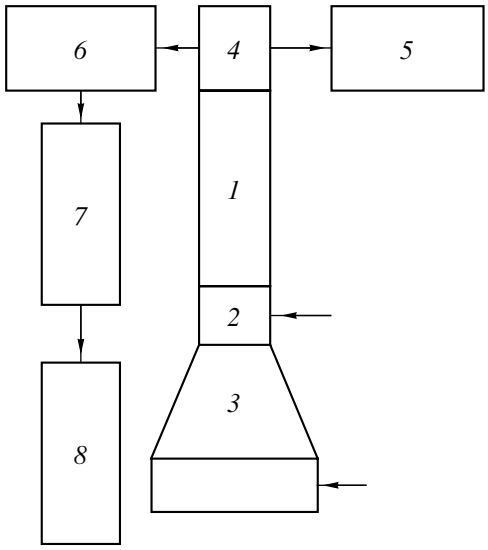

Fig. 1. Schematic diagram of the measuring setup.

$$\sigma(\varepsilon, \dot{\varepsilon}) = E[\varepsilon - f(\varepsilon, \dot{\varepsilon})] + \alpha\rho\dot{\varepsilon}, \tag{1}$$

$$f(\varepsilon, \dot{\varepsilon}) = \begin{cases} \gamma_1\varepsilon^2/2, & \varepsilon > 0, \quad \dot{\varepsilon} > 0 \\ -\dfrac{\gamma_2}{2}\varepsilon^2 + \dfrac{\gamma_1 + \gamma_2}{2}\varepsilon_m\varepsilon, & \varepsilon > 0, \quad \dot{\varepsilon} < 0 \\ -\gamma_3\varepsilon^2/2, & \varepsilon < 0, \quad \dot{\varepsilon} < 0 \\ \dfrac{\gamma_4}{2}\varepsilon^2 + \dfrac{\gamma_3 + \gamma_4}{2}\varepsilon_m\varepsilon, & \varepsilon < 0, \quad \dot{\varepsilon} > 0, \end{cases} \tag{2}$$

where σ and ε are the longitudinal stress and strain in the bar, E is the Young modulus, ρ is the density, and α is the linear attenuation coefficient. In the equations, it is assumed that $|\gamma_{1-4}\varepsilon_m| \ll 1$ and $|\gamma_{1-4}| \gg 1$. (The quadratic hysteretic nonlinearity was chosen, because, experimentally, it was found that $\Delta F_{1,4} \sim \varepsilon_m$.)

Equations of state (1) and (2) together with the equation of motion

$$\rho U_{tt} = \sigma_x(\varepsilon, \dot{\varepsilon}) \tag{3}$$

and the boundary conditions

$$U(0, t) = U_0\cos\Omega_m t + a\cos\Omega_n t, \quad U_x(L, t) = 0 \tag{4}$$

(where U is the displacement, $\varepsilon = U_x$, and $a \ll U_0$) describe the effect of an intense pumping wave on the weak wave in the resonator. We represent the solution to Eqs. (1)–(3) as a superposition of the intense ε_p and weak ε_w waves:

$$\varepsilon(x, t) = \varepsilon_p(x, t) + \varepsilon_w(x, t). \tag{5}$$

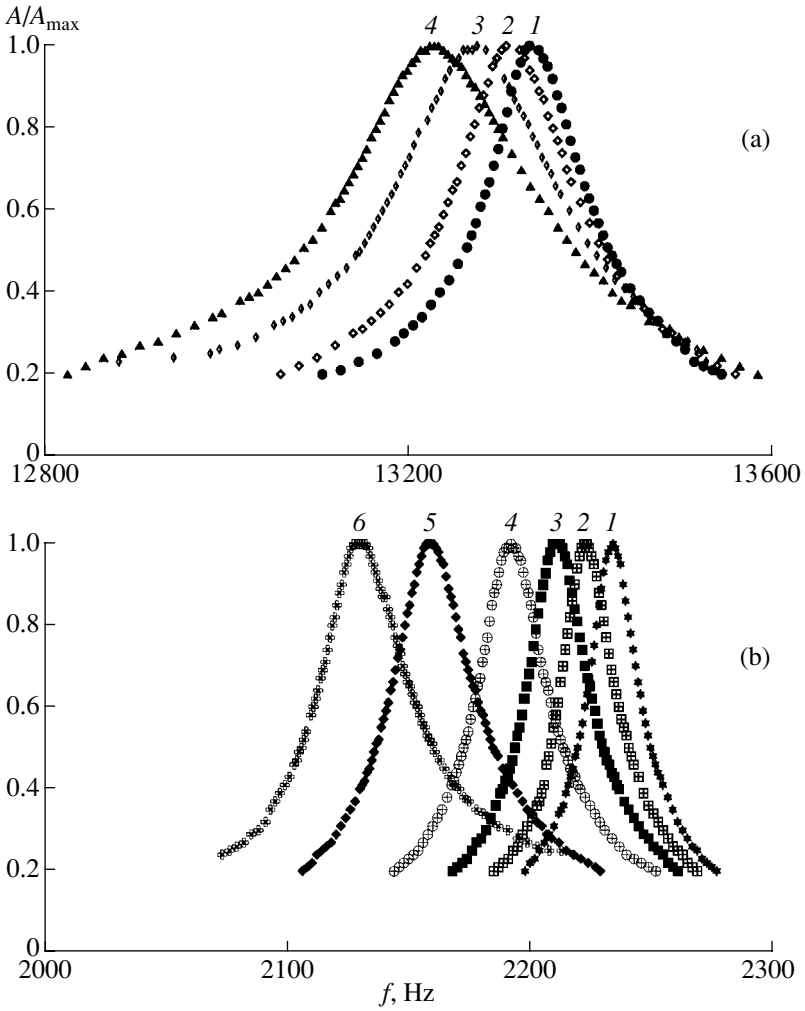

Fig. 2. (a) Resonance curves for the weak wave at the fourth mode with the strain amplitude of the pumping wave at the first mode as a parameter: ε_m = (*1*) 0, (*2*) 7.5×10^{-7}, (*3*) 1.6×10^{-6}, and (*4*) 2.5×10^{-6}. (b) Resonance curves for the weak wave at the first mode with the strain amplitude of the pumping wave at the fourth mode as a parameter: ε_m = (*1*) 0, (*2*) 4.5×10^{-7}, (*3*) 7.5×10^{-7}, (*4*) 1.3×10^{-6}, (*5*) 2.1×10^{-6}, and (*6*) 2.7×10^{-6}.

Let the pumping wave be specified as a mode of the resonator $\varepsilon_p(x, t) = \varepsilon_m \cos\Omega_m t \cos K_m x$, where $K_m = \Omega_m/C_0 = \pi/(2m-1)L$ and $C_0^2 = E/\rho$. Since $|\varepsilon_w| \ll \varepsilon_m$, we expand the function $f(\varepsilon, \dot{\varepsilon})$ into the Taylor series in ε_w, accurate to the linear term. Separating the constant component in the coefficient $f_\varepsilon(\varepsilon_p, \dot{\varepsilon}_p)$ ($\langle f_\varepsilon(\varepsilon_p, \dot{\varepsilon}_p)\rangle = \gamma_{eff}\varepsilon_m|\cos K_m x|$), we obtain the equation for the weak wave:

$$\frac{\partial^2 \varepsilon_w}{\partial t^2} - C_0^2 \frac{\partial^2 \varepsilon_w}{\partial x^2} = -\gamma_{eff} C_0^2 \varepsilon_m |\cos K_m x| \frac{\partial^2 \varepsilon_w}{\partial x^2} + \alpha \frac{\partial^3 \varepsilon_w}{\partial x^2 \partial t}, \quad (6)$$

where $\gamma_{eff} = \dfrac{\gamma_1 + \gamma_2 + \gamma_3 + \gamma_4}{4} + \dfrac{\gamma_1 - \gamma_2 + \gamma_3 - \gamma_4}{\pi}$ is the effective parameter of the hysteretic nonlinearity. Equation (6) yields the weak-wave resonance curve of the bar for the *n*th mode of the resonator [10]:

$$A = \frac{aC_0/L}{\sqrt{(\delta_n - \delta_h)^2 + \dfrac{\Omega_n^2}{4}\dfrac{1}{Q_n^2}}}, \quad (7)$$

where $\delta_n = \Omega_n - \Omega$ and $\delta_h = -(\gamma_{eff}/\pi)\Omega_m\varepsilon_m$ are the linear and nonlinear shifts in the resonance frequency, respectively, and $Q_n = C_0^2/\alpha\Omega_n$. This equation shows that the hysteretic nonlinearity model can explain only the shift in the resonance frequency, but not the decrease in the *Q* factor of the resonator with increasing amplitude of the intense wave at one mode measured with the help of the weak wave at another mode. As a matter of fact, to explain only the nonlinear shift in the resonance frequency ($\Delta F_{1,4} \sim \varepsilon_m$), it is not necessary to resort to the

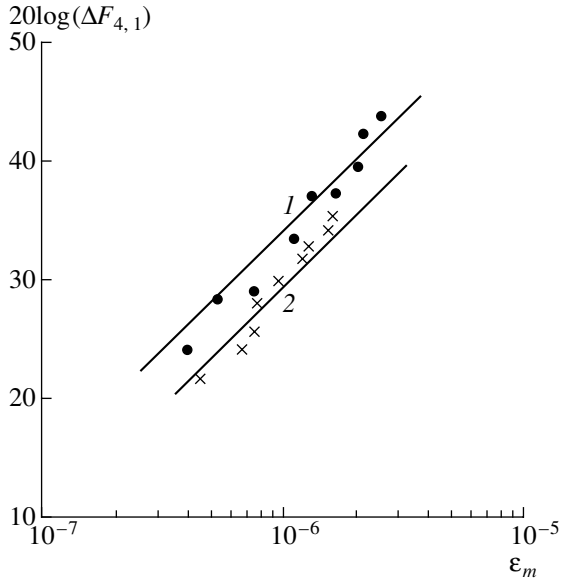

Fig. 3. Resonance frequency shift $\Delta F_{4,1}$: (*1*) for the weak wave at the fourth resonator mode versus the pumping amplitude at the first mode and (*2*) for the weak wave at the first mode versus the pumping amplitude at the fourth mode. The straight lines correspond to the dependence $\Delta F_{4,1} \sim \varepsilon_m$.

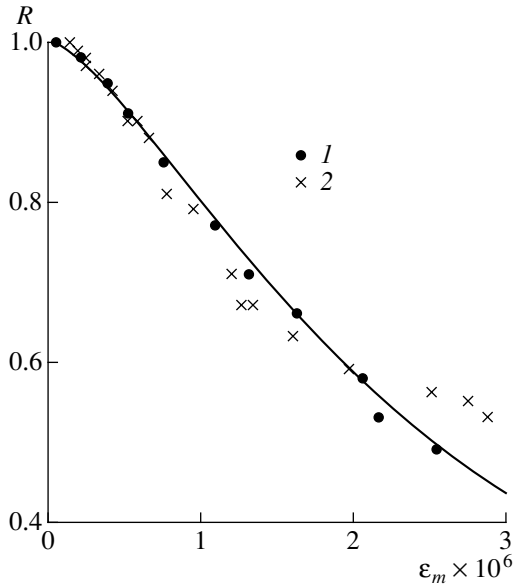

Fig. 4. Relative amplitude $R = A/A_0$: (*1*) for the weak wave at the fourth resonator mode versus the pumping amplitude at the first mode and (*2*) for the weak wave at the first mode versus the pumping amplitude at the fourth mode. The solid line is calculated by Eq. (11) with $\beta = 2.5 \times 10^9$.

hysteretic model. It is sufficient to assume that the nonlinearity is different for the positive and negative values of ε within the framework of the quadratic nonlinearity model by assuming that, in Eq. (2), $\gamma_2 = -\gamma_1$ and $\gamma_4 = -\gamma_3$, but $\gamma_1 \neq \gamma_3$, so that $\gamma_{eff} \neq 0$. The hysteretic equation of state was used here because, when the resonator is excited by the pumping wave alone, the effect of the amplitude-dependent friction both shifts the resonance frequency and decreases the Q factor. This equation was also used in order to show that the hysteretic nonlinearity does not decrease the Q factor for the weak wave in the presence of the intense one. To explain this effect, it is necessary to introduce the dissipative nonlinearity into the equation of state [6, 11, 14, 16, 17]:

$$\sigma(\varepsilon, \dot{\varepsilon}) = E[\varepsilon - f(\varepsilon)] + \alpha\rho[1 + \beta|\varepsilon|^S]\dot{\varepsilon}, \qquad (8)$$

where β and S are dimensionless constants. Similar calculations yield the resonance curve of the resonator and show that the resonance frequency shift and the Q factor for the weak wave at one mode depend on the amplitude of the pumping wave at another mode:

$$A = \frac{aC_0/L}{\sqrt{(\delta_n - \delta_h)^2 + \dfrac{\Omega_n^2}{4Q_n^2}(1 + \eta\beta\varepsilon_m^S)^2}}, \qquad (9)$$

where $\eta = \dfrac{1}{2\pi}\dfrac{\Gamma^2[(S+1)/2]}{\Gamma^2[(S+3)/2]}$.

The comparison of the experimental results (Fig. 3) with the theoretical dependence of the resonance frequency shift on the pumping amplitude at the first and fourth modes yields the effective parameter of the hysteretic nonlinearity: $\gamma_{eff}\ (m = 1) \cong 6.4 \times 10^4$ and $\gamma_{eff}\ (m = 4) \cong 6.6 \times 10^3$. As follows from these estimates, the effective parameter of the hysteretic nonlinearity decreases with increasing pumping frequency. Similar behavior is observed for polycrystalline lead and zinc [6, 13].

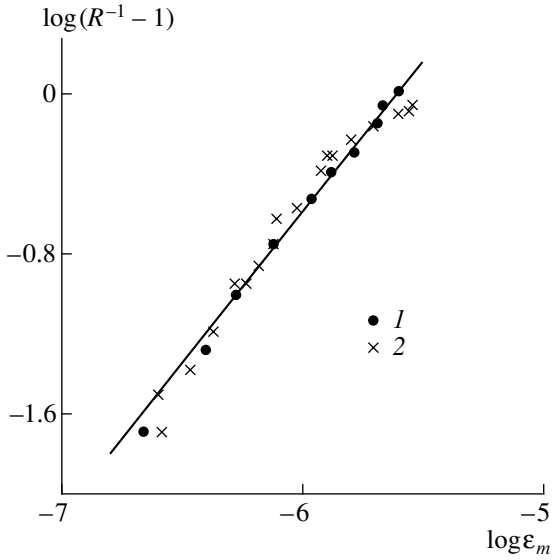

Fig. 5. Dependence of $\log(R^{-1} - 1)$ on $\log\varepsilon_m$ for the resonator excited by the pumping wave at (*1*) the first and (*2*) fourth modes. The straight line corresponds to $R^{-1} - 1 \sim \varepsilon_m^{3/2}$.

Let us determine the exponent S and the parameter of dissipative nonlinearity β. Formula (9) implies that, at resonance, the amplitude of the weak wave and the dependence $R = R(\varepsilon_m)$ are given by the expressions

$$A = 4aQ_n/[\pi(2n-1)(1+\eta\beta\varepsilon_m^S)], \quad (10)$$

$$R = 1/(1+\eta\beta\varepsilon_m^S). \quad (11)$$

As follows from Eq. (11), $\log(R^{-1}-1) = \log\eta\beta + S\log\varepsilon_m$. Using the experimental results (Fig. 4), we plot the dependences of $\log(R^{-1}-1)$ on $\log\varepsilon_m$ (Fig. 5), from which we obtain $S \cong 3/2$ and $\beta \cong 2.5 \times 10^9$. The parameter of the dissipative nonlinearity for sandstone, as for lead and zinc [6, 13], was found to be independent of the pumping frequency. This fact corroborates the assumption that the nonlinear dissipation coefficient in the equation of state (8) depends on $|\varepsilon|$ rather than on $|\dot{\varepsilon}|$.

CONCLUSION

This paper describes an experimental study (the setup and results) of the effect of an intense sound wave on the resonance frequency and the Q factor of a sandstone bar resonator when these parameters of the resonator are measured with the help of a weak wave. Based on the observed behavior of the resonance frequency and the Q factor of the resonator at one mode under the action of the intense wave at another mode, it is shown that, to explain these effects, it is necessary to assume that sandstone exhibits both hysteretic nonlinearity and dissipative acoustic nonlinearity. The comparison of the experimental and theoretical results shows that, as the frequency of the intense wave increases by a factor of 6 (from 2.2 to 13.3 kHz), the effective parameter of hysteretic nonlinearity becomes almost 10 times smaller, while the parameter of dissipative nonlinearity remains unchanged.

Note that, presumably, the majority of polycrystalline rocks exhibit dissipative acoustic nonlinearity. Therefore, the variety of nonlinear effects observed in these media is much wider than in common media, which possess only elastic nonlinearity. The study of the effects of dissipative nonlinearity can be used in the remote acoustic (and seismoacoustic) testing of natural rock.

ACKNOWLEDGMENTS

This work was supported by the Russian Foundation for Basic Research, project nos. 01-05-64417 and 00-05-64252, and by the Interdepartmental Scientific-Engineering Center, project no. 1369.

REFERENCES

1. P. L. Kapitsa, *Recollections, Letters, Documents* (Nauka, Moscow, 1994).
2. L. D. Landau and E. M. Lifshits, *Course of Theoretical Physics*, Vol. 7: *Theory of Elasticity*, 4th ed. (Nauka, Moscow, 1987; Pergamon, New York, 1986).
3. L. K. Zarembo and V. A. Krasil'nikov, *Introduction to Nonlinear Physical Acoustics* (Nauka, Moscow, 1966).
4. V. E. Nazarov, Fiz. Met. Metalloved., No. 3, 172 (1992).
5. V. Yu. Zaĭtsev, A. B. Kolpakov, and V. E. Nazarov, Akust. Zh. **45**, 235 (1999) [Acoust. Phys. **45**, 202 (1999)].
6. V. E. Nazarov, Fiz. Met. Metalloved. **88** (4), 82 (1999).
7. N. G. Cook and K. Hodgson, J. Geophys. Res. **70** (12), 2883 (1965).
8. S. B. Kustov, S. N. Golyandin, and B. K. Kardashev, Fiz. Tverd. Tela (Leningrad) **30** (7), 2167 (1988).
9. G. N. Boinott, in *Proceedings of 15th Annual Seismic Research Symposium, Vail, Colorado*, Ed. by J. F. Lewcowicz and J. M. McPhetres (Philips Laboratory of the Air Force Material Command. Hancome Air Force Base, Mass., 1993); Environ. Res. Pap., No. 125, 121 (1993).
10. V. E. Nazarov, L. A. Ostrovskiĭ, I. A. Soustova, and A. M. Sutin, Akust. Zh. **34**, 491 (1988) [Sov. Phys. Acoust. **34**, 285 (1988)].
11. S. V. Zimenkov and V. E. Nazarov, Fiz. Zemli, No. 1, 13 (1993).
12. J. A. Ten Cate and T. J. Shankland, Geophys. Res. Lett. **23**, 3019 (1996).
13. V. E. Nazarov, Akust. Zh. **46**, 228 (2000) [Acoust. Phys. **46**, 186 (2000)].
14. V. E. Nazarov and A. B. Kolpakov, J. Acoust. Soc. Am. **107**, 1915 (2000).
15. R. A. Guyer and P. A. Johnson, Phys. Today **52** (4), 30 (1999).
16. S. V. Zimenkov and V. E. Nazarov, Fiz. Met. Metalloved., No. 3, 62 (1992).
17. V. E. Nazarov, Akust. Zh. **47**, 509 (2001) [Acoust. Phys. **47**, 438 (2001)].

Translated by A. Khzmalyan

Acoustical Physics, Vol. 48, No. 1, 2002, pp. 8–11. Translated from Akusticheskiĭ Zhurnal, Vol. 48, No. 1, 2002, pp. 12–15.

Temperature Properties of Plate Modes in Quartz

I. V. Anisimkin*, V. I. Anisimkin*, Yu. V. Gulyaev*, and E. Verona**

** Institute of Radio Engineering and Electronics, Russian Academy of Sciences, ul. Mokhovaya 11, Moscow, 103907 Russia*

e-mail: ivanis@mail.cplire.ru

*** Instituto di Acustica O.M. Corbino CNR, via del Fosso del Cavaliere, Rome, 00133 Italy*

Received April 12, 2001

Abstract—The shear horizontal modes that occur in a quartz plate are studied both theoretically and experimentally. These modes are shown to possess a wide variety of temperature properties, including the characteristic behavior of the temperature coefficient of delay, which can take on negative, zero and record-breaking high positive values up to 350×10^{-6}/°C. The dependence of this coefficient on the mode number is explained by the varying partial contributions of three elastic moduli, c_{12}, c_{14}, and c_{44}, to this coefficient.

The value, sign and temperature dependence of the temperature coefficient of delay (TCD) of acoustic waves in crystals play an important role in a broad range of applications. The frequency stabilizers and narrow-band filters require small values of the TCD, which vary weakly in a wide temperature range. On the contrary, this coefficient should be as large as possible for temperature measurements in analytical chemistry and for gas detection by thermal conduction measurements. Therefore, the investigation of the temperature properties of acoustic vibrations remains a topical problem of modern acoustoelectronics. The required value of the TCD is generally provided by the choice of the crystal cut and the direction of wave propagation [1–12]. This paper shows that the value, sign, and temperature dependence of the TCD can be varied by choosing the mode number without changing the direction of propagation and the plate cut.

We studied the shear horizontal (SH) modes with the frequencies f = 12.6–44.5 MHz in an ST,X+90° quartz plate 0.5 mm thick. One face of the plate was optically polished and the other was grinded. The vibrations were excited and received using interdigital transducers with 20 pairs of Cr/Au pins and the period $\lambda = 392$ μm. The distance between the transducers was 24.1 mm. The structure under study was placed in a heat-insulated box of an MLW U10 thermostat with varying temperature (to an accuracy of ≤0.05°C). The study of the temperature sensitivity of SAW was conducted in the phase format with an HP 8753 ES quadripole analyzer. By virtue of the narrow transmission band of the transducers and the small thickness of the plate (H/λ = 1.2755), the acoustic modes of various orders n were well resolved up to n = 18 (see Fig. 1). In the experiment, we measured the relative phase shift $\Delta\varphi/\varphi$ of the vibrations under a change in temperature within t = 2–92°C at a step Δt = 5–10°C. The value of the TCD for each mode was determined according to the relation TCD = $(1/\Delta t)(\Delta\varphi/\varphi)$ at room temperature (t = 20°C) and at the temperatures of the zero and maximal TCD. To diminish the effect of electromagnetic interference on the measurement results, the vibrational modes whose amplitudes exceeded the interference by less than 10 dB were excluded from consideration. The reliability of the experimental results was monitored using a 128° Y,X $LiNbO_3$ test sample for which the Rayleigh-wave TCD was well known (72×10^{-6}/°C).

The results obtained are presented in Figs. 2–4. From Fig. 2, one can see that modes of different orders have different temperature dependences of their phases $(\varphi - \varphi_0)/\varphi_0$: for the first modes, this dependence is quasi-cubic, and for higher-order modes, it is close to linear. According to different types of the phase–temperature dependences, differences are also observed in the temperatures t, at which the curves for different modes reach their extremal values or their maximal gradients, and the corresponding values of the TCD = $(1/\Delta t)(\Delta\varphi/\varphi)$ turn to zero or reach their maximum. In our experiments, the maximal temperature sensitivity was characteristic of the 13-order mode at $t \approx 47$°C. The value of the TCD for this mode was about 350×10^{-6}/°C, which was much higher than the corresponding values for the bulk wave (-12×10^{-6}/°C) and the surface wave (-34×10^{-6}/°C) of the same polarization, which propagated in the same direction in quartz. This value is also far above the Rayleigh-wave TCD value in $Bi_{12}GeO_{20}$ (120×10^{-6}/°C) and the corresponding values for the SH modes in AT-quartz plates with double-sided grating (210×10^{-6}/°C) [13], the latter modes being the most thermally sensitive acoustic vibrations known so far. At the threshold value of the acoustic response $\Delta\varphi/\varphi = 0.5 \times 10^{-6}$ and TCD = 350×10^{-6}/°C, the threshold value of the temperature variations detected in our experiments was $\Delta t = (1/\text{TCD})(\Delta\varphi/\varphi) \approx 0.001$°C.

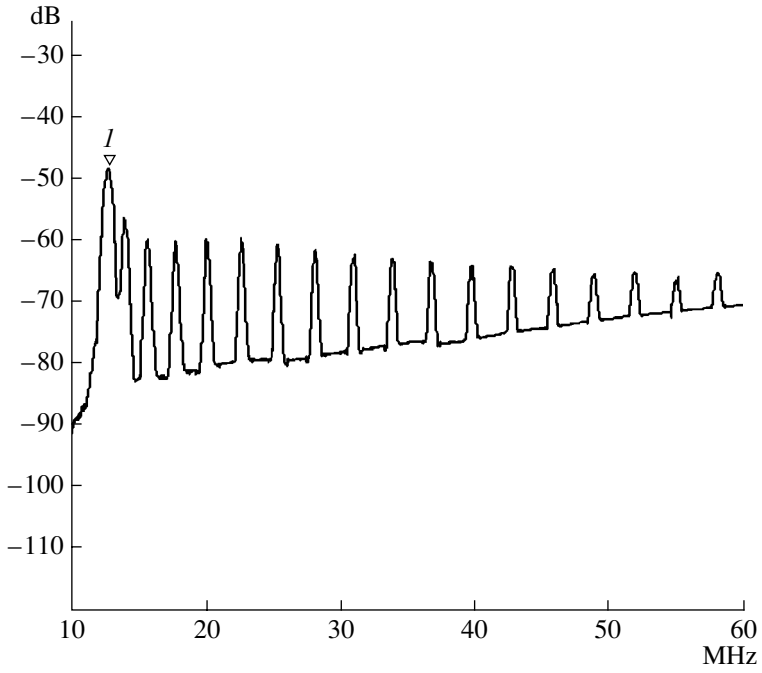

Fig. 1. Amplitude–frequency characteristics of SH modes in an ST,X+90° quartz plate. Mark *1* corresponds to a frequency of 12.78125 MHz and an amplitude of 47.943 dB.

It is seen from Fig. 3 that the value of the TCD changes rapidly with the mode number n: this value is negative for $n = 0$–4, zero for $n = 5$–7 and positive for $n \geq 8$.

To substantiate this change, we calculated the partial contributions made to the TCD by the variations of the density ρ, the elastic moduli c_{ij} and the linear coefficients of thermal expansion along the propagation direction $\alpha_\parallel$ and along the plate thickness $\alpha_\perp$. The modes of the first 17 orders were considered. The phase velocity of the nth mode v_n was presented as a total differential with respect to the variables $x = \rho$, c_{ij}, $\alpha_\perp$, and $\alpha_\parallel$:

$$\mathrm{TCD}_n = \alpha_\parallel - \frac{1}{v_n}\frac{dv_n}{dT} = \alpha_\parallel - \frac{1}{v_n}\frac{\partial v_n}{\partial(H/\lambda)}\frac{\partial(H\lambda)}{\partial T} - \frac{1}{v_n}\frac{\partial v_n}{\partial \rho}\frac{\partial \rho}{\partial T} - \frac{1}{v_n}\frac{\partial v_n}{\partial c_{ij}}\frac{\partial c_{ij}}{\partial T}. \quad (1)$$

Then, we conducted a successive variation of one of the parameters of the quartz plate x within ±1% relative to its room-temperature (20°C) value and calculated the values of the mode velocity for the room-temperature (v_{no}) and two boundary values of this parameter ($v_{n-1\%}$ and $v_{n+1\%}$). After that, we determined the temperature sensitivity dx/dt of the parameter x and the value of the corresponding partial contribution $(1/v_{no})(\Delta v_n/\Delta x)(dx/dt)$, where $\Delta v_n = v_{n+1\%} - v_{n-1\%}$. Finally, the partial contributions of different parameters x were added together, and the TCD value for this mode was calculated by Eq. (1). The mode velocities were calculated according to Adler's program [14]. The material constants of quartz and their temperature dependences were taken from [15] and [16], respectively. The thickness of the quartz plate was determined by the experimental condition $H/\lambda = 1.2755$. A comparison of the theoretically calculated and experimental

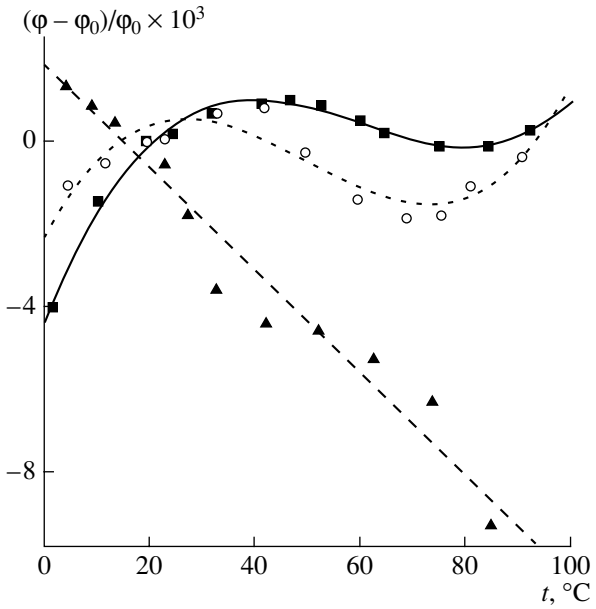

Fig. 2. Temperature dependence of the phase for some vibrational modes in the same plate. The dots represent the experimental data, and the lines represent the linear and cubic approximations; n = (■) 0, (○) 2, and (▲) 8.

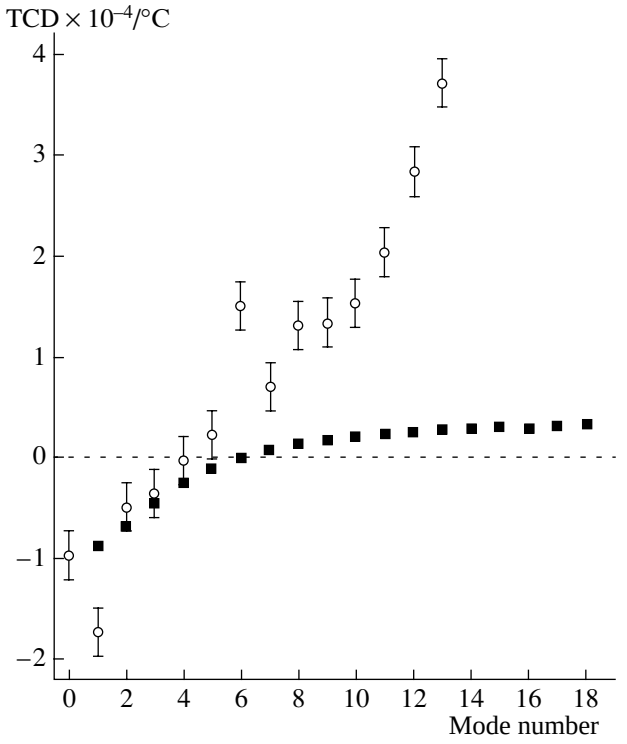

Fig. 3. Values of the TCD for SH modes in ST,X+90° SiO_2 at room temperature t = 20°C: (■) theory and (○) experiment.

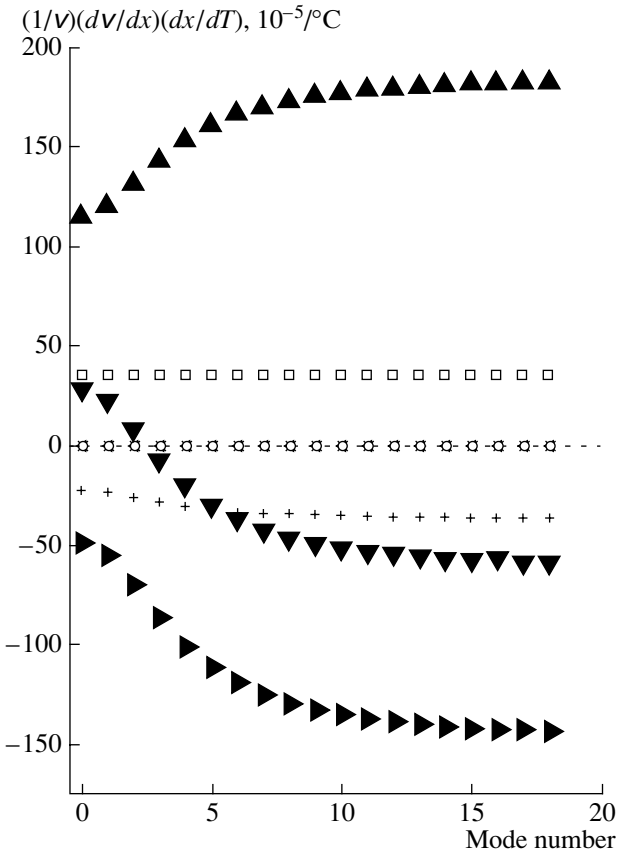

Fig. 4. Variations of the partial contributions of the following parameters of the plate to the TCD with the mode number at room temperature t = 20°C: (□) ρ, (+) c_{11}, (▲) c_{12}, (◁) c_{13}, (▼) c_{14}, (×) c_{33}, (►) c_{44}, and (○) H/λ.

velocity values measured with an accuracy of ±2% shows (see table) their agreement to within several percent (the values in parentheses). This allows us to identify the modes correctly during the experiment.

The results of the calculations are presented in Figs. 3 and 4. It is seen from Fig. 3 that the calculated and experimental dependences of the TCD on the mode number are in qualitative agreement. The quantitative difference observed for the high-order modes is presumably attributable to the effect of the interdigital transducers and the roughness of one of the sample surfaces on the measurement results. According to Fig. 4, the dependence of the TCD on n mainly results from the change in the partial contributions of the elastic moduli c_{12}, c_{14}, and c_{44} with varying mode number, because the contributions of other parameters of the plate are virtually constant for all modes, and the con-

Theoretical and experimental values of the velocities of SH modes in ST,X+90° quartz plate (H/λ = 1.2755) m/s

Mode number	Theory	Experiment	Mode number	Theory	Experiment
0	4993	5000 (+0.1%)	10	14203	14500 (+2.1%)
1	5169	5500 (+6.4%)	11	15454	15600 (+0.9%)
2	5662	6200 (+9.5%)	12	16716	16800 (+0.5%)
3	6398	7000 (+9.4%)	13	17989	18000 (+0.1%)
4	7303	7900 (+8.2%)	14	19268	19200 (–0.4%)
5	8322	8800 (+5.7%)	15	20554	20400 (–0.7%)
6	9418	10000 (+6.2%)	16	21845	21600 (–1.1%)
7	10567	11100 (+5.0%)	17	23141	22800 (–1.5%)
8	11754	12200 (+3.8%)			
9	12969	13300 (+2.6%)			

tributions of c_{11}, c_{13}, and c_{33} are negligibly small or equal to zero.

Thus, the SH modes in a quartz plate possess a wide variety of temperature properties, the temperature coefficient of delay taking on negative, zero, and record-breaking high positive values in the temperature range $t = 2$–$92°C$. A further increase in the temperature sensitivity of acoustic vibrations should be expected for the SH, Lamb, and Love plate modes after the necessary optimization of the material, the crystal cut, and the thickness of the sound-transmitting plate.

REFERENCES

1. A. Ballato, in *Physical Acoustics*, Ed. by W. P. Mason (Academic, New York, 1977), Vol. 13, pp. 115–181.
2. A. J. Slobodnik, Jr., in *Acoustic Surface Waves*, Ed. by A. A. Oliner (Springer, New York, 1978; Mir, Moscow, 1981).
3. D. S. Bailey, J. S. Andle, D. L. Lee, *et al.*, in *Proceedings of the IEEE Ultrasonics Symposium, 1983*, p. 335.
4. R. T. Webster, J. Appl. Phys. **56**, 1540 (1984).
5. R. S. Falconer and J. F. Vetelino, in *Proceedings of the IEEE Ultrasonics Symposium, 1985*, p. 241.
6. Y. Shimizu and K. Murakami, in *Proceedings of the IEEE Ultrasonics Symposium, 1986*, p. 191.
7. Y. Shimizu, Y. Endo, and T. Watanabe, in *Proceedings of the IEEE Ultrasonics Symposium, 1987*, p. 253.
8. R. T. Webster, IEEE Trans. Ultrason. Ferroelectr. Freq. Control **35**, 386 (1988).
9. A. Isobe, M. Hikita, and K. Asai, in *Proceedings of the IEEE Ultrasonics Symposium, 1993*, p. 323.
10. T. Sato and H. Abe, in *Proceedings of the IEEE Ultrasonics Symposium, 1994*, p. 287.
11. E. Bigler, S. Ballandras, C. Bonjour, *et al.*, in *Proceedings of the IEEE Ultrasonics Symposium, 1994*, p. 385.
12. W. Ma and W. Shi, IEEE Trans. Ultrason. Ferroelectr. Freq. Control **48**, 333 (2001).
13. S. Ballandras, J. B. Briot, and G. Martin, in *Proceedings of the IEEE Ultrasonics Symposium, 1996*, p. 459.
14. E. I. Adler, IEEE Trans. Ultrason. Ferroelectr. Freq. Control **41**, 876 (1994).
15. A. J. Slobodnik, Jr., E. D. Conway, and R. T. Delmonico, *Microwave Acoustic Handbook, ARFCRL-TR-73-0597* (1973).
16. A. G. Smagin and M. I. Yaroslavskiĭ, *Piezoelectricity of Quartz and Quartz Resonators* (Energiya, Moscow, 1970).

Translated by A. Kruglov

Acoustical Physics, Vol. 48, No. 1, 2002, pp. 81–86. Translated from Akusticheskiĭ Zhurnal, Vol. 48, No. 1, 2002, pp. 91–97.

Deep Scattering Layers in the Northwestern Pacific

L. L. Tarasov

Andreev Acoustics Institute, ul. Shvernika 4, Moscow, 117036 Russia

e-mail: bvp@akin.ru

Received December 28, 2000

Abstract—The large-scale horizontal variability of deep scattering layers (DSL) in the Northwestern Pacific is analyzed. The analysis is based on long-term measurements of the column strength and the volume scattering coefficient for frequencies from 0.63 to 16 kHz. The depth and frequency dependences of the scattering coefficient are presented for different regions of the aforementioned ocean region. The most pronounced changes in the DSL structure are found to occur at the boundaries between large-scale water masses or seas with different hydrological characteristics. By contrast, within such water masses and seas, the depth–frequency structure of the DSL remains relatively stable. © *2002 MAIK "Nauka/Interperiodica".*

Despite the fact that ample data on deep scattering layers (DSL) has been collected by various researchers from different countries for 50 years, many regional features of the spatial and temporal variability of volume scattering in the ocean and outlying seas remain open questions. This paper presents an attempt to summarize the results of the long-term experiments carried out by the author in the Northwestern Pacific. The volume backscattering coefficient m_v and column strength M are adopted as the basic characteristics of the volume scattering in the water column. The backscattering coefficient m_v is determined as

$$m_v = W_S/(VI),$$

where W_S is the power backscattered by a volume V per unit solid angle and I is the sound intensity incident on this volume. The column strength M is the integral of the scattering coefficient m_v with respect to the depth; this integral is usually calculated within the limits from the sea surface to the depth where the DSL are in greatest abundance. The paper considers the spatial variability of the quantities m_v and M in frequency range 0.63–16 kHz.

The experimental measurements of the volume scattering characteristics were carried out using two basic techniques of remote sensing in the bulk of the ocean: explosions and tone impulses. In the first technique, explosions of trinitrotoluene charges (200-g mass in the case under consideration) formed the sound source providing an intense broadband omnidirectional radiation that was sufficient for detecting the DSL at virtually arbitrary depths z in the ocean. In this case, the reception was performed with a spherical omnidirectional hydrophone located at a distance of only few meters from the explosion center, which, with allowance for the experiment geometry, makes it possible to consider the points of transmission and reception coincident and to interpret the term scattering as the backscattering in the following consideration. In the experiments, we used the Lesenka lowering system designed at the Andreev Acoustics Institute. This system was attached to the working end of the carrying cable-hawser and contained a receiving hydrophone with a preamplifier and 12 charges that were remotely exploded from on board the vessel during the experiment. To enhance the reliability of the measured depth-dependent scattering coefficient m_v, the charges were exploded in runs of five or six charges at two depths differing by 300–1000 m. Later, the results obtained in the runs were averaged. In the conditions of our experiments, a 95% confidence interval for the calculated scattering coefficient was usually less than 1.5–2.0 dB. At the beginning of the experiment, one or two charges were exploded below all expected DSL, at a depth of 2.0–2.5 km, which made it possible to roughly estimate the vertical structure of the scattering field and define more exactly the depths of the explosion runs. Under favorable conditions, the explosion runs were carried out day and night at the same point of the ocean, which gave the opportunity to measure the diurnal DSL variability governed by the vertical migration of biological scatterers. The explosion technique and the description of the Lesenka system are given in detail in [1]. The calculation of the dependences $m_v(z)$ from data obtained with the explosion technique assumes that, within the insonified region, the scattering properties of the medium depend only on the depth, i.e., the scattering field has a horizontally layered structure. In addition, the calculation assumes that the explosion wave is a spherical one, i.e., the depth dependence of the velocity of sound is neglected.

In the case of tone impulses, we used directed transmitting–receiving acoustic arrays usually operating in the echo-sounder mode with the axis of the directional pattern being perpendicular to the unperturbed ocean surface. The half-width of the main lobe of the pattern

1063-7710/02/4801-0081$22.00 © 2002 MAIK "Nauka/Interperiodica"

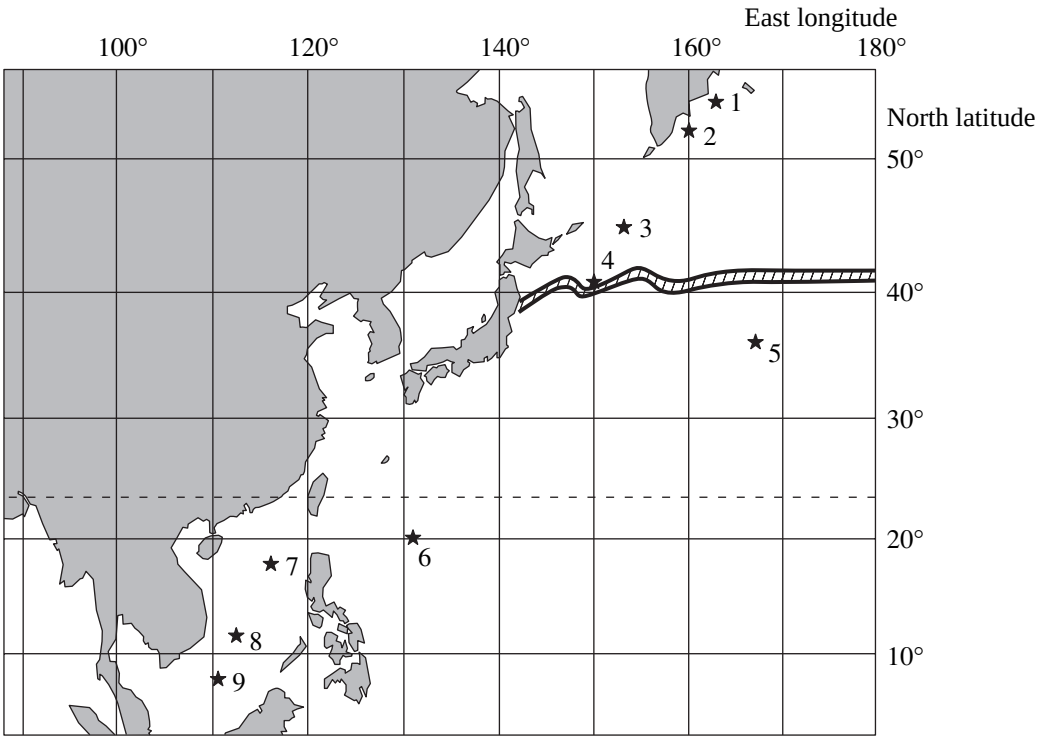

Fig. 1. Regions of experiments on DSL in the Northwestern Pacific.

at a level of –3 dB varied from 5° to 15° depending on frequency in the range 3–8 kHz. The tone impulse technique is much simpler in implementation than the explosion technique. It should be noted, however, that the directed radiation systems used in the experiment produced a pressure of only 2×10^4 Pa (reduced to a distance of 1 m) at the axis, so that, in the case of their positioning near the sea surface, they did not always allow us to detect the DSL at large depths, especially at higher frequencies. For frequencies $f \geq 8$–10 kHz, the limiting detection depth of layers with an intermediate scattering level measures about 1 km. For sounding the DSL at greater depths, it is necessary either to increase the duration of the transmitted signal, which lowers spatial resolution, or to deepen the array by several hundreds of meters, which drastically increases the duration of the experiment.

Figure 1 shows the centers of the regions in the Northwestern Pacific (asterisks) where the experiments were carried out. From three to seven runs of hydroacoustic experiments with a spacing of 20–50 km were carried out in every region. The experimental conditions of regions 2 and 6 differed from the above conditions and will be described below, before discussing the results. The hatched band shows the approximate position of the subarctic part of the frontal zone serving as the boundary that separates the subarctic and western water masses of the Pacific [2], which drastically differ in their hydrology, chemistry, and biology. This frontal zone coincides with the region where two currents meet: the warm Japan (Kuroshio) Current and the cold Oyashio (Okhotsk) Current.

The most complete data on the features of DSL in the Northwestern Pacific were obtained for the Kamchatka region (regions 1 and 2 in Fig. 1), where the measurements were carried out from 1983 to 1990 in spring, summer, and autumn, and several tens of hydroacoustic experiment runs were performed with both explosions and tone signals.

Among the characteristic features of the Kamchatka region, the first is the absence of daily migrations of DSL. As a consequence, the column strength in the daytime differed from the column strength at night only slightly (by less than 2–3 dB) for all frequencies of the 0.63–16 kHz range used in the experiments. This invariability of the scattering field during the day and its low variability in the Kamchatka region make it possible to characterize the region by the function $m_v(z, f)$ obtained in May 1986 with the explosion technique in region 2 (area about 20000 square kilometers) located mainly between the Kamchatka coast and the Kurile–Kamchatka Canal. Figure 2 shows this function as a family of lines of equal level with a spacing of 5 dB. The dotted line in the left-hand part of Fig. 2 indicates the region where no data was obtained, because the level of the received signal was below the noise level.

The second feature of this region is the deep layer about 1 km wide lying at the depths from 1 to 2 km and observed at frequencies higher than 2 kHz. This layer

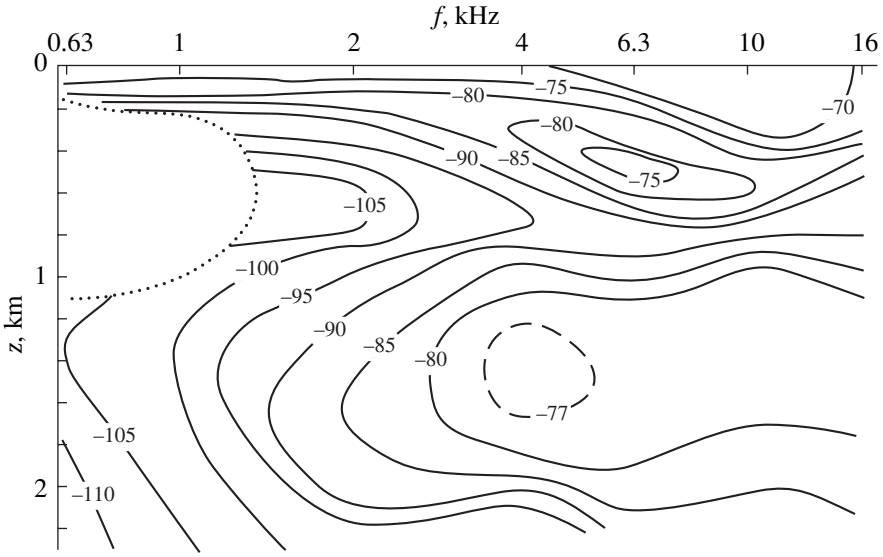

Fig. 2. Averaged function $m_V(z, f)$ characteristic of region 2 (near the Kamchatka coast).

had a weak maximum (shown in Fig. 2 by the dashed line) at a 4 kHz frequency at a depth of about 1.4 km. In similar measurements carried out in 1990 near the Kamchatka coast (region 1) with the use of directed transmitting–receiving arrays operating in the 2–7 kHz range and lowered to a 0.5 km depth, the deep layer was regularly observed. The scattering maximum in this layer occurred in the frequency range 3–4 kHz at a depth varying from 1.2 to 1.5 km. The magnitudes of the coefficient m_v only slightly differed from those given in Fig. 2 throughout the whole frequency–depth region. The layer at the depth 300–500 m at a 3 kHz frequency was also regularly observed. It should be noted that layers of such thickness and scattering level at depths exceeding 1.5 km were only rarely observed in other regions of the ocean.

Finally, the third feature of the region, which was fixed during only one expedition, is a 30- to 150-m thick layer that appeared for frequencies in the range 0.63–2 kHz and was immediately adjacent to the ocean surface. This layer was steadily observed during May in the region between the Kamchatka coast and the Kurile–Kamchatka Canal. The detection of this low-frequency layer was possible only using upward insonification, i.e., using deep-water explosions. The latter were carried out in only one expedition in the Kamchatka region because of technical reasons. Sounding the water column with surface explosions gave no way of detecting this thin layer, because, during the first 200 ms after an explosion, the receiver of our hydroacoustic system remained in the nonlinear mode caused by the overload of the hydrophone output due to the passage of the shock wave. The column strength of the surface layer exceeded the column strength of underlying water by at least 10–15 dB; it amounted to a value of –52 dB (which corresponds to the value of the scattering coefficient averaged over the layer thickness from –75 to –67 dB) and remained almost intact within the range 0.63–2 kHz. For frequencies above 2 kHz, the surface layers with a scattering coefficient exceeding –75 dB were observed nearly everywhere in the Kamchatka region, including the areas located behind the Kurile–Kamchatka Canal. Analysis showed that the recorded low-frequency surface layer presumably had a biological nature. According to our calculations, such a high scattering level at a 0.63 kHz frequency could be caused by large discrete scatterers (swimming-bladder fishes of length 30 cm and longer) with a concentration of about 2×10^{-4} m^{-3}. The invariability of the column strength M for the frequencies f within the range 0.63–2 kHz suggests that the concentration of smaller fishes must increase no slower than $\sim l^{-2}$, where l is the fish length. Since this surface layer was detected during salmon spawning near the Kamchatka coast, it, possibly, has a seasonal nature. To the west of the Kurile–Kamchatka Canal, this layer was detected neither during salmon spawning, nor in other seasons.

The investigations of the volume scattering in the Kamchatka region testify to the long-term (at least within 5–7 years) stability of the DSL parameters, such as the absolute values of the scattering coefficients and their depth-dependent profiles. If we assume that the field of volume scattering is also stable in other areas of the ocean, we can relate the differences in the layer structure observed by spaced hydroacoustic systems to specific hydrological and climatic conditions. This assumption makes it possible to estimate the parameters of the large-scale spatial variability in the Northwestern Pacific.

Figure 3 shows the frequency–depth behavior of the volume scattering coefficient during the day in regions 1–6. All these regions were located in the open

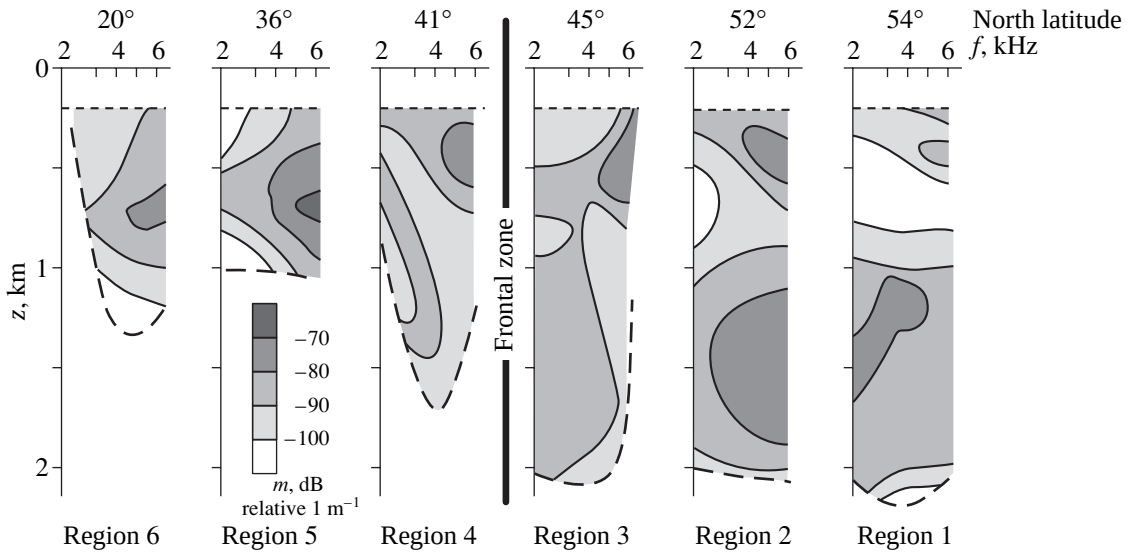

Fig. 3. Latitude variability of the volume scattering field in the Northwestern Pacific.

deep-water area of the ocean and were practically not separated by isle arcs and bottom elevations that could affect the DSL structure. However, between regions 5 and 3, there is a subarctic frontal zone that separates the global types of water mass structure and goes approximately along 41° N. According to hydrological data, the effect of frontal zones on water salinity and temperature is appreciable only to depths of 500–700 m, and, for greater depths, no jumps occur in the latitude behavior of these parameters. Despite a fairly great scatter of regions 1–6 in longitude, in view of the direction of this boundary between water masses, we will assume that Fig. 3 characterizes the latitude variability of the field of volume scattering. The validity of this interpretation is indirectly supported by the results obtained by subdividing the Atlantic Ocean into regions in accordance with the acoustic characteristics of DSL, primarily the column strength for frequencies from 3 to 20 kHz [3, 4]. It was found that the boundaries of regions with homogeneous hydrological conditions in the Atlantic could be considered in some cases as boundaries between regions with different statistical parameters of column strength. This fact allows one to suggest that the DSL parameters in the open ocean are more stable in the latitude direction than in the meridian one. To simplify the comparison, the curves of equal level of the coefficient m_v are given for the same frequency range (2.0–6.3 kHz) and the same depths (0.2–2.2 km) with a curve spacing of 10 dB.

As is seen from Fig. 3, the DSL located in the depth range from 1 to 2 km universally occurred to the north of the subarctic frontal zone (regions 1–3). As we approached the frontal zone (region 3), the scattering level in this deep-water layer decreased, and the received signal was even below the background noise for $f > 5$ kHz. A distinguishing feature of region 4 located almost immediately at the frontal boundary consists in the irregularity of the function $m_v(z, f)$ for $z > 800$ m. Only traces of the deep-water layer were observed there, the scattering coefficient being below –87 dB for all frequencies. To the south of the subarctic zone, only one DSL was discernible, in which the scattering maximum occurred at a depth of about 700 m, i.e., about 200 m deeper than the scattering maximum of a similar layer to the north of the frontal zone. It is worthwhile to mention that the frequency–depth structure of the field of volume scattering in region 5 is closer to the structure observed in region 6, which is separated from it by 4000 km, than to the structures observed in regions 1–4 located at shorter distances. A possible explanation is that both regions 6 and 5 are located in the zone affected by the same water stream consisting of the North Pacific Current continued by the Japan Current.

The curves given in Fig. 3 suggest that the frequency-depth structure of the field of volume scattering is essentially changed at the boundary between two water masses and can be considered as one of the biological and hydrological characteristics typical of these masses. An interesting point consists in the fact that the strong variability of hydrological characteristics observed in going from one water mass to the other concerns only the upper 700-m thick water layer, while changes in the DSL structure occur in the water bulk to a depth of 2000 m.

For low latitudes, the DSL were investigated in the semi-closed South China Sea and in the open Philippine Sea that can be considered a part of the Pacific, because it is involved in the dynamics of the North Pacific Current. In the Philippine Sea, measurements were carried out far from the coast, in region 6 where the sea depth exceeds 5 km. The distance between the points where two measurement runs were carried out was about 100 km. In the South China Sea, measure-

ments were carried out in three regions separated from each other by hundreds of kilometers. Region 9 is located in a small hollow that has depths about 2 km and is almost surrounded by reefs and shallow waters. Despite the separation by about 800 km, regions 7 and 8 have similar hydrological characteristics: about depths 4 km and relatively flat bottoms. The measurements were carried out in May in region 9 and in October in regions 7 and 8. As an example figure 4 shows the structure of the scattering field obtained in region 8 during daytime. Contrary to the Philippine Sea, in parallel with the layer at a depth about 700 m, an additional layer occurred here at a 200 m smaller depth. A similar double-layer structure was also characteristic of other measurement runs carried out in the South China Sea. Unfortunately, the measurements in these southern seas were performed only with directed low-frequency arrays, which restricted the maximal depth in the experimental functions $m_v(z)$ by a value of about 1 km in the frequency range 3–7 kHz. However, comparison with the data of other authors and with our own explosion measurements for other low-latitude regions of the Pacific suggests that deep-water layers similar to those detected in the Kamchatka region are unlikely for both the South China and the Philippine Seas.

To quantitatively estimate, on the one hand, whether or not the Philippine and South China Seas can be considered as different in their volume scattering characteristics and, on the other hand, what is the degree of homogeneity of these characteristics for each of the areas under consideration, we used the simple technique of cluster analysis similar to that used by McElroy [5] to select in the Atlantic regions uniform in their scattering characteristics. The essence of this technique is as follows. The same set of parameters (in the general case, not necessarily hydroacoustic ones) is measured for every point of an area. Then, this set is considered as the coordinates of the point in the N-dimensional space, where N is the number of measured parameters. The proximity of these points is characterized by the Euclidean distance in the above coordinate system. If the set of interpoint distances can be divided into subsets, within which these distances are smaller than a certain distance used as the proximity criterion, and the distances between any pair of points belonging to different subsets exceed this criterion, then, the separation of the area into homogeneous regions (clusters) is fulfilled. The above separation procedure is one of the simplest and most rigorous procedures in cluster analysis, because the distances between obvious clusters can actually be smaller than the intracluster distances (as the distances between isles in the ocean can be smaller than the sizes of the isles).

McElroy [5] used the magnitudes of the column strength in decibels for 16 frequencies ranging from 1 to 31.5 kHz as acoustic coordinates. Subsequently, the frequency-averaged magnitude M calculated for every measurement run was subtracted from these magnitudes. This way, the entire area was subdivided into

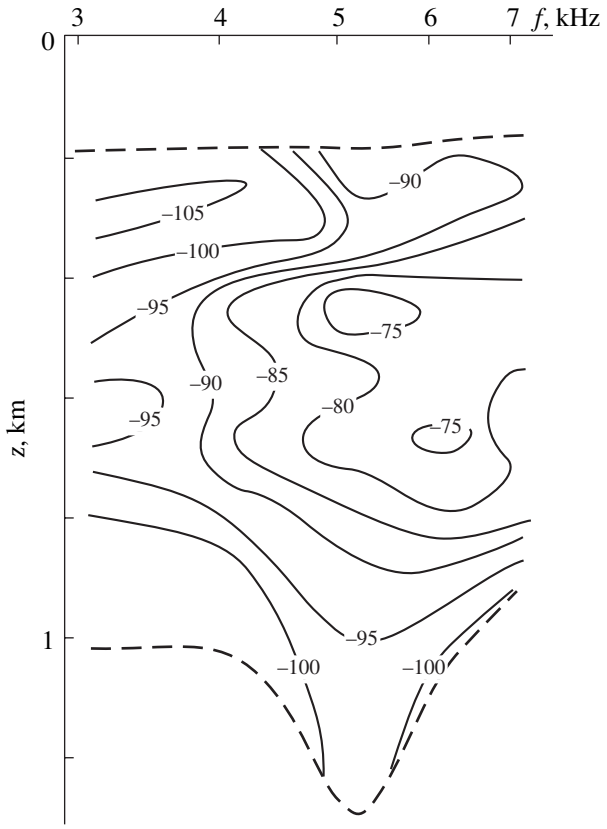

Fig. 4. One of the depth–frequency dependences obtained in the South China Sea (region 8).

regions with characteristic frequency-dependent behaviors of the column strength, i.e., with identical distributions in sets of biological scatterers. The total number of scatterers was not taken into consideration in subdividing the area into clusters. In addition, such an approach cannot include the differences in the vertical structure of the DSL.

We used the values of the scattering coefficient m_v for nine depths (from 250 to 1050 m at every 100 m) and for four frequencies 3.15, 4.2, 5.2, and 6.2 kHz as coordinates in a 36-dimensional space. All data were normalized by the average scattering coefficient over all 36 values. The table presents the matrix of the Euclidean acoustic distances for three regions of the South China Sea (7–9) and two regions of the Philippine Sea (6 and 6a). Regions 6 and 6a (on the map, region 6a is not marked by a separate asterisk) were separated by not more than 100 km.

As is seen from the table, the distance between any pair of points belonging to each single sea is smaller than the distance between any points belonging to different seas (the corresponding three groups are marked by the bold frames), which points to a relatively low variability of the frequency–depth structure of the scattering field within one sea in comparison with the variability of this structure in going from one sea to the

Acoustic distances between the investigated regions of the South China and Philippine Seas

Region no.	8	7	6	6a
9	25.0	29.5	48.7	53.4
8	–	38.8	39.6	46.2
7	–	–	46.1	48.5
6	–	–	–	23.1

other. In actual practice, the division into homogeneous regions is often performed with the use of weaker criteria than the one given above. The small average distance between the intracluster points and the small distance from the cluster points to the gravity center of the cluster in comparison with the distance between the gravity centers of these clusters are examples of such criteria. The use of such criteria would result in a more prominent subdivision of the matrix of distances into two separate compact regions.

The suggested procedure can be useful in subdividing the ocean into areas according to the DSL characteristics. The degree of detail in such a subdividing depends on the number of parameters measured for every geographic point and on the criteria of proximity of these parameters. Note that such a subdivision into homogeneous areas is closely related to the urgent problem of the general accounting of the biological resources of the ocean. This problem studied under certain international programs, one of which is the extended program "Census of Marine Life" [6]. This program includes the formation of the global Ocean Biogeographic Information System (OBIS) based on many experimental data, including acoustic data.

All abovementioned results support the hypothesis that assumes a certain relationship between the large-scale spatial variability of the DSL and the global variability of hydrological characteristics, which was pointed out in [4]. Under this assumption, every water mass or closed sea is presumably characterized by its own depth–frequency structure of the volume scattering field, this structure being relatively stable within the basin under consideration.

ACKNOWLEDGMENTS

I thank I.B. Andreeva for supervision and manifold sincere help in all my activities and N.N. Galybin for fruitful discussions and valuable advice concerning full-scale experiments.

The work was supported by the Russian Foundation for Basic Research, project no. 98-05-64849.

REFERENCES

1. *Acoustics of the Ocean*, Ed. by L. M. Brekhovskikh (Nauka, Moscow, 1974).
2. *Oceanographic Encyclopedia* (Gidrometeoizdat, Leningrad, 1974), pp. 114–118, 528–533.
3. I. B. Andreeva, N. N. Galybin, L. L. Tarasov, and V. Ya. Tolkachev, Akust. Zh. **46**, 21 (2000) [Acoust. Phys. **46**, 10 (2000)].
4. N. N. Galybin, L. L. Tarasov, and V. Ya. Tolkachev, in *Proceedings of the VIII School–Seminar of Academician L.M. Brekhovskikh* (GEOS, Moscow, 2000), p. 112.
5. P. T. McElroy, J. Acoust. Soc. Am. **56**, 394 (1974).
6. J. F. Grassle and K. I. Stocks, Oceanography **12** (3), 12 (1999).

Translated by A. Vinogradov

Acoustical Physics, Vol. 48, No. 1, 2002, pp. 87–93. Translated from Akusticheskiĭ Zhurnal, Vol. 48, No. 1, 2002, pp. 98–104.

Displacement Field Produced by a Surface Source of Vibrations in a Layered Biological Tissue

E. M. Timanin

Applied Physics Institute, Russian Academy of Sciences, ul. Ul'yanova 46, Nizhni Novgorod, 603950 Russia
e-mail: eugene@appl.sci-nnov.ru

Received October 2, 2000

Abstract—Theoretical expressions for the components of the displacement vector in a three-layer halfspace with linked and slipping layers are obtained for the case of setting an oscillatory pressure distributed evenly over a circular area at the layer surface. Numerical calculations of the displacement field in the medium are performed for the values of the parameters simulating a skin-fat layer–muscle–liver biological system. The dependences of the oscillatory displacements within tissues on the dimensions and oscillation frequency of the surface source of vibration are studied, and the possibilities of using such a source for the implementation of the sonoelastography method are discussed. *© 2002 MAIK "Nauka/Interperiodica".*

A technique for the ultrasonic visualization of the shear viscoelastic characteristics of soft biological tissues (the so-called sonoelastography method) has been actively developed in recent years [1–3]. This technique is believed to be promising for medical diagnostics of various kinds of tissue pathology. The technique is based on remote measurements by a Doppler ultrasonic gauge of the oscillatory displacements (velocities) produced by a low-frequency shear wave within tissues. Shear waves excited in various ways are used in different studies. These can be natural pulsations excited in tissues by the heart and vessel movements, forced vibrations produced by a source at the tissue surface, and even shear waves generated as a result of nonlinear effects that accompany the propagation of a focused ultrasonic beam in tissues. Although many experimental studies based on the excitation of shear waves in sample and phantom tissues from their surfaces had been conducted, no adequate theoretical description of the process of vibration penetration into the depth of real biological objects was proposed. The purpose of this paper is to introduce acoustic models of this process and to study the laws governing the vibration excitation in tissues by a surface source with the help of these models.

The models of low-frequency acoustic processes in tissues that are now known [4–15] are based on the approaches developed in the dynamic theory of elasticity and seismology [16–21]. A theoretical analysis of shear displacements within the tissue samples of finite dimensions is conducted in [4] for the case of excitation of vibration modes in them. Tissues are simulated by a viscoelastic medium with inclusions corresponding to tumors. The changes of the amplitude of surface displacements in tissues with the distance from the source of vibration are analyzed in [5, 6] on the basis of the solution of a dynamic contact problem on the interaction of a surface source with a halfspace. Several studies [7–9] describe the experimental frequency dependences of the mechanical impedance of a gelatin layer and various soft tissues on the basis of a strictly stated dynamic contact problem on the interaction of a circular flat piston with tissues, which leads to integral equations. In these studies, a soft tissue is considered as a set of linked layers on a hard base (from one to three layers). In [10–12], a soft tissue is treated as a homogeneous layer linked to a hard halfspace simulating a bone, and an approximate formulation of a dynamic contact problem that is common to solving the Lamb problem is used [16]. Experimental frequency dependences [22] of the propagation velocity and the damping factor of waves at the surface of a human hand are described in the framework of this model [10], and the frequency dependences of surface displacements at various distances from a vibrating piston are calculated theoretically [11], as well as the frequency dependences of the mechanical impedance of a piston, including different thicknesses of the soft tissue layer [12]. The models of soft tissues in the form of several linked layers (from one to three) linked with a hard base are developed within the framework of the approach using an approximate formulation of the dynamic contact problem [13–15]. The experimental frequency dependences of the mechanical impedance of a gelatin layer and soft tissues of a human arm, which were obtained using pistons of different diameters, are described within the framework of these models. In this paper, the models of this class (for brevity, we will call them the PSV-models, where PSV means pressure source of vibrations) are suggested for the calculation of the displacement field produced within tissues by a circular source of oscillatory pressure positioned at the surface. A three-layer halfspace with linked or slipping layers is taken as the model of soft tissues.

1063-7710/02/4801-0087$22.00

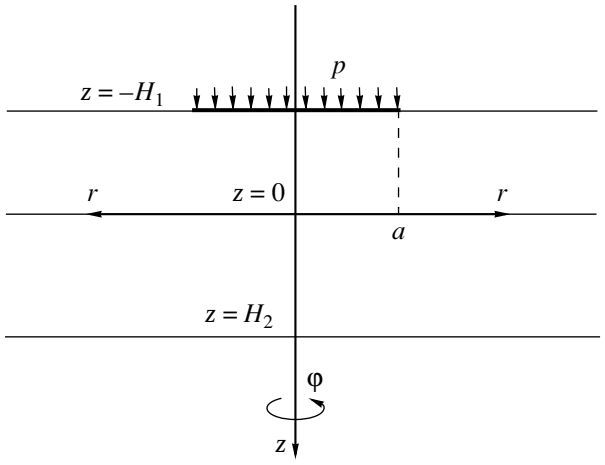

Fig. 1. Diagram of the vibration excitation in a three-layer halfspace.

We obtain expressions for the nonzero components of the displacement vector in the *i*th layer of a medium in an axisymmetric case (see Fig. 1) analogously to the solution of the Lamb problem for a homogeneous halfspace [13, 16]. Specifically, in the general equations of the dynamic elasticity theory [17], we change to scalar and vector potentials and then proceed to the equations for the Hankel transforms of elastic potentials. We write down a general solution for the last equations, express the Hankel transforms for the displacement components through the potentials, and apply the inverse Hankel transformation. Finally, we obtain the following expressions:

$$U_{z,i}(r,z) = \int_0^\infty W^0_{z,i}(k,z)kJ_0(kr)dk,$$
$$U_{r,i}(r,z) = \int_0^\infty W^1_{r,i}(k,z)kJ_1(kr)dk, \quad (1)$$

where

$$W^0_{z,i}(k,z) = -k^2 e^{\kappa_{ti}z}A_{1i}(k) - k^2 e^{-\kappa_{ti}z}A_{2i}(k) + \kappa_{li}e^{\kappa_{li}z}B_{1i}(k) - \kappa_{li}e^{-\kappa_{li}z}B_{2i}(k),$$
$$W^1_{r,i}(r,z) = k\kappa_{ti}e^{\kappa_{ti}z}A_{1i}(k) - k\kappa_{ti}e^{-\kappa_{ti}z}A_{2i}(k) - ke^{\kappa_{li}z}B_{1i}(k) - ke^{-\kappa_{li}z}B_{2i}(k). \quad (2)$$

Here, the upper indices correspond to the order of the Hankel transformation; k is the parameter of the Hankel transformation; J_0 and J_1 are the Bessel functions of the zeroth and first orders; and the parameters $\kappa_{ti} = \sqrt{k^2 - k_{ti}^2}$ and $\kappa_{li} = \sqrt{k^2 - k_{li}^2}$ are determined by the wave numbers of shear and longitudinal waves $k_{ti} = \omega/c_{ti}$ and $k_{li} = \omega/c_{li}$, where $c_{ti} = \sqrt{\mu_i/\rho_i}$ and $c_{li} = \sqrt{(\lambda_i + 2\mu_i)/\rho_i}$ are the velocities of shear and longitudinal waves that are determined by the tissue density ρ_i and the Lame constants μ_i and λ_i. The unknown functions A_{1i}, A_{2i}, B_{1i}, and B_{2i} used for expressing the general solution must be determined from the boundary conditions for the displacements and stresses at all external and internal boundaries of the layers. Expressions for the stress transforms in the medium are obtained from the expressions for the displacement transforms [Eqs. (2)] taking into account the definition of strains and the Hooke law:

$$s^0_{zz,i}(k,z) = -2\mu_i k^2 \kappa_{ti}e^{\kappa_{li}z}A_{1i}(k) + 2\mu_i k^2\kappa_{ti}e^{-\kappa_{ti}z}A_{2i}(k) + \mu_i(k^2 + \kappa_{ti}^2)e^{\kappa_{li}z}B_{1i}(k) + \mu_i(k^2 + \kappa_{ti}^2)e^{-\kappa_{li}z}B_{2i}(k),$$
$$s^1_{rz,i}(k,z) = \mu_i k(k^2 + \kappa_{ti}^2)e^{\kappa_{ti}z}A_{1i}(k) + \mu_i k(k^2 + \kappa_{ti}^2) \times e^{-\kappa_{ti}z}A_{2i}(k) - 2\mu_i k\kappa_{li}e^{\kappa_{li}z}B_{1i}(k) + 2\mu_i k\kappa_{li}e^{-\kappa_{li}z}B_{2i}(k).$$

Here, the upper indices 0 and 1 marking the quantities s_{zz} and s_{rz} also correspond to the order of the Hankel transformation.

At the external boundary of the halfspace $z = -H_1$, we adopt the following boundary conditions for the stress transforms:

$$s^0_{zz,1}(k,-H_1) = -\frac{pa}{k}J_1(ka),$$
$$s^1_{rz,1}(k,-H_1) = 0,$$

which correspond to a uniform distribution of the pressure p in the region $r \le a$ (see Fig. 1) and to the absence of shear stress at the whole surface. At the boundaries between the layers $z_1 = 0$ and $z_2 = H_2$, we adopt the conditions of total linking

$$s_{zz,i}(k,z_i) = s_{zz,i+1}(k,z_i),$$
$$s_{rz,i}(k,z_i) = s_{rz,i+1}(k,z_i),$$
$$W_{z,i}(k,z_i) = W_{z,i+1}(k,z_i),$$
$$W_{r,i}(k,z_i) = W_{r,i+1}(k,z_i),$$

or the conditions of continuity of the normal components of stress and displacements in the case of free slipping of the layers in the tangential direction

$$s_{zz,i}(k,z_i) = s_{zz,i+1}(k,z_i),$$
$$s_{rz,i}(k,z_i) = s_{rz,i+1}(k,z_i) = 0,$$
$$W_{z,i}(k,z_i) = W_{z,i+1}(k,z_i).$$

For the third infinite layer, we adopt the condition of the finiteness of solutions, which is reduced to the conditions

$$A_{13}(k) = B_{13}(k) = 0.$$

Below, we give a set of boundary conditions that corresponds to the model of tissues with linked layers:

$$
\begin{aligned}
&-2\mu_1 k^2 \kappa_{t1} A_{11} e^{-\kappa_{t1} H_1} + 2\mu_1 k^2 \kappa_{t1} A_{21} e^{\kappa_{t1} H_1} \\
&+ \mu_1 (k^2 + \kappa_{t1}^2) B_{11} e^{-\kappa_{l1} H_1} + \mu_1 (k^2 + \kappa_{t1}^2) B_{21} e^{\kappa_{l1} H_1} \\
&= -\frac{pa}{k} J_1(ka), \\
&\mu_1 k (k^2 + \kappa_{t1}^2) A_{11} e^{-\kappa_{t1} H_1} + \mu_1 k (k^2 + \kappa_{t1}^2) A_{21} e^{\kappa_{t1} H_1} \\
&- 2\mu_1 k \kappa_{l1} B_{11} e^{-\kappa_{l1} H_1} + 2\mu_1 k \kappa_{l1} B_{21} e^{\kappa_{l1} H_1} = 0, \\
&-2\mu_1 k^2 \kappa_{t1} A_{11} + 2\mu_1 k^2 \kappa_{t1} A_{21} + \mu_1 (k^2 + \kappa_{t1}^2) B_{11} \\
&+ \mu_1 (k^2 + \kappa_{t1}^2) B_{21} + 2\mu_2 k^2 \kappa_{t2} A_{12} - 2\mu_2 k^2 \kappa_{t2} A_{22} \\
&- \mu_2 (k^2 + \kappa_{t2}^2) B_{12} - \mu_2 (k^2 + \kappa_{t2}^2) B_{22} = 0, \\
&\mu_1 k (k^2 + \kappa_{t1}^2) A_{11} + \mu_1 k (k^2 + \kappa_{t1}^2) A_{21} - 2\mu_1 k \kappa_{l1} B_{11} \\
&+ 2\mu_1 k \kappa_{l1} B_{21} - \mu_2 k (k^2 + \kappa_{t2}^2) A_{12} - \mu_2 k (k^2 + \kappa_{t2}^2) A_{22} \\
&+ 2\mu_2 k \kappa_{l2} B_{12} - 2\mu_2 k \kappa_{12} B_{22} = 0, \\
&-k^2 A_{11} - k^2 A_{21} + \kappa_{l1} B_{11} - \kappa_{l1} B_{21} + k^2 A_{12} \\
&+ k^2 A_{22} - \kappa_{l2} B_{12} + \kappa_{l2} B_{22} = 0, \qquad (3) \\
&k\kappa_{t1} A_{11} - k\kappa_{t1} A_{21} - kB_{11} - kB_{21} - k\kappa_{t2} A_{12} \\
&+ k\kappa_{t2} A_{22} + kB_{12} + kB_{22} = 0, \\
&-2\mu_2 k^2 \kappa_{t2} e^{\kappa_{t2} H_2} A_{12} + 2\mu_2 k^2 \kappa_{t2} e^{-\kappa_{t2} H_2} A_{22} \\
&+ \mu_2 (k^2 + \kappa_{t2}^2) e^{\kappa_{l2} H_2} B_{12} + \mu_2 (k^2 + \kappa_{t2}^2) e^{-\kappa_{l2} H_2} B_{22} \\
&- 2\mu_3 k^2 \kappa_{t3} e^{-\kappa_{t3} H_2} A_{23} - \mu_3 (k^2 + \kappa_{t3}^2) e^{-\kappa_{l3} H_2} B_{23} = 0, \\
&\mu_2 k (k^2 + \kappa_{t2}^2) e^{\kappa_{t2} H_2} A_{12} + \mu_2 k (k^2 + \kappa_{t2}^2) e^{-\kappa_{t2} H_2} A_{22} \\
&- 2\mu_2 k \kappa_{l2} e^{\kappa_{l2} H_2} B_{12} + 2\mu_2 k \kappa_{l2} e^{-\kappa_{l2} H_2} B_{22} \\
&- \mu_3 k (k^2 + \kappa_{t3}^2) e^{-\kappa_{t3} H_2} A_{23} - 2\mu_3 k \kappa_{l3} e^{-\kappa_{l3} H_2} B_{23} = 0, \\
&-k^2 e^{\kappa_{t2} H_2} A_{12} - k^2 e^{-\kappa_{t2} H_2} A_{22} + \kappa_{l2} e^{\kappa_{l2} H_2} B_{12} \\
&- \kappa_{l2} e^{-\kappa_{l2} H_2} B_{22} + k^2 e^{-\kappa_{t3} H_2} A_{23} + \kappa_{l3} e^{-\kappa_{l3} H_2} B_{23} = 0, \\
&k\kappa_{t2} e^{\kappa_{t2} H_2} A_{12} - k\kappa_{t2} e^{-\kappa_{t2} H_2} A_{22} - ke^{\kappa_{l2} H_2} B_{12} \\
&- ke^{-\kappa_{l2} H_2} B_{22} - k\kappa_{t3} e^{-\kappa_{t3} H_2} A_{23} + ke^{-\kappa_{l3} H_2} B_{23} = 0.
\end{aligned}
$$

Only the fourth, sixth, eighth, and tenth equations are changed in the set of equations corresponding to the model of tissues with slipping layers in comparison with Eqs. (3). The sixth and tenth equations (for the displacement components U_r at the boundaries $z = 0$ and $z = H_2$) vanish, and the fourth and eighth ones (for the components of shear stress at the boundaries $z = 0$ and $z = H_2$) split into two equations each:

$$
\begin{aligned}
&\mu_1 k (k^2 + \kappa_{t1}^2) A_{11} + \mu_1 k (k^2 + \kappa_{t1}^2) A_{21} \\
&- 2\mu_1 k \kappa_{l1} B_{11} + 2\mu_1 k \kappa_{l1} B_{21} = 0, \\
&-\mu_2 k (k^2 + \kappa_{t2}^2) A_{12} - \mu_2 k (k^2 + \kappa_{t2}^2) A_{22} \\
&+ 2\mu_2 k \kappa_{l2} B_{12} - 2\mu_2 k \kappa_{l2} B_{22} = 0, \qquad (4) \\
&\mu_2 k (k^2 + \kappa_{t2}^2) e^{\kappa_{t2} H_2} A_{12} + \mu_2 k (k^2 + \kappa_{t2}^2) e^{-\kappa_{t2} H_2} A_{22} \\
&- 2\mu_2 k \kappa_{l2} e^{\kappa_{l2} H_2} B_{12} + 2\mu_2 k \kappa_{l2} e^{-\kappa_{l2} H_2} B_{22} = 0, \\
&-\mu_3 k (k^2 + \kappa_{t3}^2) e^{-\kappa_{t3} H_2} A_{23} - 2\mu_3 k \kappa_{l3} e^{-\kappa_{l3} H_2} B_{23} = 0.
\end{aligned}
$$

We take into account the viscoelastic properties of tissues in the models by the assumption that the shear moduli are complex $\mu_i = \mu_{i0} + j\omega\eta_i$, where μ_{i0} is the static shear modulus and η_i is the shear viscosity. We do not take into account the viscoelastic properties of tissues in the case of bulk deformation, which is assumed quite often in considering wave processes in soft biological tissues at frequencies lower than 20 kHz [6].

To make the models adequate to the skin-fat layer–muscle–liver system, we take the following numerical values of parameters: $H_1 = 5$ mm, $H_2 = 10$ mm, $\mu_{10} = 1$ kPa, $\mu_{20} = 4$ kPa, $\mu_{30} = 1.7$ kPa, $\eta_1 = 6$ Pa s, $\eta_2 = 3$ Pa s, $\eta_3 = 2$ Pa s, $c_{l1} = 1450$ m/s, $c_{l2} = 1570$ m/s, $c_{l3} = 1574$ m/s, $\rho_1 = 930$ kg/m^3, $\rho_2 = 1040$ kg/m^3, and $\rho_3 = 1080$ kg/m^3. The values of the tissue densities and sound velocities are taken from a handbook [23], and the values of the moduli of shear elasticity and shear viscosity of tissues are estimated using the results of our experiments [13, 24]. The size of the source and the frequency of its vibrations are set within the range of the values easily realized in practice: $a = 25$ mm and $f = 20$ Hz. We take the amplitude of vibrations $p = 1$ kPa, which approximately corresponds to 1% isothermal changes of the volume of a closed air chamber with the initial pressure 1 atm and which also can be easily realized.

We compute the displacements in tissues directly by Eqs. (1) and (2), where the unknown functions A_{1i}, A_{2i}, B_{1i}, and B_{2i} are determined from the sets of equations (3) and (4), by using the MathCAD software package. The upper limits of integration in Eqs. (1) (which are different at different points of the medium) are selected on the basis of the preliminary study of the behavior of the integrands. Selecting the points of the medium for the calculations, we provide them to be at a certain distance from the layer boundaries, because, at the boundaries and near them, the integrands in Eqs. (1) become undamped and their integrals diverge.

Further, we consider the laws governing the penetration of low-frequency vibrations into layered biological tissues within the framework of the PSV-models intro-

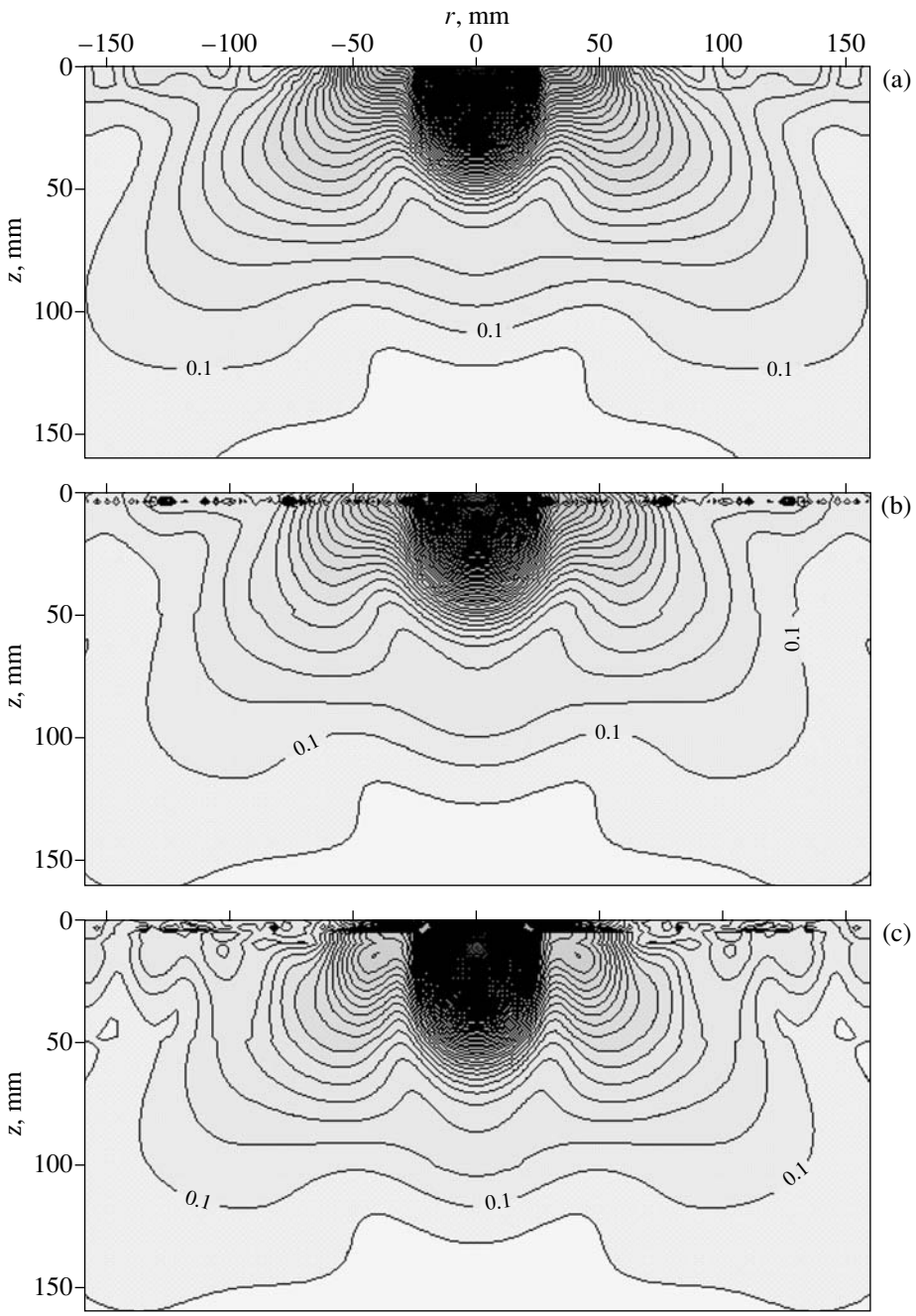

Fig. 2. Displacement distribution $U_z(r, z)$ under a vibration source in (a) a homogeneous halfspace, (b) a three-layer halfspace with linked layers, and (c) a three-layer halfspace with slipping layers. The step between the level curves is 0.05 mm.

duced above. First of all, let us clear up the possibilities of the generation of rather large displacements within tissues by a surface source and also estimate the distortions in the structure of the displacement field for the models with linked and slipping layers by using the parameters given above in comparison with a homogeneous halfspace with the properties of the third layer. The calculations are conducted in the region $r \le 160$ mm and $z \le 160$ mm at a step of 2 mm in both r and z. The calculated displacements $U_z(r, z)$ and $U_r(r, z)$ are given in Figs. 2 and 3. One can see that, if we preset the oscillatory pressure with the amplitude 1 kPa at the tissue surface, the amplitude of oscillatory displacements remains at a level higher than 0.1 mm to the depths greater than 100 mm. The best visualization conditions in the sonoelastography method can be expected when the amplitudes of oscillatory displacements are comparable with the ultrasonic wavelength. Since the wavelengths of the order of 0.3–0.6 mm are used in modern Doppler gauges, the amplitude of oscillatory displace-

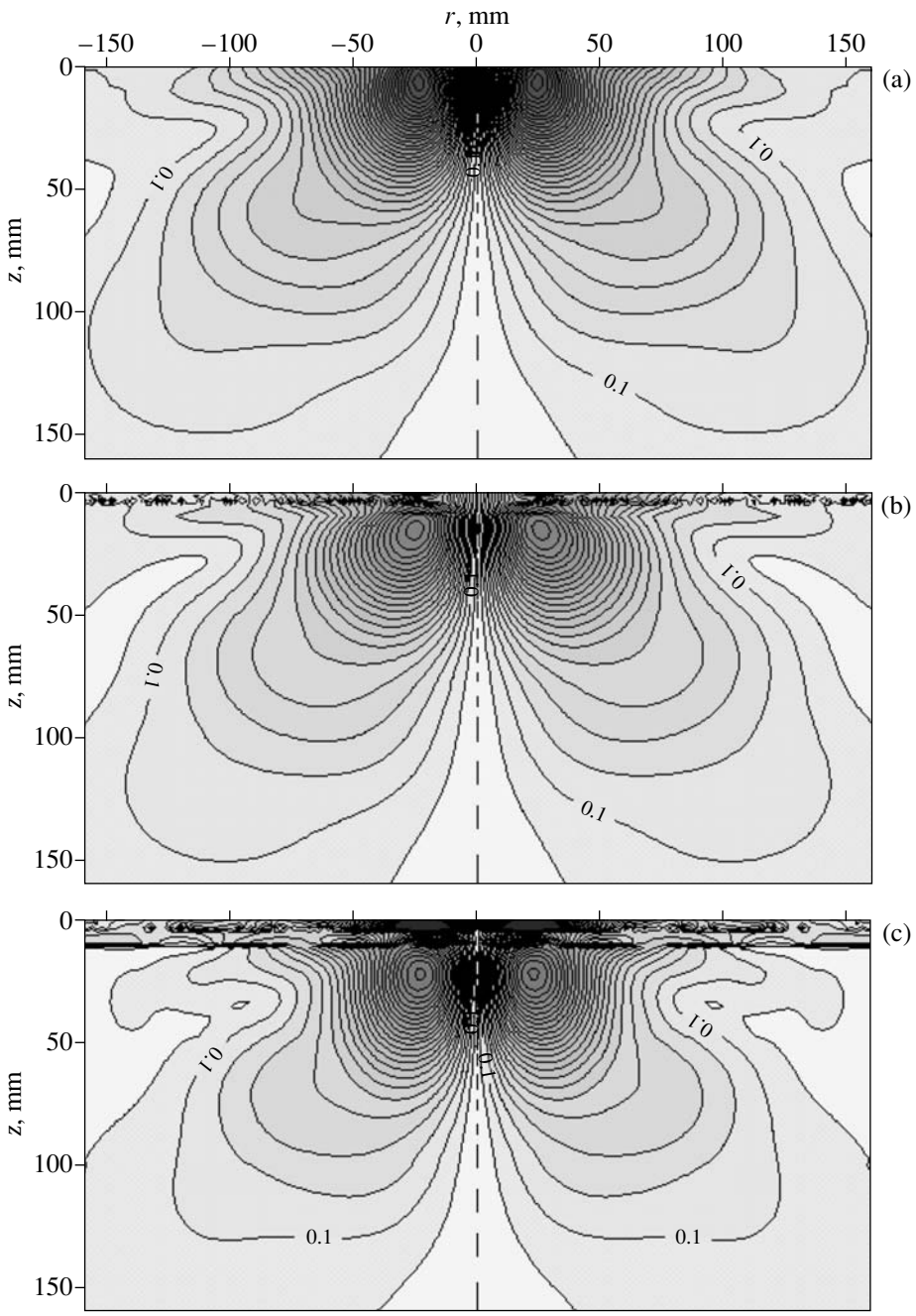

Fig. 3. Displacement distribution $U_r(r, z)$ under a vibration source. Notations are the same as in Fig. 2.

ments remains sufficient for utilization in the sonoelastography method to the depths greater than 150 mm. As for the distortions of the displacement field by surface layers, they are limited by the depth of 2–3 cm, as one can see from Figs. 2 and 3. The field in the halfspace at a large depth does not change significantly in the case of the appearance of surface layers with the adopted properties.

By the way, we can make some observations that are of interest for the sonoelastography method from the results of calculations. First, it seems remarkable that, in the first layer, near its boundary with the second layer, the model predicts the formation of the field inhomogeneities, which are very sharp in character in the case of layer linking and more smooth in the case of layer slipping. In the visualization, these inhomogeneities may be interpreted erroneously as medium inhomogeneities, although they arise close to the boundary that is homogeneous along the coordinate *r*. It is also of interest that the boundary of the second layer with the halfspace turned out to be indistinguishable in the dis-

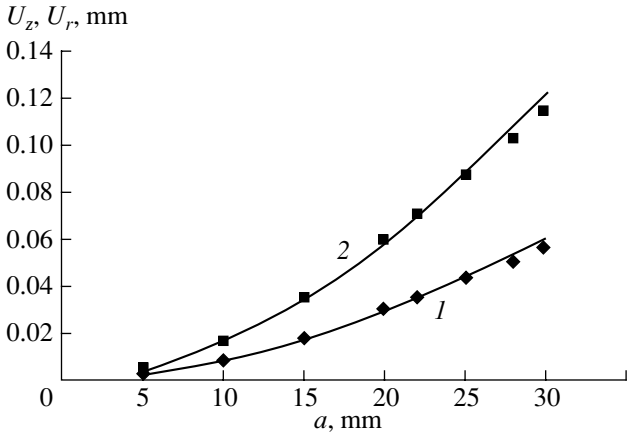

Fig. 4. Dependences of the displacement components (*1*) U_z and (*2*) U_r on the source radius a at the point r = 100 mm, z = 160 mm. Calculation for the model with linked layers.

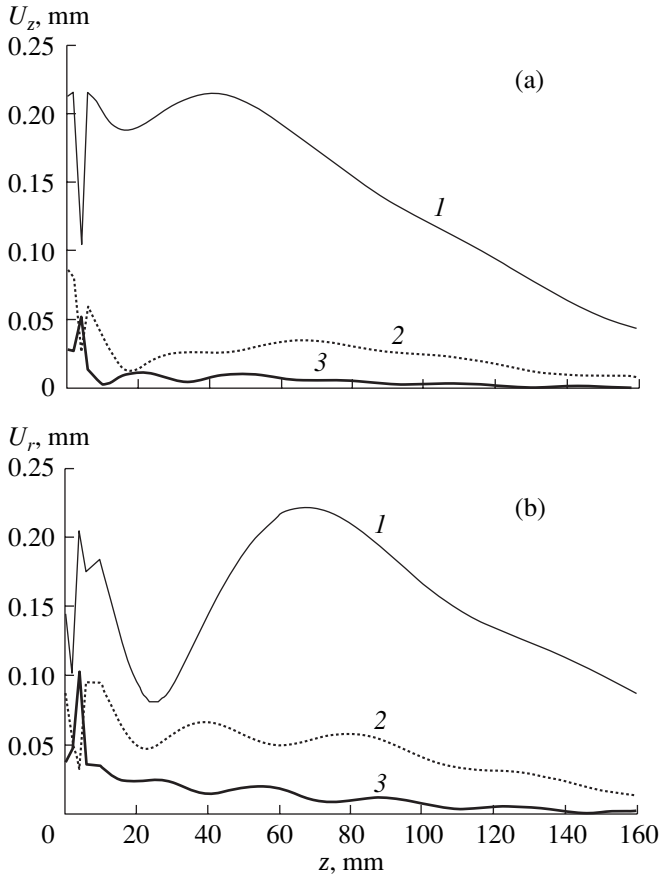

Fig. 5. Dependences of displacement components (a) U_z and (b) U_r on the depth z at the distance from the axis r = 100 mm for different frequencies of pressure oscillations: (*1*) 20, (*2*) 30, and (*3*) 40 Hz. Calculation for the model with linked layers.

placement component $U_z(r, z)$ in both cases of layer linking and slipping, whereas it is clearly visible in the displacement component $U_r(r, z)$ in the case of the layer slipping (the inhomogeneous structure of the field in r near the boundary is also formed in this). This effect may mean that it is necessary to vary the direction of ultrasonic observation to visualize some tissue inhomogeneities by the sonoelastography method.

Now, let us refine the dependences of the displacement values within tissues on the parameters of the surface source of vibrations. Figure 4 presents the calculated dependences of the displacement amplitudes U_z and U_r at the point r = 100 mm, z = 160 mm on the source radius a. One can see that these dependences are quite strong within the considered range of source dimensions: $U_r \sim a^{1.85}$ and $U_z \sim a^{1.81}$. Figure 5 presents the calculated dependences $U_z(z)$ and $U_r(z)$ at the distance 100 mm from the axis at various frequencies of vibrations. On can see that the frequency dependence of the depth of vibration penetration in tissues is very strong. A more detailed analysis of this dependence within the frequency range 20–60 Hz at the point r = 100 mm, z = 100 mm gives the following results: $U_r \sim f^{-4.79}$ and $U_z \sim f^{-5.79}$.

From the results of the last calculations, it is possible to notice the interesting effect of the rise of nonmonotonic dependences of displacements on depth as the frequency increases. This effect, as well as the formation of field inhomogeneities along a homogeneous boundary, can lead to erroneous interpretation of the results of visualization of the displacement amplitudes.

Thus, in the framework of the PSV-models, it is possible to calculate easily and sufficiently quickly the fields of displacements in layered biological tissues when setting oscillatory pressures at their surfaces. The described calculations demonstrate that it is quite possible to obtain within tissues the displacement values that are sufficient for utilization in sonoelastography by using a surface source, and to increase the efficiency of such an excitation, it is necessary to use the maximal dimensions of the source and the minimal frequencies.

REFERENCES

1. L. Gao, K. J. Parker, R. M. Lerner, and S. F. Levinson, Ultrasound Med. Biol. **22** (8), 959 (1996).
2. A. P. Sarvazyan, O. V. Rudenko, S. D. Swanson, *et al.*, Ultrasound Med. Biol. **24** (9), 1419 (1998).
3. O. V. Rudenko and A. P. Sarvazyan, Biomed. Radioelektron., No. 3, 6 (2000).
4. L. Gao, K. J. Parker, S. K. Alam, and R. M. Lerner, J. Acoust. Soc. Am. **97**, 3875 (1995).
5. V. V. Kuznetsov, V. S. Sinyakov, M. I. Kozhevnikova, *et al.*, Med. Biomekh. (Riga), **1**, 229 (1986).
6. T. J. Royston, H. A. Mansy, and R. H. Sandler, J. Acoust. Soc. Am. **106**, 3678 (1999).
7. E. V. Glushkov, N. V., Glushkova, and E. M. Timanin, Akust. Zh. **39**, 1043 (1993) [Acoust. Phys. **39**, 551 (1993)].
8. A. R. Skovoroda and S. R. Aglyamov, Mat. Model. **9** (8), 119 (1997).
9. A. R. Skovoroda and S. R. Aglyamov, Biofizika **43** (2), 348 (1998).

10. B. N. Klochkov and A. V. Sokolov, Akust. Zh. **40**, 270 (1994) [Acoust. Phys. **40**, 244 (1994)].
11. B. N. Klochkov and A. V. Sokolov, Akust. Zh. **41**, 512 (1995) [Acoust. Phys. **41**, 451 (1995)].
12. B. N. Klochkov and A. V. Sokolov, Preprint No. 445, IPF RAN (Inst. of Applied Physics, Russian Academy of Sciences, Nizhni Novgorod, 1997).
13. E. M. Timanin, Preprint No. 488, IPF RAN (Inst. of Applied Physics, Russian Academy of Sciences, Nizhni Novgorod, 1999).
14. E. M. Timanin and E. V. Eremin, Russ. J. Biomech. **3** (4), 78 (1999).
15. E. V. Eremin and E. M. Timanin, Akust. Zh. **46**, 490 (2000) [Acoust. Phys. **46**, 421 (2000)].
16. W. Nowacki, *Teoria Sprezystosci* (PWN, Warszawa, 1970; Mir, Moscow, 1975).
17. L. D. Landau and E. M. Lifshits, *Course of Theoretical Physics*, Vol. 7: *Theory of Elasticity* (Nauka, Moscow, 1987; Pergamon, New York, 1986).
18. K. Aki and P. G. Richards, *Quantitative Seismology: Theory and Methods* (Freeman, San Francisco, 1980; Mir, Moscow, 1983), Vols. 1, 2.
19. É. V. Sokolov, Preprint No. 225, NIRFI (Radiophysical Research Inst., Gorki State Univ., 1987).
20. E. V. Glushkov and N. V. Glushkova, Prikl. Mat. Mekh. **54** (3), 474 (1990).
21. E. V. Glushkov, N. V. Glushkova, and E. V. Kirillova, Prikl. Mat. Mekh. **56** (5), 780 (1992).
22. V. V. Kazakov and B. N. Klochkov, Biofizika **34** (4), 688 (1989).
23. V. A. Berezovskiĭ and N. N. Kolotilov, *Biophysical Characteristics of Human Tissue: A Handbook* (Naukova Dumka, Kiev, 1990).
24. E. M. Timanin, in *Proceedings of XI All-Union Acoustical Conference, Moscow, 1991*, Section O, p. 48.

Translated by M. Lyamshev

Acoustical Physics, Vol. 48, No. 1, 2002, pp. 94–97. Translated from Akusticheskiĭ Zhurnal, Vol. 48, No. 1, 2002, pp. 105–109.

Helmholtz Integral in the Acoustics of an Inhomogeneous Medium

E. L. Shenderov[†]

Morfizpribor Central Research Institute, Chkalovskiĭ pr. 46, St. Petersburg, 197376 Russia

e-mail: shend@peterlink.ru

Received April 20, 2001

Abstract—Integral relations that generalize the Helmholtz integral for an inhomogeneous medium with arbitrary gradients of its density and the sound velocity in it are obtained. Expressions that determine the Helmholtz integral for problems related to the diffraction and radiation of sound in an inhomogeneous medium are derived. It is shown that, in the case of an inhomogeneous medium, an additional factor depending on the density distribution in the medium appears in the integrand. © *2001 MAIK "Nauka/Interperiodica".*

The Helmholtz integral is one of the basic means of the sound field calculations in theoretical and computational acoustics. It forms the basis of an important direction of research concerned with the application of integral equations in solving the radiation and diffraction problems for sound waves—the boundary element method (BEM). This method is much studied in the literature: hundreds and maybe even thousands of publications are devoted to it. A great number of modifications of this method have been developed, most of them being concerned with overcoming the problems related to the appearance of uncertainties in the case of bodies with wave dimensions corresponding to the eigenvalues of the integral equation. Some other methods well known in acoustics (e.g., the T-matrix method or the method of auxiliary sources) are also based on the use of the Helmholtz integral. The description of the new methods involving the application of the Helmholtz integral is given in the book [1]. Comprehensive reviews on these issues and examples of the applications of the Helmholtz integral can be found in the literature [2–9]. The Kirchhoff approximation, which is based on the simplification of the Helmholtz integral for bodies with large wave dimensions (see, e.g., [10]), is also widely used in acoustics.

In most publications dealing with the Helmholtz integral, the integrand contains the Green function for free space, i.e., $\exp(ik|\mathbf{r}_1 - \mathbf{r}_2|)/(4\pi|\mathbf{r}_1 - \mathbf{r}_2|)$ or $iH_0^{(1)}(ik|\mathbf{r}_1 - \mathbf{r}_2|)/4$ for the 3D and 2D cases, respectively. Here and below, the time dependence is represented in the form $\exp(-i\omega t)$. However, in some cases (see, e.g., [11, 12]), it is advantageous to take this function not as a field of a source in free space, but as a field of a source in the presence of some surface, which makes it possible to immediately satisfy the boundary conditions at this surface. The derivation of such an integral relation for a diffraction problem is described in the previous paper [11] (in the Appendix). For the corresponding integral relation with an arbitrary Green function in the integrand, which virtually generalizes the Helmholtz integral, we will also use the term Helmholtz integral for brevity.

In all publications available to us, the Helmholtz integral is applied to either a homogeneous medium or an inhomogeneous medium, in which the field is described by an approximate Helmholtz differential equation

$$\Delta p(\mathbf{r}) + k^2(\mathbf{r})p(\mathbf{r}) = -\delta(\mathbf{r}_0 - \mathbf{r})[-i\omega\rho(\mathbf{r}_0)Q], \quad (1)$$

where Q is the strength of a point source located at a point $\mathbf{r}_0$, $\rho(\mathbf{r}_0)$ is the density of the medium at the source site, and δ is the delta-function. It is assumed that, in such a medium, the inhomogeneity is caused by the varying sound velocity, and the variations of the density of the medium affect the sound field only as a result of the sound velocity variations that follow the changes in the medium density. For this kind of a medium, the Helmholtz integral does not differ from the conventional Helmholtz integral for a homogeneous medium. This approach can be applied to a medium with a weak inhomogeneity, but its applicability in the case of a strongly inhomogeneous medium is questionable. Despite the large number of publications devoted to the use of the Helmholtz integral in acoustics, we could not find any derivation of the corresponding relations for an arbitrary inhomogeneous medium, i.e., when the sound pressure cannot be described by Eq. (1).

In an arbitrary inhomogeneous medium, the sound field in the absence of sources is described by a homogeneous differential equation presented in the monograph [13] and involving an additional term depending on the variation of the medium density. Below, this

[†] Deceased.

equation is written with another additional term on the right-hand side to allow for the presence of a point source at the point $\mathbf{r}_0$:

$$\Delta_r p(\mathbf{r}_0, \mathbf{r}) + k^2(\mathbf{r}) p(\mathbf{r}_0, \mathbf{r}) - \frac{1}{\rho(\mathbf{r})}\mathrm{grad}_r\rho(\mathbf{r})\mathrm{grad}_r p(\mathbf{r}_0, \mathbf{r}) = -\delta(\mathbf{r}_0 - \mathbf{r})[-i\omega\rho(\mathbf{r}_0)Q]. \quad (2)$$

Here and below, for the quantities depending on two arguments, we assume that the first argument indicates the point where the source is located and the second argument corresponds to the point of observation. The subscript r near the differential operators means that the differentiation is performed with respect to the coordinates of the point $\mathbf{r}$.

In the cited monograph [13], it was noted that neglect of the third term on the left-hand side of Eq. (2) can lead to large errors, and a substitution of an auxiliary function for the sound pressure is proposed to eliminate this term. The auxiliary function has the form

$$\psi(\mathbf{r}_0, \mathbf{r}) = \frac{p(\mathbf{r}_0, \mathbf{r})}{\sqrt{\rho(\mathbf{r})}}. \quad (3)$$

Using this approach and performing some transformations, we represent Eq. (2) in the form

$$\Delta_r\psi(\mathbf{r}_0, \mathbf{r}) + K^2(\mathbf{r})\psi(\mathbf{r}_0, \mathbf{r}) = -\delta(\mathbf{r}_0 - \mathbf{r})\left[-i\omega\frac{\rho(\mathbf{r}_0)}{\sqrt{\rho(\mathbf{r})}}Q\right], \quad (4)$$

where

$$K^2(\mathbf{r}) = k^2(\mathbf{r}) + \frac{\Delta\rho(\mathbf{r})}{2\rho(\mathbf{r})} - \frac{3}{4}\left(\frac{\mathrm{grad}_r\rho(\mathbf{r})}{\rho(\mathbf{r})}\right)^2. \quad (5)$$

Below, we reproduce the known derivation of the Helmholtz integral in application to Eq. (4) for the function ψ and then return to the sound pressure.

Let us first consider the diffraction problem. Suppose it is necessary to determine the sound pressure that occurs at a point $\mathbf{r}_1$ as a result of the sound radiation by a point source located at a point $\mathbf{r}_0$ in the presence of a surface S (Fig. 1a). We place an auxiliary point source of strength Q at the observation point $\mathbf{r}_1$. The field generated by this source $p_G(\mathbf{r}_1, \mathbf{r})$ satisfies an equation that has the form of Eq. (2) with $\mathbf{r}_0$ replaced by $\mathbf{r}_1$:

$$\Delta_r p_G(\mathbf{r}_1, \mathbf{r}) + k^2(\mathbf{r}) p_G(\mathbf{r}_1, \mathbf{r}) - \frac{1}{\rho(\mathbf{r})}\mathrm{grad}_r\rho(\mathbf{r})\mathrm{grad}_r p_G(\mathbf{r}_1, \mathbf{r}) = -\delta(\mathbf{r}_1 - \mathbf{r})[-i\omega\rho(\mathbf{r}_1)Q]. \quad (6)$$

Applying the substitution

$$\psi_G(\mathbf{r}_1, \mathbf{r}) = \frac{p_G(\mathbf{r}_1, \mathbf{r})}{\sqrt{\rho(\mathbf{r})}}, \quad (7)$$

we represent Eq. (6) in the form

$$\Delta_r\psi_G(\mathbf{r}_1, \mathbf{r}) + K^2(\mathbf{r})\psi_G(\mathbf{r}_1, \mathbf{r}) = -\delta(\mathbf{r}_1 - \mathbf{r})\left[-i\omega\frac{\rho(\mathbf{r}_1)}{\sqrt{\rho(\mathbf{r})}}Q\right]. \quad (8)$$

We multiply Eq. (4) by $\psi_G(\mathbf{r}_1, \mathbf{r})$ and Eq. (8) by $\psi(\mathbf{r}_0, \mathbf{r})$. Then, we subtract the second of the resulting equations from the first one and integrate the relation obtained in this way over the volume V enclosed between the surface S and a large-radius sphere S_∞, the integration being performed with respect to the coordinates of the point $\mathbf{r}$. As a result, we obtain the equation

$$\iiint_V [\Delta_r\psi(\mathbf{r}_0, \mathbf{r})\psi_G(\mathbf{r}_1, \mathbf{r}) - \psi(\mathbf{r}_0, \mathbf{r})\Delta_r\psi_G(\mathbf{r}_1, \mathbf{r})]dV_r = -\iiint_V \frac{-i\omega\rho(\mathbf{r}_0)Q}{\sqrt{\rho(\mathbf{r})}}\delta(\mathbf{r}_0 - \mathbf{r})\psi_G(\mathbf{r}_1, \mathbf{r})dV_r + \iiint_V \frac{-i\omega\rho(\mathbf{r}_1)Q}{\sqrt{\rho(\mathbf{r})}}\delta(\mathbf{r}_1 - \mathbf{r})\psi_G(\mathbf{r}_0, \mathbf{r})dV_r. \quad (9)$$

The volume integral that appears on the left-hand side can be transformed by the second Green formula to integrals over the surfaces S and S_∞ bounding the volume V. According to the radiation principle, the integral over the surface S_∞ tends to zero with increasing radius of the sphere, and, hence, only the integral over the surface S remains. The integrals that appear on the right-hand side are calculated using the properties of the delta-function. As a result, we obtain

$$\psi(\mathbf{r}_0, \mathbf{r}_1) = \sqrt{\frac{\rho(\mathbf{r}_0)}{\rho(\mathbf{r}_1)}}\psi_G(\mathbf{r}_1, \mathbf{r}_0) + \frac{1}{-i\omega\sqrt{\rho(\mathbf{r}_1)}Q} \times \iint_S \left[\psi(\mathbf{r}_0, \mathbf{r})\frac{\partial\psi_G(\mathbf{r}_1, \mathbf{r})}{\partial n_r} - \psi_G(\mathbf{r}_1, \mathbf{r})\frac{\partial\psi(\mathbf{r}_0, \mathbf{r})}{\partial n_r}\right]dS_r. \quad (10)$$

Returning to sound pressures with the use of Eqs. (3) and (7), we obtain

$$p(\mathbf{r}_0, \mathbf{r}_1) = p_G(\mathbf{r}_1, \mathbf{r}_0) + \frac{1}{-i\omega Q} \times \iint_S \frac{1}{\rho(\mathbf{r})}\left[p(\mathbf{r}_0, \mathbf{r})\frac{\partial p_G(\mathbf{r}_1, \mathbf{r})}{\partial n_r} - p_G(\mathbf{r}_0, \mathbf{r})\frac{\partial p(\mathbf{r}_0, \mathbf{r})}{\partial n_r}\right]dS_r. \quad (11)$$

This expression is an analog of the conventional Helmholtz integral and differs from it by the presence of the factor $1/\rho(\mathbf{r})$ in the integrand. The auxiliary function p_G is an analog of the Green function, which is indicated by the subscript G. The difference between the function p_G and the conventional Green function lies in the normalization determined by the factors appearing on the right-hand side of Eq. (6). However, if we set the coefficient multiplying the delta-function on the right-hand side of Eq. (8) to be equal to unity, the

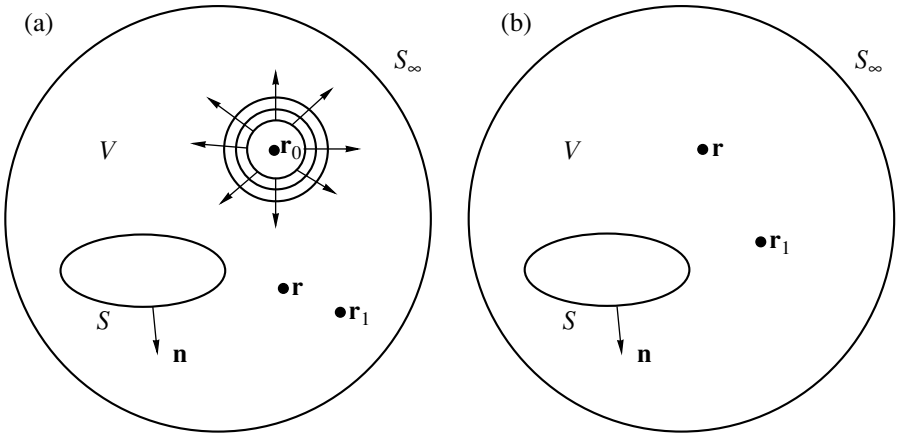

Fig. 1. Positions of the surface and the radiation and reception points; $\mathbf{r}_1$ is the point of observation and $\mathbf{r}$ is the auxiliary point with respect to which the integration is performed. (a) The problem on the diffraction of sound; a point source is located at the point $\mathbf{r}_0$. (b) The problem on the sound radiation by a surface S.

corresponding Green function will not satisfy the reciprocity principle in the inhomogeneous medium, and the introduction of additional factors depending on the ratio between the densities at the radiation and reception points will be necessary.

According to Eq. (8), the sound pressure amplitude p_G is proportional to the density of the medium at the point $\mathbf{r}_1$. Hence, the integrand in Eq. (11) is virtually proportional to the ratio between the densities of the medium at the points $\mathbf{r}_1$ and $\mathbf{r}$. If we apply the corresponding normalization to the right-hand side of Eq. (8), we can eliminate the factor $1/\rho(\mathbf{r})$ from the integrand, but, in this case, the function p_G will no longer describe the sound pressure. Therefore, the use of the auxiliary function p_G describing the sound pressure produced by the auxiliary source, which has the same strength as the real source and is located at the observation point $\mathbf{r}_1$, leads to a more illustrative and physically justified field representation than the use of an equation of the type of Eq. (8) with a dimensionless right-hand side or with the introduction of the aforementioned normalization.

We note that the introduction of an auxiliary point source located at the observation point was used earlier in [14] in the derivation of the reciprocity theorem for elastic bodies. This derivation also used the representation in the form of a field of a real source of a given strength.

Equation (11) is valid for an arbitrary distribution of density in the medium and, in particular, for a piecewise continuous distribution. Therefore, it can also be used for a body lying at the boundary between two homogeneous media with different parameters.

The boundary conditions at the surface S are taken into account by the corresponding ratios of the sound pressure $p(\mathbf{r}_0, \mathbf{r})$ and its normal derivative $\partial p(\mathbf{r}_0, \mathbf{r})/\partial n_r$ at this surface. In this case, the function p_G must not satisfy any preset boundary conditions. For example, this function can be chosen to have the form of the solution for a free space in an inhomogeneous medium. In addition, for the problems related to the determination of the fields resulting from the sound diffraction by a body located near an elastic or impedance boundary, it is convenient to choose the function p_G in the form of the field of a source in the presence of such a boundary. This allows one to immediately satisfy the boundary conditions at this boundary and to integrate only over the surface S of the body. A similar approach was used for a homogeneous medium in [11, 12].

Assuming that the observation point $\mathbf{r}_1$ tends to the body surface and taking into account the impedance or elastic properties of the surface by setting the aforementioned ratio of the sound pressure $p(\mathbf{r}_0, \mathbf{r})$ and its normal derivative $\partial p(\mathbf{r}_0, \mathbf{r})/\partial n_r$, we obtain an integral equation for the sound pressure $p(\mathbf{r}_0, \mathbf{r})$.

In a similar way, one can obtain the solution to the problem on the sound radiation by a surface S in an inhomogeneous medium. In this case, it is necessary to determine the field of the sound radiation by the surface at a given distribution of the sound pressure over the surface or a given distribution of its normal derivative proportional to the particle velocity of the surface (Fig. 1b). The sound pressure in the medium satisfies an equation that has the form of Eq. (2) with the right-hand side equal to zero and without the dependence on $\mathbf{r}_0$:

$$\Delta_r p(\mathbf{r}) + k^2(\mathbf{r}) p(\mathbf{r}) - \frac{1}{\rho(\mathbf{r})} \mathrm{grad}_r \rho(\mathbf{r}) \mathrm{grad}_r p(\mathbf{r}) = 0. \tag{12}$$

Applying the substitution

$$\psi(\mathbf{r}) = \frac{p(\mathbf{r})}{\sqrt{\rho(\mathbf{r})}}, \tag{13}$$

this equation is recast to the form

$$\Delta_r \psi(\mathbf{r}) + K^2(\mathbf{r}) \psi(\mathbf{r}) = 0, \tag{14}$$

where $K^2(\mathbf{r})$ is determined by Eq. (5). The following transformations do not differ from those performed above for the diffraction problem. We place an auxiliary source at the observation point $\mathbf{r}_1$, the field of this source being described by Eqs. (6)–(8). We multiply Eq. (14) by $\psi_G(\mathbf{r}_1, \mathbf{r})$ and Eq. (8) by $\psi(\mathbf{r}_0, \mathbf{r})$. Then, we subtract the second of the resulting equations from the first one and perform the integration with respect to the coordinates of the point $\mathbf{r}$ over the volume V enclosed between the surface S and a large-radius sphere S_∞. Returning from the functions ψ to the sound pressures and performing some transformations, we finally obtain

$$p(\mathbf{r}_1) = \frac{1}{-i\omega Q} \times \iint_S \frac{1}{\rho(\mathbf{r})}\left[p(\mathbf{r})\frac{\partial p_G(\mathbf{r}_1, \mathbf{r})}{\partial n_r} - p_G(\mathbf{r}_1, \mathbf{r})\frac{\partial p(\mathbf{r})}{\partial n_r}\right] dS_r. \quad (15)$$

This expression can be considered as the Helmholtz integral for an inhomogeneous medium, as applied to the problem of sound radiation by a surface.

ACKNOWLEDGMENTS

This work was supported by the Russian Foundation for Basic Research, project no. 00-02-17840.

REFERENCES

1. E. L. Shenderov, *Sound Radiation and Scattering* (Sudostroenie, Leningrad, 1989).
2. M. Tanaka, Appl. Mech. Rev. **36**, 627 (1983).
3. C. C. Chien, H. Rajiayk, and S. N. Atluri, J. Acoust. Soc. Am. **88**, 918 (1990).
4. W. S. Hwang, J. Acoust. Soc. Am. **101**, 3330 (1997).
5. W. S. Hwang, J. Acoust. Soc. Am. **101**, 3336 (1997).
6. W. S. Hwang, J. Acoust. Soc. Am. **102**, 96 (1997).
7. S. A. Yang, J. Acoust. Soc. Am. **105**, 93 (1999).
8. E. Dokumachi, J. Sound Vibr. **139**, 83 (1990).
9. D. T. I. Francis, J. Acoust. Soc. Am. **93**, 1700 (1993).
10. E. L. Shenderov, *Wave Problems in Hydroacoustics* (Sudostroenie, Leningrad, 1972).
11. E. L. Shenderov, Akust. Zh. **46**, 816 (2000) [Acoust. Phys. **46**, 716 (2000)].
12. E. L. Shenderov, Akust. Zh. **47** (2001) (in press).
13. L. M. Brekhovskikh, *Waves in Layered Media* (Nauka, Moscow, 1957; Academic, New York, 1960).
14. L. M. Lyamshev, Dokl. Akad. Nauk SSSR **125**, 1231 (1959) [Sov. Phys. Dokl. **4**, 406 (1959)].

Translated by E. Golyamina

Acoustical Physics, Vol. 48, No. 1, 2002, pp. 98–106. Translated from Akusticheskiĭ Zhurnal, Vol. 48, No. 1, 2002, pp. 110–119.

Noise Immunity of a Combined Hydroacoustic Receiver

V. A. Shchurov and A. V. Shchurov

Pacific Institute of Oceanology, Far East Division, Russian Academy of Sciences, ul. Baltiĭskaya 43, Vladivostok, 690041 Russia

e-mail: shchurov@poi.dvo.ru

Received December 29, 1999

Abstract—A statistical analysis of the noise immunity of a combined receiver is performed for the observation of a fluctuating tone signal against the background of underwater dynamic noise. The analysis is based on the experimental data obtained in deep ocean with the use of two four-component combined hydroacoustic receivers positioned at depths of 150 and 300 m. Theoretical expressions are obtained for the signal-to-noise ratio of a combined receiver, for reciprocal spectral levels of the signal and noise in both narrow and wide frequency bands. The definition of the combined receiver gain is introduced in terms of the functions of a common single-point coherence for the acoustic pressure and the particle velocity in an acoustic wave. According to the experimental data obtained, in the case of multiplicative processing, the maximal gain in the signal-to-noise ratio of a combined receiver, as compared to a hydrophone-based square-law detector, can reach 15–16 dB for the horizontal channel and 30 dB for the vertical channel of the combined receiver in the case of the compensation of opposing flows of the signal and noise energy. © *2002 MAIK "Nauka/Interperiodica".*

INTRODUCTION

The basis of a device measuring the acoustic intensity is a combined receiver. It includes a pressure detector (a scalar receiver) and a three-component pickup for the particle velocity or acceleration (a vector receiver). The development of more advanced combined receivers and combined arrays still remains topical [5–8].

The problem of the noise immunity of a single combined receiver is much studied. However, in the majority of theoretical studies, the noise immunity of a combined receiver was treated on the basis of the directional features of the dipole characteristics of individual channels of a vector receiver in the case of additive or multiplicative processing of acoustic data [1, 4]. A considerable number of studies are based on the methods of mathematical simulation (see, e.g., [15, 16]). The problem of evaluating the noise immunity of a combined receiver on the basis of an experiment conducted in an actual noise field is now especially important. This paper discusses multiplicative processing for a four-component combined receiver. In the theoretical part of this study, an expression for the signal-to-noise ratio is obtained and the combined receiver gain is introduced for both narrow and broad frequency bands in the case of multiplicative processing. On the basis of the experimental data, the noise immunity of a combined receiver was analyzed for a narrow frequency band in the presence of the dynamic noise of a deep ocean. The experimental studies discussed in this paper were conducted at the depths 150 and 300 m lying above the axis of an underwater sound channel, which occurred at a depth of 1200 m. The spectral intensity characteristics of underwater ambient noise differ significantly for these depths, which was confirmed by multiple measurements [9]. This paper presents the analysis of the noise immunity of a combined receiver in noise fields with various degrees of isotropy (diffuseness), depending on the averaging time. The noise immunity of a combined receiver in an anisotropic (coherent) noise field is considered for the case of compensation. Thus, the paper is devoted to the interpretation of specific experimental results on the basis of a simple mathematical model in the spectral domain, as is usually done in the case of hydrophone arrays (see, e.g., [10]). Such an approach has never before been used for the case of the measurement of the intensity vector. We assume that both signal and noise are statistically independent Gaussian processes with zero mean values.

DIRECTIVITY PATTERN OF A COMBINED RECEIVER

Transducers used in vector receivers are positioned at the x, y, and z orthogonal axes of the Cartesian coordinate system and have the following spatial directivity patterns in a spherical coordinate system:

$$R_x = \sin\theta\cos\varphi, \quad R_y = \sin\theta\sin\varphi, \quad R_z = \cos\theta, \tag{1}$$

where φ is the azimuth angle counted off from the x axis and θ is the polar angle counted off from the z axis.

The directivity pattern of a three-component vector receiver is a sphere

$$R_x^2 + R_y^2 + R_z^2 = 1. \tag{2}$$

Thus, a four-component combined receiver including a pressure detector and a three-component vector

receiver has a spherical directivity pattern, i.e., its response does not depend on the angles φ and θ [9]. A combined receiver can be treated as a point receiving system as long as its geometrical dimensions do not exceed a half-wavelength at the upper frequency of the operation frequency range. The spatial directivity patterns, Eqs. (1), of a vector receiver are identical within the whole operation frequency range, which can extend from several hundreds of hertz to 10 kHz [2, 6].

COMBINED RECEIVER GAIN IN THE FREQUENCY SPECTRUM

We set the signal-to-noise ratio $SNR(PV)$ of a single combined receiver in the case of multiplicative processing according to [5, 10, 11]. We assume that both signal and noise are statistically independent stationary Gaussian processes with zero mean values. Then, we have

$$SNR(PV) = \sqrt{\frac{B_0T_0}{2}}\sqrt{\frac{2W_{P,S}W_{V,S}}{W_{P,N}W_{V,N}(1+R_{P,V}^2-J_{P,V}^2)}}. \quad (3)$$

Here, $B_0 = \Delta f_0$ is the band of frequency analysis, which satisfies the condition $\Delta f_0 \ll f_0$, where f_0 is the frequency of a tone signal; T_0 is the averaging time; $W_{P,S}$, $W_{V,S}$, $W_{P,N}$, and $W_{V,N}$ are the powers of signals and noise at the inputs of the acoustic pressure p and particle velocity v channels; and $R_{P,V}$ and $J_{P,V}$ are the real and imaginary parts of the normalized cross-correlation function of noise at the output of the combined receiver.

If $P_N(t)$ and $V_N(t)$ are centered processes in the p and v channels, then

$$W_{P,N} = \langle|P_N(t)|^2\rangle; \quad W_{V,N} = \langle|V_N(t)|^2\rangle;$$
$$R_{P,V} = \mathrm{Re}\langle P_N(t)V_N^*(t)\rangle/\sqrt{W_{P,N}W_{V,N}}, \quad (4)$$
$$J_{P,V} = \mathrm{Im}\langle P_N(t)V_N^*(t)\rangle/\sqrt{W_{P,N}W_{V,N}},$$

where $\langle\ldots\rangle$ is the sign of averaging and * is the notation for a complex-conjugate quantity.

In Eq. (3), we divide the signal and noise powers by the analysis band. We obtain $W_{P,S}/\Delta f_0$, $W_{V,S}/\Delta f_0$, $W_{P,N}/\Delta f_0$, and $W_{V,N}/\Delta f_0$. Proceeding from [12], we determine the following spectral densities at $\Delta f_0 \longrightarrow 0$ and $T_0 \longrightarrow \infty$: $W_{P,S}/\Delta f_0 \longrightarrow S_{P^2,S}$; $W_{V,S}/\Delta f_0 \longrightarrow S_{V^2,S}$; $W_{P,N}/\Delta f_0 \longrightarrow S_{P^2,N}$; and $W_{V,N}/\Delta f_0 \longrightarrow S_{V^2,N}$. In this case, $R_{P,V} \longrightarrow \cos\varphi_N$ and $J_{P,V} \longrightarrow \sin\varphi_N$, where φ_N is the mean value of the phase difference between the acoustic pressure $P(t)$ and the particle velocity $V(t)$ in the noise at the frequency f_0. Using the above relations and the theorem on spectra, we reduce Eq. (3) to the form

$$SNR(PV) = \sqrt{\frac{B_0T_0}{2}}\frac{S_{P,S}(f_0)S_{V,S}(f_0)\cos\varphi_S}{S_{P,N}(f_0)S_{V,N}(f_0)\cos\varphi_N}. \quad (5)$$

Since we assumed the signal to be a random function, we have introduced $\cos\varphi_S$ in Eq. (5) (φ_S is the mean value of the phase difference between $P_S(t)$ and $V_S(t)$ for a signal at the frequency f_0). The expressions $S_{P,S}(f_0)S_{V,S}(f_0)\cos\varphi_S = S_{PV,S}(f_0)$ and $S_{P,N}(f_0)S_{V,N}(f_0)\cos\varphi_N = S_{PV,N}(f_0)$ are in essence the real parts of the cross spectra of signal and noise at the frequency f_0, which are normalized to the frequency band $B_0 = 1$ Hz.

Let us write Eq. (5) in a logarithmic form:

$$SNR(PV) = 10\log\sqrt{\frac{B_0T_0}{2}}\frac{S_{PV,S}(f_0)}{S_{PV,N}(f_0)}. \quad (6)$$

Proceeding from Eq. (3), we obtain the signal-to-noise ratio for a single hydrophone (a square-law detector),

$$SNR(P^2) = 10\log\sqrt{\frac{B_0T_0}{2}}\frac{S_{P^2,S}(f_0)}{S_{P^2,N}(f_0)}, \quad (7)$$

where $S_{P^2,S}(f_0)$ and $S_{P^2,N}(f_0)$ are the spectral densities of the potential energy of signal and noise, which are normalized to the frequency band $B_0 = 1$ Hz at the frequency f_0.

The noise immunity of a combined receiver relative to a square-law detector is

$$SNR(PV/P^2) = \frac{SNR(PV)}{SNR(P^2)}. \quad (8)$$

Equations (6) and (8) are convenient to study the noise immunity of a combined receiver in the spectral domain in a narrow frequency band.

Let us replace the cross-spectral densities $S_{PV,S}(f_0)$ and $S_{PV,N}(f_0)$ by the coherent powers of the signal and noise [12]: $S_{PV,S}(f_0) = \gamma_{PV,S}^2(f_0)S_{P^2,S}(f_0)$ and $S_{PV,N}(f_0) = \gamma_{PV,N}^2(f_0)S_{P^2,N}(f_0)$, where $\gamma_{PV,S}^2(f_0)$, and $\gamma_{PV,N}^2(f_0)$ are the functions of a common single-point coherence of signal and noise and $S_{P^2,S}(f_0)$ and $S_{P^2,N}(f_0)$ are the spectral power densities of signal and noise. In this case,

$$SNR(PV) = 10\log\sqrt{\frac{B_0T_0}{2}}\frac{\gamma_{PV,S}^2(f_0)S_{P^2,S}(f_0)}{\gamma_{PV,N}^2(f_0)S_{P^2,N}(f_0)}$$
$$= 10\log\frac{S_{P^2,S}(f_0)}{S_{P^2,N}(f_0)} + 10\log\sqrt{\frac{B_0T_0}{2}}\frac{\gamma_{PV,S}^2(f_0)}{\gamma_{PV,N}^2(f_0)}. \quad (9)$$

The expression $10\log\frac{S_{P^2,S}(f_0)}{S_{P^2,N}(f_0)}$ in Eq. (9) is $SNR(P^2)$ at the output of the hydrophone of a combined receiver, and the expression

$$k = 10\log\sqrt{\frac{B_0T_0}{2}}\frac{\gamma^2_{PV,S}(f_0)}{\gamma^2_{PV,N}(f_0)} \quad (10)$$

is equivalent (according to [10]) to the expression for an antenna array gain $10\log N$ (where N is the number of elements in the array), and we call this expression (by analogy with [10]) the combined receiver gain. Therefore, the combined receiver gain depends on the ratio of the signal and noise coherence functions for the pressure and particle velocity of an acoustic field and is determined by the frequency band B_0 and the averaging time T_0.

Let us estimate the limiting theoretical value of the above combined receiver gain. In the case of a totally coherent signal ($\gamma^2_{PV,S}(f_0) \longrightarrow 0$) and totally isotropic (diffusion) noise ($\gamma^2_{PV,N}(f_0) \longrightarrow 1$), it tends to infinity. A real acoustic field of ambient noise is a superposition of anisotropic (coherent) and isotropic (diffusion) fields, and, therefore, the coherence function of real ambient noise $\gamma^2_{PV,N}(f)$ differs from zero and depends on frequency. It can reach the minimal values 0.01–0.001 [9] in a real dynamic noise of a deep ocean (the 200–1000 Hz frequency range). Thus, the gain of a single combined receiver depends on the coherent properties of the signal and the noise, and in the case of a totally coherent signal and a diffusive noise, it can reach the values 20–30 dB.

The expression obtained for the combined receiver gain is simple and convenient for statistical analysis of experimental data in a narrow frequency band.

In the case of a broadband signal, Eqs. (6), (7), and (10) must be written in the form

$$SNR(PV) = 10\log\sqrt{\frac{B_0T_0}{2}}\left\{\int_{f_1}^{f_2} S_{PV,S}(f)df \Big/ \int_{f_1}^{f_2} S_{PV,N}(f)df\right\},$$

$$SNR(P^2) = 10\log\sqrt{\frac{B_0T_0}{2}}\left\{\int_{f_1}^{f_2} S_{P^2,S}(f)df \Big/ \int_{f_1}^{f_2} S_{P^2,N}(f)df\right\}, \quad (11)$$

$$k = 10\log\sqrt{\frac{B_0T_0}{2}}\left\{\int_{f_1}^{f_2} \gamma^2_{PV,S}(f)df \Big/ \int_{f_1}^{f_2} \gamma^2_{PV,N}(f)df\right\},$$

where f_2-f_1 is the width of the frequency band occupied by a broadband signal.

FORMATION OF THE *SNR* OF A COMBINED RECEIVER IN A REAL FIELD OF OCEANIC ACOUSTIC NOISE IN A NARROW FREQUENCY BAND

A fluctuating tone signal with the frequency f_0 = 622 Hz was observed. The length of the time series was 1800 s.

The experimental conditions were as follows: the sea depth was 4000 m; the axis of the underwater sound channel was at a depth of 1200 m; the underwater wind velocity was 6–7 m/s; fully developed wind waves and ripple were present; combined receivers were positioned at the depths 150 and 300 m. The x and y axes of the combined receivers were in the horizontal plane, and the z axis was directed from the surface towards the bottom. A tone emitter was positioned at a depth of 100 m and at the distance 4–6 km from the receiving system. The level of the varying signal in the autospectrum during the observation time exceeded the spectral noise level by the values from 0 to 6 dB (for the combined receiver positioned at the depth 150 m).

The x and y axes are oriented in the oceanic waveguide in such way that the horizontal component of the energy flux $I_{+x,N}$ of the anisotropic field of dynamic noise is directed along the $+x$ axis; the component of the signal energy flux $I_{-x,S}$ is directed along the $-x$ axis; the signal energy flux $I_{-y,S}$ from a local source is directed along the $-y$ axis; and the field of dynamic noise at the frequency f_0 = 622 Hz is isotropic (diffuse) along the y axis.

The component of the energy flux of the dynamic surface noise $I_{+z,N}$ is directed along the $+z$ axis, and the counter component of the signal energy flux $I_{-z,S}$ is directed along the $-z$ axis. The research vessel was drifting during the experiment. At certain moments, the drifting vessel was located exactly at the y axis of the combined receiver, and in this case the signal from the emitter was absent in the channel x of the combined receiver. A compensation of the energy fluxes $I_{-z,S}$ and $I_{+z,N}$ was observed in the vertical plane [13–16].

The Combined Receiver Gain in the Presence of Dynamic Noise with a Prevailing Isotropic Component

Investigations of the *SNR* of a combined receiver at two time series with the duration t = 1800 s corresponding to two measurement depths (150 and 300 m) at the central frequency f_0 = 622 Hz were conducted. The signal-to-noise ratios were calculated using the corresponding spectral densities according to Eqs. (6) and (7) for the following quantities: (i) the spectral density of the potential energy, $SNR(P^2)$; (ii) the Y-component

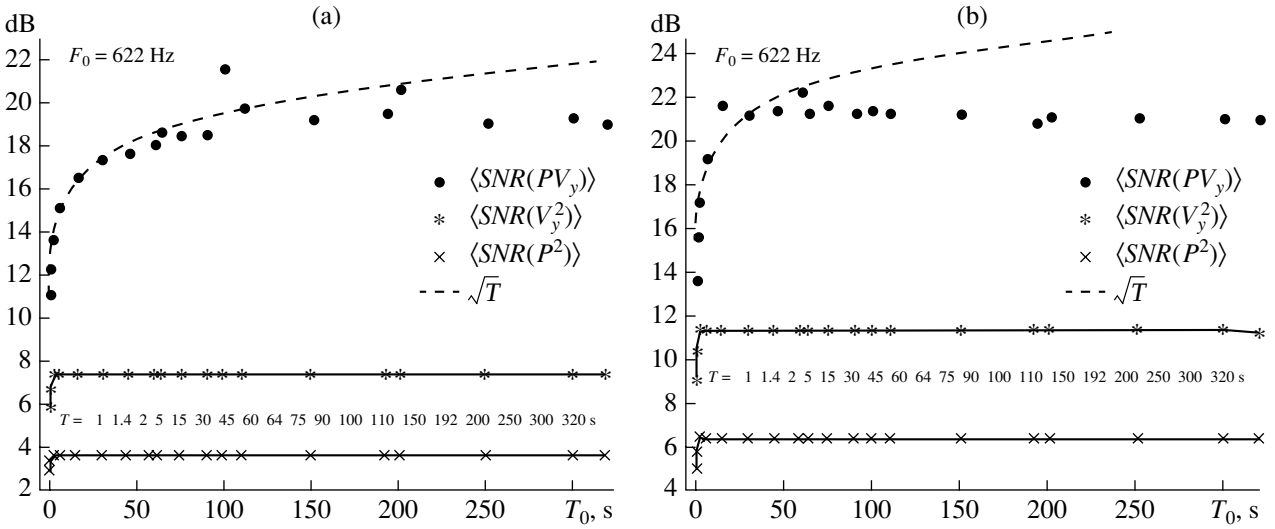

Fig. 1. Dependences of $\langle SNR(P^2)\rangle$, $\langle SNR(V_y^2)\rangle$, and $\langle SNR(PV_y)\rangle$ on the averaging time T_0. The measuring depths are (a) 150 and (b) 300 m. The dashed curve corresponds to the approximation $(a + b\sqrt{T})$, B_0 = 1 Hz.

of the spectral density of kinetic energy, $SNR(V_y^2)$; and (iii) the *Y*-component of the spectral density of the energy flux, $SNR(PV_y)$.

Equation (7) was used for the square-law detector of the scalar pressure detector, $SNR(P^2)$.

For the *Y*-component of the square-law detector of the particle velocity receiver, we have

$$SNR(V_y^2) = 10\log\sqrt{\frac{B_0T_0}{2}}\frac{S_{V_y^2,S}(f_0)}{S_{V_y^2,N}(f_0)}, \qquad (12)$$

where $S_{V_y^2,S}(f_0)$ and $S_{V_y^2,N}(f_0)$ are the *Y*-components of the spectral densities of the kinetic energies of the signal and the noise, which are normalized to the frequency band 1 Hz at the frequency f_0.

For the *Y*-component of the energy flux density, we have

$$SNR(PV_y) = 10\log\sqrt{\frac{B_0T_0}{2}}\frac{S_{PV_y,S}(f_0)}{S_{PV_y,N}(f_0)}, \qquad (13)$$

where $S_{PV_y,S}(f_0)$ and $S_{PV_y,N}(f_0)$ are the *Y*-components of the spectral densities of the energy fluxes of signal and noise, which are normalized to the frequency band 1 Hz at the frequency f_0.

Since $E_k = E_{k,x} + E_{k,y} + E_{k,z}$, the quantity $SNR(V^2)$ can be calculated for both the total kinetic energy and its components corresponding to the *x*, *y*, and *z* axes. In our case, only $SNR(V_y^2)$ is calculated. For the vector of the energy flux density $\mathbf{I} = \mathbf{i}(PV_x) + \mathbf{j}(PV_y) + \mathbf{k}(PV_z)$, we calculate $SNR(PV_y)$ and $SNR(PV_z)$. The following times of the spectrum averaging were used: T_0 = 1, 1.4, 2, 5, 15, 30, 45, 60, 64, 75, 90, 100, 110, 150, 192, 200, 250, 300, and 320 s. We selected exponential averaging. The analysis frequency band was 1 Hz. We also calculated the average values for $\langle SNR(P^2)\rangle$, $\langle SNR(V_y^2)\rangle$, and $\langle SNR(PV_y)\rangle$ for each T_0.

The dependences of the quantities $\langle SNR(P^2)\rangle$, $\langle SNR(V_y^2)\rangle$, and $\langle SNR(PV_y)\rangle$ averaged over the total length of the time series 1800 s long starting from the averaging time T_0 are given in Fig. 1. Figure 1a corresponds to the depth 150 m, and Fig. 1b, to the depth 300 m. As follows from Fig. 1, $\langle SNR(P^2)\rangle$ and $\langle SNR(V_y^2)\rangle$ attain the maximal values at the averaging time $T_k \approx 5$ s and no longer depend on the averaging time.

Reliable values are $\langle SNR(P^2)\rangle$ = 2.5 dB and $\langle SNR(V_y^2)\rangle$ = 7.3 dB (the level difference constitutes 3.8 dB) at the depth 150 m, and $\langle SNR(P^2)\rangle$ = 6.6 dB and $\langle SNR(V_y^2)\rangle$ = 11.2 dB (the level difference 4.6 dB) at the depth 300 m.

The difference in levels between $\langle SNR(P^2)\rangle$ and $\langle SNR(V_y^2)\rangle$ is explained by the dipole directivity pattern of the channels of the particle velocity pickup with a directivity factor equal to three. Therefore, the gain in an ideal isotropic noise field for $SNR(V_y^2)$ as compared to $SNR(P^2)$ must be 4.8 dB. The deviation from this value is the evidence of the presence of an anisotropic component in the field of ambient noise. The deviation value for the depth 150 m is 1 dB and for the

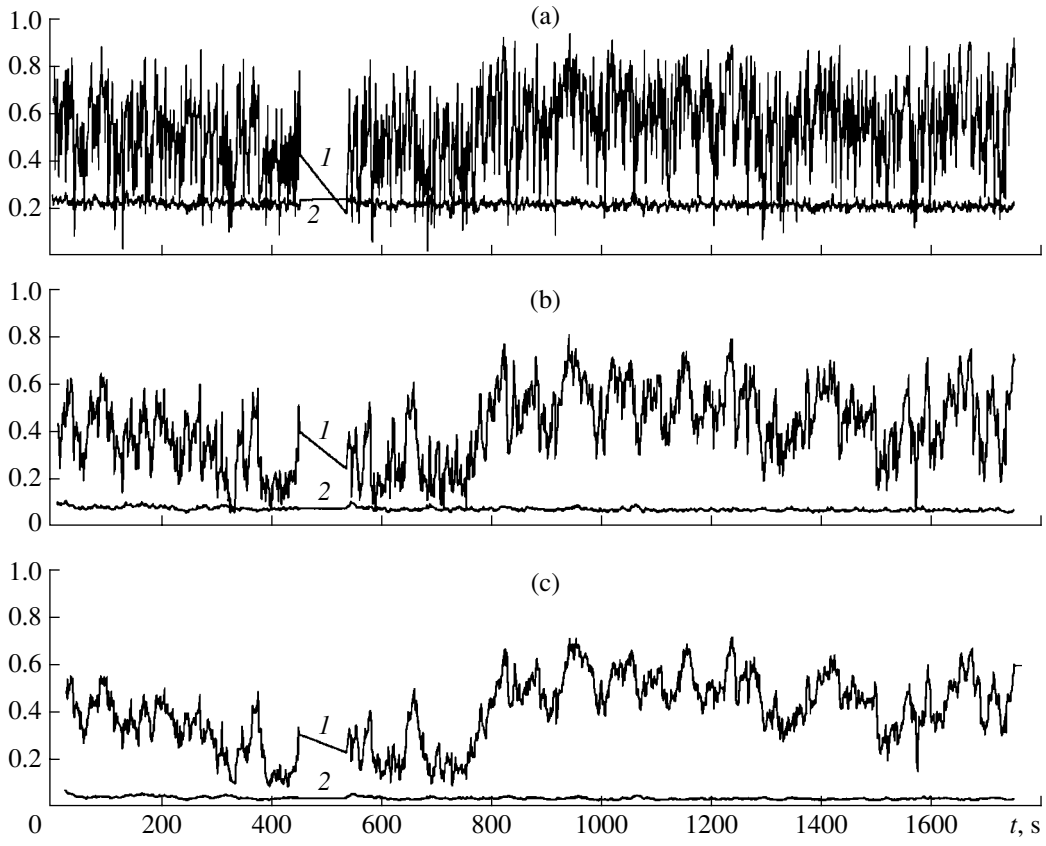

Fig. 2. Coherence functions of (*1*) signal $\gamma^2_{PV_y,S}(f_0)$ and (*2*) noise $\gamma^2_{PV_y,N}(f_0)$ at the frequency f_0 = 622 Hz. The times of spectrum averaging are (a) 5, (b) 15, and (c) 30 s. The frequency band of analysis is 1 Hz. In the interval 450–510 s, the combined receiver is switched off (the pause of the radio channel of a telemetering system).

depth 300 m, 0.2 dB. This means that the noise field at the depth 300 m is more isotropic in the horizontal plane than at the depth 150 m. Namely, at the depth 150 m, 21% of the noise energy density is connected with the anisotropic field and 79%, with the isotropic field. At the depth 300 m, the values are 5 and 95%, respectively. The dependence of $\langle SNR(PV_y)\rangle$ on T_0 is observed also up to a certain $T_0 = T_k$, and then it almost does not depend on the averaging time. An approximating function $(a + b\sqrt{T})$ is obtained for $\langle SNR(PV_y)\rangle$ (Fig. 1). The function has the following parameters: (i) for the depth 150 m, a = 12.8 and b = 7.7 $s^{-1/2}$ (the averaging times, according to which the approximating function is designed, are T_0 = 1.4, 2, 5, 15, 30, 45, 60, 64, 75, 90, 100, 110, and 150 s); (ii) for the depth 300 m, a = 37.5 and b = 17.5 $s^{-1/2}$ (the averaging times are T_0 = 1.4, 2, 5, 15, 30, 45, and 60 s, respectively).

The experimental points for $\langle SNR(PV_y)\rangle$ coincide with the approximating curve $(a + b\sqrt{T})$ up to the averaging times $T_0 = T_k \approx 120$ s for the depth 150 m and $T_0 = T_k \approx 60$ s for the depth 300 m. As it has been mentioned above, the averaging time $T_k \approx 5$ s is necessary to attain the maximal values of $\langle SNR(P^2)\rangle$ and $\langle SNR(V_y^2)\rangle$, but, as we can see, the time for $\langle SNR(PV_y)\rangle$ is $T_k \approx 60$–120 s. Thus, to obtain the maxim values of $\langle SNR(PV_y)\rangle$, an averaging time that is 12–24 times longer is necessary, as compared to that for the maximal value of $\langle SNR(P^2)\rangle$ or $\langle SNR(V_y^2)\rangle$. In this case, the gain in the noise immunity of the combined receiver, as compared to a square-law detector [according to Eq. (8)], is $SNR(PV_y/P^2) = \langle SNR(PV_y)\rangle - \langle SNR(P^2)\rangle \approx$ 15–16 dB (Fig. 1). As follows from Fig. 1, at $T_0 \le T_k$, the experimental results coincide with the approximating curve $a + b\sqrt{T}$.

In the case $T_0 \le T_k$, we can write $\sqrt{\frac{T_0}{2}} S_{PV_y,S}(f_0)/S_{PV_y,N}(f_0) = (a + b\sqrt{T})$. We assume the spectral density of the signal energy flux to be constant at the given frequency f_0, i.e., $S_{PV_y,S}(f_0)$ = const and $S_{PV_y,N}(f_0) = \sigma_N$ (where σ_N is the mean-square deviation of the noise energy flux density in the band 1 Hz at the frequency f_0). Hence, $\sigma_N \sim \text{const}/\sqrt{T}$. Thus, the mean-

square deviation of the energy flux of an isotropic field of dynamic noise decreases as $1/\sqrt{T}$ (B_0 = 1 Hz).

Coherent Properties of the Signal and Noise Energy Fluxes

Let us consider the dependence of the coherent properties of signal and noise on the averaging time T_0 for the measurement depth 150 m. We take the same time series with the duration t = 1800 s as in the previous subsection. The averaging times of the spectra are T_0 = 3, 5, 15, 30, 45, 60, 75, 90, 100, 150, 192, 200, 250, 300, and 320 s. Averaging is exponential. We study the properties of the gain of the combined receiver $k = 10\log\sqrt{\frac{B_0T_0}{2}}\frac{\gamma^2_{PV,S}(f_0)}{\gamma^2_{PV,N}(f_0)}$.

Figure 2 shows the signal and noise coherence functions $\gamma^2_{PV,S}(f_0)$ and $\gamma^2_{PV,N}(f_0)$ at the frequency f_0 = 622 Hz for three averaging times of spectra T_0 = 5, 15, and 30 s, for the whole time series t = 1800 s. It follows from Fig. 2 that the signal coherence function at the frequency f_0 = 622 Hz fluctuates in time, whereas the noise coherence function is constant (for a specific averaging time) and decreases in the case of an increase in the averaging time.

The dependences of the noise coherence function $\gamma^2_{PV_y,N}(f_0)$ and its mean-square deviation $\sigma_N(f_0)$ on the averaging time T_0 and also the signal coherence function $\gamma^2_{PV_y,N}(f_0)$ and its mean-square deviation $\sigma_S(f_0)$ are given in Fig. 3. The noise coherence function $\gamma^2_{PV_y,N}(f_0)$ and $\sigma_N(f_0)$ (Fig. 3a) and the signal coherence function $\gamma^2_{PV_y,S}(f_0)$ and $\sigma_S(f_0)$ were calculated at two time intervals of the same time series t_1 = 700–800 s (Fig. 3b) and t_2 = 1200–1500 s (Fig. 3c). The coherence of noise decreases as the averaging time grows (Fig. 3a). In the case of averaging with T_0 = 3 s, $\gamma^2_{PV_y,N}(f_0) \pm \sigma_N(f_0)$ = 0.415 ± 0.021, and in the case of averaging with T_0 = 320 s, $\gamma^2_{PV_y,N}(f_0) \pm \sigma_N(f_0) = 0.008 \pm 0.003$, so that the level of coherence drops by 17 dB in this case. Simultaneously, the mean-square deviation $\sigma_N(f_0)$ decreases approximately by 8.5 dB (from 0.021 to 0.003). Thus, we have the prevailing diffusive component of noise along the y axis. As the averaging time increases, the signal coherence (Figs. 3b and 3c) decreases at first, but then it remains constant for the averaging times up to 320 s. In the case of a weak signal (Fig. 3b), the signal coherence decreases until the averaging time reaches the value of 30 s, and its mean-square deviation $\sigma_S(f_0)$ decreases as the averaging time grows. In the case of a more powerful signal (Fig. 3c), the coherence decreases

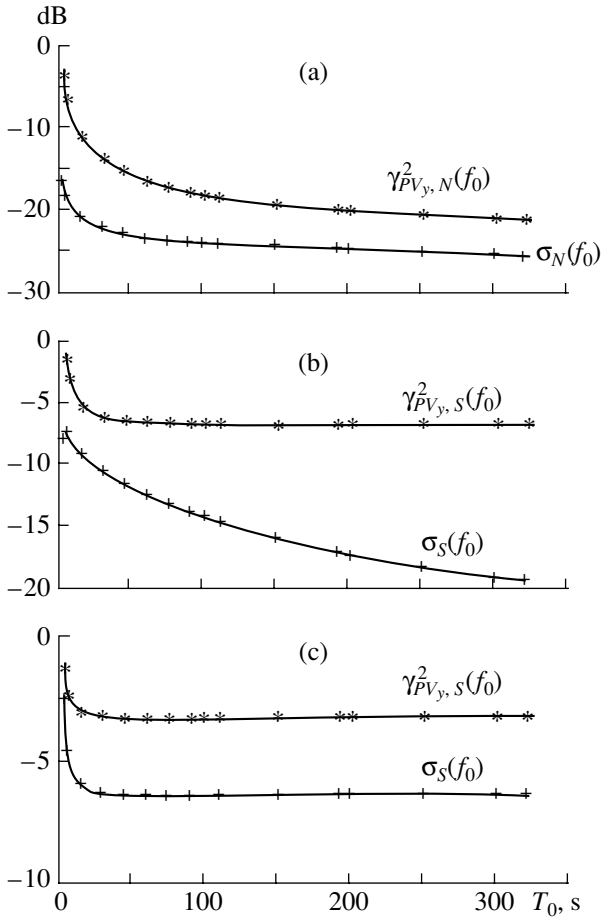

Fig. 3. Dependences of $\gamma^2_{PV_y,N}(f_0)$, $\sigma_N(f_0)$, $\gamma^2_{PV_y,S}(f_0)$, and $\sigma_S(f_0)$ on the averaging time T_0. The level 0 dB corresponds to the maximal value of the coherence function equal to unity.

until the averaging time becomes 15 s and then remains constant. The mean-square deviation in this case decreases until the averaging time becomes equal to 15 s and then remains constant. The conclusion from Fig. 3 is that, at the averaging times greater than 30 s, the signal coherence is a constant value but the noise coherence decreases along with its mean-square deviation.

Since the combined receiver gain is $10\log\sqrt{\frac{B_0T_0}{2}}\frac{\gamma^2_{PV,S}(f_0)}{\gamma^2_{PV,N}(f_0)}$, its value must increase depending on the increase in the averaging time. Figure 4 presents the curves for the combined receiver gain as a function of time t for the time series t = 1800 s at different averaging times T_0. The gain varies with time (at T_0 = const), since the signal at f_0 = 622 Hz fluctuates; however, as T_0 grows, its value increases. Figure 5 shows the dependence of the combined receiver gain on T_0 obtained by averaging over two time intervals: (i) 700–800 s and (ii) 1200–1500 s. In these

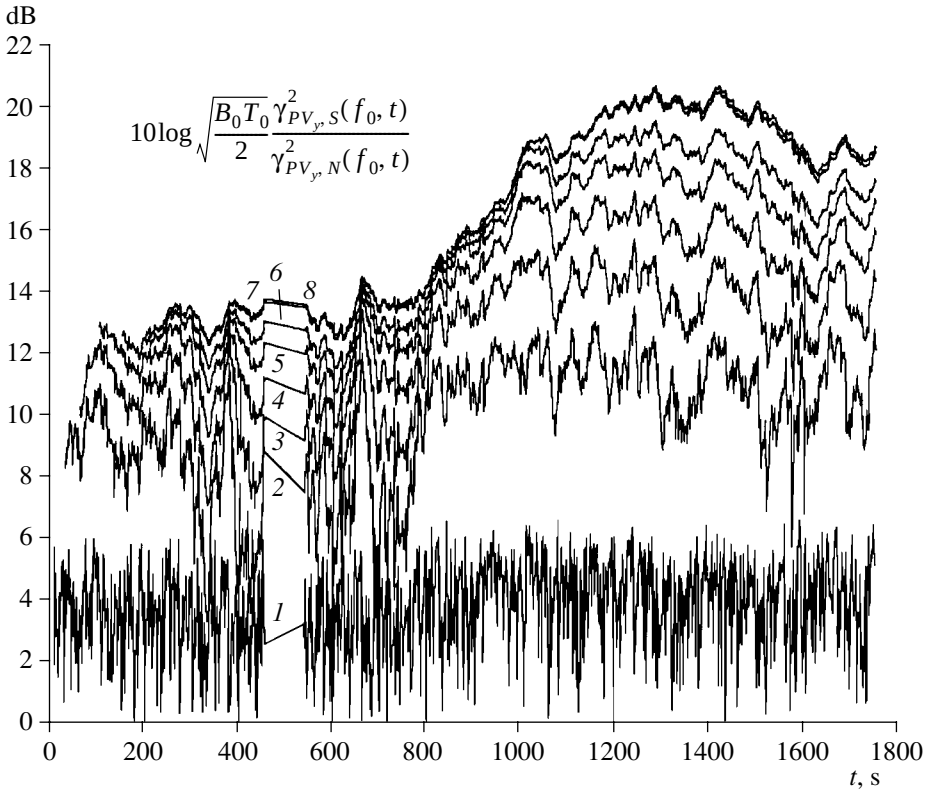

Fig. 4. Variability of the combined receiver gain at the time series t = 1800 s. The depth of measurement is 150 m. The spectrum averaging time is T_0 = (*1*) 5, (*2*) 30, (*4*) 100, (*5*) 150, (*6*) 200, (*7*) 300, and (*8*) 320 s. B_0 = 1 Hz.

intervals, the excess of the signal over the noise in the pressure spectra is constant. The signs Δ and + denote the experimental points. The solid curves correspond to the approximating dependences $a + b\sqrt{T}$ (at B_0 = 1 Hz). It follows from Fig. 5 that the dependence of $\left\langle 10\log\sqrt{\frac{B_0T_0}{2}}\frac{\gamma^2_{PV,S}(f_0)}{\gamma^2_{PV,N}(f_0)}\right\rangle$ on T_0 is analogous to the dependence $\langle SNR(PV_y)\rangle$ [Fig. 1a and Eq. (13)].

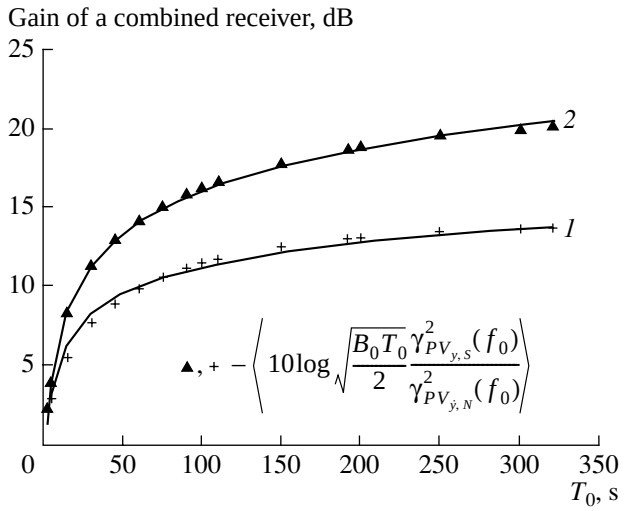

Fig. 5. Dependence of the gain on the averaging time T_0. The depth of measurement is 150 m. The experimental data for the time intervals (+) 700–800 and (▲) 1200–1500 s from Fig. 4. The solid curves (*1* and *2*) represent the approximating dependences ($a + b\sqrt{T}$), B_0 = 1 Hz.

SNR(PV) of a Combined Receiver in an Anisotropic Noise Field in the Case of the Compensation of the Signal and Noise Energy Fluxes

The vectors of the energy flux densities of signal and noise in the case of opposing superpositions can produce a resulting energy flux equal to zero. This phenomenon was observed in multiple experiments in shallow and deep seas, and it was called the compensation of opposing energy fluxes [13–15]. The compensation phenomenon can be used for the detection of a signal in noise [9, 16]. It is impossible to observe the compensation phenomenon with a hydrophone array, and, therefore, this technique of signal separation is feasible only with combined receivers. It is natural that the most interesting case is the compensation of two opposing weak energy density fluxes of signal and noise. In our case, the compensation is realized between the vertical component of the energy flux of the signal reflected from the bottom and the opposing vertical flux of energy of ambient noise that carries the noise energy of dynamic origin from the ocean surface to the bottom.

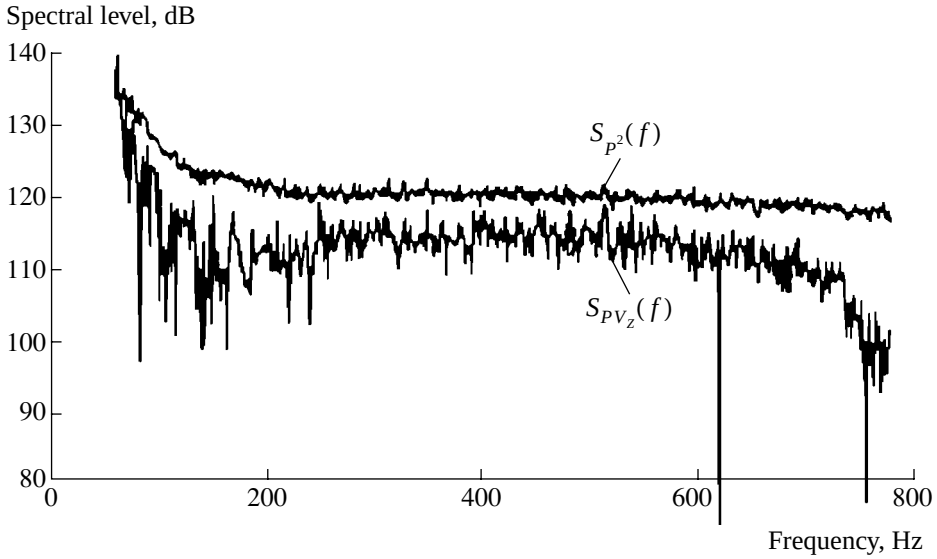

Fig. 6. Spectral densities $S_{P^2}(f)$ and $S_{PV_z}(f)$ of ambient noise. The dip at the frequency $f_0 = 622$ Hz is the result of the compensation of opposing energy fluxes of noise and a tone signal. An exponential averaging over 30 s. The depth of measurement is 150 m and the wind speed is 7 m/s.

Let us consider $SNR(PV_z)$ for the vertical component of the energy flux of a fluctuating tone signal in the conditions of compensation. Let $S_{PV_z,N}(f_0)$ be the component of the spectral density of the energy flux of noise that propagates in the direction $+z$ and $S_{PV_z,S}(f_0)$ be the component of the spectral density of the energy flux of the signal propagating in the direction $-z$. Let us form $SNR(PV_z)$ as follows. The expression $S_{PV_z,N}(f_0) - S_{PV_z,S}(f_0)$ is equal to the resulting flux along the z axis. Let us divide it by the noise level $S_{PV_z,N}(f_0)$ so that

$$SNR(PV_z) = 10\log\frac{S_{PV_z,N}(f_0) - S_{PV_z,S}(f_0)}{S_{PV_z,N}(f_0)} = 10\log\left(1 - \frac{S_{PV_z,S}(f_0)}{S_{PV_z,N}(f_0)}\right). \quad (14)$$

In the ideal limiting case of total compensation, we have $(S_{PV_z,S}(f_0))/(S_{PV_z,N}(f_0)) \longrightarrow 1$; then, $SNR(PV_z) \longrightarrow -\infty$. In the absence of a signal, $S_{PV_z,S}(f_0) = 0$ and $SNR(PV_z) = 0$. Thus, in the case of compensation of opposing energy fluxes, we always obtain $SNR(PV_z) < 0$. Let us consider an example of real compensation at the frequency of the tone signal $f_0 = 622$ Hz. Figure 6 gives the spectral levels S_{P^2} and S_{PV_z}. The time of spectrum averaging is 30 s. Averaging is exponential. The analysis band is 1.5 Hz. The depth of the dip in the spectrum S_{PV_z} (Fig. 6) reaches –30 dB, i.e., $SNR(PV_z) = -30$ dB. Physically, the dip means that, in the frequency band 1.5 Hz at the frequency $f_0 = 622$ Hz, the resulting energy flux through a unit area perpendicular to the z axis and located at the detection point is 10^3 times smaller (i.e., 30 dB smaller) than the energy flux of ambient noise in the case of the signal absence. Thus, the dip at the frequency $f_0 = 622$ Hz indicates the presence of a weak signal in ambient noise, since the value of the compensated energy flux of noise is also small.

As experiments [13–15] demonstrate, noise-like broadband signals with the spectra $S_{P^2,S}$ similar to the spectra of ambient noise $S_{P^2,N}$ are also identified in the case of the compensation. Equation (14) for a broadband signal in the frequency range f_2–f_1 has the form

$$SNR(PV_z) = 10\log\left\{1 - \int_{f_1}^{f_2} S_{PV_z,S}(f)df \Big/ \int_{f_1}^{f_2} S_{PV_z,N}(f)df\right\}.$$

CONCLUSIONS

Theoretical expressions for $SNR(PV)$ of a single combined receiver are obtained, and the combined receiver gain is introduced in the case of multiplicative processing for narrow and broad frequency bands.

From the statistical processing of experimental data, it follows that the mean-square deviation of the horizontal component of the energy flux density of dynamic noise decreases in the case of averaging as $1/\sqrt{T}$ ($B_0 = 1$ Hz) until a certain limiting averaging time is reached $T = T_k$. To obtain a reliable estimate of the value of $SNR(PV_y)$, the averaging time T_k must be 12–24 times

greater than for the reliable estimates of $SNR(P^2)$ and $SNR(V_y^2)$ for the potential and kinetic energy densities, respectively.

An experimental evaluation of $SNR(PV_y)$ and $SNR(PV_z)$ is conducted for the observation of a fluctuating tone signal against the background of underwater dynamic noise of the deep ocean.

According to the experimental estimates, the maximal gain in the signal-to-noise ratio achieved for a combined receiver measuring the energy flux density, as compared to a hydrophone measuring the potential energy density, is 15–16 dB for a horizontal energy flux and 30 dB for a vertical energy flux in the case of the compensation of opposing energy fluxes of the signal and noise.

REFERENCES

1. Kevin J. Bastyr and Gerald C. Lanchll, J. Acoust. Soc. Am. **106**, 3178 (1999).
2. G. K. Skrebnev, *Combined Hydroacoustic Receivers* (Élmor, St. Petersburg, 1997).
3. G. L. D'Spain, in *Proceedings of 2nd International Workshop on Acoustics, Engineering, and Technology* (Harbin, China, 1999), p. 143.
4. G. L. D'Spain *et al.*, in *Proceedings of Mastering the Oceans through Technology, Newport, 1992*, p. 346.
5. M. D. Smaryshev and E. L. Shendrov, Akust. Zh. **31**, 502 (1985) [Sov. Phys. Acoust. **31**, 296 (1985)].
6. V. A. Gordienko, V. I. Il'ichev, and L. N. Zakharov, *Vector-Phase Methods in Acoustics* (Nauka, Moscow, 1989).
7. I. A. Dorodnova and V. V. Ol'shevskiĭ, in *Models and Algorithms for Designing the Systems and Complexes of Acoustic Data Processing*, Ed. by V. I. Il'ichev and A. P. Lukoshkin (LIAP, Leningrad, 1990), pp. 112–117.
8. S. V. Pasechnyĭ, in *Models and Algorithms for Designing the Systems and Complexes of Acoustic Data Processing*, Ed. by V. I. Il'ichev and A. P. Lukoshkin (LIAP, Leningrad, 1990), pp. 106–112.
9. V. A. Shchurov, *Current Status and Prospects of Acoustic Intensity Measurements in Underwater Acoustics* (Preprint of TOI DVO RAN, Vladivostok Pacific Institute of Oceanology, Far East Division, Russian Academy of Sciences, 1998).
10. W. S. Burdic, *Underwater Acoustic System Analysis* (Prentice Hall, New York, 1984).
11. M. D. Smaryshev, *Handbook on Hydroacoustics* (Sudostroenie, Leningrad, 1988), Chap. 8.
12. J. S. Bendat and A. G. Piersol, *Engineering Applications of Correlation and Spectral Analysis* (Wiley, New York, 1980).
13. V. I. Il'ichev, V. P. Kuleshov, M. V. Kuyanova, and V. A. Shchurov, Akust. Zh. **37**, 99 (1991) [Sov. Phys. Acoust. **37**, 50 (1991)].
14. V. A. Shchurov, V. I. Ilyichev, V. P. Kuleshov, and M. V. Kuyanova, J. Acoust. Soc. Am. **90**, 1002 (1991).
15. V. A. Shchurov and V. I. Ilyichev, in *Natural Physical Sources of Underwater Sound*, Ed. by B. R. Kerman (Kluwer Academic, Netherlands, 1993), pp. 93–109.
16. V. A. Shchurov, V. P. Dzyuba, A. N. Shvyrev, and A. V. Shchurov, Vestn. Dal'nevost. Otd. Ross. Akad. Nauk, No. 4, 62 (1997).

Translated by M. Lyamshev